Tailoring the self-assembly, interfacial properties and rheological behaviour of sugar-based surfactants

Larsson, Johan

2021

Citation for published version (APA):
Larsson, J. (2021). *Tailoring the self-assembly, interfacial properties and rheological behaviour of sugar-based surfactants*. Lund University (Media-Tryck).

Total number of authors:
1

Tailoring the self-assembly, interfacial properties and rheological behaviour of sugar-based surfactants

JOHAN LARSSON | DIVISION OF PHYSICAL CHEMISTRY | LUND UNIVERSITY

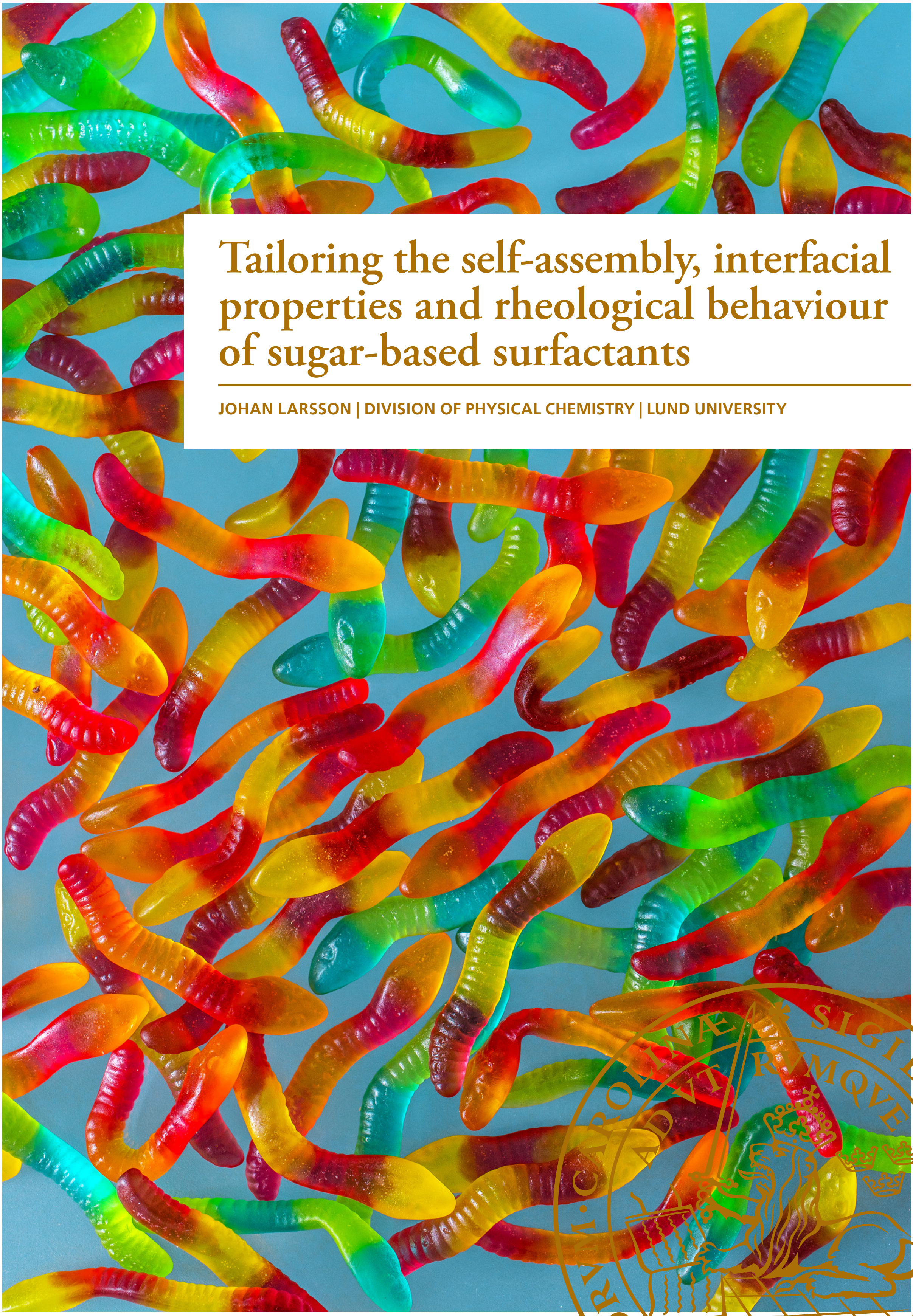

Tailoring the self-assembly, interfacial properties and rheological behaviour of sugar-based surfactants

Tailoring the self-assembly, interfacial properties and rheological behaviour of sugar-based surfactants

by

Johan Larsson

LUND
UNIVERSITY

DOCTORAL DISSERTATION

by due permission of the Faculty of Science, Lund University, Sweden.
To be defended on the 29th of January 2021 at 09:00 in Lecture hall A at the Department of Chemistry, Lund University.

Faculty opponent

Professor Motomu Tanaka
Heidelberg University, Heidelberg, Germany

Organization **LUND UNIVERSITY** Department of Chemistry Box 124 SE–221 00 LUND Sweden	Document name **DOCTORAL DISSERTATION** Date of disputation 2021-01-29 Sponsoring organization Swedish Research Counsil Formas Grant number: 2015:666
Author(s) Johan Larsson	

Title and subtitle

Tailoring the self-assembly, interfacial properties and rheological behaviour of sugar-based surfactants:

Abstract

Surfactants are important ingredients in many formulated products used in everyday life. Many of these surfactants originates from fossil-based materials and degrades slowly in aquatic systems. As society strives towards having a smaller environmental footprint, surfactants that are non-toxic, biodegradable and can be synthesized from renewable raw materials need to be developed. To this end sugar-based surfactants, or alkylglycosides, is a promising class of surfactants that have the properties that are sought after. To utilize these surfactants to their full potential more knowledge is required about their behaviour both at interfaces and in solution.

In this thesis the behaviour of the alkylglycoside $C_{16}G_2$, and how it is affected by small changes in its molecular structure, has been studied with scattering techniques and rheometry. The anomeric configuration was found to have a large impact as β-$C_{16}G_2$ allowed for a more efficient packing of the headgroup, compared to α-$C_{16}G_2$. This is apparent both at interfaces, where the adsorption was higher for the β anomer, and in solution, where β-$C_{16}G_2$ forms very elongated worm-like micelles while α-$C_{16}G_2$ forms shorter cylindrical micelles. The difference in self-assembly affects the rheological behaviour of these solutions where highly viscous, shear thinning and viscoelastic properties reflects the long micelles of β-$C_{16}G_2$, while solutions of α-$C_{16}G_2$ are Newtonian with low viscosity. The effect of introducing a double bond in the tailgroup of β-$C_{16}G_2$ was also investigated, where a significant decrease in Krafft point was seen, while the formation of worm-like micelles and viscous solutions was still evident.

Key words

Sugar-based surfactants, Self-assembly, Scattering, Rheology, Adsorption, Sustainable materials

Classification system and/or index terms (if any)

Supplementary bibliographical information	Language English
ISSN and key title	ISBN 978-91-7422-776-5 (print) 978-91-7422-777-2 (pdf)

Recipient's notes	Number of pages 169	Price
	Security classification	

I, the undersigned, being the copyright owner of the abstract of the above-mentioned dissertation, hereby grant to all reference sources the permission to publish and disseminate the abstract of the above-mentioned dissertation.

Signature ____________________ Date 2020-12-07

Tailoring the self-assembly, interfacial properties and rheological behaviour of sugar-based surfactants

by

Johan Larsson

LUND
UNIVERSITY

This doctoral thesis is constructed as a summary of research papers and consists of two parts. An introductory text puts the research work into context and summarizes the main conclusions of the papers. Then, the research publications themselves are reproduced. The research papers may either be previously published or manuscripts at various stages.

Cover illustration front: Sugar worms in solution.
Photo: Michael Gehrisch

Cover illustration back: Aligned sugar worms in solution.
Photo: Michael Gehrisch

Funding information: The thesis work was financially supported by the Swedish Research Council Formas

Faculty of Science, Department of Chemistry, Division of Physical Chemistry

ISBN: 978-91-7422-776-5 (print)
ISBN: 978-91-7422-777-2 (pdf)

Printed in Sweden by Media-Tryck, Lund University, Lund 2021

NORDIC SWAN ECOLABEL
Printed matter
3041 0903

Media-Tryck is an environmentally
certified and ISO 14001:2015 certified
provider of printed material.
Read more about our environmental
work at www.mediatryck.lu.se

We are all the winners, we are all the best.
Att vi får va tillsammans, det betyder mest.

- Nick Borgen

TABLE OF CONTENTS

Acknowledgements

There are a lot of people that supported me in the making of this book.

Thank you to the hoard of supervisors that gave me the opportunity to take on this project and that have guided me on my scientific journey. It must have been a heavy task considering how many that was needed. **Tommy Nylander**, thank you for taking on the role as my main supervisor and the responsibility that comes with that title. Thank you for showing me how a proper beam-time is done, especially regarding the importance of planning the experiments to always have time for a nice dinner. **Marie Wahlgren**, thank you for handling me during the last, stressfull time and for answering my calls at 10 pm on a Saturday. **Stefan Ulvenlund**, thank you for putting up with me ever since my master thesis and for sharing your endless knowledge about surfactants with me. **Adrian Sanchez-Fernandez**, thank you for sweeping in like a scientific superhero halfway through the journey, teaching me the art of proposal writing and climbing. **Patrick Adlercreutz**, thank you for the discussions on sugar-based surfactants. In my next PhD i promise to do more enzymatic synthesis.

Thank you to all of my colleagues at the division of Physical Chemistry for contributing to the nice environment. I am especially grateful for all the cake I was provided. The Nylander group, **Maria, Polina, Karolina, Jen and Ben**, thank you for the good times, in the office, in the lab and elsewhere. **Axel**, thank you for always taking the time to find solutions to my problems. **Linda**, thank you for making tough days easier with afternoon walks and bizarre news. **Guanqun**, thank you for taking care of me in your home country, and my plants when I forgot to water them. **Marco**, thank you for the Italian dinners.

Thank you to my family and friends outside the university for your constant support. **TSAHVL**, thank you for the board game nights and fun discussions. **Cathrine and Osman**, thank you for the barbecue dinners and Rocket League games. Tack, **Mamma, Far, Jolina och Per**, för allt. Tack, **Louise**, för att du förgyller mitt liv.

Populärvetenskaplig sammanfattning

Tensider är molekyler som är viktiga ingredienser i många produkter som används varje dag, till exempel rengöringsmedel, schampo och läkemedel. Den unika egenskapen hos tensider är att de är amfifila. Det betyder att molekylerna är uppdelade i två delar där den ena delen, huvudet, är vattenlöslig och den andra delen, svansen, är fettlöslig. Detta gör att tensider dras till, och adsorberar vid, gränsytor mellan olika material så att den vattenlösliga delen är i det materialet som är mest likt vatten och den fettlösliga delen är i materialet som är mest likt fett. När tensider adsorberar vid en yta sjunker ytspänningen vilket innebär att mindre energi krävs för att göra ytan större. Det kan till exempel bidra till att lösligheten av fettbaserade material, som smuts och olja, ökar i vatten. När tensider löses i vatten bildar de strukturer som kallas miceller. Bildandet av miceller grundas i oviljan hos svansarna att vara i kontakt med vatten. I miceller utgör svansarna en kärna som är omgiven av de vattenlösliga huvudena för att minimera kontakten mellan svansarna och vattnet. Formen och storleken av micellerna varierar beroende på tensidernas uppbyggnad och egenskaper.

Många av de tensider som används mest idag produceras från fossila råvaror. De kan även ha stor negativ påverkan i naturen om de bryts ned för långsamt på grund av deras ytaktiva egenskaper. För att minska den negativa påverkan på miljön från tensider är det därför viktigt att utveckla och ta reda på mer om tensider som kan produceras från förnybara material och som snabbt bryts ned i naturen. Detta arbete har fokuserat på en klass av tensider som tillverkas av de förnybara råvarorna socker och vegetabilisk olja och därmed är en god kandidat att ersätta mindre miljövänliga tensider. Det har utretts hur små förändringar i den molekylära strukturen av tensiden påverkar micellens form och storlek och hur tensiden adsorberar vid ytor.

Genom att ändra vinkeln på kopplingen mellan huvud och svans i tensiden kunde formen på micellerna som de bildar ändras från att vara liten och rund till att bli väldigt lång och utdragen och bilda så kallade masklika miceller. Vid tillräckligt höga tensidkoncentrationer trasslar dessa avlånga miceller ihop sig, vilket leder till att vätskan som de är i får speciella flödesegenskaper, bland annat blir den mer trögflytande. Detta är eftertraktat i många applikationer, t.ex. färg och schampo. Kopplingen mellan huvud och svans påverkar också hur mycket tensid som adsorberar vid ytor. Dessa skillnader kommer sig av att de olika tensiderna packas olika effektivt, både i miceller och vid ytor.

Vidare visade sig en liten ändring i svansens struktur leda till en ökad löslighet i vatten vid låga temperaturer, samtidigt som de övriga egenskaperna bibehålls.

Kunskapen som detta arbetet bidragit med underlättar den pågående omställningen till mer miljömässigt hållbara produkter.

List of publications

This thesis is based on the following publications, referred to by their Roman numerals:

I **Effect of the anomeric configuration on the micellization of hexadecylmaltoside surfactants**
J. Larsson, A. Sanchez-Fernandez, N. Mahmoudi, L. Barnsley, M. Wahlgren, T. Nylander, S. Ulvenlund
Langmuir **2019**, 35, 13904-13914

II **Molecular structure of maltoside surfactants controls micelle formation and rheological behavior**
J. Larsson, A. Sanchez-Fernandez, A. E. Leung, R. Schweins, B. Wu, T. Nylander, S. Ulvenlund, M. Wahlgren
Journal of Colloid and Interface Science **2021**, 581, 895-904

III **Shear-induced nanostructural changes of worm-like micelles formed by sugar-based surfactants**
J. Larsson, M. Wahlgren, L. Porcar, S. Ulvenlund, T. Nylander, A. Sanchez-Fernandez
Manuscript in preparation for submission

IV **Tail unsaturation tailors the thermodynamics and rheology of a self-assembled sugar-based surfactant**
J. Larsson, A. E. Leung, C. Lang, B. Wu, M. Wahlgren, T. Nylander, S. Ulvenlund, A. Sanchez-Fernandez
Journal of Colloid and Interface Science **2021**, 585, 178-183

V **Interfacial behaviour and structure of sugar-based surfactants at the solid-liquid interface**
J. Larsson, M. Wahlgren, A. E. Leung, A. Sanchez-Fernandez, J. Cooper, N-J. Steinke, S. Ulvenlund, T. Nylander
Manuscript in preparation for submission

All papers are reproduced with permission of their respective publishers.

Author contributions

Paper I: Effect of the anomeric configuration on the micellization of hexadecylmaltoside surfactants

Planned the project together with the co-authors. Conducted the majority of the experimental work. Analyzed the small angle scattering data together with ASF and analyzed the rest of the results. Wrote the first draft of the manuscript and edited the manuscript together with the co-authors.

Paper II: Molecular structure of maltoside surfactants controls micelle formation and rheological behavior

Planned the project together with the co-authors. Conducted the majority of the experimental work. Synthesis was performed by AL. Analyzed the small angle scattering data together with ASF and analyzed the rest of the results. Wrote the first draft of the manuscript and edited the manuscript together with the co-authors.

Paper III: Shear-induced nanostructural changes of worm-like micelles formed by sugar-based surfactants

Planned the project together with the co-authors. Conducted the majority of the experimental work. Analyzed the small angle scattering data together with MW and ASF. Wrote the first draft of the manuscript and edited the manuscript together with the co-authors.

Paper IV: Tail unsaturation tailors the thermodynamics and rheology of a self-assembled sugar-based surfactant

Planned the project together with the co-authors. Conducted the majority of the experimental work. Synthesis was performed by AL. Analyzed the small angle scattering data together with ASF. Wrote the first draft of the manuscript and edited the manuscript together with the co-authors.

Paper V: Interfacial behaviour and structure of sugar-based surfactants at the solid-liquid interface

Planned the project together with the co-authors. Conducted the majority of the experimental work. Synthesis was performed by AL. Analyzed the reflectivity data together with TN. Wrote the first draft of the manuscript and edited the manuscript together with the co-authors.

Publications not included in this thesis

Liquid crystal phantom for validation of microscopic diffusion anisotropy measurements on clinical MRI systems
M. Nilsson, **J. Larsson**, D. Lundberg, F. Szczepankiewicz, T. Witzel, C.-F. Westin, K. Bryskhe, and D. Topgaard
Magnetic Resonance in Medicine **2018**, 79, 1817-1828

CHAPTER

I

AIM OF THESIS

In this thesis the behaviour induced by different variations in the molecular structure of $C_{16}G_2$ has been investigated at interfaces and in solution. The work presented in this thesis contributes to the collective effort of expanding the knowledge about sustainable materials that facilitates the transition to more environmentally benign products.

In particular the aim has been to

- Elucidate the effect of headgroup configuration on micelle structure, rheological behaviour and adsorption to interfaces.
- Understand how mixtures of different configurations can be used to tailor these properties.
- Determine the effect of unsaturation of tailgroup on the Krafft point, micelle structure and rheological behaviour.

CHAPTER

2

INTRODUCTION

2.1 Surfactants

Surfactants, short for surface active agents, are amphiphilic materials, meaning that the molecule consists of a hydrophilic, or polar, part and a hydrophobic, or non-polar, part.[1] The polar part, referred to as the headgroup, is soluble in polar solvents, like water, while the non-polar part, referred to as the tailgroup, prefers to be in non-polar environments, like oil or air. This causes surfactants to adsorb at interfaces, which lowers the interfacial tension and the free energy of the system. Surfactants are classified based on their hydrophilic part into ionic and non-ionic surfactants. The ionic group can be further divided into anionic, cationic and zwitterionic. In contrast non-ionic surfactants have a neutral moiety as headgroup. The hydrophobic part most often consists of one or more alkyl chains with typically 8-18 carbon atoms.[2]

Surfactants are used for a wide range of applications from detergents and solubilizers to foaming agents, emulsifiers and membrane protein stabilizers.[3] Surface active molecules are plentiful in nature, most commonly in the form of polar lipids. These are the materials that make up the cell membrane of living cells, solubilizes fats and proteins in our bodies and facilitates breathing by lowering the surface tension in our lungs.[4]

2.2 Surfactant bulk behaviour

When dissolved in water the surfactants disrupt the hydrogen bonds between the water molecules. For the hydrophilic headgroup, new favourable interactions can be formed with the water, but for the hydrophobic tail this is not the case. This causes the water closest to the tails to form a solvation shell which results in loss of entropy and thus increases the free energy of the system.[5] At a certain concentration, the critical micelle concentration (cmc), surfactants start to form aggregates called micelles.[6] In micelles, the tails are in the center, shielded by the headgroups that are facing the water. The main driving force for micelle formation is the hydrophobic effect. When the surfactant tails are assembled, the water molecules in the solvation shell is released, greatly reducing the interaction between the tails and the water, and thus reducing the free energy of the system.[7] There are also forces acting against micelle formation, which is why micelles are not formed at concentrations below the cmc. The counter-acting forces are primarily the loss in entropy from the ordering of the surfactants and the repulsion between the headgroups. The repulsion can be both steric and electrostatic, depending on the class of surfactant. The cmc is thus the point at which these opposing forces are of equal value. The cmc can be seen as the solubility limit of the surfactant monomers and the lowest concentration at which micelles are formed.[8]

Temperature is an important parameter for micelle formation. The solubility of surfactants is temperature dependent since the solubility of the hydrophobic tail increases with increasing temperature. When the solubility of the surfactant monomer is lower than the cmc, micelles will not be formed. The temperature where the solubility of the surfactant is the same as the cmc is referred to as the Krafft point.[9] At temperatures above the Krafft point the solubility of the surfactants allows for formation of micelles and the solubility is greatly increased. For more hydrophilic surfactants, with large headgroups in comparison to their tails, the solubility in water is high and the Krafft point is below 0 °C and hence never becomes relevant. But for more hydrophobic surfactants, with large tailgroups compared to its heads, the Krafft point can be above room temperature and elevated temperatures are needed for the surfactant to dissolve.[10,11]

For some surfactants, e.g. polyethyleneglycol (PEG) based surfactants, there is an upper temperature limit for the solubility as well.[12] This is due to a weakening of the hydrogen bond strength between water and the headgroup, resulting in lower solvation and eventually phase separation. The temperature where the phase separation occurs is referred to as the cloud point.[13]

2.3 Surfactant self-assembly

The size and shape of micelles are determined by the characteristics and the effective size ratio of the surfactant head- and tailgroup and how these interact with each other.[14] The micelle morphology can be estimated with the critical packing parameter (cpp), defined in Equation 2.1, where v and l_c are the volume and length of the tailgroup respectively and a_0 is the surface area per monomer at the hydrocarbon aqueous interface.[15]

$$cpp = \frac{v}{a_0 l_c} \tag{2.1}$$

a_0 is highly dependent on the repulsion between headgroups, where large repulsive interactions leads to large a_0. For ionic surfactants the most important contribution comes from the electrostatic repulsion whereas for non-ionic surfactants steric hindrance is most significant. If the cpp is low ($\leq$ 1/3) spherical micelles are formed, for slightly larger cpp (1/3$\leq$ cpp $\leq$ 1/2) elongated or rod-like micelles are prefered and surfactants with 1/2 $\leq$ cpp $\leq$ 1 are most likely to assemble into vesicles or lamellar sheets. In other words, the curvature of the micelle structure is decreasing with increasing cpp. This is illustrated schematically in Figure 2.1 for three surfactants with varying tailgroup volume.

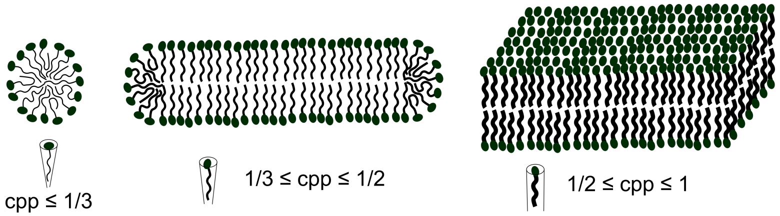

Figure 2.1: Self-assembly structure of micelles with different cpp.

At very high surfactant concentrations liquid crystalline structures are formed, e.g. hexagonal, lamellar and cubic.[16-19] If surfactants are dissolved in a non-polar solvent, reversed micelles can be formed, where the headgroup forms the core and the tails are facing the solvent.[20] The work in this thesis has been conducted exclusively in the dilute or semi-dilute regime with polar solvents.

2.3.1 Worm-like micelles

Under certain packing conditions, cpp between 1/3 and 1/2, elongated micelles are formed, which was first found by Debye and Anacker in the early 1950's.[21] An elongated micelle is made up of a cylindrical body, which is the preferred curvature of the surfactants, and two hemisherical endcaps, one in each end of the cylinder. There is an energy cost for these surfactants to be situated in the endcaps due to the unfavourable curvature. Thus, a majority of the surfactants resides in the cylidrical body of the micelle, resulting in unidimensional micelle growth and a decrease in the number of endcaps.

There are three structural dimensions that are important for elongated micelles: Contour length (L), persistence length (l_p) and radius (r).[22] These are schematically displayed in Figure 2.2. The radius is connected to the length of the extended surfactant monomer and is rarely affected by environmental changes for the system, eg. concentration or temperature. The persistence length is the length of an elongated micelle that can be considered a rigid rod. Another way to see it is that for two points within the length of l_p there is correlation in the direction of the micelle, while if the distance between the points is larger than l_p the directional correlation is lost.

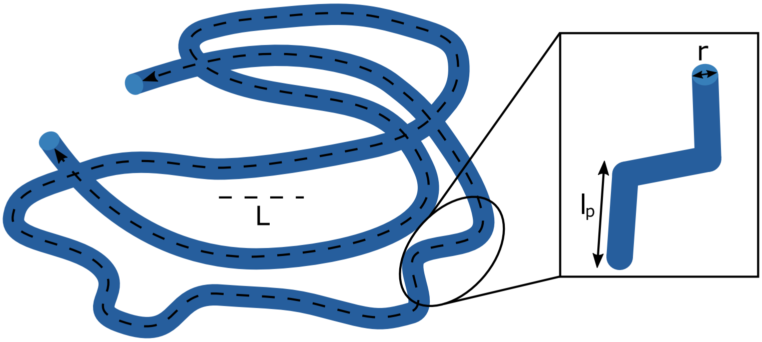

Figure 2.2: Schematic structure of an elongated micelle showing the characteristic length scales. Contour length (L), persistence length (l_p) and radius (r).

Micelles are dynamic, flexible structures, but there is an energy cost in bending the cylindrical shape originating in deviations from the desired curvature of the micelle. For short elongated micelles, $L = l_p$ and the micelle has the structure of a rigid rod. For very long micelles, kinks are introduced in the structure due to the gain in entropy leading to $L > l_p$. These very elongated, flexible micelles are called worm-like micelles (WLM) and can be up to several µm long.

There are a number of ways to facilitate micelle growth and induce the formation of WLM. Most of these decrease the effective headgroup size of the surfactant allowing closer packing and resulting in a higher cpp, close to 1/2. For ionic surfactants the ionic strength is important, which can be controlled by the addition of salt.[23] The salt ions screen the repulsive interactions between the headgroups and thus reduce a_0.[24] Non-ionic PEG surfactants are temperature sensitive and the solvation of the headgroup decreases with increasing temperature, resulting in a decrease in the steric repulsion between the headgroups.[25] Micelle growth can also be obtained by the addition of a co-surfactant with a small headgroup that can intercalate between the surfactants. This increases the volume of the hydrocarbon chain and increases the cpp.[26] The surfactant concentration is also effecting the cpp, which for most system increases with increasing concentration.[27] If the cpp is increased too much the preferred curvature of the micelle will be lower than that of a cylinder and branched networks or vesicles is formed instead.[28]

2.4 Rheology of surfactant solutions

The structure of WLM described above gives solutions of these surfactants intriguing flow behaviour.[29] In the dilute regime, at very low concentrations, there is no interactions between the micelles and the viscosity is usually low and Newtonian, i.e. independent of the shear rate. However, due to the length of WLM intermicellar interactions becomes important already at very low concentrations. The concentration of the onset of these interactions is referred to as the overlap concentration (c*), which marks the start of the semi-dilute regime were the micelles entangle, leading to an increase in viscosity. Upon shearing, WLM align in the direction of the flow resulting in a decrease in the number of entanglement points, effectively decreasing the viscosity. This results in a non-Newtonian, shear thinning behaviour, meaning that the viscosity decreases with increasing shear rate.[30] The shear thinning properties emerge in a specific shear rate region. At shear rates above and below this region they are often Newtonian, i.e. the viscosity is independent on shear rate. The value of the viscosity on the Newtonian plateau at low shear rates is called the zero-shear viscosity (η_0). The shear rate where the viscosity starts to deviate from the η_0 is called the critical shear rate. When shear is increased beyond the shear thinning region the system reaches the viscosity value η_∞. Some surfactant systems forming elongated micelles show an opposite behaviour where the viscosity increases when it is subjected to flow.[31] This shear thickening behaviour is attributed to a shear induced elongation of the micelles by end-to-end fusion, that is facilitated by the alignment of the micelles.[32,33]

The morphology of WLM also gives its solution viscoelastic properties, meaning that it has both a viscous and an elastic response when subjected to stress. A viscous material deforms through the diffusion of molecules when put under stress and does not regain its shape when the stress is removed. A classic example of a viscous material is water. An elastic material can change its shape during stress through stretches of bonds involved in the structure, but when the stress is removed the original shape is regained. A typical example of an elastic material is a spring. The viscoelastic properties are time dependent since stretching of bonds are faster than the diffusion of molecules. This means that if a stress is applied to a viscoelastic material for a short time, the response will be mainly elastic and if it is applied for a long time the viscous properties will dominate.

There are two main relaxation mechanisms in action when stress is applied to an entangled WLM system. One is called reptation, which is the diffusion of the elongated micelle along its contour length. For a single elongated micelle, the surrounding micelles practically make up a tube in which it is confined. This tube restricts diffusion through the tube walls, making reptation the only way to diffuse. This mechanism is quantified by the reptation time (τ_{rep}), which is the time it takes for the micelle to reptate out of the tube. The other relaxation mechanism is the breaking and reformation of micelles. This is characterized by the breakage time (τ_b), which is the lifetime of a micelle before it breaks, typically on the order of milliseconds for WLM.[34] These mechanisms have contrasting dependences on the micelle elongation where τ_{rep} scales with L^3 and τ_b scales with L^{-1}. This have the implication that for shorter micelles $\tau_b \gg \tau_{rep}$ and there is no micelle breakage in the time it takes for the micelle to relax through reptation. For very elongated WLM systems on the other hand $\tau_{rep} \gg \tau_b$ and there are several occurrences of micelle breakage and reformation in the time it takes for a micelle to reptate through its tube. Even though the polydispersity in WLM systems is very high,[35] the fast breaking and reformation of micelles yields a single relaxation time (τ) which depends on the two relaxation mechanisms according to Equation 2.2.[36]

$$\tau = \sqrt{\tau_{rep}\tau_b} \tag{2.2}$$

This means that the viscoelastic behaviour can be modelled with the Maxwell model.[37]

2.5 Surfactant adsorption

Non-ionic surfactants adsorb at interfaces due to two main driving forces, based on their amphiphilic properties. One is the energetic gain from reducing the number of interactions between hydrophobic and hydrophilic materials by having the surfactant headgroup interact with the hydrophilic and the tailgroup with the hydrophobic material. The other is the hydrophobic effect which is driving the tailgroup away from interactions with the polar solvent. In most systems the contribution from the hydrophobic effect is the main driving force of the two.[38] This means that, generally, surfactants with a larger hydrophobic tailgroup show stronger adsorption. In addition adsorption can be driven by a decrease if solubility of the surfactant, i.e. by temperature change for non-ionic surfactants and increasing the ionic strength, in particular multivalent counter-ions, for ionic ones. This can lead to the formation of multilayers.[39] The adsorption isotherm, describing the amount of adsorbed surfactant as a function of bulk concentration, varies depending on the properties of the interface, i.e. if it is an air-liquid, liquid-liquid or solid-liquid interface and if the materials are hydrophilic or hydrophobic.[40] In this thesis adsorption at the air-water interface and at the solid-water interface, for both a hydrophilic and a hydrophobic solid, have been investigated.

At a hydrophobic surface, including the air-water interface, the surfactants align with the tailgroup towards the surface and the headgroup facing the water. For most systems a monolayer of surfactants is formed,[41,42] but there are also examples of systems where the surfactants adsorb in other structures, eg. hemimicelles or elongated hemimicelles.[43,44] At a hydrophilic surface the headgroup faces the surface and since that leaves the tailgroup in the unfavourable situation of facing the water a monolayer is not possible for this interface. Instead the adsorbed surfactant layer have a similar structure as the micelles formed in the bulk of the solution. It is thus depending on the cpp of the surfactant. A surfactant that is prone to form globular micelles in solution will be likely to adsorb in a structure with high curvature at the interface and for a surfactant with a high cpp a low curvature structure, such as a double layer, will be preferred.[45]

A common feature for the adsorption isotherm for all of these interfaces is that the adsorbed amount of surfactant reaches a plateau at the cmc. The surfactant monomer concentration, and thus the surface activity, is essentially constant for concentrations above the cmc, causing this behaviour.[40] The adsorbed amount of surfactants above the cmc depends on how efficient the packing of the surfactants is, and hence on the molecular structure. For example, in a double layer structure twice the amount of surfactants is adsorbed, compared to a monolayer.

The onset of adsorption at a hydrophobic surface is generally at a lower concentration compared to at a hydrophilic surface, due to the impact of the hydrophobic effect. At concentrations close to the cmc the adsorption at hydrophilic interfaces is mainly driven by attractive interactions between the tailgroups of the surfactants adsorbed at the interface, leading to a cooperative adsorption isotherm.[41]

2.6 Sustainable surfactants

Enormous amount of surfactants are produced every year since they are widely used in plenty of different technologies and products. As a result, they are present in the environment and their environmental impact needs to be considered.[46,47] There are two aspects to this, namely the toxicity and the biodegradability. The ecotoxicity of surfactants is significant due to their surface activity and ability to disrupt biological membranes. The degradation of surfactants in the environment depends on the molecular structure of the surfactant. Degradation leads to a loss of the surface activity and from this follows, in most cases, a loss of toxicity. This makes the biodegradability of surfactants the most important factor in determining its ecotoxicity.[48] There are several surfactants used nowadays that have a long lifetime in the environment. As a consequence, the surfactant industry is responsible for a significant share of the environmental footprint. This can be reduced by shifting the production towards more sustainable surfactants that are non-toxic, readily biodegradable and can be synthesized with renewable resources.[49] As a part of this transition, more knowledge has to be collected about the behaviour of surfactants fitting this profile.

2.6.1 Alkylglycosides

Alkylglycosides are sugar-based, nonionic surfactants consisting of a carbohydrate headgroup and an alkyl chain tailgroup. There are plenty of different carbohydrate monomers, but the most studied alkylglycosides have glucose or maltose in the headgroup. The abreviation commonly used for alkylglycosides is C_nG_m, where n is the number of carbon atoms in the tail and m is the number of glucose units in the head. There has been a considerable amount of work on the behaviour of this class of surfactants. Regarding the micelle structure, several morphologies were found, from spherical to elongated cylinders and branched networks.[50-55] The elongated micelles of $C_{14}G_2$ also induced an elevated viscosity and a viscoelastic behavior at high surfactant concentration.[56] Regarding the adsorption at interfaces, it has been shown to depend on the surface properties. For hydrophilic surfaces, the adsorption is very low on silica but a strong adsorption is seen at the titania and aluminum surface.[41,57] High adsorption is also found for hydrophobic interfaces such as air and graphite.[41,58]

The work in this thesis has been focused on the behavioural aspects of hexadecylmaltoside, $C_{16}G_2$. The headgroup configuration of alkylglycosides, referring to the way the head- and tailgroup are connected, is also important and affects the surfactant behaviour. If the tail is connected in the axial position of the sugar, it is called α, if it is connected in the equatorial position, it is called β. Variations in the headgroup configuration have been shown to affect the self-assembly behaviour.[59,60] The effect of a double bond in the alkyl chain has also been studied through characterisation of the entirely novel surfactant palmitoleyl-β-D-maltoside, $C_{16-1}G_2$. Furthermore, these sugar-based surfactants have been shown to alter the viscosity of the system in a tailorable fashion. Figure 2.3 shows the molecular structure of α-$C_{16}G_2$, β-$C_{16}G_2$ and β-$C_{16-1}G_2$.

Alkylglycosides are beneficial from an environmental point of view since they can be synthesized from renewable raw materials and are readily biodegradable.[48] They are thus a promising candidate to replace the fossil-based surfactants that are mostly used nowadays. Alkylglycosides, as non-ionic surfactants in general, are a mild surfactants, which is a desirable property in applications like cosmetics and healthcare products.[61-63] Because of this they are already used in several products, mainly in products for per-

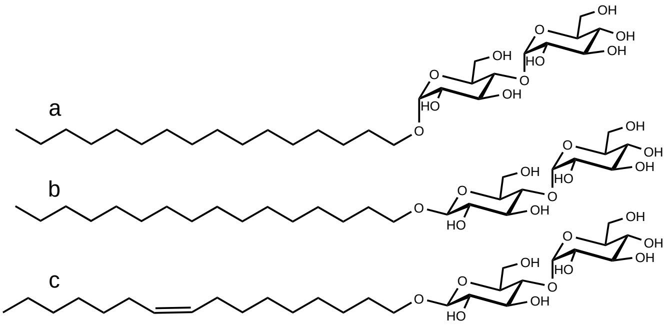

Figure 2.3: Molecular structure of α-$C_{16}G_2$ (a), β-$C_{16}G_2$ (b) and β-$C_{16-1}G_2$ (c).

sonal care, home care and crop care,[3] but also in more speciffic applications like membrane protein extraction.[64,65] However, these commercial alkylglycosides are dominated by saturated alkyl chains in the range C_8 through C_{12}. The understanding of the behaviour, and hence the applicability, of alkylglycosides with longer alkyl chains is very limited. For alkylglycosides with unsaturated chains it is non-existent.

CHAPTER

3

EXPERIMENTAL METHODS

In this chapter the experimental techniques used in this thesis are introduced. Tensiometry and calorimetry have been used to investigate the boundaries for micelle formation with respect to concentration and temperature, respectively. Micelle morphology was studied with small angle x-ray and neutron scattering, static and dynamic light scattering and cryogenic transmission electron microscopy. The flow properties of the surfactant solutions were analysed with rheometry. The behaviour of the surfactants at the solid-liquid interface was examined by ellipsometry and neutron reflectometry.

3.1 Tensiometry

Tensiometry is the measurement of surface tension and a common method to determine the critical micelle concentration (cmc) of surfactants.[66] The cmc is determined by measuring the surface tension at several concentrations around the cmc to find the concentration at which the surface tension goes from decreasing to constant values with increasing surfactant concentration. There are several techniques to measure the surface tension of a liquid. An important point to take into consideration when choosing which of these methods to use is how the surface area to volume ratio affects the measurement.[67] This is especially important when working with surfactants with low cmc. When the surfactants adsorb at the interface, the concentration in the bulk decreases.

If the surface-to-volume ratio is high the depletion effects need to be considered since they may lead to a significant decrease in the surfactant bulk concentration, resulting in an incorrect determination of the surface tension.[68] An example of a technique where the surface-to-volume ratio is high is the pendant drop method. In this method the surface tension is determined from the shape of a pendant drop with a volume of around 20 µl. The work in this thesis has been focused on $C_{16}G_2$, which has a relatively big hydrophobic tail group resulting in a low cmc. For this reason, the Du Noüy ring method was chosen to determine the cmc, since it is a technique with a low surface-to-volume ratio. A platinum ring of known dimensions is emerged in the solution and the force required to pull the ring out of the solution is used to calculate the surface tension (σ) of the air-liquid interface according to Equation 3.1.[69]

$$\sigma = \frac{F}{Lcos\theta} \tag{3.1}$$

Here F is the applied force, L is the sum of the inner and outer circumference of the ring and θ is the contact angle between the ring and the solvent. The surface-to-volume ratio of the air-liquid interface was minimized by using a narrow and tall beaker with a radius of only 1 cm larger than the platinum ring.

3.2 Differential scanning calorimetry

Differential scanning calorimetry (DSC) is a technique to measure the heat capacity (Cp) as a function of temperature. The Cp varies for different phases of the material and DSC can be used to determine these phase changes and at which temperature they occur.[2] The Krafft point is one of these transitions, which represent the onset of substantial surfactant dissolution. This is demonstrated by a sharp peak in the Cp at the Krafft point.

3.3 Scattering methods

Scattering techniques are generally used to determine the structure of materials on very small lengthscales. This is done by studying the way radiation scatters when interacting with the material. There are several different types of scattering techniques and radiations. The techniques used in this thesis are static light scattering (SLS), small angle x-ray and neutron scattering (SAXS and SANS), dynamic light scattering (DLS) and reflectometry. The following section presents an overview of these techniques and a more detailed description can be found in these references.[70-73]

A typical scattering event is schematically described in Figure 3.1. The scattering event can be either elastic or inelastic, with elastic meaning that no energy is exchanged between the radiation and the material. In this thesis only elastic scattering is discussed. The incoming planar wave vector of radiation (k) hits the sample, in this case symbolized with point scatterers i and j, resulting in a spherical scattered wave vector (k_s). Since the scattering is elastic the moduli of the incoming and scattered wave vectors are the same, $|k|=|k_s|$. From the scattered radiation, the relative positions of i and j can be determined.

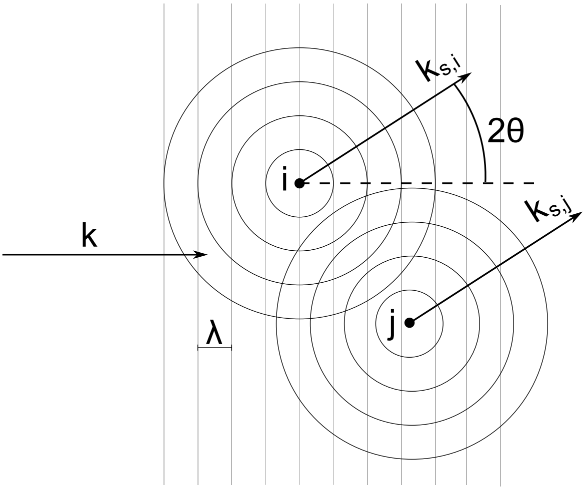

Figure 3.1: Schematics of a scattering event.

A detector collects the scattered radiation at a scattering angle 2θ, and the sample-to-detector distance is typically varied during an experiment to obtain results at a wide range of angles. The scattering vector (Q) is defined from the relation of k and k_s as $Q=k-k_s$ and the magnitude of Q can be calculated with Equation 3.2. Here, λ is the wavelength of k.

$$Q = \frac{4\pi sin(\theta)}{\lambda} \tag{3.2}$$

In a scattering event with two scatterers the distance between them (r) and their interaction with the radiation give rise to an interference pattern of the scattered radiation. The resulting scattering amplitude depends on Q according to Equation 3.3.

$$A_s(Q) = b_i b_j e^{-iQr} \tag{3.3}$$

Here, b is the scattering length of each scatterer. This is a property that describes how the radiation interacts with the material and effectively becomes the contrast of the experiment. It gives information about the probability of the radiation to interact with the material. In a real scattering experiment there are plenty of scatterers in the sample. Taking the density of the scatterers into account the scattering length density (SLD) is obtained.

In this thesis different radiation sources have been used, namely light, x-rays and neutrons. In light scattering b depends on the refractive index. For x-rays, which interacts with the electrons of the atom, b depends on electron density and thus it is proportional to the atom number of the material. For neutrons, which interact with the nucleus of the atom, the origin of the scattering is more complex. b varies, seemingly at random, between different materials and it is not straightforward to explain this phenomenon. Interestingly, since neutrons interact with the nucleus, the scattering length is different for different isotopes. For experiments with samples consisting of protiated compounds and where there otherwise is hard to get good contrast, like surfactant solutions in water, isotopic substitution is an essential tool. By changing the H_2O/D_2O ratio of the solvent or by synthesizing molecules where protium has been exchanged for deuterium it is possible to highlight different parts of the particle under investigation, see Figure 3.2. This is called contrast variation. A specific contrast variation condition is achieved when the SLD of different parts of the system is the same and thus there is no contrast. This is referred to as contrast matching.[74]

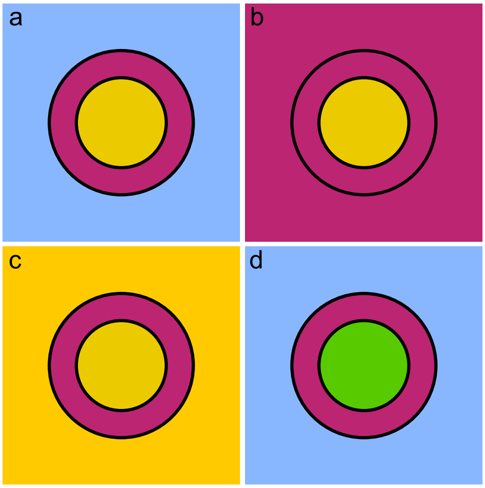

Figure 3.2: Schematic illustration of contrast in neutron scattering of a core-shell sphere. (a) Symbolises the contrast for the protiated surfactant in pure solvent. (b) The solvent is contrast matched to have the same SLD as the shell to highlight the scattering from the core. (c) The solvent is contrast matched to have the same SLD as the core to highlight the scattering from the shell. (d) The protium in the core has been exchanged for deuterium.

3.3.1 SAXS/SANS

Small angle scattering methods access structural information in the mesoscopic length scale, from a few nanometers to a few micrometers. The obtained results from a scattering experiment is the intensity of radiation as a function of Q as described in Equation 3.4 for a centrosymmetric uniform particle.

$$I(Q) = n_p V_p^2 \Delta SLD^2 P(Q) S(Q) \tag{3.4}$$

Here, n_p is the number of particles, V_p is the volume of a particle, P(Q) is the form factor and S(Q) is the structure factor. The form factor is the interference of the scattered radiation from different parts of the same particle, which means that it contains information on the morphology of the particles. The structure factor is the contribution of interference of the scattering from different particles, meaning that it contains information about the interactions between the particles or how the particles are positioned relative to each other. In dilute samples the distance between the particles is too large for S(Q) to affect the scattering, and thus S(Q)=1.

The majority of the work of a successful scattering experiment is done after the actual measurement and when the data are analysed. There are different ways to do this, and different methods give various level of details, but also require different levels of prior knowledge.

First, estimations on the dimensions of the scattering particles can be made from noticing at which Q-values different features appear by using the relation in Equation 3.5. The fact that Q is inversely proportional to the dimension (D) of the scattering particle tells us that scattering at high Q-values gives information about small structures and scattering at low Q-values elucidates large structures.

$$D = \frac{2\pi}{Q} \tag{3.5}$$

For dilute, non-interacting particles at low enough Q-values ($QR_g < 1$) the structure factor and the form factor are not contributing to the scattering and the Guinier approximation (Equation 3.6) is valid.[75] From this the radius of gyration (R_g) can be calculated from the scattered intensity when $Q \rightarrow 0$ ($I(0)$).

$$I(Q) \approx I(0)\left(1 - \frac{Q^2 R_g^2}{3}\right) \tag{3.6}$$

To obtain detailed structural information about the studied particles, mathematical models can be fitted to the data. To be able to select the best model for the data some information about the studied system is needed. There are numerous models available in the literature and in this thesis the SasView software has been used for data analysis.[76] In Figure 3.3 three examples of form factors are presented to show how the intensity is depending on Q in different regions for three common structures.

If the particles studied are larger than what can be measured with the setup of the instrument then the Guinier region is not seen, as for the lamella in Figure 3.3. This means that the overall size of the particle cannot be determined. In the mid-Q region the Q-dependence reveals information about the shape of the particle where the intensity have a Q^{-1}-dependence for cylinders and a Q^{-2}-dependence for lamellar sheets. At the highest Q the intensity relates to the surface scattering and a Q^{-4}-dependence is seen for smooth interfaces. This is referred to as the Porod region.

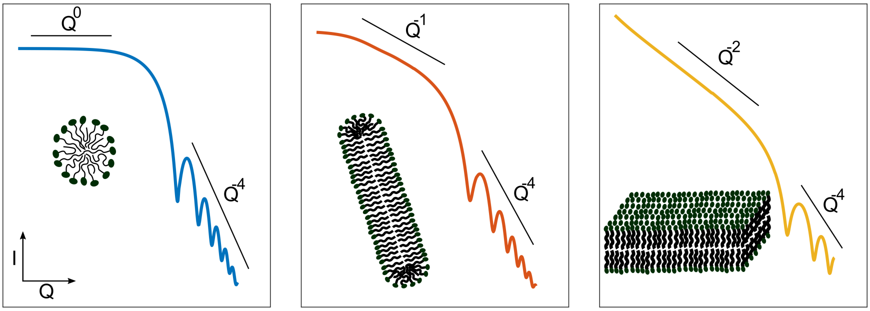

Figure 3.3: Typical small angle scattering form factor for spheres (blue), cylinders (red) and lamellas (yellow). The black lines show how the intensity (I) varies with Q in different regions.

3.3.2 Rheo-SANS

Many materials, including WLM, undergo structural changes under flow. Since the mid 1980's it has been possible to study these changes with SANS.[77,78] Rheo-SANS, which, as the name implies, is a combination of rheometry and SANS, is a powerful technique where the macroscopic flow properties and microscopic molecular structure can be studied simultaneously.[79] At sufficiently high shear rates WLM align with the flow of the solution resulting in anisotropic ordering of the micelles. This can be examined in three different shear planes: the flow-vorticity (1-3), the gradient-vorticity (2-3), and the flow-gradient plane (1-2), see Figure 3.4.[80] The scattering is different in the three planes and thus provides complementary information that contribute to the full characterisation of the system.

In this thesis rheo-SANS was performed in the 1-3 plane, where WLM are elongated in the horizontal Q-projection at high shear rates.[81] This results in an increase in the

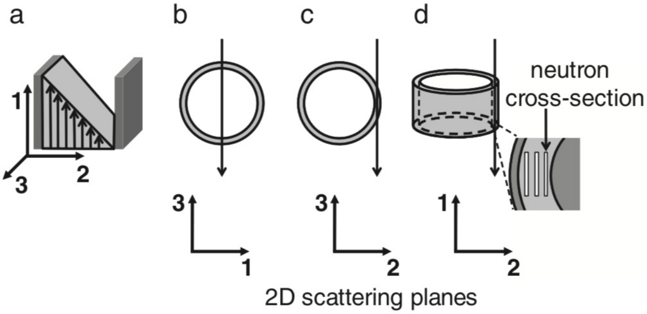

Figure 3.4: Schematic illustration of the three accessible planes for rheo-SANS experiments with a Couette cell geometry. (a) Coordinates for the direction of flow (1), gradient (2) and vorticity (3). Neutron beam path (black arrow) relative to the cell in the 1-3 (b), 2-3 (c) and 1-2 (d) plane. Reproduced from Eberle and Porcar, ***Curr. Opin. Colloid Interface Sci.*** **2012**, 17 (1), 33-43; with permission from Elsevier.

scattered intensity in the vertical projection as seen in Figure 3.5, where two different ways to analyse anisotropic scattering are also illustrated. For static SANS experiments, where an isotropic scattering is expected, the scattered intensity is averaged into one dimension for all azimuthal angles. For anisotropic scattering this can instead be done for sectors in the vertical and horizontal projection respectively. When the micelles start to align, the intensity is increasing in the vertical projection and decreasing in the horizontal projection. Another way to analyse anisotropic scattering is to compare the scattered intensity from a narrow Q-range (Q∗) at different azimuthal angles.

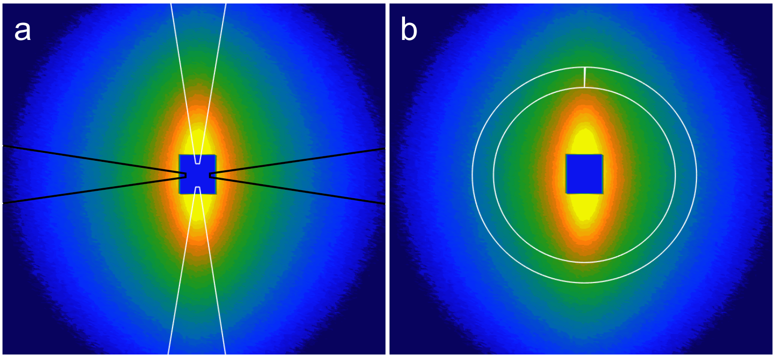

Figure 3.5: Analysis of anisotropic scattering from rheo-SANS. (a) sectors in the vertical (white) and horizontal (black) direction with an angle of 18 °C from which the scattered is averaged at different Q. (b) the scattered intensity for a narrow Q-range (0.05 ± 0.005) is analysed at different angles.

From this, an alignment factor (A_f) can be calculated according to Equation 3.7, where A_f=0 indicates isotropy and no orientation of the micelles and A_f=1 imply full alignment of all micelles with the flow.[82]

$$A_f(Q*) = \frac{\int_0^{2\pi} i(Q*, \phi)cos(2(\phi - \phi_0))d\phi}{\int_0^{2\pi} i(Q*, \phi)d\phi} \tag{3.7}$$

3.3.3 Dynamic scattering

In dynamic scattering the fluctuations resulting from e.g. Brownian motion is observed. In the case for dynamic light scattering (DLS), which is the technique used in this thesis, a laser of a specific wavelength in the visible spectrum irradiates on a liquid sample containing particles. The difference in refractive index between the particles and the solvent causes the photons to scatter resulting in a speckle pattern on a 2D detector, which is set at a specific angle. After a delay time (τ), the particles have changed position resulting in a change in the speckle pattern.[83] For small τ there is no change in the intensity and there is full correlation, while for large τ there is time for the particles to diffuse and the correlation is lost. This is described by the intensity correlation function (Equation 3.8).[84]

$$g_2(Q,\tau) = \frac{\langle I(t)I(t+\tau)\rangle}{\langle I(t)^2\rangle} \tag{3.8}$$

$g_2(Q,\tau)$ is the second-order autocorrelation function and $I(t)$ is the intensity at a time t. To extract information from this the first order correlation function ($g_1(Q,\tau)$) has to be calculated through the Siegert relation (Equation 3.9).

$$g_2(Q,\tau) = 1 + \beta[g_1(Q,\tau)]^2 \tag{3.9}$$

This can, assuming non-interacting monodisperse hard spheres, be rewritten as Equation 3.10, where Γ is the decay rate.

$$g_1(Q,\tau) = e^{-\Gamma\tau} \tag{3.10}$$

The decay rate and the the diffusion coefficient (D) are connected according to Equation 3.11.

$$\Gamma = Q^2 D \tag{3.11}$$

Through Stokes-Einsteins equation (Equation 3.12) the hydrodynamic radius (R_h) of the particles can be obtained. Here k_B is Boltzmann's constant, T is the temperature, η is the viscosity.

$$D = \frac{k_B T}{6\pi\eta R_h} \tag{3.12}$$

This calculation is only valid for non-interacting hard spheres and thus, R_h is the radius of a hard sphere with the obtained diffusion coefficient. So from this calculation no information on the shape of the particle is gained. In addition, potential hydrated solvent has to be taken into account, since this affects the diffusion of the particle.

3.4 Rheometry

Rheometry is the measurement of the flow properties of a material. The typical way to measure the rheology of a surfactant solution is shown in Figure 3.6. The solution is put between two surfaces with known areas (A) and with a narrow spacing (h). One of the surfaces is subjected to a force (F) which makes it move with a velocity (v), resulting in a strain (s) on the solution. This will create a velocity gradient in the liquid making the liquid layer closest to the moving surface flow with the same velocity as the moving surface, while the liquid layer closest to the fixed surface is at rest. The shear stress (σ) is defined as σ=F/A and the shear rate ($\dot{\gamma}$) is defined as $\dot{\gamma}$=v/h. There are different geometries that can be used in rheological measurements eg. cone-plate, plate-plate and bob-cup. The plate geometries is preferable since the sample volume needed for these geometries is low, but for measurements at elevated temperature the bob-cup geometry is the best choice as it reduces evaporation effects.

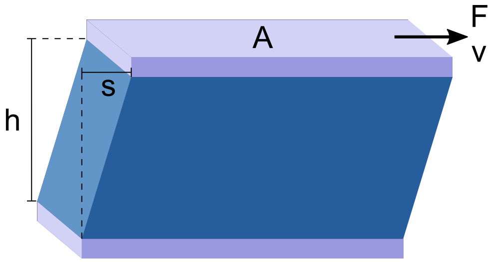

Figure 3.6: Dimensions of a rheology experiment. h is the distance between the surfaces, s is the strain, A is the area of the moving surface and F is the force put in to move the surface.

In this thesis the rheology was measured in two different ways; through continuous shear and oscillatory shear. From continuous shear experiments the viscosity (η) can be calculated as $\eta = \sigma/\dot{\gamma}$. By measuring η at different $\dot{\gamma}$ it can be determined if the sample has Newtonian or non-Newtonian properties.

With oscillatory shear experiments the viscoelastic properties of the samples are investigated. Here the moving surface is oscillated in a sinusoidal pattern at different angular frequencies (ω) with a set shear stress. Normally the shear stress is set to be within the linear viscoelastic region of the material, which is where the strain is proportional to the stress and the structure of the material is not destroyed. This yields values of the viscous (G'') and elastic modulus (G'). The relaxation time (τ) of a viscoelastic WLM solution is determined from the inverse of ω when G'=G''.

In WLM solutions the modules follow a Maxwell behaviour and can be described with the Maxwell model according to Equation 3.13 and 3.14. G'_{∞} is the plateau value of G' at high $\dot{\gamma}$.

$$G' = G'_{\infty} \frac{(\omega\tau)^2}{1 + (\omega\tau)^2} \tag{3.13}$$

$$G'' = G'_{\infty} \frac{\omega\tau}{1 + (\omega\tau)^2} \tag{3.14}$$

From the rheological properties of WLM solutions several conclusions can be drawn on the micelle structure and the interactions between the micelles.[85-87]

3.5 Ellipsometry

Ellipsometry is an optical technique where elliptically polarised light is used to study interfaces.[88] Upon reflection at the interface, the amplitude (A) and phase (δ) of the incoming polarised light is changed depending on the optical properties of the material at the interface. From the change in polarisation structural information can be obtained. The parameters that are measured in ellipsometry experiments are the ellipsometrical angles Δ and Ψ which are the changes in phase difference and amplitude ratio, respectively. These can be used to calculate the refractive index and thickness of the adsorbed layer.[89]

In this thesis in situ null ellipsometry was used to study the adsorption of surfactants at solid-liquid interfaces. In this technique the ellipsometrical angles of the incoming light is set so that reflection at a reference surface cancels out the ellipticity, resulting in linearly polarised light that can be analysed with another polarizer. This analyser position is then set so the light intensity to the detector is minimal, hence the term null-ellipsometry. When surfactants adsorb at the interface the refractive index changes and the change in ellipticity upon reflection is altered. This means that the angles for Δ, polarizer position before sample, and Ψ, analyser position after sample, leading to cancellation of the elliptically polarized light, are shifted. From this shift the change of the refractive index (n_f) and thickness (d_f) of the adsorbed film is obtained which and can be used to calculate the adsorbed amount (Γ) with Equation 3.15.[90]

$$\Gamma = \frac{(n_f - n_0) d_f}{d_n / d_c} \tag{3.15}$$

n_0 is the refrective index of the medium and d_n/d_c is the refractive index increment of the surfactant film. The adsorption is monitored in situ, meaning that also the adsorption kinetics is obtained from the experiment.

3.6 Reflectometry

The adsorption of surfactants at interfaces can result in various structures and reflectometry is a technique to study those.[73] In this thesis specular neutron reflectometry (NR) has been used. Neutron radiation follow the same laws as light, and will thus reflect and refract at interfaces between different materials. Since neutrons interact with the nucleus of the atoms the reflectivity will be dependant on the neutron SLD, which is more convenient way to express the neutron refractive index. A schematic illustration of a typical NR experiment can be seen in Figure 3.7. An incoming neutron beam of known intensity, described by the vector k_i, is reflected of the surface of a sample at different angles (θ) and the reflected beam scattering vector (k_f) is monitored at the same angle as the incoming beam by monitoring the intensity at certain wavelengths, i.e. scattering vector (Q). The critical angle (θ_{crit}) is where all neutrons are reflected and the reflection coefficient (R) equals unity. Depending on the angle, the neutrons are also refracted and continue to penetrate the sample. At the next interface they can again be either reflected or refracted, and so on. This makes it possible to examine several layers of the sample. The scattering vector (Q) is the same as for small angle scattering, see Equation 3.2.[91]

The obtained results from a reflectometry experiment is R, which is the ratio of the reflected intensity and the incoming intensity, as a function of Q, which reflects the structure perpendicular to the interface. NR results analysis is done with models, where typically the adsorbed film is divided in layers which each has its own parameters (thickness, roughness, SLD and solvation).[92] In this thesis this was done with Abeles matrix method for a stratified interface.[93] Most often multiple models fits the data, giving

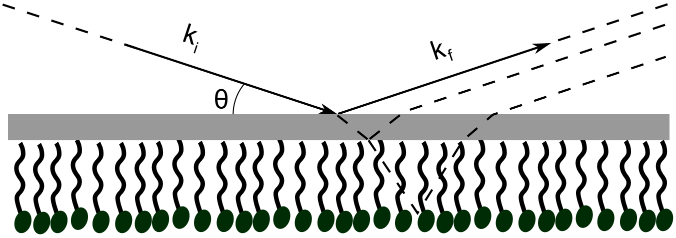

Figure 3.7: Schematic illustration of a reflectometry experiment on a surfactant monolayer.

conflicting results. It is thus crucial to perform the experiment at several different contrasts to solve this ambiguity. This can be done by either change the H_2O/D_2O ratio of the solvent or by synthesizing a deuterated version of the investigated material, as described in Figure 3.2. Prior knowledge about the studied system is also important to evaluate the models and exclude those giving unrealistic results.[94]

3.7 Transmission electron microscopy

Microscopy is used to study small objects. Light microscopes are limited by the wavelengh of light and can thus resolve objects with sizes down to hundreds of nanometres. The wavelength of electrons is on the order of pm and thanks to instrumental development, modern electron microscopes can resolve structures on an atomic level.

In transmission electron microscopy (TEM) an electron beam passes through the sample after which it is captured by a detector. Electrons interact with matter based on its electron density, which is proportional to the atom number. The electron dense parts of the sample will scatter the incoming electrons more efficiently and will appear dark whereas the parts with low electron density will appear bright.

To be able to study liquid materials, like surfactant solutions, with TEM they need to be fixated, to hinder particle diffusion in the sample and the fact that the sample has to be analysed under high vacuum conditions.[95] This can be overcome with specific sample preparation at very low temperatures (cryo-TEM). A small drop of liquid sample is applied on a carbon grid, excess liquid is removed (blotting) and the grid is rapidly frozen in liquid ethane (-183 °C). The drastic lowering of temperature is important to achieve vitrification of the sample and to avoid formation of large water crystals, which would compromise the quality of the image.[96]

CHAPTER

4

SUMMARY OF RESULTS

This chapter will be a summary of the findings in this thesis and will be divided in four sections. In the first section the effect of headgroup configuration on micelle formation and rheological behaviour will be treated (Paper I, II and III), followed by a section on how mixtures of α-$C_{16}G_2$ and β-$C_{16}G_2$ can be used to tune these properties (Paper II and III). The third section will elucidate how the Krafft point can be changed and how this affects the surfactant behaviour (Paper IV). The final and fourth section will deal with the interfacial behaviour and adsorption of the investigated surfactants (Paper I and V).

4.1 Effect of headgroup configuration

4.1.1 Micelle formation

Surfactant solutions of both α- and β-$C_{16}G_2$ show formation of micelles when dissolved in water. The morphology of these micelles were examined in Paper I and II. From DLS experiments monomodal correlation functions were obtained for all samples and the results are presented as hydrodynamic radius (R_h). R_h differs between the two surfactants and the values for β-$C_{16}G_2$ was found to be significantly larger compared to those for α-$C_{16}G_2$, at all investigated conditions (Figure 4.1). The change in R_h with the two parameters concentration and temperature was investigated. With increasing concentration there is a similar increase in R_h for both α-$C_{16}G_2$ and β-$C_{16}G_2$. This is a common trend for most micellar systems.[35] With increasing temperature there is an increase in R_h for the micelles of α-$C_{16}G_2$. There is also a slight increase for β-$C_{16}G_2$ at the lower temperatures, but between 40 and 90 °C the size of the micelles is independent of temperature. The increase in micelle size with temperature is seen also for PEG-surfactants due to dehydration of the headgroup, as explained in Chapter 2.[97] For alkylglycosides the effect of temperature on micelle size is not as straight forward. It has been shown that the micelles of C_9G_1 decreases while $C_{14}G_2$ increases in size with increasing temperature.[53,54]

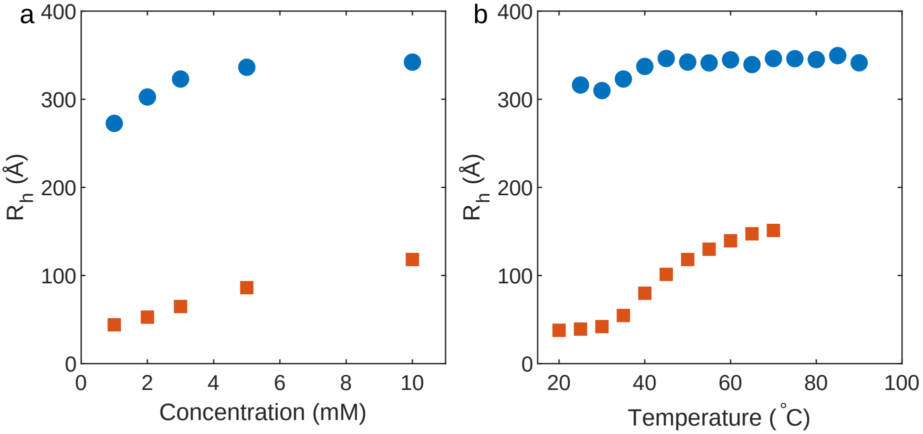

Figure 4.1: DLS results showing how the R_h of the β-$C_{16}G_2$ (○) and α-$C_{16}G_2$ (□) micelles depends on the surfactant concentration (a) and temperature (b). The temperature was 50 °C for the experiments with varying concentration and the concentration was 10 mM for the experiments with varying temperature.

For spherical micelles the radius is limited by the length of an extended surfactant monomer,[14] which is ca. 30 Å for $C_{16}G_2$. The sizes obtained from the DLS study excedes this value for β-$C_{16}G_2$ at all conditions and for α-$C_{16}G_2$ at high temperatures and concentrations. This indicates that these surfactants do not aggregate as spherical micelles.

Further detailed information on the micelle morphology was obtained from SAXS and SANS experiments, where both of these techniques showed that the large micelles have cylindrical morphology (Figure 4.2). This is evident from the Q^{-1} dependence on the intensity in the middle Q-region for both techniques.

The contour length (L) and persistencce length (l_p) of these cylindrical micelles were extracted from the SANS-data, which was fitted with a flexible cylinder model (Figure 4.2a).[98] These fits showed that the micelles of β-$C_{16}G_2$ is much more elongated than those of α-$C_{16}G_2$ (ca. 9000 Å compared to 1400 Å for 10 mM at 50 °C). The trends seen for varying concentration and temperature in the DLS results is confirmed here and the micelle growth is possible to describe as a unidimensional growth of L. The biggest difference is seen for α-$C_{16}G_2$ where a sphere-to-rod transition is found with increasing temperature, a common behaviour for non-ionic surfactants.[97,99] The length of the rigid sections of the cylindrical micelles, characterized by l_p, was found to be around 300 Å for β-$C_{16}G_2$. This shows that $L \gg l_p$ for these micelles which means that they can be properly labelled as WLM. l_p is higher than for many other non-ionic WLM,[30] which might be attributed to attractive interactions between the sugar headgroups. There is however a risk that the obtained l_p is overestimated due to that excluded volume effects are not taken into account in the model.[100,101] The α-$C_{16}G_2$ micelles have a l_p on the same order as L and are hence best categorized as rigid cylindrical micelles.

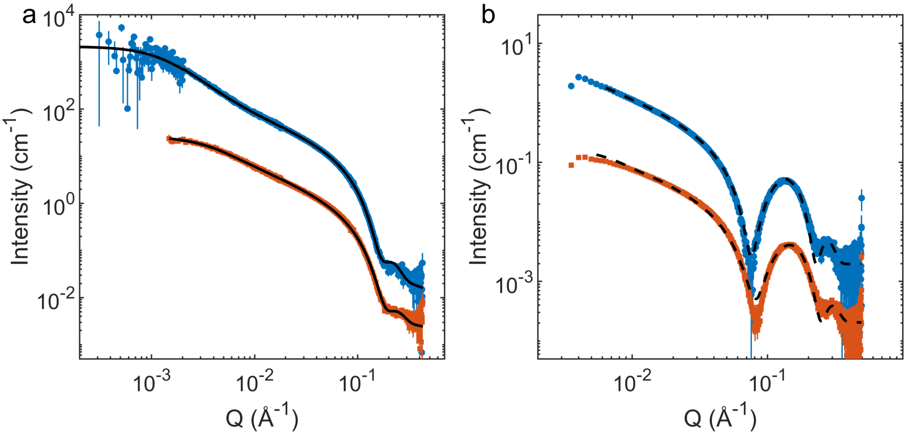

Figure 4.2: SANS (a) and SAXS (b) data for 10 mM β-$C_{16}G_2$ (blue ○) and α-$C_{16}G_2$ (red □) at 50 °C. The solid and dashed lines represent the best fits of a flexible cylinder and core-shell cylinder model respectively. The intensity for β-$C_{16}G_2$ has been offset by a factor of 10 for clarity.

The SAXS data did not provide information at low enough Q to yield information about the length of the micelles, but instead details on the cross-section dimensions can be extracted from fittings with a core-shell cylinder model (Figure 4.2b). This is possible due to the large oscillations in the high-Q region originating from the density correlation of tail-, headgroup and solvent. From this it was found that the radius of the β-$C_{16}G_2$ micelles was slightly larger compared to the α-$C_{16}G_2$ micelles (32 Å and 29 Å respectively). This can be further divided into radius of the hydrophobic core and the thickness of the headgroup shell where it was found that the core radius was 16 Å and 15 Å and the shell thickness was 16 Å and 14 Å for β-$C_{16}G_2$ and α-$C_{16}G_2$ respectively.

From these results it was concluded that the β headgroup configuration promotes a more efficient packing, probably due to a higher degree of attractive interactions between the headgroups, compared to the α headgroup configuration. These interactions could be hydogen bonds, as the hydroxyl groups act as both hydrogen bond donors and acceptors, but also hydrophobic interactions, since glucose has been shown to have amphiphilic properties in itself.[102] The more compact packing leads to a lower degree of solvation, a higher cpp and formation of more elongated cylindrical micelles with a thicker cross-section.

The micelle morphology was confirmed with cryo-TEM imaging where the difference can be seen for the very elongated WLM of β-$C_{16}G_2$ (Figure 4.3a) and the short cylindrical micelles of α-$C_{16}G_2$ (Figure 4.3b).

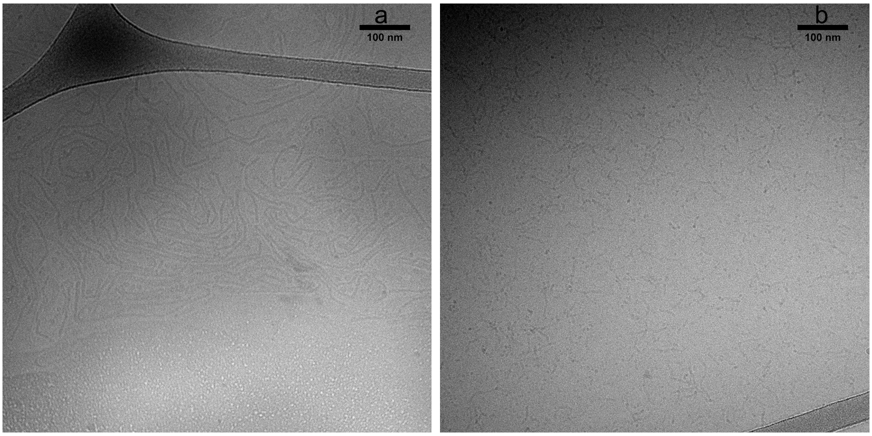

Figure 4.3: Cryo-TEM images of β-$C_{16}G_2$ (a) and α-$C_{16}G_2$ (b) at 10 mM surfactant concentration with a magnification of $6 * 10^5$x.

4.1.2 Flow behaviour

Further it was studied how the variations in micelle structure affects the macroscopic properties of the surfactant solutions through rheological measurements (Paper II). Flow curves, showing how the viscosity is varying with shear rate is presented in Figure 4.4a and b for β-$C_{16}G_2$ and α-$C_{16}G_2$ respectively. A remarkable difference is seen for the two surfactants where α-$C_{16}G_2$ solutions are Newtonian and have a relatively low viscosity even at the high concentration of 200 mM, whereas β-$C_{16}G_2$ solutions are highly viscous (700 Pas at 200 mM) and non-Newtonian for all concentrations above 10 mM. This difference is owing to the difference in elongation of the micelles for the two systems. Long micelles takes up more space than short micelles and interact and entangle to a larger extent than shorter micelles. The overlap concentration (c*) is found to be ca. 10 mM for β-$C_{16}G_2$ and at ca. 100 mM for α-$C_{16}G_2$. At increasing shear rates the micelles starts to align with the flow. This reduces the intermicellar interactions and as a result the viscosity decreases, causing the shear thinning behaviour. The

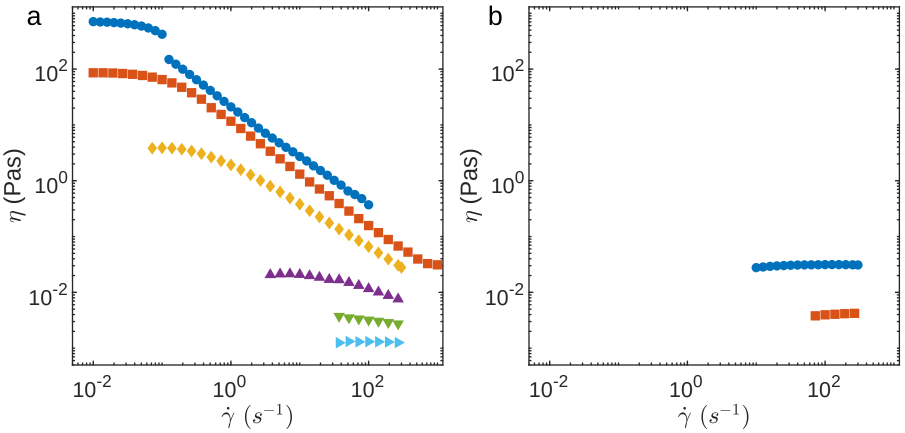

Figure 4.4: Viscosity (η) as a function of shear rate ($\dot{\gamma}$) for β-$C_{16}G_2$ (a) and α-$C_{16}G_2$ (b) at 50 °C and at different concentrations (200 (○), 100 (□), 50 (◇), 20 (△), 10 (▽) and 5 (▷) mM).

micelle alignment was studied with rheo-SANS in Paper III. Anisotropic scattering, indicating micelle alignment, was found for β-$C_{16}G_2$ at the higher shear rates (Figure 4.5a) while the scattering pattern for α-$C_{16}G_2$ was isotropic for all investigated conditions (Figure 4.5b). The rotational diffusion coefficient of cylinders decreases with increasing length.[103] The longer β-$C_{16}G_2$ micelles rotates slowly and are hence forced into alignment with the flow while the shorter α-$C_{16}G_2$ micelles rotates fast and the direction of the micelles is unaffected by the flow.[11]

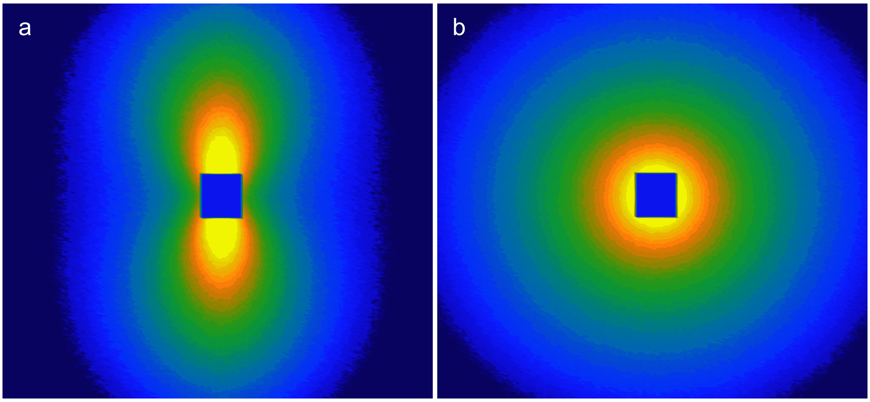

Figure 4.5: Scattering patterns from rheo-SANS for 100 mM β-$C_{16}G_2$ (a) and α-$C_{16}G_2$ (b) at a shear rate of 1000 s^{-1} and 50 °C.

The entanglements arising in a solution of WLM in the semi-dilute result in viscoelastic properties. These have been investigated by means of oscillatory rheology for β-$C_{16}G_2$. α-$C_{16}G_2$ solutions are not viscoelastic in the concentration regime and time scale studied in this thesis due to its shorter micelle length and lack of entanglements. In Figure

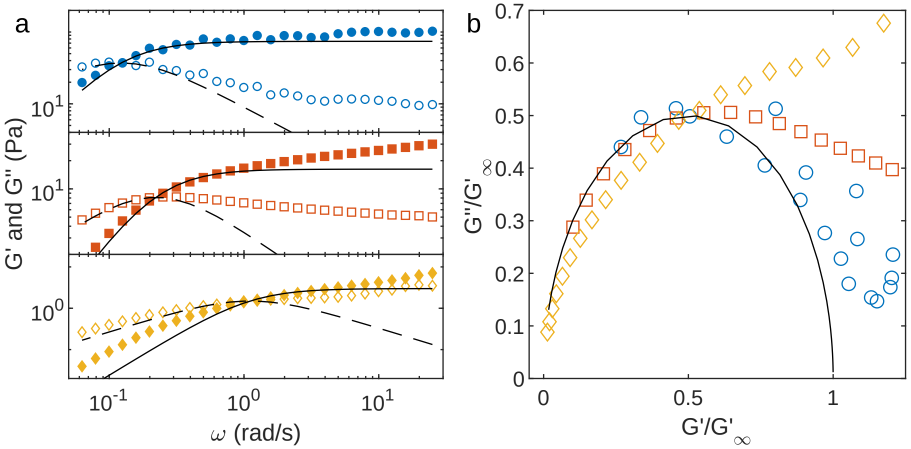

Figure 4.6: Viscoelastic behaviour of β-$C_{16}G_2$ at concentrations of 200 (○), 100 (□) and 50 (◇) mM at 50 °C. (a) G′ (filled symbols) and G″ (unfilled symbols) at varying angular frequencies. The solid and dashed lines represents the Maxwell model fit for G′ and G″ respectively. (b) Cole-Cole plot with a Maxwell model fit (solid line).

4.6a the angular frequency dependence (ω) of the viscous and elastic modulus (G″ and G′) is shown for three different concentrations of β-$C_{16}G_2$. As expected, G″ is dominating for low ω while G′ is dominating for high ω, confirming the viscoelastic properties of the material. The frequency at which G′=G″ decreases with increasing concentration, meaning that the relaxation time (τ) increases. This conforms with a growth of micelle length and an increase in the number of micelles.

The agreement of the results with the Maxwell model is also increasing with concentration, further establishing the concentration induced growth of the micelles. In this model the system is assumed to have one relaxation time as a result of $\tau_{rep} \gg \tau_b$. When the system does not follow the Maxwell model it implies that the condition $\tau_{rep} \gg \tau_b$ is not fulfilled and that the polydispersity of the WLM give rise to a range of relaxation times. A common way to display the agreement with the Maxwell model is through a Cole-Cole plot (Figure 4.6b). Here G′ and G″ are normalized with the plateau value of G′ (G'_∞) and plotted against each other. At the highest ω the Maxwell model deviates from the result for G″ also for the higher concentrations. This is seen for all WLM systems since at these time scales there are additional relaxation mechanisms that becomes relevant, such as streching of the micelle and breathing modes.[104]

As the temperature was shown to have an impact on the morphology of the micelles it is expected that it also will affect the rheological behaviour. This is confirmed with the results presented for the zero-shear viscosity (η_0) and τ in Figure 4.7a and b. It can be seen that η_0 and τ display a similar temperature dependence where both parameters go through a maximum in the studied temperature range. As L is directly connected with these parameters it is likely that this is a result of a maximum in the micelle elongation with temperature. The peak also appears to be concentration dependent as there is a shift towards lower temperatures with increasing concentration.

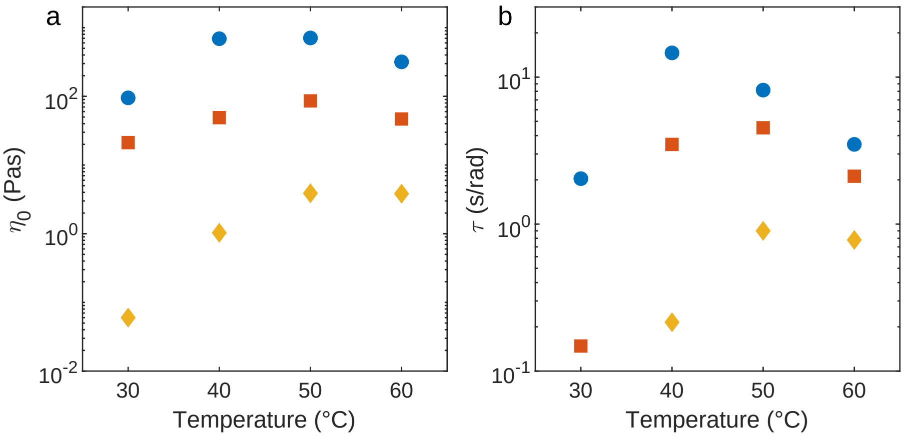

Figure 4.7: Temperature effect on the rheological behaviour of β-$C_{16}G_2$ at 200 (○), 100 (□) and 50 (◇) mM. (a) Zero-shear viscosity (η_0) and (b) relaxation time (τ).

4.2 Tuning properties with surfactant mixtures

In the last section it was shown that, despite the small difference in molecular structure, there is a considerable difference in the self-assembly and rheological behaviour of solutions of α- and β-$C_{16}G_2$. In this section it will be investigated how this behaviour is affected if the two surfactants are mixed and how mixtures can be used to tune the properties of the system (Paper II and III).

Experiments from both DLS and SANS shows that mixtures of α- and β-$C_{16}G_2$ forms micelles of intermediate size compared to solutions of the anomerically pure surfactants. For the hydrodynamic radius (r_h) presented in Figure 4.8a it can be seen that there is a gradual increase in size with increasing ratio of β-$C_{16}G_2$. The trend is the same for the contour length (L) obtained from the fitting of a flexible cylinder model to the SANS data, presented in Figure 4.8b. For all mixtures the micelles are bigger at 50 °C compared to 30 °C and there is about 1000 Å difference in L for the two temperatures at all surfactant ratios. This means that the system can be tuned from small globular micelles for α-$C_{16}G_2$ at 30 °C up to 1 µm long WLM for β-$C_{16}G_2$ at 50 °C, with the mixtures taking every size in between these extremes. There is less of a variation in the persistence length (l_p) for the surfactant mixtures (Figure 4.8c). There appears to be an increase in l_p at 30 °C with increasing α-$C_{16}G_2$ content, but it should be noted that the micelles formed at these conditions are relatively short and not perfectly suited to be fitted with a flexible cylinder model. The increase could thus be an artefact. The l_p for the other conditions is stable around 300 Å. The micelle radius (r) exhibits the same trend as L, as a gradual increase is seen for increasing ratio of β-C$_{16}$G$_2$ (Figure 4.8d).

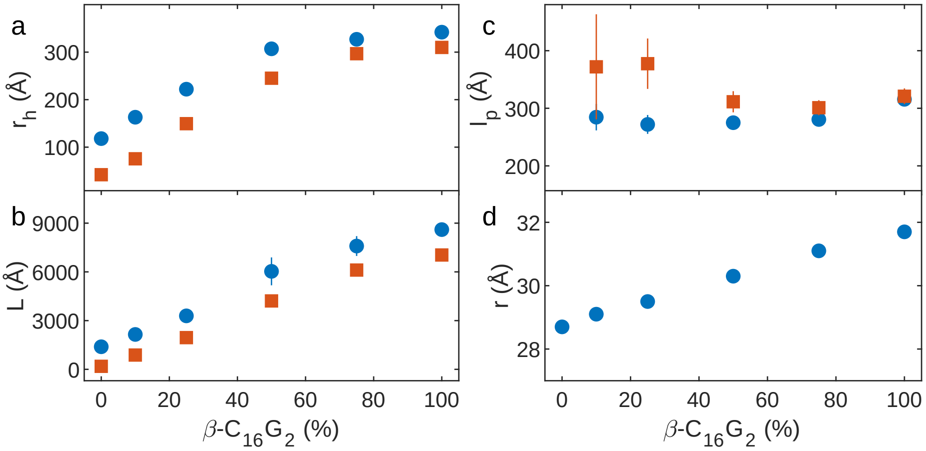

Figure 4.8: Micelle morphology for mixtures of 10 mM α- and β-C$_{16}$G$_2$ at 50 (○) and 30 °C (□). The surfactant ratios are presented as β-content where 0% is only α-C$_{16}$G$_2$ and 100% is only β-C$_{16}$G$_2$. (a) Hydrodynamic radius (r_h) obtained from DLS. (b) Contour length (L) and (c) persistence length (l_p) from fittings with a flexible cylinder model to SANS data. (d) Micelle radius (r) from fittings with a core-shell cylinder model to SAXS data.

These results indicate that the micelles formed in the mixed solutions consists of surfactants of both headgroup configurations, i.e. mixed micelles. The mixed micelle composition was investigated with contrast variation SANS complemented with SAXS for mixtures of α- and β-C$_{16}$G$_2$ where the tailgroup of the β-anomer was deuterated. From these experiments it was found that α-C$_{16}$G$_2$ is more prone to form micelles, as the ratio of α-C$_{16}$G$_2$ was higher in the micelles compared to in the bulk solution. This is in agreement with the tensiometry results which showed that the cmc of α-C$_{16}$G$_2$ is slightly lower than β-C$_{16}$G$_2$. In this study it was also found that the radius of the micelles formed by the deuterated surfactant is considerably larger than for the protiated. This is surprising considering that C-D bonds are shorter than C-H ones,[105] and a good explanation for the observation is currently lacking.

The rheological behaviour of the mixtures follow that of the micelle structure, as can be seen in Figure 4.9a. The zero-shear viscosity (η_0) goes from the low, almost water-like, value of α-C$_{16}$G$_2$, gradually increasing more than four orders of magnitude, up to ca. 100 Pas with increasing ratio of β-C$_{16}$G$_2$. This change is a reflection of the micelle growth, as the same trend is seen in Figure 4.8b. The viscosity decreases with shear rate and the shear thinning properties become more pronounced with increasing ratio of β-C$_{16}$G$_2$. In Paper III the change in micelle structure with flow was investigated with rheo-SANS (Figure 4.9b). Anisotropic scattering patterns, indicating micelle alignment, was obtained from which an alignment factor (A_f) was calculated (Figure 4.9c).

A_f is higher for the systems with the more elongated micelles and the onset of alignments also starts at lower shear rates for these. A_f reaches a plateau for 100% β-$C_{16}G_2$ at a value around 0.45, which is also seen for other WLM systems.[82]

The viscoelastic properties can also be tuned in the same way for the mixtures as displayed in Figure 4.9d. For the longer micelles formed by the systems with higher ratio of β-$C_{16}G_2$ the relaxation time is higher since it promotes a higher number of entanglement points. For the experimental setup used in this work, the 50% sample was the last to have a cross-over point from which τ could be calculated. Mixtures with higher ratio of α-$C_{16}G_2$ were found to be viscous at all investigated conditions.

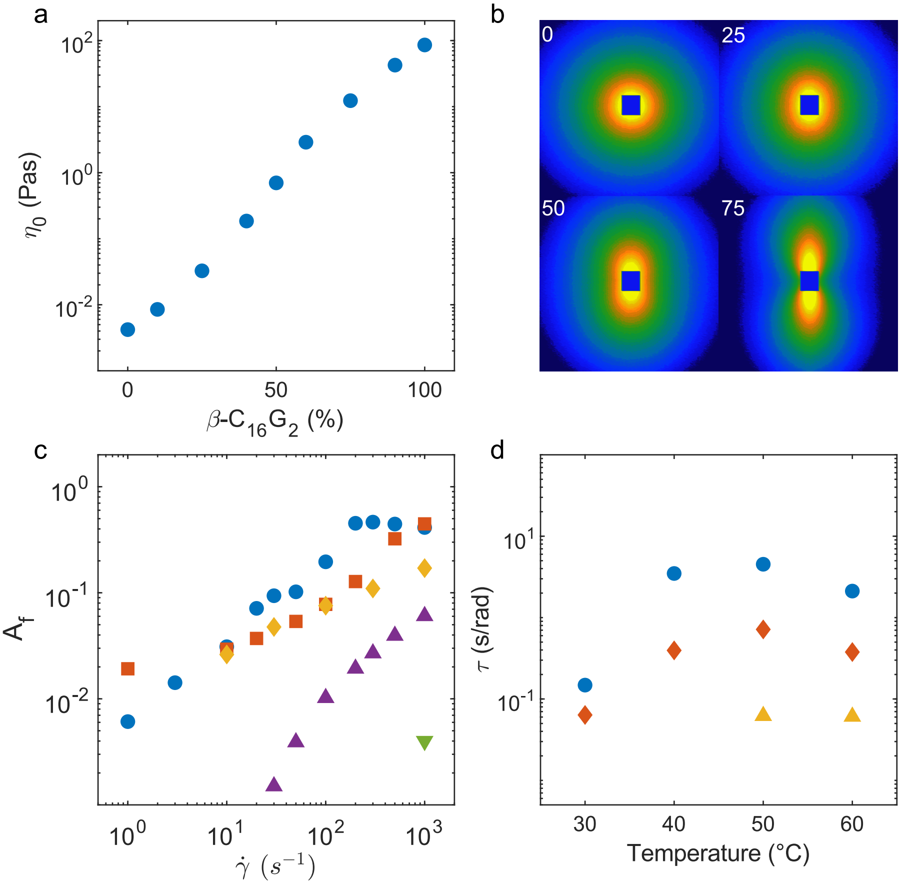

Figure 4.9: Rheological behaviour for mixtures of α- and β-$C_{16}G_2$ at a surfactant concentration of 100 mM. (a) Zero-shear viscosity (η_0) at 50 °C. (b) Rheo-SANS scattering patterns for 0, 25, 50 and 75% β-$C_{16}G_2$ at 1000 s^{-1}. (c) Alignment factor (A_f) as a function of shear rate ($\dot{\gamma}$) for 100 (○), 75 (□), 50 (◇), 25 (△) and 0% (▽) β-$C_{16}G_2$. (d) Relaxation time (τ) versus temperature for 100 (○), 90 (□), 75 (◇) and 50% (△) β-$C_{16}G_2$.

4.3 Lower Krafft point with unsaturation in tailgroup

A long alkyl chain in the tailgroup of surfactants promotes formation of very elongated WLM, but this comes with the cost of a lower solubility. The Krafft point of $C_{16}G_2$ was found to be higher than room temperature, as it was not possible to dissolve in water without heating. It has been shown that the introduction of a double bond in the tailgroup significantly decreases the Krafft point,[106] and thus β-$C_{16-1}G_2$ was synthesized in order to investigate the difference between saturated and unsaturated $C_{16}G_2$ (Paper IV). DSC was used to determine how the heat capacity (Cp) varies with temperature for the two surfactants and the thermogram is presented in Figure 4.10. There is a sharp peak for β-$C_{16}G_2$ at ca. 27 °C which is connected to the dissolution enthalpy of the surfactant and hence indicating that the Krafft point is close to 27 °C. For β-$C_{16-1}G_2$ on the other hand Cp is independent on temperature in the investigated temperature range displaying substantial increase in solubility. Solutions of β-$C_{16-1}G_2$ has been stored at 4 °C for several weeks indicating a Krafft point lower than this. The inset in Figure 4.10 shows samples of β-$C_{16}G_2$ (left) and β-$C_{16-1}G_2$ (right) which has been stored in room temperature for 72 hours. The white solids in the bottom of the cell of the β-$C_{16}G_2$ sample shows that is has precipitated, while the β-$C_{16-1}G_2$ sample is still a homogeneous solution.

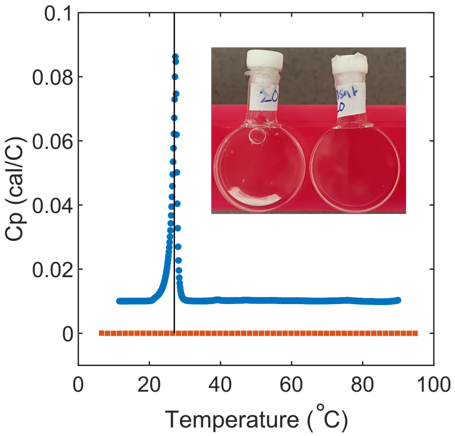

Figure 4.10: Thermogram for 50 mM β-$C_{16}G_2$ (blue ○) and β-$C_{16-1}G_2$ (red □). The vertical black line marks 27 °C. The image in the inset shows β-$C_{16}G_2$ (left) and β-$C_{16-1}G_2$ (right) which has been stored in room temperature for 72 hours.

The effect of the double bond on the micellisation was investigated. With the results of SANS and SAXS it was shown that the micelle structure of β-$C_{16-1}G_2$ is very similar to that of β-$C_{16}G_2$, as it also assembles into very elongated WLM (Figure 4.11a). The obtained contour length from the flexible cylinder model fitted to the SANS data was in the same range as for the saturated surfactant (ca 9000 Å). The persistence length obtained from the same model was 215 Å, which is significantly shorter than that of β-$C_{16}G_2$, indicating a more flexible WLM. A slight difference was also found for the cross section dimension obtained from the core-shell cylinder model fitted to the SAXS data. Both the core radius and the shell thickness was determined to be 15 Å, yielding a total radius of 30 Å, compared to 32 Å for β-$C_{16}G_2$. The double bond causes a decrease in the effective length of the surfactant monomer resulting in a smaller micelle radius.[107] The radius is connected to the stiffness of a cylindrical micelle because the energy required to bend increases with increasing micelle thickness.[108] The effect of varying concentration and temperature on the micelle size was studied with DLS. In Figure 4.11b it can be seen that β-$C_{16}G_2$ follows the ordinary trend with increasing micelle size with increasing concentration, similar to β-$C_{16}G_2$. For the temperature dependence on the other hand there is an opposite effect on the unsaturated β-$C_{16-1}G_2$, compared to its saturated analog, as the micelles becomes smaller for increasing temperatures (Figure 4.11c).

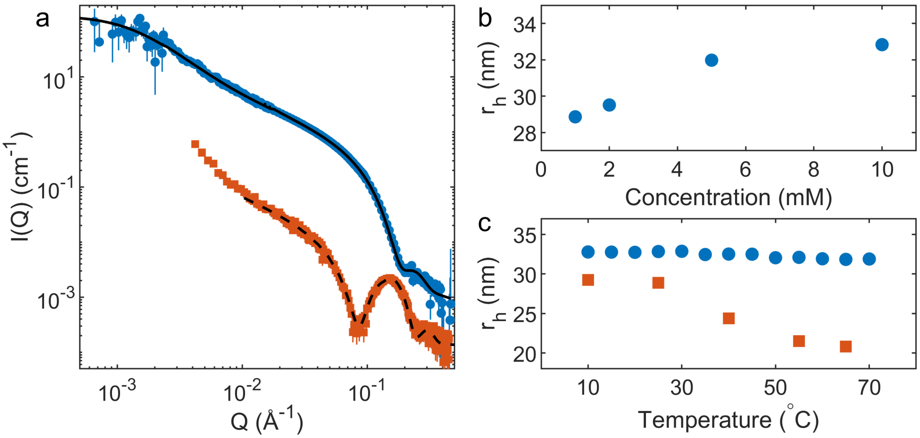

Figure 4.11: Scattering results for β-$C_{16-1}G_2$. (a) SANS (blue ○) and SAXS (red □) data for 10 mM at 50 °C. The solid and dashed lines represent the best fit of a flexible cylinder and core-shell cylinder model respectively. (b) r_h obtained from DLS as a function of concentration for at 25 °C. (c) r_h obtained from DLS as a function of temperature at a concentration of 10 (○) and 1 mM (□).

Both the linear and oscillatory rheological properties of β-$C_{16-1}G_2$ is resembling that of β-$C_{16}G_2$, which is consistent with the small differences seen in the structural determination of the micelles. In Figure 4.12a the shear thinning behaviour is presented and the zero-shear viscosity was found to be 150 Pas, slightly higher than the saturated surfactant. The viscoelastic properties is shown in Figure 4.12b. τ is almost identical to the one of β-$C_{16}G_2$ (5 s), but the unsaturated tail resulted in a slightly more Maxwellian behaviour as there is a better fit to the model. Both of these differences indicate that the double bond induces formation of more elongated micelles. In addition, when handling solutions of β-$C_{16-1}G_2$ it was found to have a stringy texture not seen for the other surfactants (Figure 4.12c). This was quantified with a tensile strength texture analysis experiment where it was shown that significantly more force was needed to pull a probe out of the solution of the unsaturated surfactant and that this force needed to be applied for a longer time. This feature was unexpected and so far no explanation has been found for it.

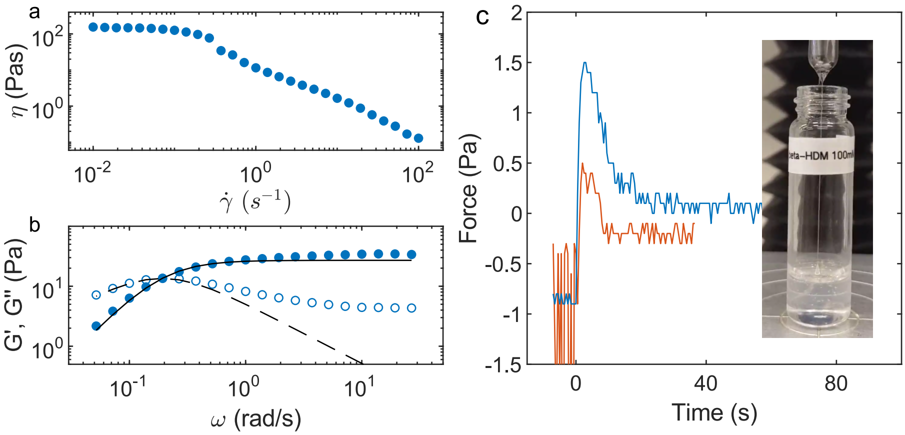

Figure 4.12: Rheologic characterization of 100 mM β-C$_{16-1}$G$_2$ at 25 °C. (a) Linear rheology with viscosity (η) versus shear rate ($\dot{\gamma}$). (b) Oscillatory rheology with G′ (filled) and G″ (unfilled) at varying angular frequencies. The solid and dashed lines represents the Maxwell model fit for G′ and G″ respectively. (c) Tensile strength texture analysis for β-C$_{16-1}$G$_2$ (blue) and β-C$_{16}$G$_2$ (red). Inset is an image showing the stringy character of β-C$_{16-1}$G$_2$.

4.4 Interfacial adsorption

4.4.1 Air-water interface

In Paper I tensiometric measurements were conducted to study the surfactant adsorption at the air-water interface and to determine the critical micelle concentration (cmc) of α- and β-C$_{16}$G$_2$. Initial experiments were performed using the pendant drop technique, which yielded values that were one order of magnitude higher than expected. The cmc for surfactants with long alkyl chains is low, and in the present case of C$_{16}$G$_2$ measurements at concentrations in the submicromolar concentration range is needed for an accurate determination. It was found that at these concentrations, the experiment was suffering from depletion effects because the surface to volume ratio of the drop was too high and it did not contain enough surfactants to fully cover the surface. Instead the Du Noüy ring method was used, where a large beaker of surfactant solution could be used to ensure a sufficiently low surface to volume ratio.

The results obtained from the measurements of surface tension versus concentrations with the Du Noüy ring method is presented in Figure 4.13. The results are similar for the two surfactants and the surface tension of solutions of both α- and β-C$_{16}$G$_2$

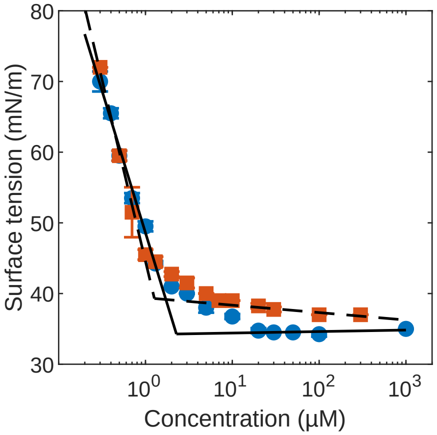

Figure 4.13: Surface tension as a function of concentration for β-$C_{16}G_2$ (○) and α-$C_{16}G_2$ (□) at 23 °C. The solid and dashed lines are fitted to the pre- and post micellar regime for β- and α-$C_{16}G_2$ respectively to determine the cmc.

decreases with increasing concentration, from just over 70 mN/m for water down to 37 and 35 mN/m at high concentrations for α- and β-$C_{16}G_2$ respectively. The slightly lower value for β-$C_{16}G_2$ indicates a higher adsorption of this anomer. The cmc was determined from the intersection of fits to the pre- and post micellar regime. The transition between the two regimes is not sharp, indicating contamination of another surface active compound.[109] The values obtained were 1 µM for α-$C_{16}G_2$ and 2 µM for β-$C_{16}G_2$. The α anomer have a lower cmc also for C_8G_1 and $C_{12}G_2$.[59,60] This indicates that the α anomer is slightly more hydrophobic and more prone to form micelles, as also strongly suggested by the contrast matched SANS experiment of the mixed micelles in Paper II.

4.4.2 Solid-water interface

In Paper V the adsorption at the solid-water interface was studied for both a bare silica surface and a hydrophobized silica surface. No adsorption was detected on the bare silica surface of any of the studied surfactants. This complies with previous reports for other alkylglycosides showing no, or very low adsorption.[41,57] In contrast, strong adsorption is observed on hydrophobized silica and the isotherm for α- and β-$C_{16}G_2$ is presented in Figure 4.14a.

The onset of adsorption is at 0.1 µM for both surfactants after which a steep increase in adsorbed amount (Γ) is seen. The maximum adsorbed amount is reached at 3 µM, just above the cmc. The value of Γ above the cmc differs for the two anomers and it is higher for β-$C_{16}G_2$ compared to α-$C_{16}G_2$ (3.9 and 3.4 µmol/m^2 respectively). The

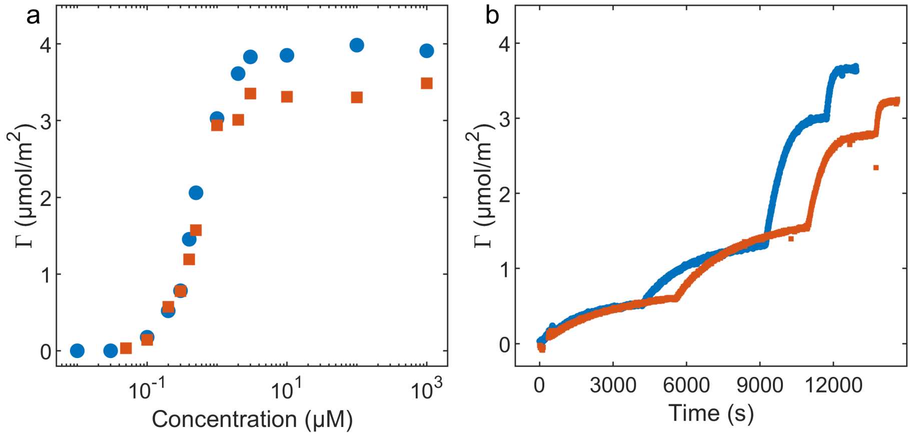

Figure 4.14: Ellipsometry results for adsorption of β-$C_{16}G_2$ (○), α-$C_{16}G_2$ (□) and β-$C_{16}G_2$ (◇) on a hydrophobized silica surface. (a) Adsorbed amount (Γ) versus concentration. (b) Γ over time for β-$C_{16}G_2$ with stepwise addition of surfactant (0.2 μM at 83 s, 0.4 μM at 4214 s, 1 μM at 9218 s and 2 μM at 11700 s).

values for the area per surfactant monomer at the surface calculated from these values, assuming a surfactant monolayer, was 50 and 43 Å^2 for α- and β-$C_{16}G_2$, respectively. This difference is indicative of a tighter packing being allowed for the β headgroup. This is probably originating from more attractive interactions between the headgroups for the β anomer, as suggested in the section for micelle formation. In Figure 4.14b the adsorption kinetics for α- and β-$C_{16}G_2$ is presented, showing similar adsorption rates for the surfactants. At concentrations below 1 μM it takes more than an hour for the Γ to stabilize while at 2 μM equilibrium is reached in ca. 500 s.

A more detailed study on the structure of the adsorbed surfactant films on hydrophobized silica was performed using neutron reflectometry (NR). To obtain the dimensions of the structure of the surfactant film, models were fitted to the NR data. The starting point for this fitting was a monolayer structure, as this is the most reported structure for surfactants on amorphous hydrophobic surfaces.[110-112] It was not possible to satisfactory fit the data with a model of a surfactant monolayer as shown in Figure 4.15a and b for five contrasts of β-$C_{16}G_2$. In this model the tailgroup, with a thickness of 20 Å, is adsorbed to the hydrophobic surface and the headgroup, with a thickness of 10 Å, is facing the solvent. The fit was not improved when varying the parameters within reasonable values for $C_{16}G_2$.

Models with more complex structures were explored and the best fit obtained for 20 μM β-$C_{16}G_2$ is shown in Figure 4.15c and d. This model suggests that a very thin layer of surfactants is laying on the hydrophobized surface on top of which cylindrical micelles are adsorbed. A schematic illustration of this modelled structure is presented in Figure 4.16.

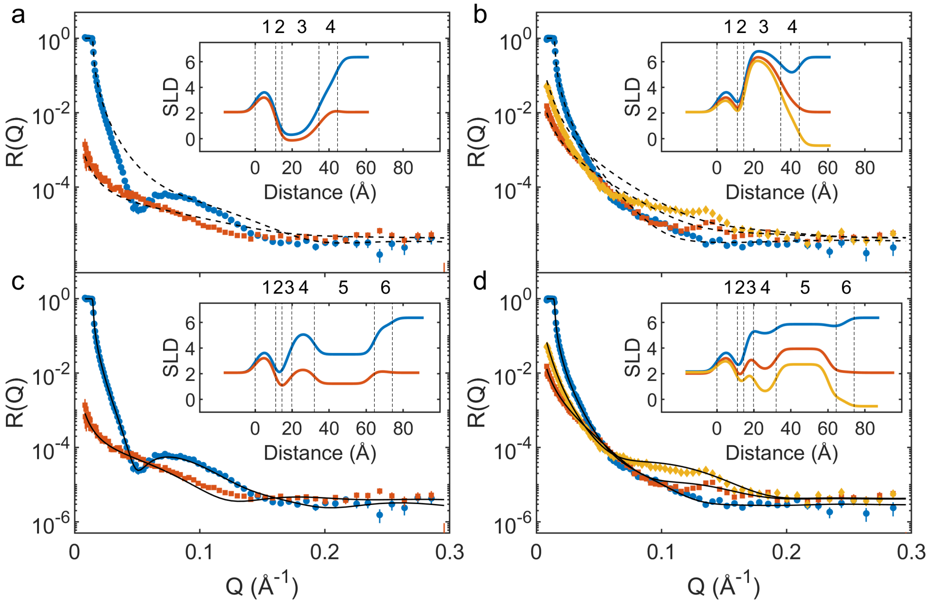

Figure 4.15: NR results for five contrasts of 20 μM β-$C_{16}G_2$ at 30 °C. (a and c) Protiated surfactant in D_2O (blue ○) and CMSi (red □), (b and d) tail deuterated surfactant in D_2O (blue ○), CMSi (red □) and H_2O (yellow ◇). The dashed lines are fits of a monolayer model and the solid lines are fits for the model that best fitted the data. The inset in each graph illustrates the SLD profile as a function of distance from the silicon surface obtained from the fitted model. The dashed lines and numbers in the insets shows the thickness of each layer.

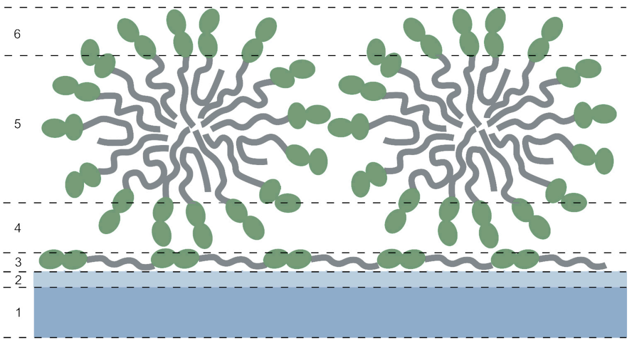

Figure 4.16: Schematic illustration of the structure obtained from fitting of NR results $C_{16}G_2$.

The adsorbed film of α-$C_{16}G_2$ can be fitted with the same model, but with parameters describing a thinner micelle layer, see Figure 4.17a. This is in line with the results of the SAXS experiments where the radius of α-$C_{16}G_2$ was determined to be smaller than that of the β anomer.

The 1:1 mixture of α- and β-$C_{16}G_2$ was not possible to fit to the same model as the anomerically pure systems, indicating that mixing the surfactants changes the structure of the adsorbed film. The detailed structure could not be resolved, but a one-layer surfactant model with a thickness similar to that of the α-$C_{16}G_2$ film was fitted to the data (Figure 4.17b). Through contrast variation it could be determined that the ratio of anomers in the adsorbed layer was 40:60 α:β, opposite to what was seen for the ratio in the micelles from SANS experiments. The conditions at the interface is different than in the bulk. There is a forced flat curvature and the available area is finite which both favours adsorption of β-$C_{16}G_2$ as it has been shown to pack more efficiently.

None of the systems were found to form the commonly reported monolayer structure for adsorption on isotropic hydrophobic solid surfaces. The multiple layers, that is suggested here, is rare for solid-liquid interfaces, but more frequently found for adsorption at the air-liquid interface.[39] The possibility for the sugar headgroup to form hydrogen bonds facilitates the formation of these structures, where the inner layer anchors the micelles to the surface.

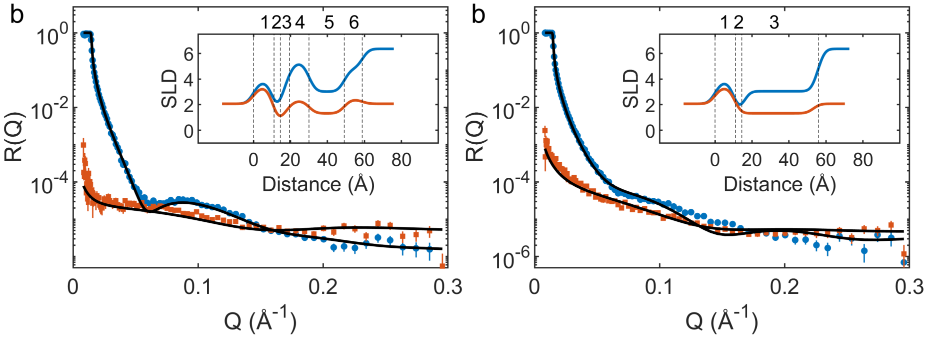

Figure 4.17: NR results for 20 μM α-$C_{16}G_2$ (a) and 1:1 mixture of α- and β-$C_{16}G_2$ (b) at 30 °C. The two contrasts are protiated surfactants in D_2O (blue ○) and CMSi (red □). The solid lines are fits for the model that best fitted the data. The inset in each graph illustrates the SLD profile as a function of distance from the silicon surface obtained from the fitted model. The dashed lines and numbers in the insets shows the thickness of each layer.

CHAPTER

5

CONCLUSIONS AND OUTLOOK

This work has been focused on the characterisation of the alkylglycoside $C_{16}G_2$ by studying the behaviour at interfaces and in solution and how it is affected by changes in the structure of the tail and headgroup. It was shown that the headgroup configuration has a considerable contribution to the self-assembly behaviour. The equatorial position of the β headgroup facilitated formation of very elongated worm-like micelles (WLM), while the axial position of the α headgroup promoted formation of shorter micelles. This difference was suggested to originate in stronger attractive interactions between the β headgroups allowing them to be more efficiently packed in the micelle. The difference in micelle morphology was found to have implications for the rheological properties of the surfactant solutions as β-$C_{16}G_2$ formed highly viscous, shear thinning and viscoelastic solutions compared to the low viscous, Newtonian solutions formed by α-$C_{16}G_2$.

Mixtures of the two surfactants possessed intermediate properties to the pure anomers. Samples with high ratio of β-$C_{16}G_2$ formed more elongated micelles which became entangled at higher concentrations, resulting in viscoelastic and shear thinning properties. Structural determinations during flow showed that the shear thinning behavior arouse from alignment of the elongated micelles. This means that the rheologic response of these surfactant solutions can be tuned through variations in the ratio of the surfactant mixture.

The tighter packing for the β headgroup was seen also in the interfacial behaviour, where the surface tension was lower and the adsorbed amount at the hydrophobic solid interface was higher for β-$C_{16}G_2$ compared to α-$C_{16}G_2$. The structure of the adsorbed layer at the solid-liquid interface was determined not to be a monolayer. Instead a structure where a thin bottom layer of surfactants laying on the interface on top of which micelles are adsorbed, is suggested.

The high Krafft point of $C_{16}G_2$ was shown to decrease with the introduction of a double bond in the alkyl tailgroup. The micelle solution of the unsaturated β-$C_{16-1}G_2$ was found to be stable from the freezing to the boiling temperature of water. Other bulk behaviour was relatively unaffected by this change and formation of WLM and viscolastic solutions were revealed, as for its saturated counterpart. This discovery makes the surfactant suitable to be used as a rheology modifier for several applications in a wide temperature range.

Plans for future work involves synthesis and characterisation of alkylglycosides with a more elongated sugar headgroup. It would also be interesting to find out more about the role of unsaturations in the tailgroup and how the surfactant behaviour is affected by its location and if the number of unsaturations increase.

REFERENCES

[1] Kronberg, B.; Holmberg, K.; Lindman, B. *Surface Chemistry of Surfactants and Polymers*; John Wiley & Sons, Ltd., 2014.

[2] Evans, D. F.; Wennerström, H. *The Colloidal Domain: Where Physics, Chemistry, Biology, and Technology Meet, 2nd Edition*; Wiley, 1999.

[3] Balzer, D.; Lüders, H. *Nonionic surfactants : alkyl polyglucosides*; Marcel Dekker: New York, 2000.

[4] Holmberg, K. Natural surfactants. *Current Opinion in Colloid & Interface Science* **2001**, *6*, 148–159.

[5] Nagarajan, R.; Ruckenstein, E. Theory of surfactant self-assembly: a predictive molecular thermodynamic approach. *Langmuir* **1991**, *7*, 2934–2969.

[6] McBain, J. W. General discussion on colloids and their viscosity. *Transactions of the Faraday Society* **1913**, *9*, 99–101.

[7] Mukerjee, P. The nature of the association equilibria and hydrophobic bonding in aqueous solutions of association colloids. *Advances in Colloid and Interface Science* **1967**, *1*, 242–275.

[8] Wennerström, H.; Lindman, B. Micelles. Physical chemistry of surfactant association. *Physics Reports* **1979**, *52*, 1–86.

[9] Gaudin, T.; Lu, H.; Fayet, G.; Berthauld-Drelich, A.; Rotureau, P.; Pourceau, G.; Wadouachi, A.; Van Hecke, E.; Nesterenko, A.; Pezron, I. Impact of the chemical structure on amphiphilic properties of sugar-based surfactants: A literature overview. *Advances in Colloid and Interface Science* **2019**, *270*, 87–100.

[10] Lu, H.; Pezron, I.; Gaudin, T.; Drelich, A. Non-equilibrium micelles formed by sugar-based surfactants under their Krafft temperature. *Colloids and Surfaces A: Physicochemical and Engineering Aspects* **2018**, *540*, 167–176.

[11] Moore, J. E.; McCoy, T. M.; de Campo, L.; Sokolova, A. V.; Garvey, C. J.; Pearson, G.; Wilkinson, B. L.; Tabor, R. F. Wormlike micelle formation of novel alkyl-tri(ethylene glycol)-glucoside carbohydrate surfactants: Structure–function relationships and rheology. *Journal of Colloid and Interface Science* **2018**, *529*, 464–475.

[12] Cummins, P. O.; Hayter, J. B.; Penfold, J.; Staples, E. A small-angle neutron scattering investigation of shear-aligned hexaethyleneglycolmonohexadecylether ($C_{16}E_6$) micelles as a function of temperature. *Chemical Physics Letters* **1987**, *138*, 436–440.

[13] Lindman, B.; Medronho, B.; Karlström, G. Clouding of nonionic surfactants. *Current Opinion in Colloid & Interface Science* **2016**, *22*, 23 – 29.

[14] Tanford, C. Micelle shape and size. *The Journal of Physical Chemistry* **1972**, *76*, 3020–3024.

[15] Israelachvili, J. N.; Mitchell, D. J.; Ninham, B. W. Theory of self-assembly of hydrocarbon amphiphiles into micelles and bilayers. *Journal of the Chemical Society, Faraday Transactions 2: Molecular and Chemical Physics* **1976**, *72*, 1525–1568.

[16] Tiddy, G. Surfactant-water liquid crystal phases. *Physics Reports* **1980**, *57*, 1 – 46.

[17] Strey, R.; Schomäcker, R.; Roux, D.; Nallet, F.; Olsson, U. Dilute lamellar and L3 phases in the binary water–$C_{12}E_5$ system. *Journal of the Chemical Society, Faraday Transactions* **1990**, *86*, 2253–2261.

[18] Nilsson, P. G.; Wennerström, H.; Lindman, B. Structure of micellar solutions of nonionic surfactants. Nuclear magnetic resonance self-diffusion and proton relaxation studies of poly (ethylene oxide) alkyl ethers. *The Journal of Physical Chemistry* **1983**, *87*, 1377–1385.

[19] Moore, J. E.; McCoy, T. M.; Marlow, J. B.; Pottage, M. J.; Mudie, S. T.; Pearson, G. R.; Wilkinson, B. L.; Tabor, R. F. Rich liquid crystal phase behavior of novel alkyl-tri(ethylene glycol)-glucoside carbohydrate surfactants. *Journal of Colloid and Interface Science* **2019**, *540*, 410–419.

[20] Urano, R.; Pantelopulos, G. A.; Straub, J. E. Aerosol-OT Surfactant Forms Stable Reverse Micelles in Apolar Solvent in the Absence of Water. *The Journal of Physical Chemistry B* **2019**, *123*, 2546–2557.

[21] Debye, P.; Anacker, E. W. Micelle Shape from Dissymmetry Measurements. *The Journal of Physical Chemistry* **1951**, *55*, 644–655.

[22] Dreiss, C. A. Wormlike micelles: where do we stand? Recent developments, linear rheology and scattering techniques. *Soft Matter* **2007**, *3*, 956–970.

[23] Porte, G.; Appell, J.; Poggi, Y. Experimental investigations on the flexibility of elongated cetylpyridinium bromide micelles. *The Journal of Physical Chemistry* **1980**, *84*, 3105–3110.

[24] Magid, L. J. The Surfactant–Polyelectrolyte Analogy. *The Journal of Physical Chemistry B* **1998**, *102*, 4064–4074.

[25] Mitchell, D. J.; Tiddy, G. J. T.; Waring, L.; Bostock, T.; McDonald, M. P. Phase behaviour of polyoxyethylene surfactants with water. Mesophase structures and partial miscibility (cloud points). *Journal of the Chemical Society, Faraday Transactions 1: Physical Chemistry in Condensed Phases* **1983**, *79*, 975–1000.

[26] Stradner, A.; Glatter, O.; Schurtenberger, P. A Hexanol-Induced Sphere-to-Flexible Cylinder Transition in Aqueous Alkyl Polyglucoside Solutions. *Langmuir* **2000**, *16*, 5354–5364.

[27] Schurtenberger, P.; Cavaco, C.; Tiberg, F.; Regev, O. Enormous Concentration-Induced Growth of Polymer-like Micelles. *Langmuir* **1996**, *12*, 2894–2899.

[28] McCoy, T. M.; Valiakhmetova, A.; Pottage, M. J.; Garvey, C. J.; Campo, L. d.; Rehm, C.; Kuryashov, D. A.; Tabor, R. F. Structural Evolution of Wormlike Micellar Fluids Formed by Erucyl Amidopropyl Betaine with Oil, Salts, and Surfactants. *Langmuir* **2016**, *32*, 12423–12433.

[29] Cates, M. E.; Candau, S. J. Statics and dynamics of worm-like surfactant micelles. *Journal of Physics: Condensed Matter* **1990**, *2*, 6869–6892.

[30] Ezrahi, S.; Tuval, E.; Aserin, A. Properties, main applications and perspectives of worm micelles. *Advances in Colloid and Interface Science* **2006**, *128-130*, 77–102.

[31] Iwase, H.; Kawai, R.; Morishima, K.; Takata, S.-i.; Yoshimura, T.; Shibayama, M. Rheo-SANS study on relationship between micellar structures and rheological behavior of cationic gemini surfactants in solution. *Journal of Colloid and Interface Science* **2019**, *538*, 357–366.

[32] Cates, M. E.; Turner, M. S. Flow-Induced Gelation of Rodlike Micelles. *Europhysics Letters (EPL)* **1990**, *11*, 681–686.

[33] Berret, J. F.; Gamez-Corrales, R.; Séréro, Y.; Molino, F.; Lindner, P. Shear-induced micellar growth in dilute surfactant solutions. *Europhysics Letters (EPL)* **2001**, *54*, 605–611.

[34] Turner, M. S.; Cates, M. E. Linear viscoelasticity of wormlike micelles: a comparison of micellar reaction kinetics. *J. Phys. II France* **1992**, *2*, 503–519.

[35] Mukerjee, P. Size distribution of small and large micelles. Multiple equilibrium analysis. *The Journal of Physical Chemistry* **1972**, *76*, 565–570.

[36] Cates, M. Reptation of living polymers: dynamics of entangled polymers in the presence of reversible chain-scission reactions. *Macromolecules* **1987**, *20*, 2289–2296.

[37] Barnes, H. A. *A handbook of elementary rheology*; University of Wales, Institute of Non-Newtonian Fluid Mechanics Aberystwyth, 2000.

[38] Zhang, R.; Somasundaran, P. Advances in adsorption of surfactants and their mixtures at solid/solution interfaces. *Advances in Colloid and Interface Science* **2006**, *123-126*, 213–229.

[39] Thomas, R. K.; Penfold, J. Multilayering of Surfactant Systems at the Air–Dilute Aqueous Solution Interface. *Langmuir* **2015**, *31*, 7440–7456.

[40] Paria, S.; Khilar, K. C. A review on experimental studies of surfactant adsorption at the hydrophilic solid–water interface. *Advances in Colloid and Interface Science* **2004**, *110*, 75–95.

[41] Zhang, L.; Somasundaran, P.; Maltesh, C. Adsorption of n-Dodecyl-β-d-maltoside on Solids. *Journal of Colloid and Interface Science* **1997**, *191*, 202–208.

[42] Tiberg, F.; Brinck, J.; Grant, L. Adsorption and surface-induced self-assembly of surfactants at the solid–aqueous interface. *Current Opinion in Colloid & Interface Science* **1999**, *4*, 411–419.

[43] Manne, S.; Gaub, H. E. Molecular Organization of Surfactants at Solid-Liquid Interfaces. *Science* **1995**, *270*, 1480.

[44] Wolgemuth, J. L.; Workman, R. K.; Manne, S. Surfactant Aggregates at a Flat, Isotropic Hydrophobic Surface. *Langmuir* **2000**, *16*, 3077–3081.

[45] Tiberg, F. Physical characterization of non-ionic surfactant layers adsorbed at hydrophilic and hydrophobic solid surfaces by time-resolved ellipsometry. *Journal of the Chemical Society, Faraday Transactions* **1996**, *92*, 531–538.

[46] Scott, M. J.; Jones, M. N. The biodegradation of surfactants in the environment. *Biochimica et Biophysica Acta (BBA) - Biomembranes* **2000**, *1508*, 235–251.

[47] Rebello, S.; Asok, A. K.; Mundayoor, S.; Jisha, M. Surfactants: toxicity, remediation and green surfactants. *Environmental chemistry letters* **2014**, *12*, 275–287.

[48] von Rybinski, W.; Hill, K. Alkyl Polyglycosides—Properties and Applications of a new Class of Surfactants. *Angewandte Chemie International Edition* **1998**, *37*, 1328–1345.

[49] De, S.; Malik, S.; Ghosh, A.; Saha, R.; Saha, B. A review on natural surfactants. *RSC Advances* **2015**, *5*, 65757–65767.

[50] He,; Garamus, V. M.; Funari, S. S.; Malfois, M.; Willumeit, R.; Niemeyer, B. Comparison of Small-Angle Scattering Methods for the Structural Analysis of Octyl-β-maltopyranoside Micelles. *The Journal of Physical Chemistry B* **2002**, *106*, 7596–7604.

[51] Ivanović, M. T.; Bruetzel, L. K.; Lipfert, J.; Hub, J. S. Temperature-Dependent Atomic Models of Detergent Micelles Refined against Small-Angle X-Ray Scattering Data. *Angewandte Chemie International Edition* **2018**, *57*, 5635–5639.

[52] Lipfert, J.; Columbus, L.; Chu, V. B.; Lesley, S. A.; Doniach, S. Size and Shape of Detergent Micelles Determined by Small-Angle X-ray Scattering. *The Journal of Physical Chemistry B* **2007**, *111*, 12427–12438.

[53] Ericsson, C. A.; Söderman, O.; Garamus, V. M.; Bergström, M.; Ulvenlund, S. Effects of Temperature, Salt, and Deuterium Oxide on the Self-Aggregation of Alkylglycosides in Dilute Solution. 1. n-Nonyl-β-d-glucoside. *Langmuir* **2004**, *20*, 1401–1408.

[54] Ericsson, C. A.; Söderman, O.; Garamus, V. M.; Bergström, M.; Ulvenlund, S. Effects of temperature, salt, and deuterium oxide on the self-aggregation of alkylglycosides in dilute solution. 2. n-Tetradecyl-β-D-maltoside. *Langmuir: The ACS Journal Of Surfaces And Colloids* **2005**, *21*, 1507–1515.

[55] Nilsson, F.; Söderman, O.; Hansson, P.; Johansson, I. Physical–Chemical Properties of C_9G_1 and $C_{10}G_1$ β-Alkylglucosides. Phase Diagrams and Aggregate Size/Structure. *Langmuir* **1998**, *14*, 4050–4058.

[56] Ericsson, C. A.; Söderman, O.; Ulvenlund, S. Aggregate morphology and flow behaviour of micellar alkylglycoside solutions. *Colloid and Polymer Science* **2005**, *283*, 1313–1320.

[57] Matsson, M. K.; Kronberg, B.; Claesson, P. M. Adsorption of Alkyl Polyglucosides on the Solid/Water Interface: Equilibrium Effects of Alkyl Chain Length and Head Group Polymerization. *Langmuir* **2004**, *20*, 4051–4058.

[58] Boyd, B. J.; Drummond, C. J.; Krodkiewska, I.; Grieser, F. How Chain Length, Headgroup Polymerization, and Anomeric Configuration Govern the Thermotropic and Lyotropic Liquid Crystalline Phase Behavior and the Air–Water Interfacial Adsorption of Glucose-Based Surfactants. *Langmuir* **2000**, *16*, 7359–7367.

[59] Nilsson, F.; Söderman, O.; Johansson, I. Four Different C_8G_1 Alkylglucosides. Anomeric Effects and the Influence of Straight vs Branched Hydrocarbon Chains. *Journal of Colloid and Interface Science* **1998**, *203*, 131–139.

[60] Dupuy, C.; Auvray, X.; Petipas, C.; Rico-Lattes, I.; Lattes, A. Anomeric Effects on the Structure of Micelles of Alkyl Maltosides in Water. *Langmuir* **1997**, *13*, 3965–3967.

[61] Hill, K.; Rhode, O. Sugar-based surfactants for consumer products and technical applications. *Lipid / Fett* **1999**, *101*, 25–33.

[62] Effendy, I.; Maibach, H. I. Surfactants and experimental irritant contact dermatitis. *Contact Dermatitis* **1995**, *33*, 217–225.

[63] Williams, A. C.; Barry, B. W. Penetration enhancers. *Advanced Drug Delivery Reviews* **2004**, *56*, 603–618.

[64] Alpes, H.; Allmann, K.; Plattner, H.; Reichert, J.; Rick, R.; Schulz, S. Formation of large unilamellar vesicles using alkyl maltoside detergents. *BBA - Biomembranes* **1986**, *862*, 294–302.

[65] Seddon, A. M.; Curnow, P.; Booth, P. J. Membrane proteins, lipids and detergents: not just a soap opera. *Biochimica et Biophysica Acta (BBA) - Biomembranes* **2004**, *1666*, 105–117.

[66] Zhmud, B.; Tiberg, F. Interfacial dynamics and structure of surfactant layers. *Advances in Colloid and Interface Science* **2005**, *113*, 21–42.

[67] Kairaliyeva, T.; Aksenenko, E. V.; Mucic, N.; Makievski, A. V.; Fainerman, V. B.; Miller, R. Surface Tension and Adsorption Studies by Drop Profile Analysis Tensiometry. *Journal of Surfactants and Detergents* **2017**, *20*, 1225–1241.

[68] Fainerman, V. B.; Kovalchuk, V. I.; Aksenenko, E. V.; Miller, R. Dilational Viscoelasticity of Adsorption Layers Measured by Drop and Bubble Profile Analysis: Reason for Different Results. *Langmuir* **2016**, *32*, 5500–5509.

[69] du Noüy, P. L. An interfacial tensiometer for universal use. *Journal of General Physiology* **1925**, *7*, 625–631.

[70] Obiols-Rabasa, M. In *Nanocolloids*; Domínguez, M. S., Abreu, C. R., Eds.; Elsevier: Amsterdam, 2016; pp 299 – 330.

[71] Zemb, T.; Lindner, P. *Neutron, X-Rays and Light. Scattering Methods Applied to Soft Condensed Matter*; North-Holland Delta; Elsevier Science, 2002.

[72] Anderson, I. S.; Hurd, A. J.; McGreevy, R. L. *Neutron scattering applications and techniques*; Springer, 2008.

[73] Jackson, A. J. Introduction to small-angle neutron scattering and neutron reflectometry. *NIST Center for Neutron Research* **2008**, 1–24.

[74] Schurtenberger, P. In *Neutron, X-rays and Light: Scattering Methods Applied to Soft Condensed Matter*; Zemb, T., Lindner, P., Eds.; North-Holland Delta Series; Elsevier: Amsterdam, 2009; pp 145–170.

[75] Guinier, A.; Fournet, G. *Small-angle Scattering of X-rays*; Structure of matter series; Wiley, 1955.

[76] Doucet, M. C. et al. SasView version 4.2.2. **2019**,

[77] Lindner, P.; Oberthür, R. Apparatus for the investigation of liquid systems in a shear gradient by small angle neutron scattering (SANS). *Revue de Physique Appliquee* **1984**, *19*, 759–763.

[78] Hayter, J. B.; Penfold, J. Use of viscous shear alignment to study anisotropic micellar structure by small-angle neutron scattering. *The Journal of Physical Chemistry* **1984**, *88*, 4589–4593.

[79] Calabrese, M. A.; Wagner, N. J. *Wormlike Micelles: Advances in Systems, Characterisation and Applications*; The Royal Society of Chemistry, 2017; pp 193–235.

[80] Eberle, A. P. R.; Porcar, L. Flow-SANS and Rheo-SANS applied to soft matter. *Current Opinion in Colloid & Interface Science* **2012**, *17*, 33–43.

[81] Liberatore, M. W.; Nettesheim, F.; Vasquez, P. A.; Helgeson, M. E.; Wagner, N. J.; Kaler, E. W.; Cook, L. P.; Porcar, L.; Hu, Y. T. Microstructure and shear rheology of entangled wormlike micelles in solution. *Journal of Rheology* **2009**, *53*, 441–458.

[82] Calabrese, M. A.; Rogers, S. A.; Porcar, L.; Wagner, N. J. Understanding steady and dynamic shear banding in a model wormlike micellar solution. *Journal of Rheology* **2016**, *60*, 1001–1017.

[83] Pusey, P. N.; Megen, W. v. Detection of small polydispersities by photon correlation spectroscopy. *The Journal of Chemical Physics* **1984**, *80*, 3513–3520.

[84] Hassan, P. A.; Rana, S.; Verma, G. Making Sense of Brownian Motion: Colloid Characterization by Dynamic Light Scattering. *Langmuir* **2015**, *31*, 3–12.

[85] De Gennes, P.-G. *Scaling concepts in polymer physics*; Cornell university press, 1979.

[86] Cates, M. Dynamics of living polymers and flexible surfactant micelles: scaling laws for dilution. *Journal de Physique* **1988**, *49*, 1593–1600.

[87] Berret, J. F.; Appell, J.; Porte, G. Linear rheology of entangled wormlike micelles. *Langmuir* **1993**, *9*, 2851–2854.

[88] Cuypers, P. Dynamic Ellipsometry: Biochemical and Biomedical Applications. Thesis, 1976.

[89] Tiberg, F.; Landgren, M. Characterization of thin nonionic surfactant films at the silica/water interface by means of ellipsometry. *Langmuir* **1993**, *9*, 927–932.

[90] De Feijter, J. A.; Benjamins, J.; Veer, F. A. Ellipsometry as a tool to study the adsorption behavior of synthetic and biopolymers at the air–water interface. *Biopolymers* **1978**, *17*, 1759–1772.

[91] Penfold, J.; Thomas, R. K. The application of the specular reflection of neutrons to the study of surfaces and interfaces. *Journal of Physics: Condensed Matter* **1990**, *2*, 1369–1412.

[92] R. Lu, J.; K. Thomas, R. Neutron reflection from wet interfaces. *J. Chem. Soc., Faraday Trans.* **1998**, *94*, 995–1018.

[93] Abelès, F. La théorie générale des couches minces. *Journal de Physique et le Radium* **1950**, *11*, 307–309.

[94] Braun, L.; Uhlig, M.; von Klitzing, R.; Campbell, R. A. Polymers and surfactants at fluid interfaces studied with specular neutron reflectometry. *Advances in Colloid and Interface Science* **2017**, *247*, 130 – 148, Dominique Langevin Festschrift: Four Decades Opening Gates in Colloid and Interface Science.

[95] González, Y. I.; Kaler, E. W. Cryo-TEM studies of worm-like micellar solutions. *Current opinion in colloid & interface science* **2005**, *10*, 256–260.

[96] Danino, D.; Bernheim-Groswasser, A.; Talmon, Y. Digital cryogenic transmission electron microscopy: an advanced tool for direct imaging of complex fluids. *Colloids and Surfaces A: Physicochemical and Engineering Aspects* **2001**, *183-185*, 113 – 122.

[97] Glatter, O.; Fritz, G.; Lindner, H.; Brunner-Popela, J.; Mittelbach, R.; Strey, R.; Egelhaaf, S. U. Nonionic Micelles near the Critical Point: Micellar Growth and Attractive Interaction. *Langmuir* **2000**, *16*, 8692–8701.

[98] Pedersen, J. S.; Schurtenberger, P. Scattering Functions of Semiflexible Polymers with and without Excluded Volume Effects. *Macromolecules* **1996**, *29*, 7602–7612.

[99] Puvvada, S.; Blankschtein, D. Molecular-thermodynamic approach to predict micellization, phase behavior and phase separation of micellar solutions. I. Application to nonionic surfactants. *The Journal of Chemical Physics* **1990**, *92*, 3710–3724.

[100] Pedersen, J. S. Analysis of small-angle scattering data from colloids and polymer solutions: modeling and least-squares fitting. *Advances in Colloid and Interface Science* **1997**, *70*, 171–210.

[101] Jerke, G.; Pedersen, J. S.; Egelhaaf, S. U.; Schurtenberger, P. Flexibility of Charged and Uncharged Polymer-like Micelles. *Langmuir* **1998**, *14*, 6013–6024.

[102] Alves, L.; Medronho, B. F.; Antunes, F. E.; Romano, A.; Miguel, M. G.; Lindman, B. On the role of hydrophobic interactions in cellulose dissolution and regeneration: Colloidal aggregates and molecular solutions. *Colloids and Surfaces A: Physicochemical and Engineering Aspects* **2015**, *483*, 257–263.

[103] Keep, G. T.; Pecora, R. Reevaluation of the dynamic model for rotational diffusion of thin, rigid rods in semidilute solution. *Macromolecules* **1985**, *18*, 1167–1173.

[104] Rouse, P. E. A Theory of the Linear Viscoelastic Properties of Dilute Solutions of Coiling Polymers. *The Journal of Chemical Physics* **1953**, *21*, 1272–1280.

[105] Whiddon, C.; Söderman, O. Unusually Large Deuterium Isotope Effects in the Phase Diagram of a Mixed Alkylglucoside Surfactant/Water System. *Langmuir* **2001**, *17*, 1803–1806.

[106] Tanford, C. *The hydrophobic effect: Formation of micelles and biological membranes*; John Wiley & Sons, Inc.: New York, 1980.

[107] Deleu, M.; Paquot, M.; Nylander, T. Effect of Fengycin, a Lipopeptide Produced by Bacillus subtilis, on Model Biomembranes. *Biophysical Journal* **2008**, *94*, 2667–2679.

[108] Appell, J.; Porte, G.; Poggi, Y. Quantitative estimate of the orientational persistence length of flexible elongated micelles of cetylpyridinium bromide. *Journal of Colloid and Interface Science* **1982**, *87*, 492–499.

[109] Clint, J. H. Micellization of mixed nonionic surface active agents. *Journal of the Chemical Society, Faraday Transactions 1: Physical Chemistry in Condensed Phases* **1975**, *71*, 1327–1334.

[110] Thirtle, P. N.; Li, Z. X.; Thomas, R. K.; Rennie, A. R.; Satija, S. K.; Sung, L. P. Structure of Nonionic Surfactant Layers Adsorbed at the Solid/Liquid Interface on Self-Assembled Monolayers with Different Surface Functionality: A Neutron Reflection Study. *Langmuir* **1997**, *13*, 5451–5458.

[111] Patrick, H. N.; Warr, G. G.; Manne, S.; Aksay, I. A. Self-Assembly Structures of Nonionic Surfactants at Graphite/Solution Interfaces. *Langmuir* **1997**, *13*, 4349–4356.

[112] Holland, N. B.; Ruegsegger, M.; Marchant, R. E. Alkyl Group Dependence of the Surface-Induced Assembly of Nonionic Disaccharide Surfactants. *Langmuir* **1998**, *14*, 2790–2795.

SCIENTIFIC PUBLICATIONS

Paper I

Effect of the anomeric configuration on the micellization of hexadecylmaltoside surfactants

J. Larsson, A. Sanchez-Fernandez, N. Mahmoudi, L. Barnsley, M. Wahlgren, T. Nylander, S. Ulvenlund

Langmuir **2019**, 35, 13904-13914

LANGMUIR
Cite This: *Langmuir* 2019, 35, 13904−13914
Article
pubs.acs.org/Langmuir

Effect of the Anomeric Configuration on the Micellization of Hexadecylmaltoside Surfactants

Johan Larsson,[*,†] Adrian Sanchez-Fernandez,[‡] Najet Mahmoudi,[∥] Lester C. Barnsley,[⊥] Marie Wahlgren,[‡,#] Tommy Nylander,[*,†,§] and Stefan Ulvenlund[‡,#]

[†]Physical Chemistry, Department of Chemistry, [‡]Food Technology, Engineering and Nutrition, and [§]NanoLund, Lund University, Box 124, 221 00 Lund, Sweden
[∥]ISIS Neutron and Muon Source, Science & Technology Facilities Council, Rutherford Appleton Laboratory, Chilton OX11 0QX, U.K.
[⊥]Jülich Centre for Neutron Science (JCNS) at Heinz Maier-Leibnitz Zentrum (MLZ), Forschungszentrum Jülich GmbH, Lichtenbergstr. 1, 85748 Garching, Germany
[#]Enza Biotech AB, Scheelevägen 22, 22363 Lund, Sweden

Supporting Information

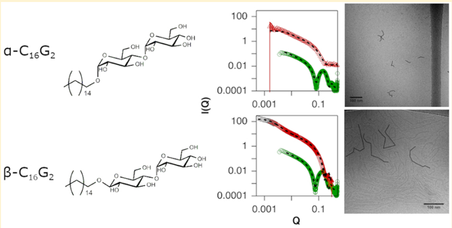

ABSTRACT: The self-assembly of the two anomeric forms of *n*-hexadecyl-D-maltopyranoside (denoted α-$C_{16}G_2$ and β-$C_{16}G_2$) has been studied in dilute aqueous solution by means of surface tension measurements, scattering methods (dynamic light scattering, static light scattering, and small-angle X-ray and neutron scattering), and cryo-transmission electron microscopy at different surfactant concentrations and temperatures. Surface tension measurements demonstrate differences in the surfactant adsorption at the air−water interface, where α-$C_{16}G_2$ shows a lower CMC than β-$C_{16}G_2$. Similarly, micelle morphology was found to profoundly depend on anomerism. β-$C_{16}G_2$ preferentially forms very elongated micelles with large persistence lengths, whereas α-$C_{16}G_2$ assembles into smaller micelles for which the structure varies with concentration and temperature. The differences between the two surfactant anomers in terms of self-assembly can be attributed to the interaction between neighboring headgroups. Specifically, β-$C_{16}G_2$ allows for a closer packing in the palisade layer, hence reducing the micelle curvature and promoting the formation of more elongated micelles. Strong intermolecular headgroup interactions may also account for the observed rigidity of the micelles.

INTRODUCTION

Nonionic surfactants are key ingredients in many types of consumer goods, for instance, formulated products in pharmaceutics, cosmetics, and personal care. However, the majority of these surfactants are currently produced from nonrenewable resources, for example, the large family of ethoxylated surfactants (e.g., polysorbates) that are normally manufactured from ethylene oxide of fossil origin. The search for new sustainable components, as well as the characterization of existing ones, is the subject of substantial research efforts. Since the late 1990s, alkylglycosides are extensively used in formulated products,[1−4] since they are recognized as environmentally friendly and nontoxic materials, while still being highly functional and cost-efficient. Furthermore, these surfactants have been implemented in high-end niche applications, such as the solubilization and stabilization of membrane proteins.[5] In spite of their extensive and varied commercial use, alkylglycosides are still not fully understood in terms of their complex self-assembly and interfacial behavior, limiting the exploitation of these in new applications. In contrast to alkylglycosides, ethoxylated surfactants are understood in great detail in terms of the influence of surfactant structure (length of alkyl chain and degree of headgroup polymerization) on general phase behavior (concentration and temperature dependence),[6−8] micelle formation (CMC and micelle morphology),[9,10] and adsorption to various interfaces.[11] This knowledge has been shown to be crucial for the design of formulated products containing this type of surfactant. Thus, our ultimate aim is to provide the same level of knowledge for alkylglycosides in order to expand the use of these sustainable materials in established as well as new applications.

In line with this ambition, previous investigations have focused on the study of the self-assembly of sugar-based surfactants with different tail length and sugar units in the

Received: June 26, 2019
Revised: September 11, 2019
Published: September 30, 2019

ACS Publications

DOI: 10.1021/acs.langmuir.9b01960
Langmuir 2019, 35, 13904−13914

headgroup. Some key results from previous studies are summarized in Table 1

Table 1. CMC and Morphology of Alkylglycoside Micelles (Glucoside: G$_1$; Maltoside G$_2$) in Aqueous Solutions[a]

surfactant	CMC (mM)	micelle morphology
β-C$_7$G$_1$	71.8[12]	short cylinder[12]
β-C$_8$G$_1$	23.6[12]	prolate ellipsoid,[13,14] cylinder[12,15]
α-C$_8$G$_1$	17.1[14]	prolate ellipsoid[14]
β-C$_9$G$_1$	6.9[16]	prolate ellipsoid,[13,17] cylinder[12,16]
β-C$_{10}$G$_1$	2.2[17]	network of thread-like micelles[17]
β-C$_8$G$_2$	19.1[18]	sphere[18]
β-C$_{10}$G$_2$	2.2[19]	oblate ellipsoid,[13] prolate ellipsoid[20]
α-C$_{12}$G$_2$	0.15[21]	sphere[21]
β-C$_{12}$G$_2$	0.20[21]	oblate ellipsoid,[13,21−24] prolate ellipsoid[20,25]
β-C$_{14}$G$_2$	0.014[26]	cylinder[26]

[a] All of the reported morphologies were determined at room temperature, with the exception of the data for β-C$_{14}$G$_2$, which was measured at 35 °C.

When rationalizing micelle morphology based on molecular structure, the simple concept of critical packing parameter (CPP) has proved to be a valuable qualitative tool. CPP is defined as $v/(a_0 l_c)$, where v is the volume of the hydrophobic moiety, l_c is the critical length of the surfactant tail, and a_0 is the area of the headgroup−tail interface of the monomer.[27] For ethoxylated surfactants the morphology of the micellar assemblies, as well as their dependence on temperature, follows the expected trends, e.g., surfactants with long hydrophobic tail and/or short headgroups form more elongated aggregates ($1/3 < \text{CPP} < 1/2$), whereas shorter tail and longer headgroup promote spherical or quasi-spherical micelles ($\text{CPP} = 1/3$). Similarly, micelle formation of alkylglucoside surfactants (i.e., G$_1$ species) follow the trend expected from CPP arguments, namely, that increasing length of the alkyl chain leads to a shift from spherical symmetry to ellipsoidal to cylindrical structures (Table 1). From the meagre information available, α/β-anomerism does not seem to have a major influence on the micellar structures for the glucosides.[28] For alkylmaltoside surfactants (G$_2$ species), increasing alkyl chain length from C$_8$ to C$_{14}$ gives several morphology transitions, as the formation of spherical, prolate, oblate, and cylindrical aggregates has been reported.[20,26] The micelle morphology seems also to be temperature dependent for these surfactants. For example, smaller aggregates are formed in the case of C$_{12}$G$_2$ when temperature increases, while C$_{14}$G$_2$ micelles increase in size at higher temperatures. Furthermore, headgroup anomerism seems to have an influence in micelle morphology, as judged from the data on the α- and β-anomers of dodecylmaltoside (C$_{12}$G$_2$).[20,21]

From the existing data, it is clear that the self-assembly of alkylmaltoside surfactants is complex and not readily rationalized from the behavior of other nonionic surfactants. When discussing differences in morphology and dynamics between ethoxylate and alkylglycoside micelles, it is critical to consider the fundamental differences between the headgroups. The headgroups in the first case consist of freely jointed chains, in which the intermolecular interactions are dominated by hydrogen bonding with the solvent, where the ether units act as hydrogen bond acceptors. This limits the opportunities for strong specific interactions between headgroups.[10] The alkylglycoside surfactant headgroups, on the other hand, consist of rigid subunits that can be oriented in such a way that different types of (attractive) intermolecular interactions become important. The most obvious type of interaction is hydrogen bonding, as elsewhere reported for other sugar-based materials (e.g., cellulose). For micelles in aqueous solution, the formation of hydrogen bonds between headgroups competes with hydrogen bonding between glucose units and water molecules, as the glucose unit can act as both hydrogen bond donor and acceptor. However, NMR T_2 relaxation experiments suggest that hydrogen bonding between OH groups of glucose moieties is of critical importance when describing alkylglycoside micelles.[29] Similarly, intermolecular hydrogen bonds in foam lamellae have been proposed as an explanation for the unusually good foaming properties of alkylglycosides.[30] Also, the importance of hydrogen bonding with neighboring water molecules, combined with the rapid proton exchange between glucose hydroxyl groups and water, is demonstrated by the sometimes dramatic difference in behavior of alkylglycosides between H$_2$O and D$_2$O.[16,26,31]

In addition to their propensity to form hydrogen bonds, the glucose units in alkylglycosides are also weakly amphiphilic. This property is often overlooked but manifests itself in the complexing ability of cyclodextrins, in which the hydrophobic cavity may act as a host to nonpolar guest molecules[32,33] More recently, the amphiphilicity of glucose residues has also been proposed as an explanation of the low solubility of cellulose in water ("the Lindman hypothesis").[34,35] It would seem likely that the same amphiphilicity, and the resulting hydrophobic interactions between adjacent headgroups, may influence the properties of alkylglycoside surfactants in the micellar state.

In this study, we discuss how the headgroup interaction affects the assembly of the alkylglycoside in bulk solution and at interfaces by comparing the α- and β-anomer of n-hexadecylmaltoside (α-C$_{16}$G$_2$ and β-C$_{16}$G$_2$). The interfacial behavior of the surfactants has been investigated by means of surface tension, and the bulk behavior has been explored by using dynamic light scattering (DLS), static light scattering (SLS), small-angle X-ray scattering (SAXS), small-angle neutron scattering (SANS), and cryo-transmission electron microscopy (cryo-TEM). Apart from the fundamental interest, α-C$_{16}$G$_2$ and β-C$_{16}$G$_2$ are also interesting from an applied point of view because of their long alkyl chain. Surfactants with long alkyl chains tend to be good solubilizers, efficient emulsifiers, and thickening agents. However, the self-assembly of long-chain alkylglycosides is almost entirely unknown, and in particular the effect of headgroup orientation has not been studied before.

■ EXPERIMENTAL SECTION

Materials and Sample Preparation. n-Hexadecyl-α-D-maltopyranoside (α-C$_{16}$G$_2$; Figure 1) was purchased from Ramidus (Lund,

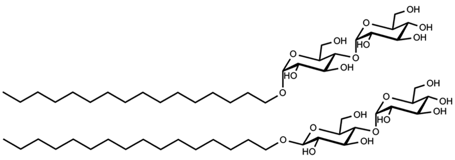

Figure 1. Molecular structure of α-C16G2 (top) and β-C16G2 (bottom).

Sweden) and had a purity of >97%. The β-anomer of the same compound (β-$C_{16}G_2$; Figure 1) was purchased from Anatrace Inc. (Maumee, OH) and was of Anagrade quality. According to the supplier, the purity of this product is ≥97%, out of which ≥95% is the β-$C_{16}G_2$ anomer. As a part of this study, the purity of the materials claimed by the suppliers was verified by HPLC and mass spectroscopic analyses. The results from the characterization are presented in the Supporting Information. Samples were prepared by mixing α- or β-$C_{16}G_2$ with the desired solvent under agitation with magnetic stirring in water bath at 45 °C. H_2O used in this work was of Milli-Q quality, and D_2O was purchased from Sigma-Aldrich (Darmstadt, Germany) and had an isotropic purity of 99.9%.

The Krafft temperature of both α-$C_{16}G_2$ and β-$C_{16}G_2$ was estimated to be between 25 and 35 °C through visual inspection and therefore above room temperature. Thus, the solutions are physically unstable and prone to precipitation at room temperature. The rate of precipitation was found to depend on concentration. At concentrations above 10 mM, precipitate was observed after about 1 h at 25 °C, while at 1 μM, samples were found to be stable overnight. Thus, all measurements for high surfactant concentration conducted at temperatures below the Krafft point were performed within 1 h after preparation to avoid confounding effects stemming from precipitation.

Methods. *Tensiometry.* A Du Noüy ring tensiometer from Krüss (Hamburg, Germany) was used to determine the surface tension of α- and β-$C_{16}G_2$ solutions at ambient temperature as a function of surfactant concentration. The Du Noüy ring was made of platinum. The 100 mL surfactant samples were prepared in a narrow beaker with a radius of 2.5 cm. As will be discussed in more detail in the Results section, the ratio of surface area to volume of the vessel was found to be critical to get reliable results due to the low CMC of the surfactant.

The surface tension was measured as a function of time, until a stable value was reached. This stable value was recorded as the equilibrium surface tension value. The time required to reach stable readings for samples with concentrations around and below the CMC was found to be 90 ± 15 min, but the time required for equilibration decreased significantly with concentration. Thus, at concentrations more than 2 orders of magnitude higher than the CMC, stable readings were achieved in less than a minute. Duplicate measurements were performed for each concentration.

Dynamic Light Scattering (DLS). The effective hydrodynamic radius (R_H) of the micelles was determined by using a Zetasizer Nano-ZS (Malvern Instruments Ltd., Worshestershire, UK) with noninvasive backscatter (NIBS) technology operating with a scattering angle of 173°. The light source was a 4 mW He−Ne laser with a wavelength of 632.8 nm. For each experiment, 0.5 mL of sample was transferred to PMMA semi-microdisposable cuvettes purchased from BRAND GmbH (Wertheim, Germany). For measurements above 70 °C, quartz glass SUPRASIL cuvettes from Hellma Analytics (Müllheim, Germany) were used.

The correlation function data did not reveal any bimodality under the applied experimental conditions. Thus, DLS data were analyzed by using the cumulants method implemented in the Malvern software supplied with the instrument, where a single-exponential function provided a good fit to the experimental data. Results from these measurements were presented as hydrodynamic radius.

Static Light Scattering (SLS). For the SLS experiments an ALV/DLS/SLS-5022F, CGF-8F-based compact goniometer system from ALV GmbH (Langen, Germany) was used. The laser source was a 22 mW He−Ne laser with a wavelength of 632.8 nm, and an automatic attenuator was used to vary the intensity. The temperature was controlled by a F32 Julabo heating circulator with an accuracy of ±0.01 °C. Measurements were made at 24 angles with corresponding Q values between 5.72×10^{-4} and 2.52×10^{-3} Å^{-1}, where Q is the scattering momentum transfer ($Q = 4\pi \sin \theta/\lambda$). For every angle, three measurements at 40 °C were performed and averaged. Data were reduced, normalized, and scaled to match the neutron scattering excess of the hydrogenated surfactant in D_2O. Output data were the angular-dependent scattered intensity versus momentum transfer Q.

Small-Angle X-ray and Neutron Scattering. Small-angle X-ray scattering (SAXS) experiments were performed on beamline BM29 at the European Synchrotron Radiation Facility (Grenoble, France).[36] The wavelength was 0.99 Å, and the distance from sample to the detector was 2.867 m, resulting in a Q range of 0.0040−0.49 Å^{-1}. Measurements were performed at 25, 40, and 50 °C using the temperature-controlled sample stage. The acquisition time was 10 s (1 s exposure, 10 frames) per sample, and frames affected by radiation damage were removed. The absolute scale for the scattered intensity was obtained using the standard protocols of the beamline.[37]

SANS measurements were performed on the KWS-1 instrument at the Heinz Maier-Leibnitz Zentrum (Garching, Germany) and on the SANS2D instrument at the ISIS Neutron and Muon Source (Didcot, UK).[38−40] On KWS-1, the wavelength of the neutrons was 7 Å, and three different sample-to-detector distances were used (2, 8, and 20 m), yielding to a combined Q range of 0.0015−0.3 Å^{-1}. For the experiment on SANS2D, the front and rear detector were placed at 5 and 12 m from the sample position, respectively. Neutrons with wavelengths between 1.75 and 12.5 Å were used, providing a combined Q range of 0.0016−0.5 Å^{-1}. In both experiments, samples were loaded in quartz cuvettes with a path length of 2 mm for D_2O and 1 mm for H_2O and measured at 50 °C. Data were corrected for detector efficiency, background noise, sample transmission, and scattering from an empty cell by using the standard protocols of each beamline. The solvent contribution was subtracted from the scattering of the samples. The output data were absolute intensity ($I(Q)$, cm^{-1}) versus momentum transfer (Q, Å^{-1}).[38]

Small-angle scattering data were analyzed by using form factor models that appropriately describe the scattering from the micelles in the particular system. These models were implemented in SasView 4.2.2. and were fitted to the experimental data by using a Levenberg−Marquardt algorithm.[41] The X-ray and neutron scattering length density (SLD) of each component of the system was calculated from the scattering length of the unit (b) and the volume it occupies (V_m). These values are presented in Table 2.

Table 2. Volume, Scattering Length, and Scattering Length Density for X-rays and Neutrons of Each Constituent of the System

unit	V_m/Å^3	b X-ray/fm	SLD X-ray/ 10^{-6} Å^{-2}	b neutron/ fm	SLD neutron/ 10^{-6} Å^{-2}
α-/β-G_2	368[a]	510	13.9	65.1	1.77
$C_{16}H_{33}$	431[b]	363	8.44	−17.1	−0.40
H_2O	29.9[c]	28.2	9.42	−1.68	−0.56
D_2O	29.9[c]			19.15	6.40

[a] The molecular volume of the maltoside unit was calculated from the physical density of maltose. [b] The molecular volume of the hydrophobic tail of the surfactant has been calculated by using the Tanford equation.[42] [c] The molecular volume of H_2O and D_2O have been calculated from the physical density of those at 25 °C.

The high Q expansion of X-ray and neutron data ($Q > 0.006$ Å^{-1}) were fitted by using a core−shell cylinder model that satisfactorily describes the cross section of elongated micelles (elongation >10 times the radius of the cross section).[43] For shorter micelles (elongation ≤10 times the radius of the cross section), a core−shell ellipsoid model was found to be more appropriate to model the experimental scattering data. The fitting approach was performed as follows: the micelle core SLD and solvent SLD were fixed to the calculated values (Table 2). The structural parameters (L_{core} = core length, r_{core} = core radius, t_{shell} = shell thickness; for the prolate ellipsoid model L_{core} corresponds to twice the size of the core along the rotational axis and r_{core} corresponds to the core size perpendicular to the rotational axis of the ellipsoid) and shell SLD (SLD_{shell}) were simultaneously fitted for all the contrasts available. The structural features of the micelle cross section were subsequently used to guide the fit of the X-ray data at different concentrations and temperatures.

To do this, r_{core} was fixed to the value obtained through the previous data co-refinement, as it is assumed that the solvation of the hydrophobic domains will not be greatly affected by changes in concentration or temperature. Therefore, the volume fraction of scatterers (φ_{fit}), L_{core}, t_{shell}, and $\mathrm{SLD}_{\mathrm{shell}}$ were determined for these samples.

A polydispersity function (p) was also included for the length of the micelles, whereas the cross section of the micelle was assumed to be monodisperse. The length distribution is represented using a Schulz function with $p = \sigma/L$, where L is the average length of the micelle and σ is the root-mean-square deviation from L. The width of the distribution is defined by a parameter z such that $z = (1 - p^2)/p^2$.[44] As shown in the description in the SasView manual, the function is better behaved with a large N_{pts} and N_σ, where N_{pts} is the number of points used to compute the function and N_σ defines how far into the tails the distribution is considered in the calculation. In the present work and considering the previous indications, the distribution function was parametrized by using $N_{\mathrm{pts}} = 160$ and $N_\sigma = 15$.

The formation of semiflexible cylinders have been previously reported for amphiphile-based systems, where the morphology of elongated micelles can be described as a worm-like body composed by a succession of rigid sections interconnected by flexible nods.[45,46] Information on the length and flexibility of micelles that fall within that description (elongation >100 times the radius of the cross section) were obtained from the combined SANS and SLS data. It should be noted that the Q range covered by our individual scattering experiments was not sufficient to cover the characteristic features of the scattering curve that contain this information. These data were fitted to a flexible cylinder model, which neglects the internal density distribution of the micelle (uniform body) but enables the calculation of the contour length of the micelle (L) and the length of the statistical segments or persistence length (l_p, where $2l_p$ is the Kuhn length of the micelle).[45] The elongation of the micelles was subsequently used to refine the fits of the core−shell cylinder model, providing a global model that satisfactorily describes the features of these micelles.

Cryogenic Transmission Electron Microscopy (Cryo-TEM). Small drops (about 4 μL) of the sample were applied on TED PELLA INC F/C 300 mesh Cu grids (Redding, US). The grids had been plasma cleaned in a Blazers SCD004 Sputter coater. The grids were gently blotted with a filter paper and then rapidly frozen in an automatic plunge freezer into liquid ethane (−183 °C) with a Leica EM GP. The vitrified samples were stored in liquid nitrogen (−196 °C) until they were transferred into the microscope by using a Fischione Model 2550 cryo-transfer tomography holder. The grids were examined using a JEOL JEM-2200FS electron microscope (Peabody, US), operated at 200 kV. A TVIPS TemCam-F416 digital camera using Serial EM under low-dose conditions with a 10 eV slit was used to record zero-loss images while keeping the working temperature below −175 °C.

RESULTS AND DISCUSSION

Surfactant Adsorption at the Air−Water Interface. For nonionic surfactants with a given headgroup, the CMC generally decreases by an order of magnitude with every two CH_2 groups added to the alkyl chain.[47] Based on this relationship and previous studies of shorter-chain congeners (Table 1), the expected CMC of $C_{16}G_2$ is ca. 1 μM. To determine CMC values, the method used should be sensitive enough to allow for accurate measurements at surfactant concentrations of about an order of magnitude lower. This means that in the present case accurate measurements should be possible to conduct at submicromolar concentrations, which is experimentally very challenging. More specifically, the main challenge for measuring the surface tension of the systems investigated here is to have a sufficiently large bulk reservoir of surfactant molecules that can adsorb at the interface without depleting the bulk solution. As previously reported, techniques that involve large volumes of solution, such as the Du Noüy ring method, are significantly less affected by bulk depletion.[48] Therefore, we have selected such a method for our measurements.

The dependence of the surface tension on concentration is shown in Figure 2. As expected, both α- and β-$C_{16}G_2$ show a decrease in surface tension upon addition of surfactant down to a minimum value, after which the surface tension remains constant even if the surfactant concentration is increased. The intersection between these two regions marks the CMC, above which micelles form in solution. For the surfactants studied here the transition is not sharply defined. The more gradual change of surface tension may be attributed to the presence of small amounts of surface-active contaminants and complicates the definition of the CMC.[49] As presented in the Experimental Section, part of the impurities may be also surface-active components, such as the glucoside surfactant or the other anomeric form of the surfactant, which would cause the effect observed in these results. Taking this into account, we have decided to label the CMC as the intersection between the premicellar region trend and the section where the surface tension levels out to a constant value (see Figure 2). The CMC defined in this way was found to be 1.4 ± 0.1 and 2.3 ± 0.2 μM for α- and β-$C_{16}G_2$, respectively, which is in good agreement with the expected value presented above.

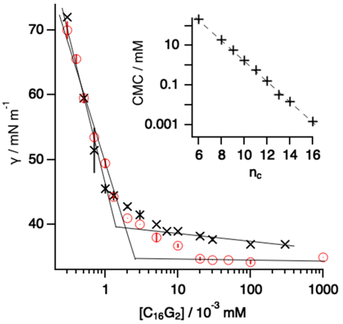

Figure 2. Surface tension of α-$C_{16}G_2$ (×) and β-$C_{16}G_2$ (○) in water (23 °C) against the concentration of surfactant. The solid lines represent the pre- and postmicellar trends and help to find the CMC. Inset: CMC trend displays the CMC for a homologous series of β-alkylmaltosides with different carbon tail lengths.[50]

Self-Assembly in Solution. The self-assembly of α- and β-$C_{16}G_2$ bulk phase as a function of temperature, surfactant concentration, and solvent deuteration was studied by means of DLS, SLS, SAXS, SANS, and cryo-TEM.

A summary of the DLS results (Figure 3) reveals the presence of micellar aggregates, as inferred by the surface tension data. A complete record of the DLS results for all the concentrations and temperatures can be found in the Supporting Information. It should be noted that the R_H values calculated from DLS by using the Stokes−Einstein equation refer to the radius of a sphere with the same diffusion coefficient as the scatterer. As will be discussed below, the self-assembled structures studied here are not spherical. As such, the apparent diffusion coefficient measured by DLS will present contributions from the diffusion of the particle,

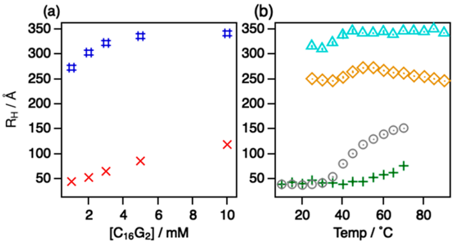

Figure 3. Hydrodynamic radius obtained from cumulants analysis of DLS data and assuming spherical particles at (a) different surfactant concentrations at 50 °C (×: α-$C_{16}G_2$; #: β-$C_{16}G_2$) and (b) temperatures (+: 1 mM α-$C_{16}G_2$; ○: 10 mM α-$C_{16}G_2$; ◇: 1 mM β-$C_{16}G_2$; △: 10 mM β-$C_{16}G_2$).

solvation layer, and trapped solvent as well as the rotational diffusion of those. Hence, the hydrodynamic radius (R_H) does not constitute an absolute measure of the physical size of the micelles but an apparent dimension that relates to the size and conformation of the micelle. With this in mind, there is still important information that can be extracted from the DLS results about these systems. In particular, we have used DLS to identify trends and morphology transitions that can subsequently be confirmed by means of small-angle scattering.

Based on the DLS data, the micelles of β-$C_{16}G_2$ (R_H = 342 ± 1 Å, 50 °C, 10 mM) are considerably larger than those of α-$C_{16}G_2$ (R_H = 118 ± 1 Å, 50 °C, 10 mM) at all of the conditions measured here. This shows again that there is a major impact of the conformation at the anomeric carbon on the surfactant behavior in solution. Surfactant concentration appears to also affect the size of the micelles in the dilute regime, since the diffusion coefficients suggest a transition from smaller aggregates at low concentrations to larger micelles at higher concentrations (see Figure 3a). For α-$C_{16}G_2$ the apparent R_H changes from 44.1 ± 0.3 Å at 1 mM to 118 ± 1 Å at 10 mM surfactant concentration (50 °C). However, this difference is less pronounced for β-$C_{16}G_2$ as it increases from 273 ± 1 Å at 1 mM to 341 ± 1 Å at 10 mM surfactant concentration (50 °C).

The size of the micelles is also influenced by the temperature of the system, and significant differences exist between the two isomeric forms of the surfactant. The α-$C_{16}G_2$ aggregates appears to be larger when increasing the temperature, where the largest increase appears when the temperature passes above the Krafft temperature of the surfactant, which has been observed to be between 25 and 35 °C. The apparent R_H increases from 39.1 ± 0.1 Å at 25 °C to 140 ± 1 Å at 60 °C for a 10 mM surfactant solution. The β-$C_{16}G_2$ surfactant forms large structures at low temperature, and the variation in size with temperature is less pronounced than in the case of α-$C_{16}G_2$. At low temperatures, close to or below the Krafft temperature, the kinetically arrested aggregates show a slightly smaller hydrodynamic radius, 316 ± 1 Å at 25 °C, which increases to an apparent size of 345 ± 1 Å at 60 °C for the 10 mM sample (see Figure 3b).

As DLS only give an indication of the changes in aggregate size, further structural characterization of the surfactant micelles was performed by using SLS, SAXS, SANS, and cryo-TEM. A detailed description of the approach used to fit the data is provided in the Experimental Section. The data and best fits of the applied model to the experimental data are presented in Figure 4. The fitting parameters from the simultaneous fits of SLS, SAXS, and SANS are presented in

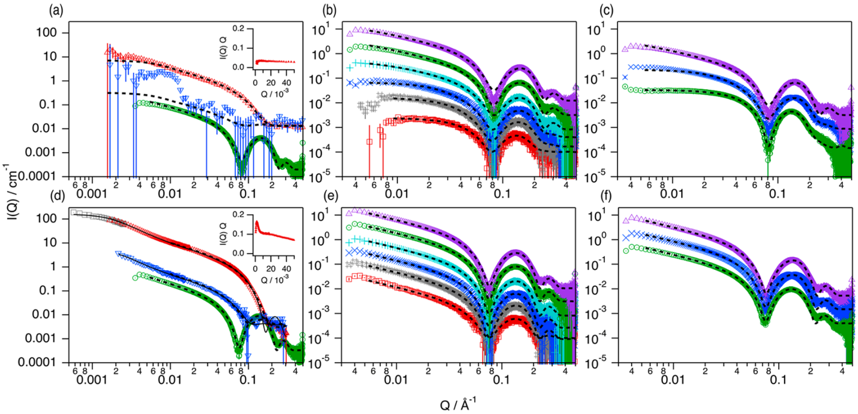

Figure 4. SAXS and SANS data and fits from α- and β-$C_{16}G_2$ micelles in water. (a) SAXS (○) and SANS (△: α-$C_{16}G_2$ in D_2O; ▽: α-$C_{16}G_2$ in H_2O) of 10 mM of α-$C_{16}G_2$ at 50 °C. (b) SAXS at different surfactant concentrations of α-$C_{16}G_2$ at 50 °C (□: 1 mM; #: 2 mM; ×: 3 mM; +: 5 mM; ○: 10 mM; and △: 20 mM). (c) SAXS at different temperatures of 10 mM α-$C_{16}G_2$ solutions (○: 25 °C; ×: 40 °C; and △: 50 °C). (d) SAXS (○), SANS (△: β-$C_{16}G_2$ in D_2O; ▽: β-$C_{16}G_2$ in H_2O) and SLS (□) of 18 mM of β-$C_{16}G_2$ at 50 °C. (e) SAXS at different surfactant concentrations of β-$C_{16}G_2$ at 50 °C (□: 1 mM; #: 2 mM; ×: 3 mM; +: 5 mM; ○: 10 mM; and △: 18 mM). (f) SAXS at different temperatures of 10 mM β-$C_{16}G_2$ solutions (○: 25 °C; ×: 40 °C; and △: 50 °C). The black dashed lines represent the fits using the core−shell ellipsoid or cylinder model, and the flexible cylinder fits are plotted as black solid lines. The insets shown in (a) and (d) present the Holtzer plots ($I(Q)Q$ vs Q) of the SANS data for $C_{16}G_2$ in D_2O. Data and fits have been offset in the Y-axis for clarity. Where not seen, error bars are within the markers.

Table 3. Parameters from the Combined Fit of SAXS and SANS Data Presented in Figure 4a,d[a]

system	r_{core}/Å	t_{shell}/Å	L_{core}/Å	l_p/Å	$\varphi_{fit}/10^{-2}$	φ_{solv}	N_{agg}	a_0/Å^2
α-$C_{16}G_2$	14.7 ± 0.3	14.4 ± 0.2	520 ± 10		0.78 ± 0.01	0.81 ± 0.01	830 ± 20	60.1 ± 2.5
β-$C_{16}G_2$	16.1 ± 0.1	15.1 ± 0.1	6700 ± 200	310 ± 10	1.11 ± 0.02	0.78 ± 0.01	12600 ± 300	53.8 ± 1.8

[a] 10 mM α-$C_{16}G_2$ at 50 °C and 18 mM β-$C_{16}G_2$ at 50 °C. These results were obtained through the co-refinement of the X-ray and neutron data using the core–shell cylinder and flexible cylinder models.

Table 3. A complete record of the fit parameters is included in the Supporting Information.

The exchange of H_2O for D_2O has been previously shown to alter the hydrogen bonding network of the solvent, which in turn affects the micellization of sugar-based surfactants.[26] This effect was further explored by means of DLS and SAXS in the two contrasts used here (see the Supporting Information for these results). The difference between H_2O and D_2O in terms of apparent size of α-$C_{16}G_2$ and β-$C_{16}G_2$ micelles can be seen for the conditions investigated here, with larger aggregates being formed in D_2O. While the difference in R_H is rather small for β-$C_{16}G_2$ micelles, the apparent size of α-$C_{16}G_2$ micelles is more significantly affected. This difference may be due to shifts in the transition temperature when exchanging the solvent, which therefore result in shifts in the temperature-induced morphology transition. The influence of the solvent substitution in the headgroup solvation was evaluated by using SAXS. These results show that the micelle shell is affected and shows a larger thickness in D_2O, while the core of the micelle remains practically unchanged. This implies that the structure of $C_{16}G_2$ micelles vary between the two contrasts measured by using the scattering methods presented here, and therefore this effect must be accounted for when determining the structural characteristics of the aggregates. As the features of the SAXS data at high Q are more pronounced and have a lower experimental error, they will have a larger weight than the neutron data. This will minimize the impact of the isotopic effect from the neutron contrasts. Similarly, information about the elongation of the worm-like micelles is contained in the SLS data (low Q region, data scaled to match the scattering excess of β-$C_{16}G_2$ in D_2O), which is not affected by isotopic substitution as it corresponds to a sample containing surfactant in H_2O. For shorter micelles, where the elongation can be resolved from the X-ray data, no isotope effect is present. Finally, information about the flexibility of the micelle is contained in the intermediate Q range, which is covered by the neutron data. As two contrasts were investigated (hydrogenated surfactant in either H_2O or D_2O) the results from the simultaneous fit will be an error-weighted average of those two contrasts.

Therefore, the results obtained through the corefinement provide an averaged result from both solvents, where this may be more inclined to either the actual values in H_2O or D_2O depending on which technique is mainly driving the fitting. More importantly, the trends observed in the data are the same in H_2O and D_2O, where the beta anomer self-assembles into larger structures than its α-analogue. Furthermore, α-$C_{16}G_2$ was found to undergo a sphere-to-rod transition with temperature in both solvents.

The model used in this study describes a core–shell structure, where the nonsolvated hydrophobic core of the micelle is surrounded by a hydrated shell that contains the surfactant headgroups. To experimentally probe the different characteristics of worm-like micelles, a wide Q range is required for the scattering experiments. From the scattering model of a worm-like micelle three regions can be defined: (1) low Q ($Q < 0.003$ Å^{-1}), which is the Guinier region that corresponds to the contour length of the aggregate; (2) intermediate Q (0.003 Å$^{-1} < Q < 0.01$ Å^{-1}) where the oscillation in the data corresponds to the persistence length of the micelle; and (3) high Q ($Q > 0.01$ Å^{-1}) where a second Guinier region is observed, which corresponds to the cross section of the micelle and is followed by a decrease in the scattering intensity.[10,45] The oscillation that corresponds to the persistence length of the micelle can be easily observed in a Holtzer plot ($I(Q)Q$ vs Q). In this plot, the change in scattering cross section arising from the persistence length is seen as a peak at low Q and, where absent, indicates the lack of significant flexibility. SAXS data also show a strong oscillation at high Q (between ca. 0.07 and 0.2 Å^{-1}), which arises from the density correlation core–shell–solvent and can be used, in conjunction with the neutron data, to determine the characteristics of the headgroup region of the micelle (structure and solvation). Therefore, accessing the entire Q range is of utter importance to build a detailed model of the markedly elongated micelles, and this was possible through the combination of SANS, SAXS, and SLS.

From the structural parameters obtained through the data analysis, other micelle properties may be calculated. The changes in assembly morphology can, at least in part, be described through the packing parameter.[27] As the hydrophobic moiety of both α- and β-$C_{16}G_2$ is the same, differences in the a_0 relate to changes of packing of the surfactants within the micelles. This parameter can be calculated from the aggregation number of the micelle (N_{agg}) and structural characteristics of the micelle core as follows:

$$N_{agg} = \frac{v_{core}}{v}$$

$$a_0 = \frac{S_{core}}{N_{agg}}$$

where v_{core} is the volume of the core as calculated from the micelle structure, v is the volume of a single tail (same as introduced above for the CPP), and S_{core} is the surface area of the micelle core. Similarly, the headgroup solvation (as solvent volume fraction at the headgroup shell, φ_{solv}) can be calculated from the fitted SLD of the headgroup shell as

$$\mathrm{SLD_{shell}} = \mathrm{SLD_{hg}}(1 - \phi_{solv}) + \mathrm{SDL_{solv}}\phi_{solv}$$

where $\mathrm{SLD_{shell}}$ corresponds to the fitted SLD of the shell, $\mathrm{SLD_{hg}}$ is the calculated SLD of the "anhydrous" headgroup (Table 2), and $\mathrm{SLD_{solv}}$ is the calculated SLD of the solvent (Table 2). The variation of these parameters with surfactant concentration and temperature as derived from the analysis of SAXS data is presented in Figure 5.

For each of the systems studied here, the core cross section radius is assumed to remain unchanged with temperature and concentration, as well as type of solvent (H_2O and D_2O), as no major variations in the solvent penetration to the hydrophobic

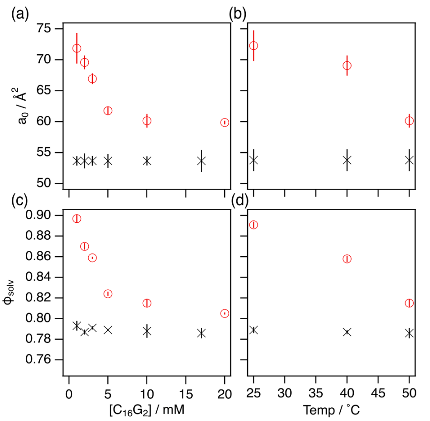

Figure 5. Results derived from the analysis of SAXS data at different surfactant concentrations and temperatures for (a, b) area-per-monomer at the tail−headgroup interface (a_0) and (c, d) solvent volume fraction in the headgroup shell (φ_{solv}) for α-$C_{16}G_2$ (○) and β-$C_{16}G_2$ (×).

region are expected. This value was obtained through the co-refinement of neutron and X-ray data, giving the values of 14.7 ± 0.3 and 16.1 ± 0.1 Å for α- and β-$C_{16}G_2$, respectively.

The differences in these values suggest that the β configuration of the headgroup provides a stronger headgroup interaction, which is likely to be a combination of hydrophobic interaction and hydrogen bonding. This type of interaction increases the degree of the headgroup orientation, which in turn also affects the chain packing. We therefore see strong effects of the position of the anomeric carbon, where the core appears to be larger for the β-$C_{16}G_2$ than for the α-$C_{16}G_2$ micelles with smaller effects on the headgroup region. The reason for the smaller effect on the shell thickness is that it contains much more water (about 80%) than the core. Hence, the apparent increase of layer thickness is much less pronounced than for the core that contains almost no water.

Here it should be noted that we used the same SLD for the two anomers to reduce the number of fitting parameters. However, as pointed out by Campbell et al.,[51] the SLD cannot strictly be regarded as a constant entity for a molecule but depends on the extent of packing of the assembly. In fact, they demonstrated that this can be used to demonstrate a particular phase of a phospholipid interface. Furthermore, the chain packing and headgroup interactions are not independent quantities. Stronger attractive interactions between headgroups are expected to promote a stretching of the acyl chain, and as a result a larger core for the β-anomer is observed.

We would also like to point out that the modeling assumes a homogeneous distribution of the headgroups in the shell, and such a model cannot capture highly complex assembly of the surfactant that is likely to be the case for our system. A more complex mathematical model could be used to identify this phenomenon (e.g., multishell or complex interface); however, this would significantly increase the number of variables to fit and decrease the robustness of the approach, as we do not have enough constraints to our model (e.g., neutron contrasts).

As previously shown by DLS, the overall size of the micelles is strongly affected by the configuration of the anomeric carbon in the surfactant headgroup. β-$C_{16}G_2$ micelles were found to be significantly larger than those of α-$C_{16}G_2$, where the difference in size mainly relies on the differences in the length of the micelle as shown by initial analysis of the scattering data. The contour length of the micelle was considered to be polydisperse in the model fitting and is verified in the cryo-TEM images (see Figure 6). Proper quantification of the polydispersity of the micelle length becomes crucial for the correct evaluation of not only the contour length of the micelle but also of the micelle flexibility.[10] Previous investigations have shown that for spherical and spheroidal micelles the size distribution is rather narrow; thus, the systems are relatively monodisperse. However, Mukerjee predicted that the aggregation number distribution index tends to be 2 for large, asymmetric micelles, and therefore the size distribution is wide.[52,53] To account for polydispersity effects, a Schulz distribution was used to describe the length distribution of the self-assembled structures. For globular and moderately elongated aggregates (elongation ≤10 times the radius of the cross section), the p was fixed at a value of 0.1, as these are more likely relatively monodisperse. The p value was fixed at 0.7 for the elongated micelles (elongation >10 times the radius of the cross section), as this appropriately describes the broad length distribution of the micelles, as observed in our cryo-TEM images (Figure 6). Using this approach, we determined the contour length (and the persistence length, where present) of the micelles. α-$C_{16}G_2$ forms significantly shorter micelles than β-$C_{16}G_2$, as seen in Table 3. As the only difference between these two surfactants is the configuration of the headgroup, this difference can be attributed to this structural difference. This, in turn, is correlated to the different solvation of the sugar headgroups of the two anomers, with the α-anomer being more extensively hydrated.

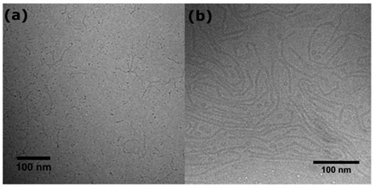

Figure 6. Cryo-TEM images of (a) α-$C_{16}G_2$ 10 mM in H_2O (50 °C prior blotting) and (b) β-$C_{16}G_2$ 10 mM in H_2O (25 °C prior blotting).

At intermediate Q (around 0.003 Å^{-1}), a shoulder is observed in the scattering curves, and a peak appears in the Holtzer plots from β-$C_{16}G_2$ micelles (Figure 4d). This arises from the persistence length of the micelle and relates to the flexibility of the assembly (i.e., longer persistence lengths are attributed to higher levels of micelle stiffness).[45] From the simultaneous analysis of SANS and SLS data the contour and persistence length of the micelles could be determined: L = 6700 ± 200 Å and l_p = 310 ± 10 Å, at 18 mM β-$C_{16}G_2$ concentration, 50 °C ($L/l_p \sim 22$). This value can be directly compared with the reported values for other systems that were determined by using a similar approach. Appell et al. derived the factors that control the persistence length in micelles and defined two contributions: a steric hindrance, due to geometric constraints, and short-range electrostatic interactions, due to the repulsion between polar headgroups. This investigation showed that a minimum of 90 Å could be found for nonionic micelles, and this value was around 200 Å for ionic micelles.[54] By use of SANS, the anionic surfactant sodium dodecyl sulfate (SDS) in the presence of sodium chloride has been reported to form semiflexible aggregates with variable contour and persistence length depending on surfactant and salt concentration.[55] Micelles of the nonionic surfactant $C_{12}E_5$ and $C_{16}E_6$ have persistence lengths of 120 and 170 Å, respectively,[10,56] and β-$C_{14}G_2$ also forms polymer-like micelles with variable length and flexibility.[26] The persistence length of β-$C_{16}G_2$ aggregates is similar to that observed for β-$C_{14}G_2$, although the aggregates of the former are larger in general, unlike $C_{12}E_5$ and $C_{16}E_6$ micelles which are reported to be more flexible. This is indicative of the dominant effect of the surfactant headgroup on the flexibility of the aggregates, where the sugar-based surfactants show similar persistence lengths despite the different tail lengths. Similarly, β-$C_{16}G_2$ micelles show increased stiffness compared to the SDS assemblies in the presence of salt, confirming the remarkable rigidity of the sugar-based micelles. The degree of flexibility can also be qualitatively compared to that of polymers or polymer-like systems, where the flexibility for synthetic polymers is often higher (e.g., poly(acrylic) acid) and for biopolymers is lower (e.g., DNA strands).[46] Thus, the flexibility of β-$C_{16}G_2$ micelles is situated between those two non-surfactant-based systems. Although α-$C_{16}G_2$ also forms elongated micelles under certain conditions, the scattering curve did not show any evidence of statistical length. This means that the persistence length of these micelles is on the order of their contour length.

The surfactant concentration has been found to affect the morphology of the micelles, as observed for other maltoside and ethoxylated surfactants, where increasing the concentration of surfactant promotes elongation of the micelles.[26,53,57] The growth of the micelles with increasing concentration is remarkable for α-$C_{16}G_2$ micelles, where these evolve from globular aggregates at low concentrations ($L = 86 \pm 3$ Å, 50 °C, 1 mM) to elongated micelles at higher concentrations ($L = 650 \pm 10$ Å, 50 °C, 20 mM). The β-$C_{16}G_2$ aggregates were found to be more elongated ($L = 6700 \pm 200$ Å, 50 °C, 18 mM) than the α-analogue in the whole range of concentrations investigated here. Because of the limited experimental Q range of our SAXS experiments, the contour length of the β-$C_{16}G_2$ micelles could not be resolved for all of the concentrations. Nonetheless, we would expect the elongation of these micelles to be longer than 2000 Å (as the maximum dimension that can be measured with the current SAXS setup) and of similar dimensions as those of the one we could determine through the combination of all the scattering methods. Therefore, it can be concluded that the β-$C_{16}G_2$ micelles do not go through a morphology transition at the conditions explored in this work. This assumption is based on the trends observed in the DLS results, where we have seen that changes in elongation of the micelles are not as remarkable as those occurring for the α-$C_{16}G_2$ system.

In a similar fashion to the concentration-induced growth, the elongation of α-$C_{16}G_2$ micelles was found to considerably vary with the temperature of the system, going from rod-like aggregates at 50 °C ($L = 520 \pm 10$ Å, 10 mM) to shorter, ellipsoidal nonequilibrium self-assembled structures at 25 °C ($L = 81 \pm 3$ Å, 10 mM). On the other hand, β-$C_{16}G_2$ micelles appear to show similar elongation in the temperature range explored here. The growth of α-$C_{16}G_2$ micelles with increasing temperature can be explained through an increase in the conformational disorder of the tails and the dehydration of the nonionic headgroup. The system favors the formation of shorter, highly hydrated micelles at low temperature that then evolve to more elongated micelles at high temperature. This change in morphology, commonly reported as sphere-to-rod transition in micellar systems, has been previously investigated for nonionic surfactants following theoretical,[58] experimental,[53] and computational approaches.[59] The absence of this transition in the β-$C_{16}G_2$ micelles with temperature appears to be more complicated to explain. From the results observed here, this distinctive phenomenon must arise from the headgroup interactions, where the β-configuration may favor a stronger intermolecular attractive interaction between headgroups. Thus, a change of the spontaneous curvature of the aggregate would require a significant amount of energy to disrupt the arrangement of the headgroups. This may not be compensated by the entropy gain of more flexible tails, and thus temperature will not greatly affect the morphology of the micelles.

Interestingly, this behavior is the opposite of what was found for shorter maltoside surfactants. Micelles of β-$C_{10}G_2$ and β-$C_{12}G_2$ shrink to smaller assemblies with increasing temperature, as seen through the combination of SAXS and molecular dynamics simulations.[20] In contrast, neutron and light scattering results showed that β-$C_{14}G_2$ micelles increase monotonically in size with temperature.[26] The change in behavior for the longer surfactant tails may be due to a change in the energy balance between headgroup−headgroup and tail−tail interactions, where the entropic contribution of longer tails may become more significant above a threshold tail length.

As shown in Figure 5, the a_0 for β-$C_{16}G_2$ micelles are smaller than those of α-$C_{16}G_2$. The smaller area (thus larger packing parameter for a given surfactant chain) relates to the formation of longer aggregates, as seen for β-$C_{16}G_2$. As the micelles grow in length, the change in a_0 diminishes asymptotically as it approaches the value for an infinite rod. This means that for very elongated cylinders, such as those of β-$C_{16}G_2$, variations in length result in small changes in a_0 (e.g., $a_0(L = 4000\ \text{Å}) = 53.9\ \text{Å}^2$; $a_0(L = 6000\ \text{Å}) = 53.8\ \text{Å}^2$; $a_0(L = 8000\ \text{Å}) = 53.6\ \text{Å}^2$, as calculated for the cross section of a β-$C_{16}G_2$ micelle). The elongation of the micelles could not be resolved for all the conditions used here but appears to be in the same order of magnitude as the one we could determine. Therefore, we assumed that the micelle length will remain constant, i.e., independent of concentration and temperature, for comparison. Hence, no change in a_0 is observed for β-$C_{16}G_2$. The α-$C_{16}G_2$ system, on the other hand, shows significant variations with surfactant concentration and temperature. These changes correlate to the morphology transitions of the assemblies, for which smaller a_0 relate to longer aggregates.

The results for the headgroup solvation show that φ_{solv} for β-$C_{16}G_2$ micelles (∼0.79) is consistently lower than that for α-$C_{16}G_2$ micelles (>0.82). This shows that the headgroup hydration is different for these surfactants, which confirms that differences in the morphology between α- and β-$C_{16}G_2$ micelles arises from a distinct solvation mechanism. Micelles of α-$C_{16}G_2$ present a higher solvation that varies with temperature and surfactant concentration, where larger values relate to higher curvature and thus the formation of shorter micelles. This feature is remarked at temperature below the

Krafft point, where α-$C_{16}G_2$ aggregates adopt globular morphologies in what seems to be a kinetically arrested state, where surfactant remains dissolved for several hours before precipitation. A similar behavior in the headgroup solvation has been previously reported for ethylene glycol-linked carbohydrate-based surfactants, where the formation of worm-like micelles is reported to happen at temperatures above 50 °C.[60] The hydration of β-$C_{16}G_2$ micelles, on the other hand, remains rather unchanged with temperature and concentration. The higher solvation levels of α-$C_{16}G_2$ may arise from the packing of the surfactant headgroups, which favors the interaction of the headgroup with water molecules instead of with neighboring headgroups due to the inherent headgroup tilt of the α-anomer. The β-monomer is characterized by a planar geometry, where the (hydrogen bond and hydrophobic) interactions between headgroups may be more likely. This reduces the available interactions of surfactant headgroups with solvent molecules and prompts the dehydration of the micelle shell, thus reducing the curvature of the aggregate and leading to the formation of elongated micelles. These interactions between headgroups, together with water−headgroup interactions, have been reported for the solvation of glucoside and maltoside surfactants using relaxation NMR.[29] Hydrophobic interactions between headgroups have been also hypothesized to play a role in the solvation of sugar strands.[34,35] In a similar scenario to the hydrogen bond interactions, hydrophobic interactions may be also favored in the β configuration and contribute to the observed dehydration of the headgroup.

Cryo-TEM was used to verify the selection of scattering models as well as to lend support for the results from the scattering data analysis. The images provide direct visualization of the aggregates and can be used to estimate the elongation of the micelles. In agreement with the scattering results, the cryo-TEM images (Figure 6) show that the β-$C_{16}G_2$ micelles are significantly more elongated than those of α-$C_{16}G_2$, whereas the cross section of the micelle is similar within the image resolution. The images also reveal the polydisperse character of the micelles, where a distribution of contour and persistence lengths is easily observable. Thus, these results are in good agreement with the models elaborated from the results of the scattering methods.

CONCLUSIONS

The behavior of sugar-based surfactants is of utter importance for fundamental and applied science (e.g., solubilization of membrane proteins), and it is therefore surprising that some fundamental concepts remain rather unexplored and unclear, in particular the effect of surfactant chirality. Here we have explored the effect of the position of the anomeric carbon on the behavior of two long-chain maltoside surfactants, namely α- and β-$C_{16}G_2$, in dilute aqueous solutions. Surface tension measurements were used to determine the CMC of the surfactants, where the two surfactants show different CMCs and α-$C_{16}G_2$ presents a lower value for that.

Structural investigations of micelle morphology by means of scattering techniques and cryo-transmission electron microscopy showed that significant morphological differences are induced when changing in the anomeric carbon. We provide evidence that β-$C_{16}G_2$ forms semiflexible worm-like micelles, which only undergo subtle morphological changes with concentration and temperature. Unlike what was observed for the β-isomer of the surfactant, α-$C_{16}G_2$ micelles show a variety of different morphologies. The self-assembly is strongly influenced by the temperature of the system, where a sphere-to-rod transition is observed when increasing the temperature from 25 to 50 °C. A similar transition is observed with surfactant concentration, as the micelles grow longer with increasing the concentration.

The structural changes presented here are therefore induced by the characteristics of the surfactant headgroup, where the only difference between the two surfactants is the configuration of the anomeric carbon. Interestingly, different anomers self-assemble in completely different fashions. This in turn may be explained through the solvation and arrangement of headgroups in the micelles, where the β-configuration provides a more efficient packing than the α-anomer. This suggests that headgroup−headgroup interactions (hydrogen bond and/or hydrophobic) are more dominant in β-$C_{16}G_2$ micelles than in α-$C_{16}G_2$ micelles, where headgroup−solvent interactions (hydrogen bond) are favored.

The increase of fundamental understanding of these systems, as presented in this study, will assist in the development of sustainable technologies using sugar-based surfactants. As such, the macroscopic response of the system and molecular interactions could be easily tuned through variations in the microstructure of the aggregates and thus in the characteristics of the surfactant molecules.

ASSOCIATED CONTENT

Supporting Information

The Supporting Information is available free of charge on the ACS Publications website at DOI: 10.1021/acs.langmuir.9b01960.

> HPLC chromatograms of the surfactants; dynamic light scattering and small-angle scattering results; dynamic light scattering and SAXS of isotope-substituted samples (PDF)

AUTHOR INFORMATION

Corresponding Authors

*E-mail: johan.larsson@fkem1.lu.se.
*E-mail: tommy.nylander@fkem1.lu.se.

ORCID

Johan Larsson: 0000-0001-9210-5069
Adrian Sanchez-Fernandez: 0000-0002-0241-1191
Lester C. Barnsley: 0000-0002-1341-905X
Tommy Nylander: 0000-0001-9420-2217

Notes

The authors declare no competing financial interest.

ACKNOWLEDGMENTS

This work is based upon experiments performed at the KWS-1 instrument operated by JCNS at the Heinz Maier-Leibnitz Zentrum (MLZ), Garching, Germany. The SANS experiments on Sans2d at the ISIS Pulsed Neutron and Muon Source were supported by a beamtime allocation from the Science and Technology Facilities Council. The SAXS experiments were performed on beamline BM29 at the European Synchrotron Radiation Facility (ESRF), Grenoble, France. We are grateful to Martha Brennich at the ESRF for providing assistance in using the beamline. We thank Prof. Karin Schillén for the fruitful discussions on light scattering and Dr. Stephen King for the constructive input into micelle polydispersity. This work benefited from the use of the SasView application, originally developed under NSF award DMR-0520547. SasView contains code developed with funding from the European Union's Horizon 2020 research and innovation programme under the SINE2020 project, grant agreement No. 654000. The National Center for High Resolution Electron Microscopy, Lund University, is gratefully acknowledged for providing experimental resources. We also thank Anna Carnerup at the Physical Chemistry Department, Lund University, for the support provided during the cryo-TEM measurements. The authors are also thankful to Swedish Research Council Formas (Grant 2015-666) for the funding for J.L. The research in this study was performed with financial support from Vinnova - Swedish Governmental Agency for Innovation Systems within the NextBioForm Competence Centre.

REFERENCES

(1) Hill, K.; Rhode, O. Sugar-based surfactants for consumer products and technical applications. *Lipid/Fett* **1999**, *101* (1), 25−33.

(2) Foley, P.; Kermanshahi pour, A.; Beach, E. S.; Zimmerman, J. B. Derivation and synthesis of renewable surfactants. *Chem. Soc. Rev.* **2012**, *41* (4), 1499−1518.

(3) Chatterjee, C.; Pong, F.; Sen, A. Chemical conversion pathways for carbohydrates. *Green Chem.* **2015**, *17* (1), 40−71.

(4) Balzer, D.; Lüders, H. *Nonionic Surfactants: Alkyl Polyglucosides*; Marcel Dekker: New York, 2000.

(5) Seddon, A. M.; Curnow, P.; Booth, P. J. Membrane proteins, lipids and detergents: not just a soap opera. *Biochim. Biophys. Acta, Biomembr.* **2004**, *1666* (1), 105−117.

(6) Strey, R.; Schomäcker, R.; Roux, D.; Nallet, F.; Olsson, U. Dilute lamellar and L3 phases in the binary water−C12E5 system. *J. Chem. Soc., Faraday Trans.* **1990**, *86* (12), 2253−2261.

(7) Nilsson, P. G.; Wennerström, H.; Lindman, B. Structure of micellar solutions of nonionic surfactants. Nuclear magnetic resonance self-diffusion and proton relaxation studies of poly (ethylene oxide) alkyl ethers. *J. Phys. Chem.* **1983**, *87* (8), 1377−1385.

(8) Mitchell, D. J.; Tiddy, G. J. T.; Waring, L.; Bostock, T.; McDonald, M. P. Phase behaviour of polyoxyethylene surfactants with water. Mesophase structures and partial miscibility (cloud points). *J. Chem. Soc., Faraday Trans. 1* **1983**, *79* (4), 975−1000.

(9) Patist, A.; Bhagwat, S. S.; Penfield, K. W.; Aikens, P.; Shah, D. O. On the measurement of critical micelle concentrations of pure and technical-grade nonionic surfactants. *J. Surfactants Deterg.* **2000**, *3* (1), 53−58.

(10) Jerke, G.; Pedersen, J. S.; Egelhaaf, S. U.; Schurtenberger, P. Flexibility of Charged and Uncharged Polymer-like Micelles. *Langmuir* **1998**, *14* (21), 6013−6024.

(11) Tiberg, F.; Joensson, B.; Tang, J.-A.; Lindman, B. Ellipsometry Studies of the Self-Assembly of Nonionic Surfactants at the Silica-Water Interface: Equilibrium Aspects. *Langmuir* **1994**, *10* (7), 2294−2300.

(12) Zhang, R.; Marone, P. A.; Thiyagarajan, P.; Tiede, D. M. Structure and Molecular Fluctuations of n-Alkyl-*β*-d-glucopyranoside Micelles Determined by X-ray and Neutron Scattering. *Langmuir* **1999**, *15* (22), 7510−7519.

(13) Lipfert, J.; Columbus, L.; Chu, V. B.; Lesley, S. A.; Doniach, S. Size and Shape of Detergent Micelles Determined by Small-Angle X-ray Scattering. *J. Phys. Chem. B* **2007**, *111* (43), 12427−12438.

(14) Nilsson, F.; Söderman, O.; Johansson, I. Four Different C8G1 Alkylglucosides. Anomeric Effects and the Influence of Straight vs Branched Hydrocarbon Chains. *J. Colloid Interface Sci.* **1998**, *203*, 131−139.

(15) Nilsson, F.; Söderman, O.; Johansson, I. Physical-Chemical Properties of the n-Octyl *β*-d-Glucoside/Water System. A Phase Diagram, Self-Diffusion NMR, and SAXS Study. *Langmuir* **1996**, *12* (4), 902−908.

(16) Ericsson, C. A.; Söderman, O.; Garamus, V. M.; Bergström, M.; Ulvenlund, S. Effects of Temperature, Salt, and Deuterium Oxide on the Self-Aggregation of Alkylglycosides in Dilute Solution. 1. n-Nonyl-*β*-d-glucoside. *Langmuir* **2004**, *20* (4), 1401−1408.

(17) Nilsson, F.; Söderman, O.; Hansson, P.; Johansson, I. Physical-Chemical Properties of C9G1 and C10G1 *β*-Alkylglucosides. Phase Diagrams and Aggregate Size/Structure. *Langmuir* **1998**, *14* (15), 4050−4058.

(18) He, L.; Garamus, V. M.; Funari, S. S.; Malfois, M.; Willumeit, R.; Niemeyer, B. Comparison of Small-Angle Scattering Methods for the Structural Analysis of Octyl-*β*-maltopyranoside Micelles. *J. Phys. Chem. B* **2002**, *106* (31), 7596−7604.

(19) Alpes, H.; Allmann, K.; Plattner, H.; Reichert, J.; Rick, R.; Schulz, S. Formation of large unilamellar vesicles using alkyl maltoside detergents. *Biochim. Biophys. Acta, Biomembr.* **1986**, *862* (2), 294−302.

(20) Ivanović, M. T.; Bruetzel, L. K.; Lipfert, J.; Hub, J. S. Temperature-Dependent Atomic Models of Detergent Micelles Refined against Small-Angle X-Ray Scattering Data. *Angew. Chem., Int. Ed.* **2018**, *57* (20), 5635−5639.

(21) Dupuy, C.; Auvray, X.; Petipas, C.; Rico-Lattes, I.; Lattes, A. Anomeric Effects on the Structure of Micelles of Alkyl Maltosides in Water. *Langmuir* **1997**, *13* (15), 3965−3967.

(22) Jensen, G. V.; Lund, R.; Gummel, J.; Monkenbusch, M.; Narayanan, T.; Pedersen, J. S. Direct Observation of the Formation of Surfactant Micelles under Nonisothermal Conditions by Synchrotron SAXS. *J. Am. Chem. Soc.* **2013**, *135* (19), 7214−7222.

(23) Putra, E. G. R.; Ikram, A. A 36m SANS BATAN spectrometer (SMARTer): Probing n-dodecyl-*β*-d-maltoside micelles structures by a contrast variation. *Nucl. Instrum. Methods Phys. Res., Sect. A* **2009**, *600* (1), 288−290.

(24) Bäverbäck, P.; Oliveira, C. L. P.; Garamus, V. M.; Varga, I.; Claesson, P. M.; Pedersen, J. Structural Properties of *β*-Dodecylmaltoside and C12E6Mixed Micelles. *Langmuir* **2009**, *25* (13), 7296−7303.

(25) Cecutti, C.; Focher, B.; Perly, B.; Zemb, T. Glycolipid self-assembly: micellar structure. *Langmuir* **1991**, *7* (11), 2580−2585.

(26) Ericsson, C. A.; Söderman, O.; Garamus, V. M.; Bergström, M.; Ulvenlund, S. Effects of temperature, salt, and deuterium oxide on the self-aggregation of alkylglycosides in dilute solution. 2. n-Tetradecyl-beta-D-maltoside. *Langmuir* **2005**, *21* (4), 1507−1515.

(27) Israelachvili, J. N.; Mitchell, D. J.; Ninham, B. W. Theory of self-assembly of hydrocarbon amphiphiles into micelles and bilayers. *J. Chem. Soc., Faraday Trans. 2* **1976**, *72* (0), 1525−1568.

(28) Boyd, B. J.; Drummond, C. J.; Krodkiewska, I.; Grieser, F. How Chain Length, Headgroup Polymerization, and Anomeric Configuration Govern the Thermotropic and Lyotropic Liquid Crystalline Phase Behavior and the Air-Water Interfacial Adsorption of Glucose-Based Surfactants. *Langmuir* **2000**, *16* (19), 7359−7367.

(29) Cardoso, M. V. C.; Sabadini, E. Before and Beyond the Micellization of n-Alkyl Glycosides. A Water-1H NMR Relaxation Study. *Langmuir* **2013**, *29* (51), 15778−15786.

(30) Ranieri, D.; Preisig, N.; Stubenrauch, C. On the Influence of Intersurfactant H-Bonds on Foam Stability: A Study with Technical Grade Surfactants. *Tenside, Surfactants, Deterg.* **2018**, *55* (1), 6−16.

(31) Whiddon, C.; Söderman, O. Unusually Large Deuterium Isotope Effects in the Phase Diagram of a Mixed Alkylglucoside Surfactant/Water System. *Langmuir* **2001**, *17* (6), 1803−1806.

(32) Szejtli, J. Introduction and General Overview of Cyclodextrin Chemistry. *Chem. Rev.* **1998**, *98* (5), 1743−1754.

(33) Funasaki, N.; Ishikawa, S.; Neya, S. Advances in physical chemistry and pharmaceutical applications of cyclodextrins. *Pure Appl. Chem.* **2008**, *80* (7), 1511−1524.

(34) Alves, L.; Medronho, B. F.; Antunes, F. E.; Romano, A.; Miguel, M. G.; Lindman, B. On the role of hydrophobic interactions in cellulose dissolution and regeneration: Colloidal aggregates and molecular solutions. *Colloids Surf., A* **2015**, *483*, 257−263.

(35) Glasser, W. G.; Atalla, R. H.; Blackwell, J.; Malcolm Brown, R.; Burchard, W.; French, A. D.; Klemm, D. O.; Nishiyama, Y. About the

structure of cellulose: debating the Lindman hypothesis. *Cellulose* **2012**, *19* (3), 589−598.

(36) Pernot, P.; Round, A.; Barrett, R.; De Maria Antolinos, A.; Gobbo, A.; Gordon, E.; Huet, J.; Kieffer, J.; Lentini, M.; Mattenet, M.; Morawe, C.; Mueller-Dieckmann, C.; Ohlsson, S.; Schmid, W.; Surr, J.; Theveneau, P.; Zerrad, L.; McSweeney, S. Upgraded ESRF BM29 beamline for SAXS on macromolecules in solution. *J. Synchrotron Radiat.* **2013**, *20* (4), 660−664.

(37) Orthaber, D.; Bergmann, A.; Glatter, O. SAXS experiments on absolute scale with Kratky systems using water as a secondary standard. *J. Appl. Crystallogr.* **2000**, *33* (2), 218−225.

(38) Frielinghaus, H.; Feoktystov, A.; Berts, I.; Mangiapia, G. KWS-1: Small-angle scattering diffractometer. *Journal of large-scale research facilities JLSRF* **2015**, *1*, 28.

(39) Heenan, R. K.; Rogers, S. E.; Turner, D.; Terry, A. E.; Treadgold, J.; King, S. M. Small Angle Neutron Scattering Using Sans2d. *Neutron News* **2011**, *22* (2), 19−21.

(40) Feoktystov, A. V.; Frielinghaus, H.; Di, Z.; Jaksch, S.; Pipich, V.; Appavou, M.-S.; Babcock, E.; Hanslik, R.; Engels, R.; Kemmerling, G.; Kleines, H.; Ioffe, A.; Richter, D.; Bruckel, T. KWS-1 high-resolution small-angle neutron scattering instrument at JCNS: current state. *J. Appl. Crystallogr.* **2015**, *48* (1), 61−70.

(41) Doucet, M.; Cho, J. H.; Alina, G.; Bakker, J.; Bouwman, W.; Butler, P.; Campbell, K.; Gonzales, M.; Heenan, R.; Jackson, A.; Juhas, P.; King, S.; Kienzle, P.; Krzywon, J.; Markvardsen, A.; Nielsen, T.; O'Driscoll, L.; Potrzebowski, W.; Ferraz Leal, R.; Richter, T.; Rozycko, P.; Washington, A. SasView version 4.1, 2017.

(42) Tanford, C. Micelle shape and size. *J. Phys. Chem.* **1972**, *76* (21), 3020−3024.

(43) Pedersen, J. S. Analysis of small-angle scattering data from colloids and polymer solutions: modeling and least-squares fitting. *Adv. Colloid Interface Sci.* **1997**, *70*, 171−210.

(44) Kotlarchyk, M.; Chen, S. H. Analysis of small angle neutron scattering spectra from polydisperse interacting colloids. *J. Chem. Phys.* **1983**, *79* (5), 2461−2469.

(45) Pedersen, J. S.; Schurtenberger, P. Scattering Functions of Semiflexible Polymers with and without Excluded Volume Effects. *Macromolecules* **1996**, *29* (23), 7602−7612.

(46) Dreiss, C. A. Wormlike micelles: where do we stand? Recent developments, linear rheology and scattering techniques. *Soft Matter* **2007**, *3* (8), 956−970.

(47) Mattei, M.; Kontogeorgis, G. M.; Gani, R. Modeling of the Critical Micelle Concentration (CMC) of Nonionic Surfactants with an Extended Group-Contribution Method. *Ind. Eng. Chem. Res.* **2013**, *52* (34), 12236−12246.

(48) Kairaliyeva, T.; Aksenenko, E. V.; Mucic, N.; Makievski, A. V.; Fainerman, V. B.; Miller, R. Surface Tension and Adsorption Studies by Drop Profile Analysis Tensiometry. *J. Surfactants Deterg.* **2017**, *20* (6), 1225−1241.

(49) Elworthy, P. H.; Mysels, K. J. The surface tension of sodium dodecylsulfate solutions and the phase separation model of micelle formation. *J. Colloid Interface Sci.* **1966**, *21* (3), 331−347.

(50) Anatrace; https://www.anatrace.com/ (accessed 15-11-2018).

(51) Campbell, R. A.; Saaka, Y.; Shao, Y.; Gerelli, Y.; Cubitt, R.; Nazaruk, E.; Matyszewska, D.; Lawrence, M. J. Structure of surfactant and phospholipid monolayers at the air/water interface modeled from neutron reflectivity data. *J. Colloid Interface Sci.* **2018**, *531*, 98−108.

(52) Mukerjee, P. Size distribution of small and large micelles. Multiple equilibrium analysis. *J. Phys. Chem.* **1972**, *76* (4), 565−570.

(53) Glatter, O.; Fritz, G.; Lindner, H.; Brunner-Popela, J.; Mittelbach, R.; Strey, R.; Egelhaaf, S. U. Nonionic Micelles near the Critical Point: Micellar Growth and Attractive Interaction. *Langmuir* **2000**, *16* (23), 8692−8701.

(54) Appell, J.; Porte, G.; Poggi, Y. Quantitative estimate of the orientational persistence length of flexible elongated micelles of cetylpyridinium bromide. *J. Colloid Interface Sci.* **1982**, *87* (2), 492−499.

(55) Magid, L. J.; Li, Z.; Butler, P. D. Flexibility of Elongated Sodium Dodecyl Sulfate Micelles in Aqueous Sodium Chloride: A Small-Angle Neutron Scattering Study. *Langmuir* **2000**, *16* (26), 10028−10036.

(56) Kwon, S. Y. Length Control in Rigid Cylindrical Nanoassembly by Tuning Molecular Interactions in Aqueous Solutions. *Langmuir* **2008**, *24* (19), 10674−10679.

(57) Schurtenberger, P.; Cavaco, C.; Tiberg, F.; Regev, O. Enormous Concentration-Induced Growth of Polymer-like Micelles. *Langmuir* **1996**, *12* (12), 2894−2899.

(58) Puvvada, S.; Blankschtein, D. Molecular-thermodynamic approach to predict micellization, phase behavior and phase separation of micellar solutions. I. Application to nonionic surfactants. *J. Chem. Phys.* **1990**, *92* (6), 3710−3724.

(59) Velinova, M.; Sengupta, D.; Tadjer, A. V.; Marrink, S.-J. Sphere-to-rod transitions of nonionic surfactant micelles in aqueous solution modeled by molecular dynamics simulations. *Langmuir* **2011**, *27* (23), 14071−14077.

(60) Moore, J. E.; McCoy, T. M.; de Campo, L.; Sokolova, A. V.; Garvey, C. J.; Pearson, G.; Wilkinson, B. L.; Tabor, R. F. Wormlike micelle formation of novel alkyl-tri(ethylene glycol)-glucoside carbohydrate surfactants: Structure−function relationships and rheology. *J. Colloid Interface Sci.* **2018**, *529*, 464−475.

Electronic Supporting Information for:

The effect of the anomeric configuration on the micellization of hexadecylmaltoside surfactants

Johan Larsson,[a] Adrian Sanchez-Fernandez,[b] Najet Mahmoudi,[c] Lester C. Barnsley,[d] Marie Wahlgren,[b,e] Tommy Nylander,[a,f] Stefan Ulvenlund[b,e]

[a]Physical Chemistry, Department Chemistry, Lund University, Box 124, 221 00 Lund, Sweden.

[b]Food Technology, Nutrition and Engineering, Lund University, Box 124, 221 00 Lund, Sweden.

[c]ISIS Spallation Source, STFC, Rutherford Appleton Laboratory, Didcot, UK.

[d]Jülich Centre for Neutron Science (JCNS) at Heinz Maier-Leibnitz Zentrum (MLZ), Forschungszentrum Jülich GmbH, Lichtenbergstr. 1, 85748 Garching, Germany.

[e]Enza Biotech AB, Getingevägen 60, 222 41 Lund, Sweden.

[f]NanoLund, Lund University, Lund, Sweden

HPLC characterization of the surfactants

The surfactants used in this work were characterized using HPLC. The chromatograms resulting from the measurements are presented in Figure S1 and the values calculated of purity are included in the Experimental section of the main text.

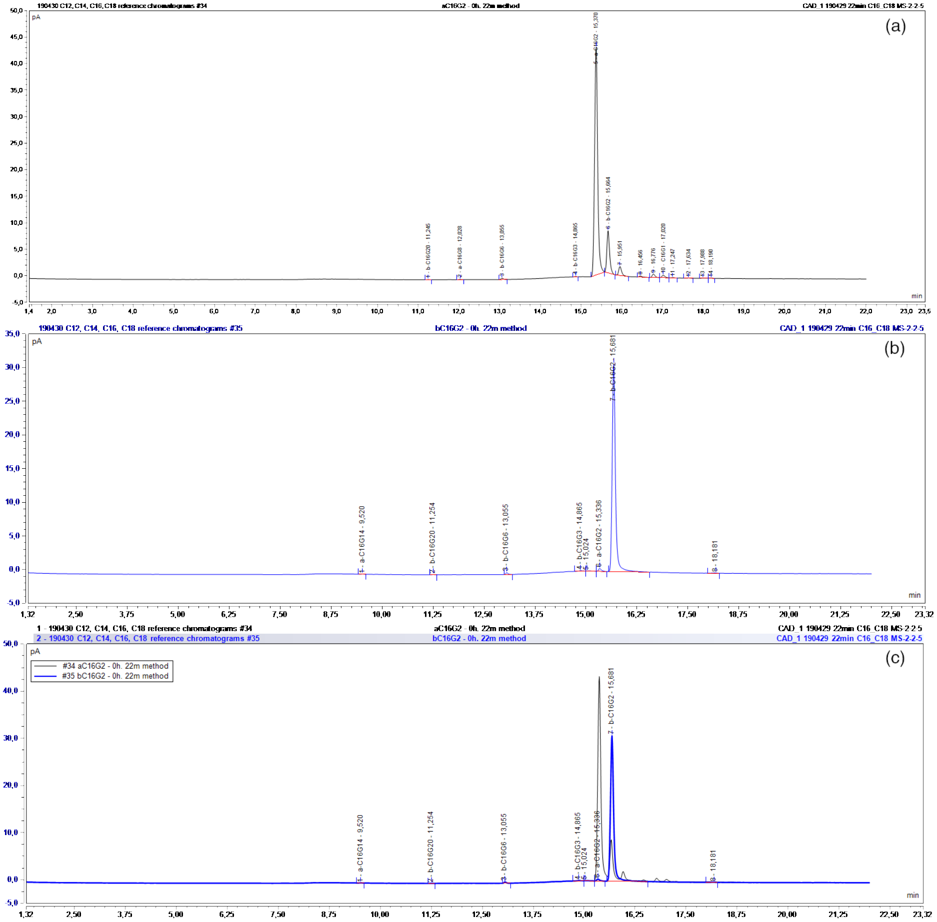

Figure S1 HPLC chromatograms of (a) α-$C_{16}G_2$ and (b) β-$C_{16}G_2$. For comparison, (c) shows the overlap of (black line) α-$C_{16}G_2$ and (blue line) β-$C_{16}G_2$ chromatograms.

Dynamic light scattering

Results from dynamic light scattering (DLS) measurements of α-$C_{16}G_2$ and β-$C_{16}G_2$ at different concentrations and temperatures are presented in Figure S2 and Figure S3, respectively. The hydrodynamic radius was obtained by fitting the experimental auto-correlation function using the Cumulant method.

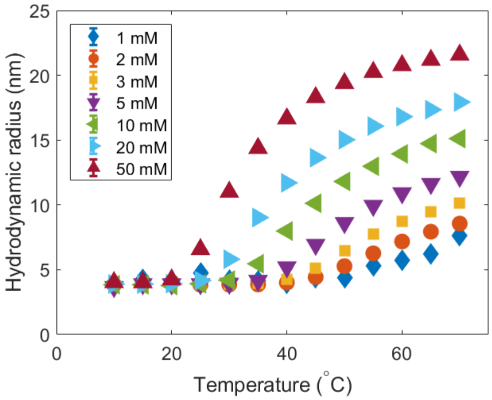

Figure S2 Hydrodynamic radius of α-$C_{16}G_2$ micelles versus temperature at different concentrations.

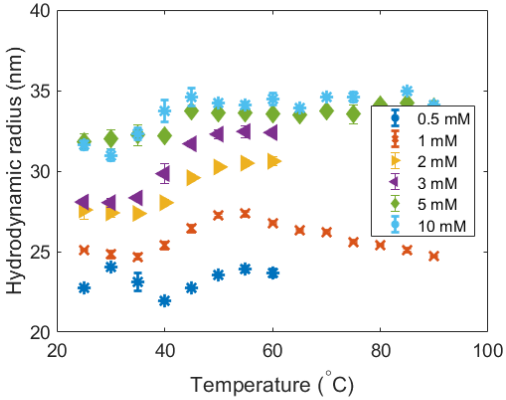

Figure S3 Hydrodynamic radius of β-$C_{16}G_2$ micelles versus temperature at different concentrations.

As shown by these results, the effect of temperature and concentration appear to differ between the two surfactants. A detailed description of these results is found in the main text.

Solvent isotope effect on micelle structure

As presented in the main manuscript, isotope substitution tends to affect the structure of the surfactant aggregates. The small-angle neutron scattering measurements presented here were performed in D_2O, and since previous investigations have revealed a quite substantial effect of D_2O on alkylglycoside micelle size,[1] we have evaluated the effect of isotope substitution by means of DLS. The results from these experiments are presented in Figure S4, where the hydrodynamic radius of protonated β-$C_{16}G_2$ micelles in D_2O is compared to that in H_2O at different temperatures.

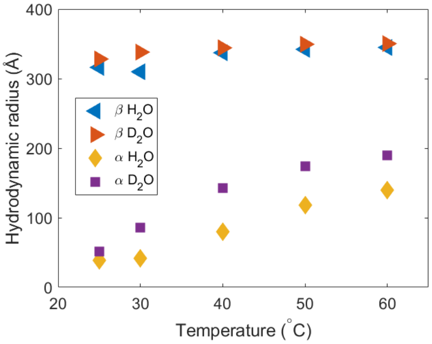

Figure S4 Hydrodynamic radius of α-$C_{16}G_2$ and β-$C_{16}G_2$ micelles versus temperature for 10 mM samples in H_2O and D_2O at different temperatures.

In aqueous solution, the hydrodynamic radius of the micelles was found to be slightly larger in D_2O than in H_2O, which demonstrates that the substitution of protonated solvent for deuterated solvent has an impact on the overall size of the surfactant aggregates. In the case of α-$C_{16}G_2$, the differences between the two solvents were found to be significant, in some cases 50 % larger when the surfactant self-assembles in D_2O. Furthermore, and despite the differences in size, the morphology transition observed for the alpha anomer is maintained when changing the solvent, with micelles growing at higher temperatures. For β-$C_{16}G_2$, the micelles are still larger in D_2O, although difference in size is less pronounced than in the case of the alpha configuration. The hydrodynamic radius of the micelles as measured by DLS was found to be around 5 % larger in the case of the deuterated solvent.

In order to quantify differences occurring at molecular level as a result of the isotopic substitution, small-angle X-ray scattering (SAXS) measurements at high momentum transfer (> 0.01 Å^{-1}) were performed using an in-house SAXSLAB's Ganesha 300 XL. The SAXS curves and models from such measurements are presented in Figure S5, and the results from those fits are presented in Table S1.

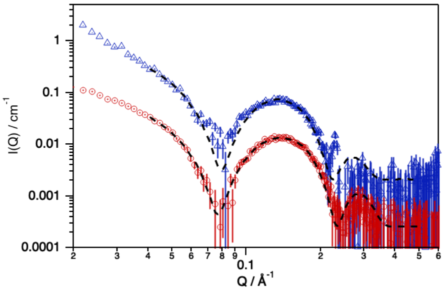

Figure S5 SAXS data and fits of 10 mM of β-$C_{16}G_2$ in (red circles) H_2O and (blue triangles) D_2O at 50 °C. The black dashed lines represent the best fits using a core-shell cylinder model. Data and fits have been offset for clarity.

Table S1 Results from the fits of SAXS data of 10 mM of β-$C_{16}G_2$ in H_2O and D_2O at 50 °C, presented in Figure S4. The elongation of the micelle was fixed at 4300 Å and significant variations in this value were not found to affect the results presented here.

System	r_{core} / Å	t_{shell} / Å	SLD_{shell} / 10^{-6} Å^{-2}
H_2O	16.2±0.3	14.2±0.2	10.4±0.2
D_2O	16.1±0.3	15.9±0.1	10.6±0.1

The SAXS analysis of the surfactant solution in two different isotopic solvents shows differences in the cross-section of the micelle. The micelle core appears to remain unaffected by the substitution of the solvent. Differences can be however found in the characteristics of the headgroup region, where the surfactant solvated in H_2O shows a thickness around 12 % smaller than that for the surfactant in D_2O. The SLD of the shell is also slightly different but such a difference remains within the experimental error.

This demonstrates that the exchange of H_2O for D_2O will have an effect on the scattering data that we use to determine the morphology of the micelles. Although the main trends are preserved with varying the isotopic composition of the solvent, the interpretation of the results shall be carefully approached. The discussion regarding this matter can be found in the main text.

Small-angle scattering

The small-angle scattering data presented in the main text were fitted using a core-shell density distribution for an ellipsoid, cylinder and flexible cylinder, depending on the elongation of the micelle. A detailed list of the parameters from these fits is presented in Table S2, S3, S4 and S5. These parameters were subsequently used to calculate the results presented in the main text.

Table S2 Fitting parameters derived from the analysis of small-angle scattering data of α-$C_{16}G_2$ at different concentrations of surfactant and 50 ˚C.

[α-$C_{16}G_2$] / mM	r_{core} / Å	t_{shell} / Å	L_{core} / Å	lp / Å	φ_{fit} / 10^{-2}	SLD_{shell} / 10^{-6} Å^{-2}
1	14.7±0.3	20.7±0.2	86±3	-	0.14±0.03	9.90±0.05
2	14.7±0.3	18.3±0.2	150±10	-	0.24±0.02	10.00±0.05
3	14.7±0.3	17.4±0.2	220±10	-	0.35±0.02	10.05±0.02
5	14.7±0.3	14.6±0.2	270±10	-	0.41±0.02	10.19±0.01
10	14.7±0.3	14.4±0.2	520±10	-	0.78±0.01	10.24±0.01
20	14.7±0.3	14.1±0.1	650±10	-	1.46±0.01	10.28±0.01

Table S3 Fitting parameters derived from the analysis of small-angle scattering data of α-$C_{16}G_2$ at 10 mM surfactant concentration and different temperatures.

T / ˚C	r_{core} / Å	t_{shell} / Å	L_{core} / Å	lp / Å	φ_{fit} / 10^{-2}	SLD_{shell} / 10^{-6} Å^{-2}
25	14.7±0.3	21.8±0.4	81±3	-	1.01±0.01	9.90±0.06
40	14.7±0.3	17.7±0.2	230±10	-	0.91±0.01	10.05±0.07
50	14.7±0.3	14.4±0.2	570±10	-	0.78±0.01	10.24±0.01

Table S4 Fitting parameters derived from the analysis of small-angle scattering data of β-$C_{16}G_2$ at different concentrations of surfactant and 50 ˚C.

[β-$C_{16}G_2$] / mM	r_{core} / Å	t_{shell} / Å	L / Å	lp / Å	φ_{fit} / 10-2	SLD_{shell} / 10^{-6} Å^{-2}
1	16.1±0.1	15.4±0.2	>2000	-	0.07±0.02	10.34±0.06
2	16.1±0.1	15.1±0.2	>2000	-	0.13±0.09	10.37±0.04
3	16.1±0.1	15.3±0.1	>2000	-	0.20±0.05	10.35±0.04
5	16.1±0.1	15.2±0.1	>2000	-	0.32±0.04	10.36±0.02
10	16.1±0.1	15.1±0.1	>2000	-	0.63±0.03	10.36±0.01
18	16.1±0.1	15.1±0.1	6700±200	310±10	1.11±0.02	10.36±0.01

Table S5 Fitting parameters derived from the analysis of small-angle scattering data of β-$C_{16}G_2$ at 18 mM surfactant concentration and different temperatures.

T / ˚C	r_{core} / Å	t_{shell} / Å	L_{core} / Å	2lp / Å	φ_{fit} / 10^{-2}	SLD_{shell} / 10^{-6} Å^{-2}
25	16.2±0.1	15.3±0.3	>2000	-	1.11±0.02	10.39±0.06
40	16.2±0.1	15.2±0.1	>2000	-	1.11±0.02	10.37±0.07
50	16.1±0.1	15.1±0.1	6700±200	310±10	1.10±0.02	10.36±0.01

Reference

1. Ericsson, C. A.; Soderman, O.; Garamus, V. M.; Bergstrom, M.; Ulvenlund, S., Effects of temperature, salt, and deuterium oxide on the self-aggregation of alkylglycosides in dilute solution. 2. n-Tetradecyl-beta-D-maltoside. *Langmuir* **2005,** *21* (4), 1507-15.

Paper II

Molecular structure of maltoside surfactants controls micelle formation and rheological behavior

J. Larsson, A. Sanchez-Fernandez, A. E. Leung, R. Schweins, B. Wu, T. Nylander, S. Ulvenlund, M. Wahlgren

Journal of Colloid and Interface Science **2021**, 581, 895-904

Journal of Colloid and Interface Science 581 (2021) 895–904

Contents lists available at ScienceDirect

Journal of Colloid and Interface Science

journal homepage: www.elsevier.com/locate/jcis

Regular Article

Molecular structure of maltoside surfactants controls micelle formation and rheological behavior

Johan Larsson [a,*], Adrian Sanchez-Fernandez [b], Anna E. Leung [c], Ralf Schweins [d], Baohu Wu [e], Tommy Nylander [a,f], Stefan Ulvenlund [b,g], Marie Wahlgren [b,g]

[a] Physical Chemistry, Department of Chemistry, Lund University, Box 124, 221 00 Lund, Sweden
[b] Food Technology, Nutrition and Engineering, Lund University, Box 124, 221 00 Lund, Sweden
[c] European Spallation Source, Box 176, 221 00 Lund, Sweden
[d] Institut Laue-Langevin, DS / LSS, 71 Avenue des Martyrs, 38000 Grenoble, France
[e] Jülich Centre for Neutron Science (JCNS) at Heinz Maier-Leibnitz Zentrum (MLZ), Forschungszentrum Jülich GmbH, Lichtenbergstr. 1, 85748 Garching, Germany
[f] NanoLund, Lund University, Lund, Sweden
[g] Enza Biotech AB, Scheelevägen 22, 22363 Lund, Sweden

GRAPHICAL ABSTRACT

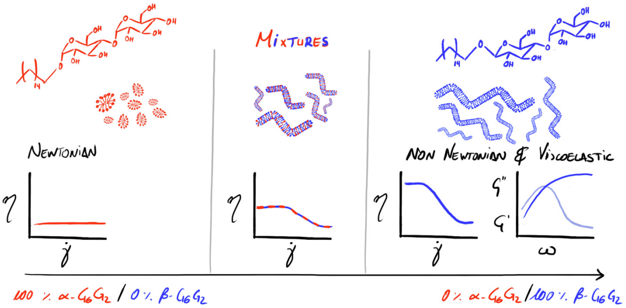

ARTICLE INFO

Article history:
Received 6 July 2020
Revised 27 August 2020
Accepted 28 August 2020
Available online 9 September 2020

Keywords:
Worm-like micelle
Viscoelastic
Sugar-based surfactant
Alkylglycoside
Rheology
Small-angle neutron scattering

ABSTRACT

Hypothesis: The anomeric configuration (α or β) of *n*-hexadecyl-D-maltopyranoside ($C_{16}G_2$) has been shown to affect the morphology of the micelle, from elongated for α-$C_{16}G_2$ to worm-like micelles for β-$C_{16}G_2$. The entanglement of worm-like micelles often leads to strong modifications of the rheological behavior of the system and, as such, the anomeric configuration of $C_{16}G_2$ could also provide the possibility of controlling this. Furthermore, mixing these surfactants are hypothesized to result in mixed micelles allowing to finely tune the rheology of a system containing these sustainable surfactants.

Experiments: The rheology of α- and β-$C_{16}G_2$, and mixtures of those, was determined by rotational and oscillatory rheology at different temperatures and surfactant concentrations. Micelle structure and composition for these systems were characterized using contrast variation small-angle neutron scattering and small-angle X-ray scattering. The results from these were connected in order to elaborate a molecular understanding of the rheological response of the system.

Findings: The self-assembly of these surfactants have been found to result in different rheological properties. β-$C_{16}G_2$ show a high viscosity with a non-Newtonian viscoelastic behavior, which was linked to

---

* Corresponding author.
E-mail address: johan.larsson@fkem1.lu.se (J. Larsson).

https://doi.org/10.1016/j.jcis.2020.08.116

the formation of worm-like micelles. In contrast, α-$C_{16}G_2$ self-assembled into short cylindrical micelles, resulting in a Newtonian fluid with low viscosity. Furthermore, mixtures of these two surfactants lead to systems with intermediate rheological properties as a result of the formation of micelles with intermediate morphology to those of the pure anomers. These results also show that the rheological properties of the system can be tuned to change the micelle morphology, which in turn depends on the anomeric configuration of the surfactant. Also, surfactant concentration, temperature of the system, and micelle composition for surfactant mixtures provide control over the rheological properties of the system in a wide temperature range. Therefore, these results open new possibilities in the development of sustainable excipients for formulation technology, where the characteristics of the system can be easily tailored through geometric variations in the monomer structure whilst maintaining the chemical composition of the system.

---

1. Introduction

A majority of surfactants used daily in e.g. detergents and as emulsifiers are produced from raw materials of fossil-based origin. As society moves towards more environmentally friendly products and processes, these surfactants need to be replaced with surfactants that are biodegradable and synthesized from renewable raw materials [1]. For this purpose alkylglycosides, which are surfactants with carbohydrate units as the hydrophilic headgroup, are particularly interesting and are therefore already used in applications like personal care products [2,3].

In previous work, we have demonstrated the formation of very elongated worm-like micelles (WLM) of the alkylglycoside *n*-hexadecyl-β-D-maltopyranoside (β-$C_{16}G_2$) and shown that the elongation was reduced substantially when changing to the anomer *n*-hexadecyl-α-D-maltopyranoside (α-$C_{16}G_2$) [4]. Here we will elaborate on the rheological behavior of these systems. It is well known that WLM behave as fluid thickeners, which is relevant for a range of products where surfactants are used. Among the most studied systems with WLM are ionic surfactants in salt solutions. These systems are sensitive to the ionic strength of the solution as the addition of salt modifies micelle morphology through screening the electrostatic repulsion between surfactant headgroups [5]. Some examples of ionic WLM are hexadecylpyridinium bromide in a sodium bromide solution [6], and sodium dodecylsulfate (SDS) in a NaCl solution [7]. A particular case is that of hydrotropic salts, which greatly modify the packing of surfactants through electrostatic screening and embedding hydrophobic domains into the micelle core. This is the case of hexadecyltrimethylammonium chloride in combination with sodium salicylate [8], and SDS with *p*-toluidine hydrochloride [9]. There are far fewer non-ionic surfactant systems that form WLM, and in most cases a co-surfactant is needed to obtain these structures [5]. One example where a co-surfactant is not required to form WLM is hexaethylene glycol hexadecyl ether ($C_{16}E_6$) [10]. Recently, very long WLM structures were also reported for a novel type of non-ionic surfactant, where the surfactant headgroup consists of a polyethylene glycol (PEG) linker with terminal carbohydrate units [11]. The formation of elongated micelles has also been reported for sugar-based surfactants, where the characteristics of those depend on the length of the hydrophobic tail and on the number of sugar units in the headgroup [12–14]. An advantage of non-ionic over ionic surfactants is that they are less sensitive to the salt concentration, generally less potent irritants and more environmentally friendly [15]. They can therefore be used in a wider range of formulated products [16].

WLM are elongated, dynamic surfactant self-assembled structures, which contain kinks, since a straight dynamic cylinder would be entropically unfavorable. Therefore, the contour length of the micelle (L) is much longer than the length of each rigid rod-like segment (the persistence length, l_p) [5]. A range of methods such as static and dynamic light scattering (SLS and DLS), small angle X-ray and neutron scattering (SAXS and SANS) and cryogenic transmission electron microscopy (cryo-TEM) are commonly used to reveal the hierarchical structure of these kinds of systems [5]. At low surfactant concentrations, the large distance between micelles precludes inter-micellar interactions, i.e. the solution is considered to be in the dilute regime. With increasing concentration, the number of WLM per unit volume increases and, in many cases, they also become longer [10]. This leads to shorter distances between micelles and at a threshold concentration (c^* or overlap concentration) they start to interact and entangle, defining the onset of the semi-dilute regime. Due to the length of the micelles this concentration is often very low for WLM (0.05–0.5 wt%). At c^* the viscosity (η) of the solution starts to increase and it behaves as a non-Newtonian fluid with increasing surfactant concentration, as a result of the collective motion of micelles [10].

The rheological behavior of WLM can be compared to that of polymers. As is commonly observed in polymer solutions, WLM solutions are most often shear thinning, meaning that the viscosity decreases with increasing shear rate (γ). This is due to an alignment of the micelles parallel to the flow [5]. When stress is applied, solutions of both WLM and polymer systems respond with a mode of relaxation called reptation, which is the diffusion along the length of the structure. The reptation time (τ_{rep}) is highly dependent on the contour length and scales with L [3,17]. While polymers are covalently bound and do not break, micelles are dynamic equilibrium self-assembly structures, meaning that they constantly break and reform. This gives WLM a second mode of relaxation, breaking time (τ_b), which makes their rheologic behavior different from that of polymers. The likelihood that a WLM breaks is the same for all parts of the micelle, which is why τ_b scales with L^{-1} [18]. These two relaxation modes respond differently to the micelle lengths. For shorter cylindrical micelles $\tau_{rep} \ll \tau_b$, the system behaves as polymers where reptation is the primary mode of relaxation. For WLM $\tau_b \ll \tau_{rep}$, Cates showed that the system can be described with a single relaxation time (τ) according to Equation (1) [19].

$$\tau = \sqrt{\tau_b * \tau_{rep}} \tag{1}$$

Under these conditions, a WLM system behaves as a Maxwellian fluid [20]. Thus, it can be considered to be viscoelastic, where at short timescales they behave as elastic solids and at longer timescales they behave as viscous liquids. τ is obtained by determining the frequency (τ^{-1}) at which the elastic modulus (G’) and the viscous modulus (G”) are equal. The viscoelastic behavior can be modelled with a Maxwellian model, where the G’ and G” are described as in Equations (2) and (3) [21].

$$G' = G'_{\infty} \frac{(\omega\tau)^2}{1 + (\omega\tau)^2} \tag{2}$$

$$G'' = G'_{\infty} \frac{\omega\tau}{1 + (\omega\tau)^2} \qquad (3)$$

Here, ω is the angular frequency and G'_{∞} is the plateau value of G' at high frequencies. For Maxwellian fluids, it follows from the equations (2) and (3) that G'_{∞} is twice the value of the intersect between G' and G" (from here on labelled as $G_{1/2}$). Several structural micellar dimensions, e.g. contour length, persistence length and distance between entanglements, can be estimated from rheological data [22].

In this work, the rheological properties of $C_{16}G_2$ will be discussed in relation to molecular and self-assembly structure of the surfactant. The static and dynamic rheology of the surfactant in its two anomeric configurations (α- and β-$C_{16}G_2$) and mixtures of those is probed at different temperatures and concentrations. The molecular organization of these surfactants was investigated using SAXS and contrast variation SANS. The rheology of these systems was then linked to the micellar structure observed in each case, thus connecting the macroscopic response of the system to the molecular organization of the surfactants.

2. Experimental section

2.1. Materials

n-Hexadecyl-α-D-maltopyranoside (α-$C_{16}G_2$) was purchased from Ramidus AB (Lund, Sweden) and *n*-hexadecyl-β-D-maltopyranoside (β-$C_{16}G_2$) was purchased from Anatrace Inc. (Maumee, Ohio). The structure of these surfactants is presented in Fig. S1 in the ESI. The purity of both surfactants was stated to be ≥97% by the suppliers and was verified by HPLC spectroscopy in this work. Tail-deuterated β-$C_{16}G_2$ (d_{31}-β-$C_{16}G_2$, 98.5 ± 2.0%D) was synthesized by the Deuteration and Macromolecular Crystallisation DEMAX platform (ESS, Sweden) according to the procedure in the ESI [23]. The purity and deuteration of the surfactant were assessed by ^{1}H (Figs. S2 and S3) and ^{13}C NMR spectroscopy (Figs. S4 and S5), and mass spectrometry. The water used in this work was of Milli-Q purity and the D_2O was purchased from Sigma Aldrich (Darmstadt, Germany) and was of 99.9 atom % D.

2.2. Methods

2.2.1. Sample preparation

The Krafft point of $C_{16}G_2$ is above room temperature (about 27 °C) [4]. Thus, to dissolve the surfactants, stock solutions were prepared under agitation at 45 °C until homogeneous solutions were obtained. Samples were prepared by diluting these stock solutions to the desired concentration and equilibrating at 45 °C prior to measurement. When dissolved at a temperature above its Krafft point, the surfactant does not precipitate from solution for at least 1 h at 25 °C, which provides enough time to characterize the assemblies in the kinetically arrested state below the Krafft point.

2.2.2. Rheology

The rheology experiments were performed on a Malvern Kinexus rheometer (Malvern Instruments limited, Worcestershire, UK). The data were analyzed using the software *rSpace for Kinexus* by Malvern Panalytical. The geometry used for the experiment was a 15.4 mm cup and a 14 mm cylinder. Complementary experiments were performed on a TA Instruments ARES rheometer (New Castle, USA). In this case, analysis of the data was done in the software *TA Orchestrator* and the geometry used was a 16.5 mm cylinder and 17 mm cup. The flow curves were recorded at a shear rate range of 0.01–300 s^{-1} with 7 measurements per decade. The linear viscoelastic region (LVER) was determined for each system, and subsequent experiments were conducted at a constant shear stress of 0.05 Pa over the frequency range 0.01–10 Hz. These conditions were such that every measurement was conducted in the LVER. The systems were equilibrated and analyzed at 30, 40, 50 and 60 °C.

The oscillatory rheology data were modelled using Maxwellian model fits, see Equations (2) and (3). As it proved difficult to estimate G'_{∞}, $2xG_{1/2}$ was used instead, keeping in mind that the equality $G'_{\infty} = 2xG_{1/2}$ is true for Maxwellian fluids only.

2.2.3. Dynamic light scattering (DLS)

The hydrodynamic radius (R_H) of the investigated systems was determined with a Zetasizer Nano-ZS (Malvern Instruments Ltd., Worshestershire, UK). The laser was a 4 mW He-Ne laser with a wavelength of 632.8 nm. Measurements were conducted in backscattering mode, with a scattering angle of 173°. The surfactant samples (0.5 ml, 10 mM) were injected in PMMA semi-micro disposable cuvettes purchased from BRAND GmbH (Wertheim, Germany) and analyzed from 70 °C to 10 °C with steps of 5 °C. Subsequent to any change in temperature the sample was equilibrated for 5 min and triplicates were measured for every point. Precipitation was detected at 20 °C and below for samples with high β-$C_{16}G_2$ ratios and results from such measurements were thus removed from the data set. Correlation functions showed a single exponential decay and data were analyzed with the Malvern Zetasizer software using the cumulants method.

2.2.4. Small angle X-ray and neutron scattering

Small angle X-ray scattering (SAXS) experiments were performed at the European Synchrotron Radiation Facility on the BM29 beamline (Grenoble, France). A wavelength of 0.99 Å and a sample-to-detector distance of 2.867 m were used, resulting in a Q range of 0.004–0.49 Å^{-1}, where Q is the scattering vector defined as $Q = 4\pi \sin\theta/\lambda$. Every sample was exposed to the beam for 10 frames of 1 s each and the final curve was obtained by averaging those frames for which beam damage was not observed. The samples were investigated at 25, 40 and 50 °C. The scattered intensity was converted to absolute scale according to the protocols of the beamline and the solvent contribution to the scattering was subtracted. The data output was absolute scattered intensity, I(Q), vs. scattering vector, Q [24].

Small angle neutron scattering (SANS) experiments were performed at the Institut Laue-Langevin (ILL) on the D11 instrument (Grenoble, France) [25] and at the Heinz Maier-Leibnitz Zentrum (MLZ) on the KWS-3 instrument (Garching, Germany) [26]. On D11, the neutron wavelength was 5.5 Å and the sample-to-detector distances were 1.65, 8 and 39 m resulting in a Q range of 0.0014–0.43 Å^{-1}, whereas on KWS-3 the wavelength of the neutrons was 12.8 Å, and two different sample-to-detector distances were used, 1.15 and 9.15 m, yielding a combined Q range of 0.00 0183–0.0187 Å^{-1}. The samples were injected in cylindrical quartz cuvettes ("banjo cells") with 1- and 2-mm path length for H_2O and D_2O samples respectively, and measured at 30 and 50 °C. The raw data were reduced according to the protocol of each beamline to obtain the output files in I(Q), in absolute intensity, vs. Q.

Analysis of the SAXS and SANS data was performed in SasView 4.2.2 by fitting to form factor models conforming to the micellar shape [27]. As the Q-range covered in the SAXS experiment did not reach sufficiently low-Q values to observe the longest dimension of the micelles, the model used for the SAXS data was a core–shell cylinder model describing the cross-section dimensions of the micelles. The SANS data were fitted with a flexible cylinder model, as these experimental data allowed the length and stiffness of the micelles to be determined. For a detailed description of the analysis of the SAXS and SANS data, see previous work [4].

3. Results

3.1. Structure-function coupling in α- and β-$C_{16}G_2$ micelles

The key results from the rheology measurements of α-$C_{16}G_2$ and β-$C_{16}G_2$ are summarized in Fig. 1. The linear rheology of these surfactants directly reveal significant differences between the two anomeric configurations when it comes to the magnitude of the viscosity and the flow curves (Fig. 1a). First, the viscosity is significantly lower for α-$C_{16}G_2$ and flow curves could only be recorded at high surfactant concentration and at a limited range of shear rates. Furthermore, α-$C_{16}G_2$ behaves as a Newtonian fluid where the viscosity does not vary with shear rate, while β-$C_{16}G_2$ shows a non-Newtonian behavior above 10 mM. At high concentration, the viscosity of β-$C_{16}G_2$ solutions decreases with increasing shear rate, i.e. the systems display a shear thinning behavior. The β-$C_{16}G_2$ solutions show an increase in viscosity with increasing surfactant concentration and, at the highest concentration studied (200 mM), the viscosity extrapolated to zero-shear (710 Pas) is more than six orders of magnitude higher than that of water at 50 °C (0.547×10^{-3} Pas) (Fig. 1b). The largest relative increase in viscosity with concentration is observed between 5 and 10 mM, i.e. at the concentration where the behavior of the system transforms from Newtonian to non-Newtonian. This change marks the onset of the semi-dilute regime, where the micellar-micellar interactions become the determining factor for the rheological behavior [20]. The observed interactions are expected to be relatively weak and therefore sensitive to the flow conditions, and this effect is more pronounced with increasing concentration (Fig. 1a). Interestingly, the flow curve for the most concentrated system (200 mM) shows a sharp discontinuity at 0.5 s^{-1}. This feature was confirmed to be reproducible in several independent experiments, using different instruments and configurations, and bears the character of a yield point. However, its physical underpinnings are not understood at the current point in time.

The zero-shear viscosity appears to increase in a sigmoidal fashion with concentration (Fig. 1b). The steepest increase is observed at surfactant concentration between 20 and 70 mM. In this range the viscosity shows a power law dependence on the surfactant concentration with an exponent of 5.52. This should be compared with the value of 5.8 observed for semi-dilute solutions of unbreakable polymers [28], indicating that, in this region, the fastest mode of relaxation for the micelles is reptation. For Maxwellian systems, where the micelles break much faster than they reptate along the contour length ($\tau_{break} \ll \tau_{rep}$), the power law exponent has been shown to be 3.7 for concentrations in the semi-dilute regime [28]. Indeed, when increasing the concentration of β-$C_{16}G_2$ above 70 mM, the exponent decreases to a value of 3.23. This indicates that the system goes through a transition around 70 mM, from which the dominant relaxation mode is reptation of intact micelles at lower concentration to fast-breaking micelles at higher concentration, where the system behaves as a Maxwellian fluid.

The rheological properties of the $C_{16}G_2$ system were further investigated by determining the viscoelastic properties at different frequency of oscillating strain (Fig. 1c–e). For β-$C_{16}G_2$, the viscous modulus (G'') is dominating at low frequencies and the elastic modulus (G') is dominating at high frequencies, which is the expected behavior of a viscoelastic system. The τ value is obtained from the inverse of the angular frequency (ω) at the point where G''=G'. Both τ and $G_{1/2}$ increase with the surfactant concentration. This is expected, since an increase in surfactant concentration results in an increasing number of interacting micelles. Therefore, the solution shows a more elastic behavior over larger time scales and requires larger forces to make it flow [21]. The solid and dashed lines in Fig. 1c–e represent the fit of the Maxwell model to the experimental data. The model fits the data reasonably well at high concentrations (≥100 mM), but not at lower concentrations. This conforms with the results from the viscosity measurements discussed above. For the system to behave according to Maxwell's model, the micelles must be sufficiently long and entangled so that the relaxation through breaking the micelles is much faster than through reptation along its contour length and, consequently, only a single relaxation time of the system upon deformation is observed [19]. The fit to Maxwell's model is poor for G'' at high frequencies. This is common for WLM systems, since at shorter time-scales additional relaxation mechanisms, for instance stretching of the micelles, which are not accounted for in the Maxwell model become significant [21].

The differences in the rheological behavior of α- and β-$C_{16}G_2$ anomers can be explained by the formation of different micellar structures, as confirmed by SANS. We found that α-$C_{16}G_2$ behaves as a Newtonian fluid, consistent with the previous report that this anomer forms elongated micelles that are not sufficiently long to confer the system non-linear response to stress, even at high surfactant concentration [4]. Scattering data show that β-$C_{16}G_2$ forms WLM [4], which in the semi-dilute regime correlates well with the non-linear response to stress, i.e. the shear thinning behavior of the system. In the present study, the morphology of α- and β-$C_{16}G_2$ is further investigated using a wider Q-range and over a wider range of concentrations. We note that the analysis of scattering data becomes challenging at higher surfactant concentrations (>10 mM), i.e. when reaching the semi-dilute regime for β-$C_{16}G_2$,

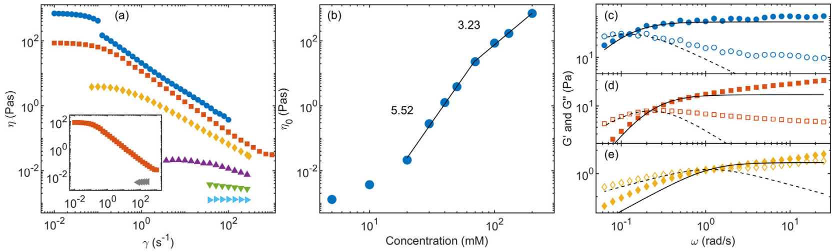

Fig. 1. Summary of the key results from rheology measurements of $C_{16}G_2$ at 50 °C. (a) Viscosity versus shear rate for β-$C_{16}G_2$ at 200 (○), 100 (□), 50 (◇), 20 (△), 10 (▽) and 5 (▷) mM surfactant concentration. The inset compares the viscosity for α-$C_{16}G_2$ (◁) and β-$C_{16}G_2$ (□) at 100 mM. (b) Zero-shear viscosity of β-$C_{16}G_2$ versus concentration where the slopes of two different regions are indicated using solid lines. Viscoelastic properties of β-$C_{16}G_2$ at (c) 200, (d) 100 and (e) 50 mM respectively as the G' (filled markers) and G'' (unfilled markers) versus the angular frequency. The solid and dashed lines are the G' and G'' Maxwell model fit of the data.

as it requires that the excluded volume effects due to intermicellar interactions are properly taken into account [29]. Therefore, the detailed investigation of the micelle morphology was performed in the dilute regime, i.e. at surfactant concentrations of 10 mM and below for β-$C_{16}G_2$. The dilute regime of α-$C_{16}G_2$ extends to higher concentrations since it is forming shorter micelles and, thus, a sample of 20 mM α-$C_{16}G_2$ was included in the analysis. SANS data and best fits of the flexible cylinder model for the anomerically pure samples are presented in Fig. 2a and in the ESI in Fig. S8, and the results from the fits are presented in Fig. 2c and d and in the ESI in Table S1.

The results of the SANS measurements at 50 °C revealed that α-$C_{16}G_2$ forms elongated micelles that have a contour length which is longer than their persistence length at all investigated concentrations. We also see an increase of contour length with increasing surfactant concentration, as expected for long-tailed surfactants in the dilute regime [10]. However, the contour length remains <2000 Å for all concentrations studied. For β-$C_{16}G_2$, on the other hand, formation of WLM with contour length >8000 Å is shown already at concentrations as low as 1 mM (Fig. S8 and Table S1). The length of the micelles seems to increase up to ~10000 Å at 5 mM surfactant. This type of micelle growth was also observed through the hydrodynamic radius determined by DLS as reported in the previous study [4]. An apparent decrease in the obtained contour length is observed at 10 mM. This is probably due to interactions between micelles at the onset of the semi-dilute regime, i.e. at the surfactant concentration c*. The observation is in line with results from the rheology measurements that also indicate onset of the semi-dilute regime at a surfactant concentration of 10 mM. A maximum in the apparent micelle size at c*, was also found by Jerke et al. for two other WLM systems [10]. They also show that if the structure factor is not taken into account, the flexible cylinder model overestimates the stiffness of the WLM. However, Chen et al. showed that even when the micellar interactions are considered, the stiffness of WLM increases with concentration [30]. This is also observed in the present study, where the persistence length increases with concentration in the dilute regime of β-$C_{16}G_2$-solutions (205 ± 10 Å at 1 mM, 273 ± 10 Å at 5 mM and 316 ± 10 Å at 10 mM). However, this variation in persistence length induced by concentration effects could be an artefact of the fitting approach, as the modelling underestimates the excluded volume effects. As previously reported, there is no major effect on the micelle cross-section with changes in concentration and the average micelle radius is 22.8 ± 0.2 Å for β-$C_{16}G_2$ and 20.4 ± 0.3 Å for α-$C_{16}G_2$ [4].

These results are in line with previous results for α- and β-$C_{16}G_2$, where the differences in the micelle morphology were attributed to changes in the mechanism of headgroup solvation between the two anomeric configurations [4]. The structure of the α anomer favored headgroup-solvent interactions, resulting in a higher degree of hydration than the β configuration and, thus, inducing a higher curvature and the formation of smaller micelles. The packing of the β anomer was instead driven by the stronger headgroup-headgroup attractive interactions, possibly through hydrogen bonds. This results in a more efficient packing of the headgroups, a lower degree of solvation, and the formation of larger aggregates.

3.2. Effect of temperature on the rheology and micellar structure

It has been previously shown that α-$C_{16}G_2$ undergoes a globular-to-elongated micelle morphology transition with temperature, while β-$C_{16}G_2$ forms WLM over the whole temperature and concentration range [4]. In connection to the distinct microscopic features of the micelles, the rheological behavior is affected by temperature. In this work we see that a Newtonian behavior is maintained over the whole temperature range investigated for 200 mM α-$C_{16}G_2$, meaning that the temperature-induced micellar growth is not extensive enough to induce a non-Newtonian behavior (Fig. S9). In contrast, the rheological behavior of β-$C_{16}G_2$ above 10 mM concentration was found to be non-Newtonian at all temperatures. The change in zero-shear viscosity with temperature for β-$C_{16}G_2$ is shown in Fig. 3a. For all concentrations the curves feature a maximum, where the highest viscosity extrapolated to zero-shear rate is achieved at temperatures between 40 and 50 °C. These zero-shear values were found to be lower at 30 °C and 60 °C by up to a factor of *ca.* 5 for 100 and 200 mM, and a factor of *ca.* 50 for 50 mM. Interestingly, the maximum in viscosity as a function of temperature is also concentration dependent, where it appears to occur at decreasing temperatures with increasing concentration.

The rheological behavior can be directly correlated to changes in micelle morphology. It is well-known that the microscopic structure and dynamics of micelles correlate to the macroscopic behavior of the system. For instance, longer micelles lead to higher viscosities, since the extent of entanglement increases with micellar length. Similarly, micellar flexibility has been shown to affect the entanglement of a micellar system and, thus, its rheology [20]. For the system studied here, the results from SANS measurements of 10 mM β-$C_{16}G_2$ at 30 °C and 50 °C show that the micelles are around 1000 Å shorter, but slightly more rigid at 30 °C, see

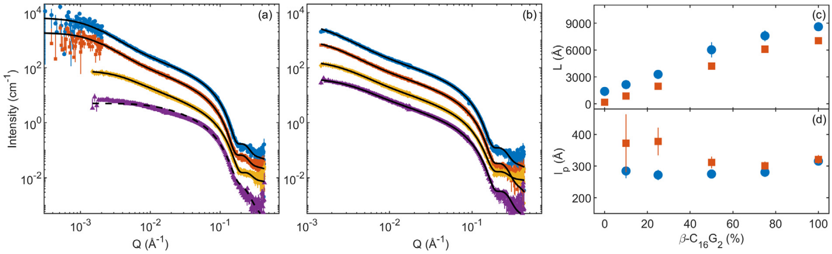

Fig. 2. SANS data for α- and β-$C_{16}G_2$ micelles at 10 mM in water. (a) β-$C_{16}G_2$ at 50 °C (blue ○) and 30 °C (red □) and α-$C_{16}G_2$ at 50 °C (yellow ◇) and 30 °C (purple △). (b) Mixtures of α- and β-$C_{16}G_2$ at: 75% (blue ○), 50% (red □), 25% (yellow ◇) and 10% (purple △) β-$C_{16}G_2$. Solid lines represent fits from a flexible cylinder model and dashed line represents fit from ellipsoid model. (c) Contour length, L, and (d) persistence length, l_p, obtained from flexible cylinder model fit of micelles at different mole % of β-$C_{16}G_2$ at 50 °C (○) and 30 °C (□). The intensity of the data and fits in (a) and (b) have been offset for clarity by a factor of 3, 10 and 30. (For interpretation of the references to color in this figure legend, the reader is referred to the web version of this article.)

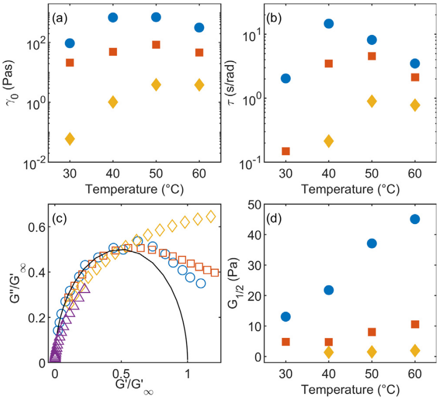

Fig. 3. The effect of temperature on the rheological behavior of β-$C_{16}G_2$ at 200 mM (○), 100 mM (□) and 50 mM (◇) surfactant concentration: (a) effect of zero-shear viscosity and (b) effect of relaxation time. (c) Normalized Cole-Cole plot for 100 mM β-$C_{16}G_2$ at 60 °C (○), 50 °C (□), 40 °C (◇) and 30 °C (△) with the solid line showing the Maxwell model fit. (d) The effect of temperature on the modulus at the intersection ($G_{1/2}$) of G' and G''.

Fig. 2c and d. This is in agreement with previous investigations that showed that the hydrodynamic radius of the micelles, obtained from DLS measurements, goes through a maximum between 40 and 55 °C [4]. This, in turn, suggests that the system diverges from a Maxwellian behavior and explains the lower viscosity at zero-shear under these conditions. The increase in length of the micelles shows the same temperature trend as the zero-shear viscosity (Fig. 3a) indicating that the primary temperature effect on these values comes from the change in micelle length.

It is thus clear that the temperature dependence of the rheological properties reflects changes in micelle morphology. Interestingly, mean-field theory applied to these type of systems predicts a decrease in the micelle length with increasing temperature according to Equation (4) [22].

$$\bar{L} = \sqrt{\varphi}\exp\left(\frac{E}{2k_BT}\right) \tag{4}$$

Here $\bar{L}$ is the average length of the micelles, φ is the volume fraction of micelles, E is the scission energy and T is the temperature. The observed maximum in zero-shear viscosity with temperature reflects the sum of two effects, where transitions in viscosity are observed at different temperatures depending on the concentration.

The relaxation time behaves in a similar fashion to the zero-shear viscosity (Fig. 3b), where the τ values again show a maximum at temperatures between 40 °C and 50 °C, and this variation is also attributed to the morphological changes observed in the micelles. Furthermore, the temperature increase results in a more Maxwellian behavior, as evident in the normalized Cole-Cole plots for 100 mM β-$C_{16}G_2$ at different temperatures (Fig. 3c) (G'' and G' are both normalized to G'$_\infty$). Cole-Cole plots for 50 and 200 mM are shown in Fig. S10. The variation in the τ values, together with changes in the Maxwellian behavior, confirm that the individual components of the relaxation time (τ_{break} and τ_{rep}) are affected differently by temperature. Here, we hypothesize that the presence of longer, less mobile micelles (and thus an increase in τ_{rep}) is accompanied by an increase in micelle breakage (and thus a decrease in τ_{break}) [17,18]. Thus, we will reach a condition where $\tau_{break} \ll \tau_{rep}$ and the system becomes more Maxwellian with increasing temperature.

The modulus at the G'-G'' intersect ($G_{1/2}$) is not affected by temperature changes in the same way as the zero-shear viscosity and the relaxation time (Fig. 3d). For Maxwellian WLM systems, it has been shown that G'$_\infty$, and thus $G_{1/2}$, increase linearly with temperature [31], which is also the trend observed for β-$C_{16}G_2$ at 200 mM and for 100 mM above 40 °C. This confirms that the Maxwell regime starts around 100 mM at 40 °C, which is consistent with the previous results of zero-shear viscosity of β-$C_{16}G_2$ at different concentrations (Fig. 1b), that indicate the Maxwell model regime to start around 100 mM at this temperature.

It has previously been shown that α-$C_{16}G_2$ undergoes a globular-to-elongated micelle morphology transition with temperature, while β-$C_{16}G_2$ forms WLM over the whole temperature and concentration range [4]. This was again attributed to changes in the solvation mechanism, which were different for the two anomers. Whilst the solvation and, therefore, the morphology of β-$C_{16}G_2$ micelles remains relatively unaffected by temperature, the degree of solvation of α-$C_{16}G_2$ increases with decreasing temperature. This results in the formation of smaller aggregates of α-$C_{16}G_2$ at a lower temperature as induced by the increase in the apparent size of the α headgroup.

3.3. Mixtures of α-$C_{16}G_2$ and β-$C_{16}G_2$

α- and β-$C_{16}G_2$ display drastically different microscopic and macroscopic behavior. In terms of rheology, mixing the two surfactants results in solutions with intermediate viscosity between the two anomerically pure surfactants, where higher contents of the β anomer display higher viscosities (Fig. 4a). Similar to the concentration dependence of β-$C_{16}G_2$ in Fig. 1b, there is a weak sigmoidal dependence of zero-shear viscosity on the anomeric ratio, where the largest change is observed around 50% β-$C_{16}G_2$. As for β-$C_{16}G_2$, the mixtures are shear thinning, but the onset of the curve shifts to higher shear rates with increasing amount of α-$C_{16}G_2$ and becomes close to Newtonian at low β-$C_{16}G_2$ contents (<25%) (Fig. S11).

Large changes are also seen for the viscoelastic properties of the surfactant solutions when mixing α- and β-$C_{16}G_2$ (Fig. 4b-d). These oscillatory rheology results show that increasing amount of β-$C_{16}G_2$ in the mixture results in a more elastic solution, as seen by the shift of the intersection to lower angular frequencies. For mixtures with more than 50% α-$C_{16}G_2$ the viscous modulus is dominating over the whole frequency range investigated and no cross-over frequency could be detected. The temperature behavior of the mixtures with high ratios of β-$C_{16}G_2$ (>75%) is similar to that of pure β-$C_{16}G_2$. The τ decreases with increasing ratio of α-$C_{16}G_2$ meaning that the solutions are viscous over larger timescales (Fig. 4e). A maximum in τ appears at temperatures between 40 °C and 50 °C for the higher β-$C_{16}G_2$ ratios. At temperatures below 50 °C, $G_{1/2}$ is unaffected by changes in surfactant ratio. However, a significant increase is observed at higher temperatures for the systems with higher β-$C_{16}G_2$ ratio (Fig. 4f). Interestingly, such an increase is observed under conditions where a Maxwellian behavior is expected, as discussed earlier. The normalized Cole-Cole plot for the mixtures of α- and β-$C_{16}G_2$ is presented in Fig. 4g. Cole-Cole plots for the mixtures at all investigated temperatures are presented in Fig. S10. From the comparison of the curves, it is seen that the surfactant solution becomes more Maxwellian with increasing β-$C_{16}G_2$ ratio, as expected.

Again, the observed changes in rheological behavior can be related to the structural changes of the micelles. The hydrodynamic radius of the micelles, determined from DLS, shows a gradual increase in size with increasing ratio of β-$C_{16}G_2$ at constant

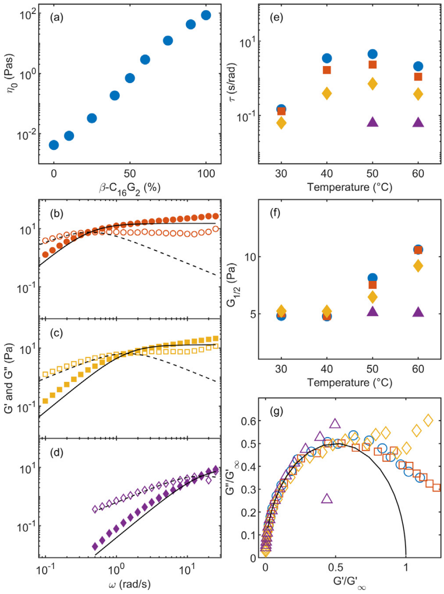

Fig. 4. Rheology results for mixtures of α- and β-$C_{16}G_2$ at 100 mM surfactant concentration. (a) Zero-shear viscosity at 50 °C. Frequency sweep measurements for (b) 90%, (c) 75%, (d) 50% β-$C_{16}G_2$, with G' (filled markers) and G'' (unfilled markers). Maxwell model fits are included for G' (solid line) and G'' (dashed line). Temperature dependence of relaxation time (e) and modulus at G'=G'' (f) for 100% (○), 90% (□), 75% (◇), 50% (△) β-$C_{16}G_2$. (g) Cole-Cole plot for 100% (○), 90% (□), 75% (◇), 50% (△) β-$C_{16}G_2$ at 60 °C with a Maxwell model fit represented by the solid line.

surfactant concentration of 10 mM (Fig. S12). The same trend is observed for the contour length of the micelles obtained from a flexible cylinder model fit of the SANS data (Fig. 2b and c). Both these methods show a close to linear increase in size with increasing β-ratio, except at the highest ratios of β-$C_{16}G_2$, where the increase levels off. This may explain the sigmoidal zero-shear viscosity dependence on the surfactant ratio (Fig. 4a), where the trend micelle elongation reaches a plateau as seen by SANS and DLS. At high α-$C_{16}G_2$ ratios the surfactant micelles are shorter and correlate to the Newtonian behavior of the system.

Changing the temperature of the mixed solutions results in composition- and temperature-dependent variations in terms of micellar structure. For all compositions investigated here, the contour length obtained from SANS measurements is consistently *ca.* 1000 Å larger at 50 °C than 30 °C (Fig. 2c). This is in agreement with the variations in hydrodynamic radius obtained from DLS (Fig. S12). The onset of micelle growth with temperature is dependent on the surfactant ratio, where the onset occurs at lower temperatures for higher ratios of β-$C_{16}G_2$ (Fig. S13). In terms of variations in micellar flexibility with temperature, it is seen that, whilst the persistence length at 50 °C remains rather constant with micelle composition, micelle stiffness increases and becomes more variable at 30 °C (Fig. 2d). These structural features again correlate with the rheological behavior of the system, where more viscous systems are seen at 50 °C than at 30 °C. The scattering curves from the SANS data with the fitted flexible cylinder model and the obtained parameters is shown in Fig. S14 and Table S2.

In order to determine the internal structure of the micelles in the mixed-surfactant systems, contrast variation SANS was combined with SAXS. One of the main advantages of SANS is that the use of isotopically labelled compounds can provide detailed structural information and micelle composition through the co-refinement of model fits to the scattering data from these contrasts [32–34]. In addition to the SANS contrast presented above, protiated surfactants in D_2O (Contrast 1), analogous samples containing h-α-$C_{16}G_2$ and d_{31}-β-$C_{16}G_2$ in D_2O (Contrast 2) were measured. Data from this contrast were analyzed using a similar protocol to that presented in the Experimental section and ESI, with the difference that the volume fraction of micelles of Contrast 2 was fixed to the values obtained from Contrast 1 and the SLD of the micelle calculated (SLD_{fit}). SLD_{fit} was subsequently used to determine the amount of each surfactant in the micelle using Equation (5):

$$\varnothing_{\beta-C16G2,micelle} = \frac{SLD_{fit} - SLD_{h-C16}}{SLD_{d-C16} - SLD_{h-C16}} \qquad (5)$$

where $\phi_{\beta\text{-}C16G2,micelle}$ is the volume fraction of β-$C_{16}G_2$ in the micelle, and $SLD_{h\text{-}C16G2}$ and $SLD_{d\text{-}C16G2}$ are the SLD of the protiated and deuterated surfactant tails, -0.39×10^{-6} Å^{-2} and 6.93×10^{-6} Å^{-2} respectively.

Data and results from the analysis are presented in Fig. S14 and Table S3 in the ESI. The results from Contrast 2 show similar structural characteristics to those obtained from Contrast 1. The main difference appears in the cross-sectional size of the micelles, where the radius is between 1 and 20% larger in the presence of d_{31}-β-$C_{16}G_2$ with respect to its protiated analogue. We are not sure about the reason of this difference. Interestingly, this difference does not seem to affect the elongation or flexibility of the micelles, as the differences between contrasts are within the error of the fits. The composition of the mixed micelles was determined at the two temperatures and shows that α-$C_{16}G_2$ is more prone to form micelles than β-$C_{16}G_2$ (Fig. S15). These results agree with previous investigations where it was shown that α-$C_{16}G_2$ has a lower CMC and thus relates to a more hydrophobic character [4,35]. SAXS data were used to determine the structural characteristics of the headgroup region, as the density correlation core–shell-solvent results in the strong oscillation at high q which enables the structure of this region to be depicted. Data and results from the analysis are presented in Fig. S16 and Table S4 in the ESI. In agreement with previous investigations, the cross-section thickness increases with increasing ratio of β-$C_{16}G_2$, which was attributed to the distinct differences in monomer packing that depends on the anomeric configuration of the surfactant [4].

4. Discussion

4.1. Comparison of $C_{16}G_2$ to other surfactants that form WLM

The results obtained for $C_{16}G_2$ in this study shows that only minor changes in the architecture of the surfactant have pronounced effect on micellar structure and rheology. Whilst the effect of changing the tail length or headgroup size of surfactant has been intensively studied [36], the effects of anomers have not been previously reported. The majority of studies on WLM were performed on ionic surfactant systems, especially when it comes to connection between rheology and micellar structure [5,37]. In particular, the addition of hydrotropic salts have a strong influence on the rheology of the system. An example is a 30 mM hexadecyltrimethylammonium tosylate solution where a zero-shear viscosity increases from around 10^{-2} Pas to about 50 Pas when potassium phthalic acid 2 mM was added [38]. Similarly, the addition of sodium salicylate to 50 mM hexadecyltrimethylammonium chloride results in a strong non-Newtonian behavior, where the zero-shear viscosity increases to 10^4 Pas. These systems often require the presence of salts to form non-Newtonian fluids, which often are derived from aromatic hydrocarbons and thus present an adverse environmental impact.

The relationship between structure and rheological properties of non-ionic surfactants, such as sugar surfactants, is not as well understood as for other surfactant systems. The self-assembly structure of poly(oxyethylene) surfactants in solutions with non-Newtonian behavior has been shown to vary with the number of ethylene units in the headgroup [39]. Ericson *et al* also showed that for homologous series of maltosides and glucosides ($C_{14}G_2$, $C_{12}G_2$, $C_{10}G_1$, and C_9G_1) both size of head group and alkyl chain length affects the rheological properties and micellar structure formed [12–14]. The formation of non-Newtonian surfactant solutions was reported for β-$C_{14}G_2$, where the observed zero-shear viscosities were considerably lower than for the β-$C_{16}G_2$ solutions investigated here, with the highest zero-shear viscosity at 0.5 Pas for 18.5 wt% $C_{14}G_2$ solution. Despite the concentration of β-$C_{14}G_2$ being almost twice the highest concentration of β-$C_{16}G_2$ used in this study, the intersection between the viscous and elastic moduli occurs at a similar value (G', G'' ≈ 40 Pa) and the relaxation time is about two orders of magnitude higher for β-$C_{16}G_2$ at 200 mM (τ = 15 s) than for β-$C_{14}G_2$ at *ca.* 350 mM (τ = 0.03 s) [14]. This difference is attributed to the formation of more elongated and entangled micelles for β-$C_{16}G_2$.

To the best of the Author's knowledge, there are only two other sugar surfactant systems that have been reported to form viscoelastic solutions. These are sucrose monohexadecanoate [40,41], and a novel type of sugar surfactants with an ethylene oxide linker between the alkyl chain and the sugar headgroup as well as a double bond in the alkyl chain [11,42]. The sucrose monohexadecanoate showed a zero-shear viscosity of *ca.* 1 Pas for 10 wt% (172 mM) surfactant solutions, which is similar to the value obtained for a 100 mM 50% mixture of α- and β-$C_{16}G_2$ and almost three orders of magnitude lower than for a similar concentration of β-$C_{16}G_2$. The novel ethylene oxide-based sugar surfactants synthesized and studied by Moore *et al.* show a rheological behavior that is strongly dependent on the length of both head group and tail [11,42]. Interestingly, they also report the formation of WLM at a chain length of 16 carbons and above, which seems to be the tail length threshold above which alkylmaltopyranosides induce the type of viscoelastic behavior observed in the present study. Their results also showed that the differences in rheological behavior correlated with the structure of the sugar head group. The zero-shear viscosity for the surfactants with the highest viscosity, labelled as Gal-EO3-C18:1 and Glc-EO4-C22:1, was found to be 30 and 40 Pas at surfactant concentrations of 19.2 and 25.6 mM, respectively. These values are 1000 times higher than for β-$C_{16}G_2$ at 20 mM (0.02 Pas), i.e. these ethylene oxide-based sugar surfactant systems become more viscous at lower concentrations than β-$C_{16}G_2$. In contrast, the concentration of β-$C_{16}G_2$ needed to reach the same viscosity values is 70 mM. For 19.2 mM Glc-EO4-C22:1 the relaxation time was *ca.* 200 s, compared to *ca.* 15 s for 200 mM β-$C_{16}G_2$ at 40 °C [11]. This means that those surfactants form more elongated and entangled micelles than those of β-$C_{16}G_2$.

Additionally, the thermal stability of the non-Newtonian β-$C_{16}G_2$ solutions, where no clouding was observed up to 90 °C (Fig. S13), differs from that of poly(oxyethylene) surfactants, where high temperatures prompts system instability [43]. Therefore, the thermal resilience of the system allows to access a wide temperature range where the system remains stable.

5. Conclusions

The rheological behavior of aqueous systems can be tuned through the self-assembly of surfactants into worm-like micelles [5]. The formation of these assemblies has been previously reported for a variety of surfactants. Ionic surfactants often require the addition of salts or other surfactants to modify the monomer packing and lead to the co-assembly of those into elongated micelles [6–9,38]. In contrast, some non-ionic amphiphiles, e.g. poly(oxyethylene)-based surfactants, present the advantage of not requiring the addition of salts to form worm-like micelles, which simplifies the formulation of non-Newtonian fluids [10–11,42]. The molecular architecture of these (tail length and degree of headgroup polymerization) has been reported to control micelle morphology and, as such, the rheology of the system. Sugar-based surfactants have also been shown to self-assemble into micelles of different morphology depending on the monomer structure (tail length, degree of headgroup polymerization, and anomeric configuration), and worm-like micelles were also reported [4,12,14].

In this study, we present how the rheology of hexadecyl maltoside solutions is coupled to the microstructure of the system, with particular emphasis on the effect of the anomeric configuration of the surfactant (α and β). Surfactants in the α-configuration show a Newtonian behavior, in connection to the formation of globular or short cylindrical micelles in the whole concentration and temperature range studied here. For the β-configuration, we observed an increase of almost six orders of magnitude in viscosity with increasing concentration from the onset of the semi-dilute regime, at 10 mM, to the highest concentration investigated, 200 mM. These solutions were shear thinning and a distinct viscoelastic behavior was observed, where they behave as Maxwellian fluids at high concentrations. The structural characterization of the micelles in the dilute regime through scattering techniques shows the formation of WLM, which relates to the rheological behavior of the system upon entanglement, as previously reported for other systems [18,31,44,45]. Interestingly, it was also found that the temperature affects the rheological response of the system, where both the viscosity and the relaxation time go through a maximum with increasing temperature. These rheological properties are correlated to transitions in morphology and entanglement as induced by temperature changes. Interestingly, no phase separation was observed in the temperature range studied here. This confirms that the cloud point of the surfactant is higher than that for poly(oxyethylene)-based surfactants [43].

Furthermore, when mixing these two surfactants, the rheological properties fall between those of the two pure anomers, in connection to the microscopic structure. At higher β-$C_{16}G_2$ content, micelles are longer and, potentially, more entangled in the semi-dilute regime. This explains the increase in viscosity and why the elastic modulus is dominating over a larger timeframe, showing that mixtures of these surfactants allow to finely tune the system's response to stress.

Interestingly, one of the key features for these $C_{16}G_2$-systems is how the behavior of two surfactants of identical chemical composition can differ so greatly by altering the anomeric configuration, which to the best of our knowledge has not been previously reported for this type of systems. Furthermore, the green character of these, which can be synthesized using renewable raw materials, opens new possibilities in the use of sustainable surfactants as rheology modifiers for formulated products. Therefore, increasing the physicochemical understanding of these surfactants and exploring other conditions (e.g. formation of liquid crystals at high surfactant concentration) will expand the application of these to replace fossil fuel-derived compounds.

CRediT authorship contribution statement

Johan Larsson: Conceptualization, Methodology, Investigation, Formal analysis, Writing - original draft, Writing - review & editing, Visualization. **Adrian Sanchez-Fernandez:** Conceptualization, Methodology, Investigation, Formal analysis, Writing - original draft, Writing - review & editing, Visualization. **Anna Leung:** Investigation, Resources, Writing - review & editing. **Ralf Schweins:** Investigation, Resources, Writing - review & editing. **Baohu Wu:** Investigation, Resources. **Tommy Nylander:** Conceptualization, Investigation, Writing - review & editing, Funding acquisition. **Stefan Ulvenlund:** Conceptualization, Investigation, Writing - review & editing, Funding acquisition. **Marie Wahlgren:** Conceptualization, Methodology, Investigation, Writing - original draft, Writing - review & editing, Funding acquisition.

Declaration of Competing Interest

The authors declare that they have no known competing financial interests or personal relationships that could have appeared to influence the work reported in this paper.

Acknowledgements

The authors are also thankful to Swedish Research Council Formas (Grant 2015-666) for the funding for J.L. The research in this study was performed with financial support from Vinnova - Swedish Governmental Agency for Innovation Systems within the NextBioForm Competence Centre. This work is based upon experiments performed on the KWS-3 instrument, operated by JCNS at the Heinz Maier-Leibnitz Zentrum (MLZ), Garching, Germany (Proposal No. 15556), and on the D11 instrument at the Institute Laue-Langevin, Grenoble, France (Proposal No. 9-10-1587). Experimental data from the D11 experiment has been made freely available at DOI:10.5291/ILL-DATA.9-10-1587. The SAXS experiments were performed on beamline BM29 at the European Synchrotron Radiation Facility (ESRF), Grenoble, France. We are grateful to Dr Martha Brennich at the ESRF for providing assistance in using the beamline. This work benefited from the use of the SasView application, originally developed under NSF award DMR-0520547. SasView contains code developed with funding from the European Union's Horizon 2020 research and innovation programme under the SINE2020 project, grant agreement No 654000.

Appendix A. Supplementary material

Supplementary data to this article can be found online at https://doi.org/10.1016/j.jcis.2020.08.116.

References

[1] R. Lebeuf, C.-Y. Liu, C. Pierlot, V. Nardello-Rataj, Synthesis and surfactant properties of nonionic biosourced alkylglucuronamides, ACS Sustainable Chem. Eng. 6 (2) (2018) 2758–2766.
[2] D. Balzer, H. Lüders, Nonionic Surfactants: Alkyl Polyglucosides, Marcel Dekker, New York, 2000.
[3] A.M. Seddon, P. Curnow, P.J. Booth, Membrane proteins, lipids and detergents: not just a soap opera, Biochim. Biophys. Acta (BBA) – Biomembr. 1666 (1) (2004) 105–117.
[4] J. Larsson, A. Sanchez-Fernandez, N. Mahmoudi, L.C. Barnsley, M. Wahlgren, T. Nylander, S. Ulvenlund, Effect of the anomeric configuration on the micellization of hexadecylmaltoside surfactants, Langmuir 35 (43) (2019) 13904–13914.
[5] C.A. Dreiss, Wormlike micelles: where do we stand? Recent developments, linear rheology and scattering techniques, Soft Matter 3 (8) (2007) 956–970.
[6] G. Porte, J. Appell, Y. Poggi, Experimental investigations on the flexibility of elongated cetylpyridinium bromide micelles, J. Phys. Chem. 84 (23) (1980) 3105–3110.
[7] L.J. Magid, Z. Li, P.D. Butler, Flexibility of elongated sodium dodecyl sulfate micelles in aqueous sodium chloride: a small-angle neutron scattering study, Langmuir 16 (26) (2000) 10028–10036.
[8] N.C. Das, H. Cao, H. Kaiser, G.T. Warren, J.R. Gladden, P.E. Sokol, Shape and size of highly concentrated micelles in CTAB/NaSal solutions by small angle neutron scattering (SANS), Langmuir 28 (33) (2012) 11962–11968.
[9] P.A. Hassan, S.R. Raghavan, E.W. Kaler, Microstructural changes in SDS micelles induced by hydrotropic salt, Langmuir 18 (7) (2002) 2543–2548.
[10] G. Jerke, J.S. Pedersen, S.U. Egelhaaf, P. Schurtenberger, Flexibility of charged and uncharged polymer-like micelles, Langmuir 14 (21) (1998) 6013–6024.
[11] J.E. Moore, T.M. McCoy, A.V. Sokolova, L. de Campo, G.R. Pearson, B.L. Wilkinson, R.F. Tabor, Worm-like micelles and vesicles formed by alkyl-oligo (ethylene glycol)-glycoside carbohydrate surfactants: the effect of precisely tuned amphiphilicity on aggregate packing, J. Colloid Interface Sci. 547 (2019) 275–290.
[12] C.A. Ericsson, O. Söderman, V.M. Garamus, M. Bergström, S. Ulvenlund, Effects of temperature, salt, and deuterium oxide on the self-aggregation of alkylglycosides in dilute solution. 2. n-Tetradecyl-beta-D-maltoside, Langmuir: ACS J. Surf. Colloids 21 (4) (2005) 1507–1515.
[13] C.A. Ericsson, O. Söderman, V.M. Garamus, M. Bergström, S. Ulvenlund, Effects of temperature, salt, and deuterium oxide on the self-aggregation of alkylglycosides in dilute solution. 1. n-nonyl-β-d-glucoside, Langmuir 20 (4) (2004) 1401–1408.
[14] C.A. Ericsson, O. Söderman, S. Ulvenlund, Aggregate morphology and flow behaviour of micellar alkylglycoside solutions, Colloid Polym. Sci. 283 (12) (2005) 1313–1320.
[15] A.C. Williams, B.W. Barry, Penetration enhancers, Adv. Drug Deliv. Rev. 56 (5) (2004) 603–618.
[16] B. Kronberg, K. Holmberg, B. Lindman, Surface Chemistry of Surfactants and Polymers, John Wiley & Sons Ltd, 2014.
[17] P.-G. De Gennes, Scaling Concepts in Polymer Physics, Cornell University Press, 1979.
[18] B.A. Schubert, E.W. Kaler, N.J. Wagner, The microstructure and rheology of mixed cationic/anionic wormlike micelles, Langmuir 19 (10) (2003) 4079–4089.
[19] M. Cates, Reptation of living polymers: dynamics of entangled polymers in the presence of reversible chain-scission reactions, Macromolecules 20 (9) (1987) 2289–2296.
[20] J.F. Berret, J. Appell, G. Porte, Linear rheology of entangled wormlike micelles, Langmuir 9 (11) (1993) 2851–2854.
[21] S. Ezrahi, E. Tuval, A. Aserin, Properties, main applications and perspectives of worm micelles, Adv. Colloid Interface Sci. 128–130 (2006) 77–102.
[22] M.E. Cates, S.J. Candau, Statics and dynamics of worm-like surfactant micelles, J. Phys.: Condens. Matter 2 (33) (1990) 6869–6892.
[23] S.R. Midtgaard, T.A. Darwish, M.C. Pedersen, P. Huda, A.H. Larsen, G.V. Jensen, S.A.R. Kynde, N. Skar-Gislinge, A.J.Z. Nielsen, C. Olesen, M. Blaise, J.J. Dorosz, T. S. Thorsen, R. Venskutonytė, C. Krintel, J.V. Møller, H. Frielinghaus, E.P. Gilbert, A. Martel, J.S. Kastrup, P.E. Jensen, P. Nissen, L. Arleth, Invisible detergents for structure determination of membrane proteins by small-angle neutron scattering, FEBS J. 285 (2) (2018) 357–371.
[24] P. Pernot, A. Round, R. Barrett, A. De Maria Antolinos, A. Gobbo, E. Gordon, J. Huet, J. Kieffer, M. Lentini, M. Mattenet, C. Morawe, C. Mueller-Dieckmann, S. Ohlsson, W. Schmid, J. Surr, P. Theveneau, L. Zerrad, S. McSweeney, Upgraded ESRF BM29 beamline for SAXS on macromolecules in solution, J. Synchrot. Radiat. 20 (4) (2013) 660–664.
[25] K. Lieutenant, P. Lindner, R. Gahler, A new design for the standard pinhole small-angle neutron scattering instrument D11, J. Appl. Crystallogr. 40 (6) (2007) 1056–1063.
[26] V. Pipich, Z. Fu, KWS-3: Very small angle scattering diffractometer with focusing mirror, J. Large-Scale Res. Facil. JLSRF 1 (A31) (2015).
[27] M.C. Doucet, Jae Hie, Alina, Gervaise, Bakker, Jurrian, Bouwman, Wim, Butler, Paul, Campbell, Kieran, Gonzales, Miguel, Heenan, Richard, Jackson, Andrew, Juhas, Pavol, King, Stephen, Kienzle, Paul, Krzywon, Jeff, Markvardsen, Anders, Nielsen, Torben, O'Driscoll, Lewis, Potrzebowski, Wojciech, Ferraz Leal, Ricardo, Richter, Tobias, Rozycko, Piotr, Snow, Tim, Washington, Adam SasView version 4.2.2. https://doi.org/10.5281/zenodo.2652478.
[28] M. Cates, Dynamics of living polymers and flexible surfactant micelles: scaling laws for dilution, J. Phys. 49 (9) (1988) 1593–1600.
[29] J.S. Pedersen, P. Schurtenberger, Scattering functions of semiflexible polymers with and without excluded volume effects, Macromolecules 29 (23) (1996) 7602–7612.
[30] W.-R. Chen, P.D. Butler, L.J. Magid, Incorporating intermicellar interactions in the fitting of SANS data from cationic wormlike micelles, Langmuir 22 (15) (2006) 6539–6548.
[31] R.D. Koehler, S.R. Raghavan, E.W. Kaler, Microstructure and dynamics of wormlike micellar solutions formed by mixing cationic and anionic surfactants, J. Phys. Chem. B 104 (47) (2000) 11035–11044.
[32] P.A. Hassan, G. Fritz, E.W. Kaler, Small angle neutron scattering study of sodium dodecyl sulfate micellar growth driven by addition of a hydrotropic salt, J. Colloid Interface Sci. 257 (1) (2003) 154–162.
[33] J.S. Pedersen, Analysis of small-angle scattering data from colloids and polymer solutions: modeling and least-squares fitting, Adv. Colloid Interface Sci. 70 (1997) 171–210.
[34] M. Bergström, J. Skov Pedersen, Structure of pure SDS and DTAB micelles in brine determined by small-angle neutron scattering (SANS), PCCP 1 (18) (1999) 4437–4446.

[35] F. Nilsson, O. Söderman, I. Johansson, Four different C8G1 alkylglucosides. anomeric effects and the influence of straight vs branched hydrocarbon chains, J. Colloid Interface Sci. 203 (1998) 131–139.

[36] K.D. Danov, P.A. Kralchevsky, S.D. Stoyanov, J.L. Cook, I.P. Stott, E.G. Pelan, Growth of wormlike micelles in nonionic surfactant solutions: quantitative theory vs. experiment, Adv. Colloid Interface Sci. 256 (2018) 1–22.

[37] L.M. Walker, Rheology and structure of worm-like micelles, Curr. Opin. Colloid Interface Sci. 6 (5) (2001) 451–456.

[38] K.N. Silva, R. Novoa-Carballal, M. Drechsler, A.H.E. Müller, E.K. Penott-Chang, A. J. Müller, The influence of concentration and pH on the structure and rheology of cationic surfactant/hydrotrope structured fluids, Colloids Surf., A 489 (2016) 311–321.

[39] P.G. Cummins, E. Staples, J. Penfold, R.K. Heenan, The geometry of micelles of the poly(oxyethylene) nonionic surfactants C16E6 and C16E8 in the presence of electrolyte, Langmuir 5 (5) (1989) 1195–1199.

[40] K. Aramaki, S. Hoshida, S. Arima, Effect of carbon chain length of cosurfactant on the rheological properties of nonionic wormlike micellar solutions formed by a sugar surfactant and monohydroxy alcohols, Colloids Surf., A 366 (1) (2010) 58–62.

[41] H. Kunieda, C. Rodriguez, Y. Tanaka, M.H. Kabir, M. Ishitobi, Effects of added nonionic surfactant and inorganic salt on the rheology of sugar surfactant and CTAB aqueous solutions, Colloids Surf., B 38 (3) (2004) 127–130.

[42] J.E. Moore, T.M. McCoy, L. de Campo, A.V. Sokolova, C.J. Garvey, G. Pearson, B.L. Wilkinson, R.F. Tabor, Wormlike micelle formation of novel alkyl-tri(ethylene glycol)-glucoside carbohydrate surfactants: structure–function relationships and rheology, J. Colloid Interface Sci. 529 (2018) 464–475.

[43] P.O. Cummins, J.B. Hayter, J. Penfold, E. Staples, A small-angle neutron scattering investigation of shear-aligned hexaethyleneglycolmonohexadecylether (C16E6) micelles as a function of temperature, Chem. Phys. Lett. 138 (5) (1987) 436–440.

[44] B.F. García, S. Saraji, A new insight into the dependence of relaxation time on frequency in viscoelastic surfactant solutions: From experimental to modeling study, J. Colloid Interface Sci. 517 (2018) 265–277.

[45] W. Zou, G. Tan, H. Jiang, K. Vogtt, M. Weaver, P. Koenig, G. Beaucage, R.G. Larson, From well-entangled to partially-entangled wormlike micelles, Soft Matter 15 (4) (2019) 642–655.

Electronic supporting information for

Molecular structure of maltoside surfactants controls micelle formation and rheological behaviour

Johan Larsson,[a*] *Adrian Sanchez-Fernandez,*[b] *Anna Leung,*[c] *Ralf Schweins,*[d] *Baohu Wu,*[e] *Tommy Nylander,*[a,f] *Stefan Ulvenlund,*[b,g] *Marie Wahlgren*[b,g]

[a]Physical Chemistry, Department of Chemistry, Lund University, Box 124, 221 00 Lund, Sweden.

[b]Food Technology, Nutrition and Engineering, Lund University, Box 124, 221 00 Lund, Sweden.

[c]European Spallation Source, Box 176, 221 00 Lund, Sweden.

[d]Institut Laue-Langevin, DS / LSS, 71 avenue des Martyrs, 38000, Grenoble, France.

[e]Jülich Centre for Neutron Science (JCNS) at Heinz Maier-Leibnitz Zentrum (MLZ), Forschungszentrum Jülich GmbH, Lichtenbergstr. 1, 85748 Garching, Germany.

[f]NanoLund, Lund University, Lund, Sweden

[g]Enza Biotech AB, Scheelevägen 22, 22363 Lund, Sweden.

*corresponding author: Box 124, 221 00 Lund, +46 46 222 82 16, johan.larsson@fkem1.lu.se

Experimental section

The molecular structure of α- and β-$C_{16}G_2$ is presented in Figure S1.

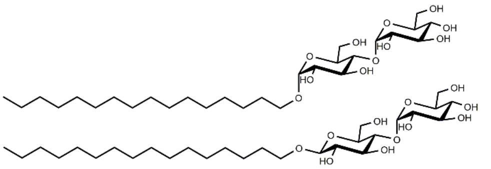

Figure S1. Molecular structure of α-$C_{16}G_2$ (top) and β-$C_{16}G_2$ (bottom).

Synthesis

n-Hexadecyl-d_{31}-β-D-maltopyranoside was synthesised according to literature procedures for the *n*-dodecyl-d_{25} analogue,[1] starting from 2,3,6,2’,3’,4’,6’-hepta-O-acetyl-α-D-maltosyl bromide and *n*-hexadecanoic acid-d_{31}.

General experimental

2,3,6,2’,3’,4’,6,’-Hepta-O-acetyl-α-D-maltosyl bromide was purchased from Carbosynth Ltd, United Kingdom. All other reagents and solvents, including D_2O (99.8 %D) were purchased from Sigma-Aldrich. Low resolution electrospray ionisation mass spectra were recorded on an Agilent 1260 Infinity II system coupled with an Agilent InfinityLab LC/MSD XT. The column was by-passed and the sample was pumped into the mass spectrometer. High resolution electrospray ionisation mass spectra were recorded on a Waters QTOF XEVO-G2 mass spectrometer. The overall deuterium incorporation across the molecule was calculated by mass spectrometry using the relative distribution of the isotopologues. This calculation accounted for the ^{13}C natural abundance by subtracting this contribution from the peak area of each M+1 isotopologue. NMR spectra were recorded on a Varian Unity INOVA 400 MHz spectrometer with a 5 mm $^{1}H/^{13}C$ auto-switchable gradient-probe, operating at 400 and 100 MHz respectively for proton (^{1}H) and carbon (^{13}C) nuclei. ^{13}C NMR spectra were ^{1}H-decoupled but not ^{2}H-decoupled. Spectra were recorded at 298 K. Chemical shifts, expressed in parts per million (ppm), were referenced to the residual signal of the solvent.

n-Hexadecanoic acid-d_{31}

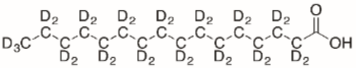

n-Hexadecanoic acid (20.1 g, 78.4 mmol), NaOD in D_2O (40% w/w in D_2O, 8.05 g, 78.5 mmol), Pt/C (5% wt., 1.00 g, 256 µmol) and D_2O (200 mL) were added to a Parr reactor which was purged with nitrogen whilst stirring, then sealed and heated to 220 °C for three days with constant stirring (maximum pressure reached: 23.2 bar). The mixture was allowed to cool to 55 °C, transferred to a beaker and kept warm using a stirrer hotplate. Aqueous 1 M HCl and ethyl acetate were added to ensure everything except for the catalyst was dissolved (the aqueous layer had a pH of 1-2) and the entire mixture was filtered, whilst warm, through a short celite plug. The biphasic mixture was transferred to a separating funnel and the phases were separated. The aqueous phase was washed with ethyl acetate (2 x 200 mL) and the combined organic phases were combined, dried ($MgSO_4$), concentrated under reduced pressure and then dried under vacuum at 65 °C overnight. The resulting solid was washed with hexane and re-dried under vacuum at 65 °C overnight. This material was subjected to two more cycles of H/D exchange under the same conditions, using the same amounts of D_2O and Pt/C, and an equimolar amount of a 40% w/w/ solution of NaOD in D_2O. After the third cycle, *n*-hexadecanoic acid-d_{31} was obtained (16.58 g, 99% deuterated by MS, 74% yield). ^{1}H NMR ($CDCl_3$, 400 MHz) δ 0.82 (br s, residual), 1.19-1.27

(complex, residual), 1.58 (br s, residual), 2.31 (br s, residual). ^{13}C NMR ($CDCl_3$, 100 MHz) δ 13.1 (m), 21.5 (m), 23.8 (m), 28.5 (m), 30.7 (m), 33.5 (m), 180.8 (s). MS (ESI−) *m/z* calculated for $C_{16}D_{31}O_2$ $[M-H]^-$ as 286.4275; found: 286.4265. Isotope distribution: d_{28} 1.9%; d_{29} 6.7%; d_{30} 25.5%; d_{31} 64.5%.

n-Hexadecanol-d_{31}

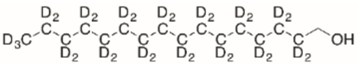

$LiAlH_4$ (1.82 g, 43.4 mmol) was suspended in anhydrous THF (80 mL). The mixture was cooled with an external ice bath. A solution of *n*-hexadecanoic acid-d_{31} (7.30 g, 25.4 mmol, 99% D by MS) in anhydrous THF (30 mL) was added dropwise to the suspension. The mixture was allowed to warm to room temperature, fitted with a water condenser and then heated to refluxing temperature overnight under argon. The mixture was allowed to cool to room temperature and was determined by TLC (70:30:1 hexane:diethyl ether:acetic acid; bromocresol green as visualising agent) to contain none of the starting material. An external ice bath was used to further cool the mixture and water (25 mL) was added dropwise to quench remaining reducing agent. Aqueous 1 M H_2SO_4 (120 mL) was added to dissolve the resultant precipitate and the solution was transferred to a separating funnel. The mixture was extracted into diethyl ether (100 mL); the organic phase was then washed with saturated aqueous $NaHCO_3$ (100 mL), dried ($MgSO_4$), filtered and concentrated in vacuo to afford a white solid (6.92 g, 100%), which required no further purification. ^1H NMR (400 MHz, $CDCl_3$) δ 0.83 (br s, residual), 1.20-1.29 (br complex, residual), 1.42 (br s, OH), 1.53 (br t, $J = 7.6$ Hz, residual), 3.63 (s, 2H). ^{13}C NMR (100 MHz, $CDCl_3$) δ 12.9 (m), 21.5 (m), 24.6 (m), 28.1-29.1 (complex), 30.9 (m), 31.9 (m), 63.0 (s).

2,3,6,2’,3’,4’,6’-Hepta-O-acetyl-*n*-hexadecyl-d_{31}-β-D-maltopyranoside

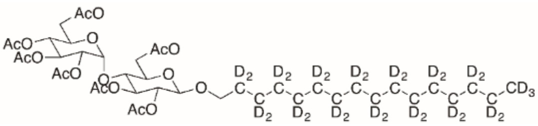

n-Hexadecanol-d_{31} (3.29 g, 12.0 mmol), 2,3,6,2’,3’,4’,6’-hepta-O-acetyl-α-D-maltosyl bromide (1.39 g, 1.99 mmol) and 4 Å molecular sieves (2.5 g) were added to anhydrous DCM (20 mL). The mixture was stirred for one hour and then silver carbonate (676 mg, 2.45 mmol) and silver perchlorate (503 mg, 2.43 mmol) were added. The mixture was covered with foil and stirred vigorously for two hours under argon, then filtered through a celite plug, which was washed with DCM (20 mL). The solvent was removed from the filtrate under reduced pressure to provide a pink solid. Purification via flash column chromatography (gradient elution: 25-40% EtOAc in hexane; visualised with Hanessian’s stain) provided the pure title compound as a white solid (618 mg, 35% yield). Residual protons are not reported in the ^1H NMR spectroscopic data. Due to C-D splitting in the ^{13}C NMR spectrum, some deuterated carbon atoms are not reported in the ^{13}C NMR spectroscopic data. ^1H NMR (400 MHz, $CDCl_3$) δ 2.00-2.02 (complex, 12 H), 2.04 (s, 3H), 2.10 (s, 3H), 2.14 (s, 3H), 3.44 (d, $J = 9.6$ Hz, 1H), 3.67 (m, 1H), 3.82 (d, $J = 9.6$ Hz, 1H), 3.94-4.05 (complex, 3 H), 4.24 (m, 2H), 4.46 (dd, $J = 12.1$, 2.7 Hz, 1H), 4.78-4.87 (complex, 2H), 5.04 (t, $J = 9.9$ Hz, 1H), 5.24 (t, $J = 9.1$ Hz, 1H), 5.35 (t, $J = 10.0$ Hz, 1H), 5.41 (d, $J = 4.0$ Hz, 1H).^{13}C NMR (100 MHz, $CDCl_3$) δ 20.67 (s), 20.68 (s), 20.70 (s), 20.78 (s), 20.9 (s), 21.0 (s), 24.7 (m), 28.4 (m), 61.6 (s), 63.0 (s), 68.1 (s), 68.6 (s), 69.5 (s), 70.1 (s), 70.2 (s), 72.1 (s), 72.3 (s), 72.9 (s), 75.6 (s), 95.6 (s), 100.4 (s), 169.5 (s), 169.7 (s), 170.0 (s), 170.4 (s), 170.57 (s), 170.606 (s), 170.613 (s). MS (ESI+) *m/z* calculated for $C_{42}H_{37}D_{31}NaO_{18}$ $[M+Na]^+$ as 914.6; found: 914.5. Isotope distribution: d_{29} 8.6%; d_{30} 27.4%; d_{31} 64.0%.

n-Hexadecyl-d31-Î²-D-maltopyranoside

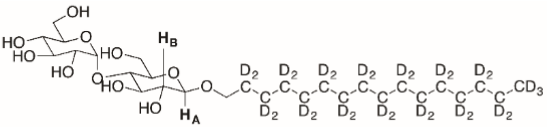

2,3,6,2’,3’,4’,6’-Hepta-O-acetyl-*n*-hexadecyl-d_{31}-β-D-maltopyranoside (375 mg, 420 µmol) was dissolved in anhydrous methanol (14 mL). A solution of sodium methoxide in methanol (0.5 M, 1.2 mL, 600 µmol) was added and the mixture was stirred at room temperature under argon for 18 h. Amberlite IR-120 (H+) was added, and the mixture was stirred until the pH reached 5. The resin was removed via filtration and the solvent removed to provide the title compound as a white solid (241 mg, 96%). The anomeric configuration of the β-maltopyranoside was confirmed by the magnitude of the $J_{A,B}$ coupling constant in the ^{1}H NMR spectrum (7.8 Hz, indicative of axial-axial and not axial-equatorial coupling), see Figure S2 and S3. Residual protons are not reported in the ^{1}H NMR spectroscopic data; deuterated carbon atoms are not reported in the ^{13}C NMR spectroscopic data, see Figure S4 and S5. Heteronuclear single quantum coherence (edited) and heteronuclear multiple bond correlation NMR spectra are presented in Figure S6 and Figure S7 respectively. ^{1}H NMR (400 MHz, CD_3OD) δ 3.20-3.29 (complex, 2H), 3.36 (ddd, J = 9.5, 4.4, 2.0 Hz, 1H), 3.44 (dd, J = 9.7, 3.7 Hz, 1H), 3.51-3.55 (complex, 2H), 3.59-3.63 (complex, 2H), 3.67-3.71 (complex, 2H), 3.79-3.90 (complex, 4H), 4.26 (d, J = 7.8 Hz, 1H), 5.16 (d, J = 3.8 Hz, 1H). ^{13}C NMR (400 MHz, CD_3OD) δ 62.2, 62.8, 70.9, 71.5, 74.2, 74.7, 74.8, 75.1, 76.6, 77.9, 81.4, 102.9, 104.3. MS (ESI+) *m/z* calculated for $C_{28}H_{23}D_{31}NaO_{11}$ [M+Na]$^+$ as 620.6; found: 620.5. Isotope distribution: d_{29} 7.7%; d_{30} 28.3%; d_{31} 64.1%.

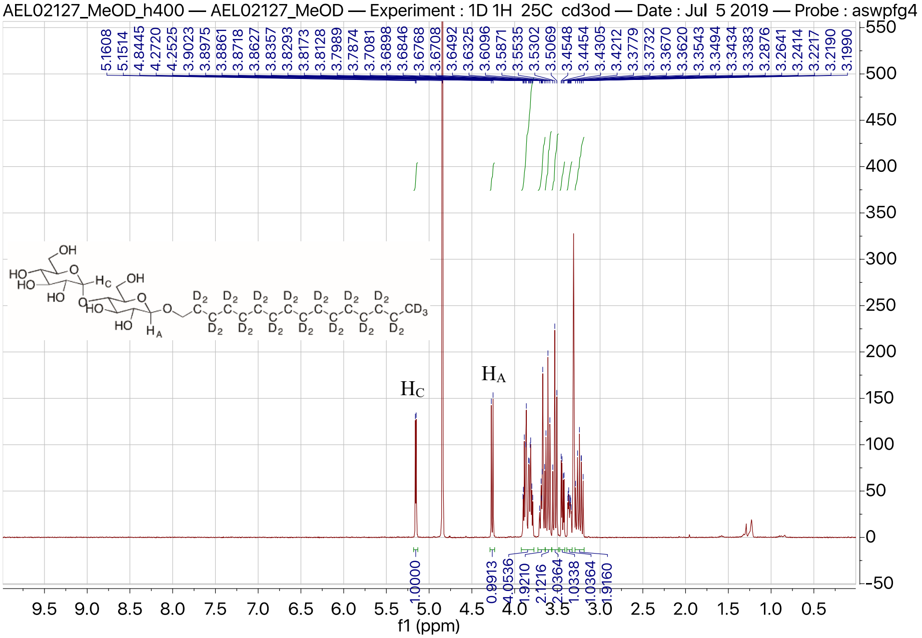

Figure S2. ^{1}H NMR spectrum of *n*-hexadecyl-d_{31}-β-D-maltopyranoside (400 MHz, CD_3OD).

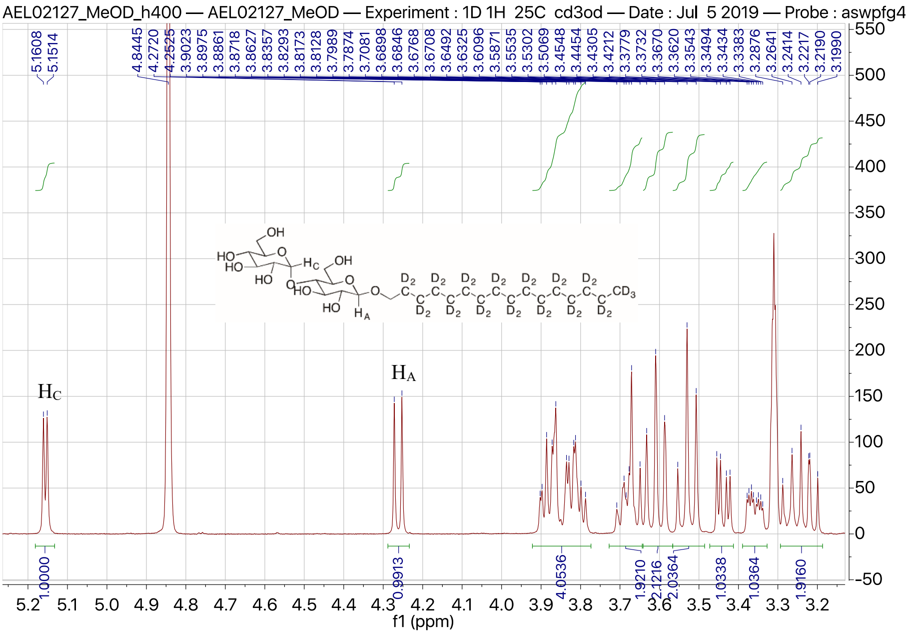

Figure S3. ^{1}H NMR spectrum of *n*-hexadecyl-d_{31}-β-D-maltopyranoside (400 MHz, CD_3OD) (expansion).

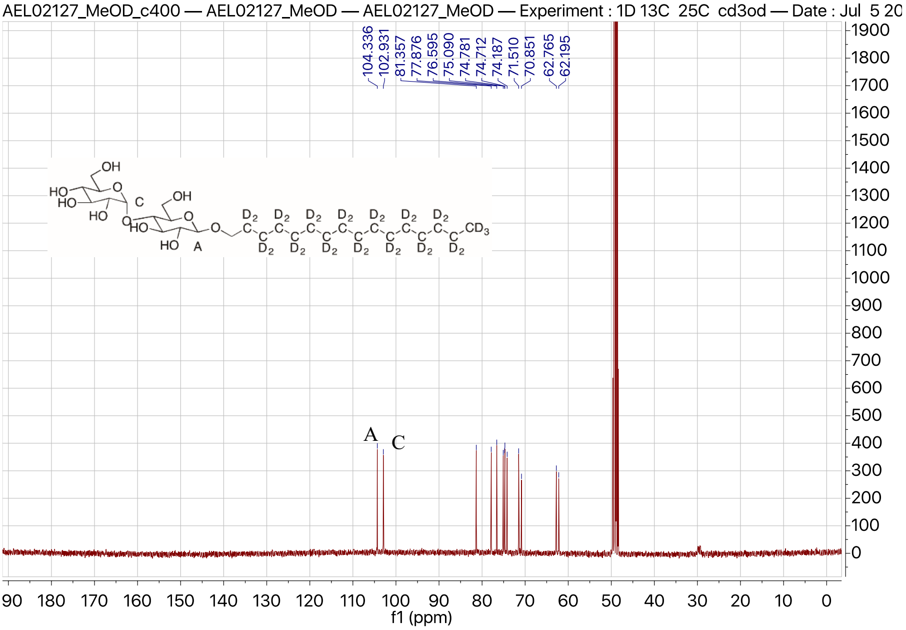

Figure S4. ^{13}C NMR spectrum of *n*-hexadecyl-d_{31}-β-D-maltopyranoside (100 MHz, CD_3OD).

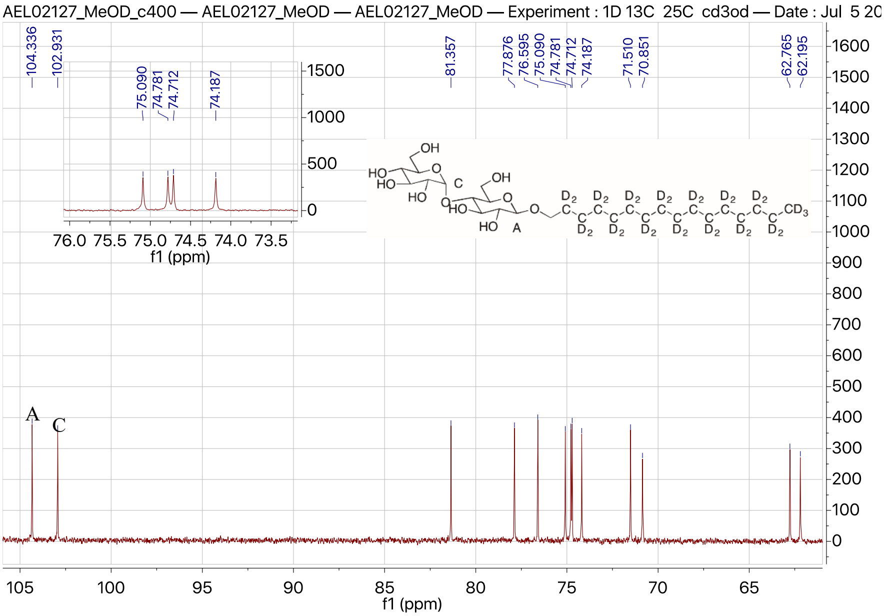

Figure S5. ^{13}C NMR spectrum of *n*-hexadecyl-*d*$_{31}$-β-D-maltopyranoside (100 MHz, CD_3OD) (expansion).

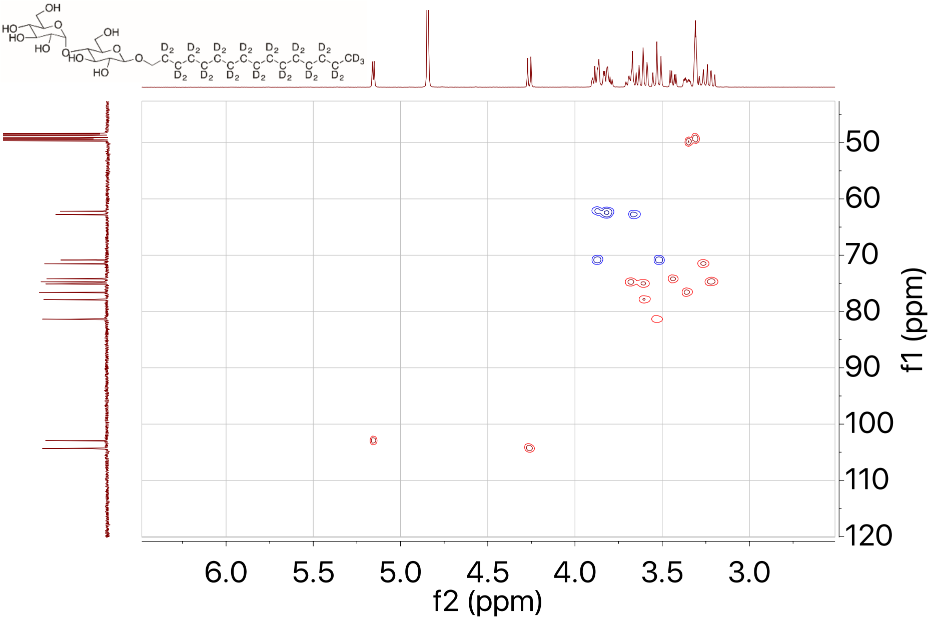

Figure S6. Heteronuclear single quantum coherence NMR spectrum (edited) of *n*-hexadecyl-*d*$_{31}$-β-D-maltopyranoside (400 MHz, CD_3OD). Blue signals represent methylene groups and red signals represent methine groups.

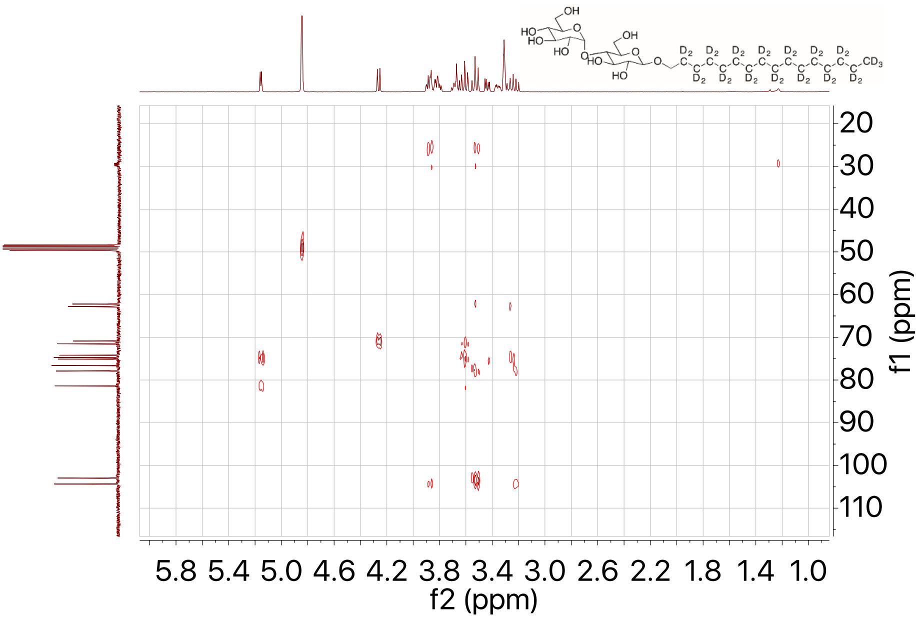

Figure S7. Heteronuclear multiple bond correlation NMR spectrum of *n*-hexadecyl-d_{31}-β-D-maltopyranoside (400 MHz, CD_3OD).

Results

The α- and β-$C_{16}G_2$ SANS data and best fits of a flexible cylinder model is presented in Figure S8 and the parameters obtained from the fit is presented in Table S1.

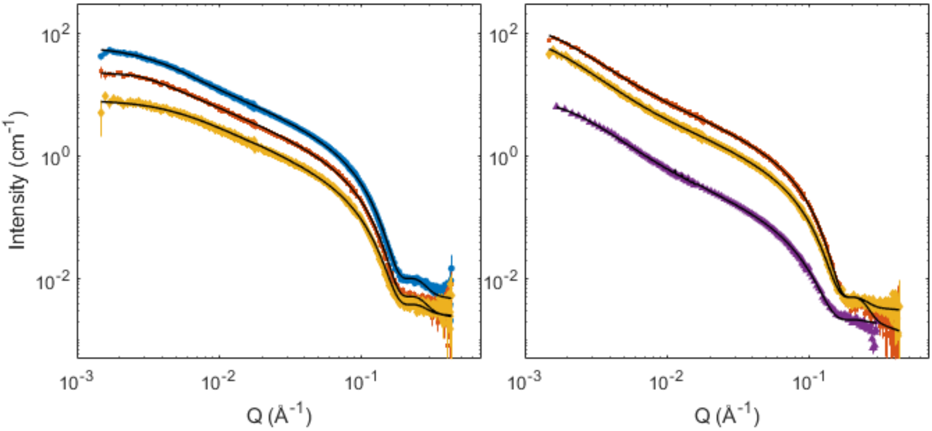

Figure S8 SANS data for α-$C_{16}G_2$ (left) and β-$C_{16}G_2$ (right) at 50 °C. 20 mM (blue ○), 10 mM (red □), 5 mM (yellow ◊) and 1 mM (purple △). The black solid lines are the fit of a flexible cylinder model to the data.

Table S1. Parameters obtained from fitting a flexible cylinder model to the SANS data recorded for $C_{16}G_2$ solutions at 50 °C. Surfactant concentration (c), radius (r), contour length (L) and persistence length (l_p).

	α-$C_{16}G_2$			β-$C_{16}G_2$		
c / mM	r / Å	L / Å	l_p / Å	r / Å	L / Å	l_p / Å
1	-	-	-	22.9±0.1	6000±200*	205±10
5	20.1±0.1	873±50	318±60	22.7±0.1	10500±300*	273±10
10	20.4±0.1	1390±100	351±60	22.7±0.1	8600±200	316±10
20	20.6±0.1	1610±100	309±10	-	-	-

*The maximum dimension that could be probed with the experimental set up was ~4000 Å and greater values resulted from the mathematical model of the experimental data.

The viscosity of α-$C_{16}G_2$ at 200 mM at different temperatures is presented in Figure S9.

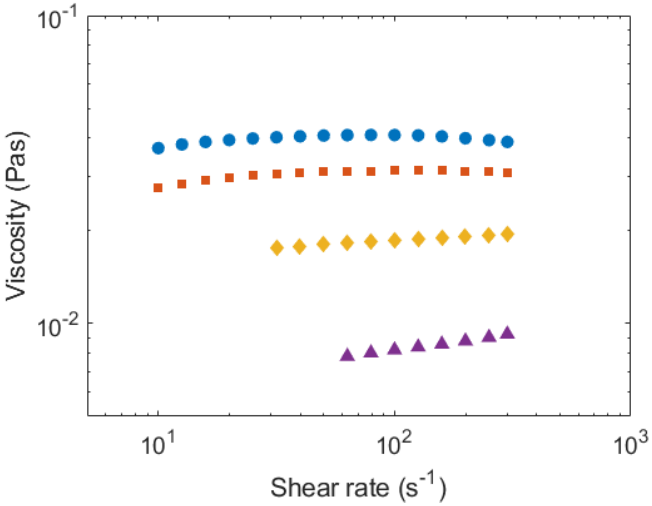

Figure S9 Viscosity of α-$C_{16}G_2$ at 200 mM Experiments were performed at 4 temperatures: 60 (○), 50 (□), 40 (◊) and 30 °C (△).

Cole-Cole plots for β-$C_{16}G_2$ at 200, 100 and 50 mM (Figure S10 a-c) and 100 mM mixtures of α- and β-$C_{16}G_2$ with 90, 75 and 50% β-$C_{16}G_2$ (Figure S10 d-f).

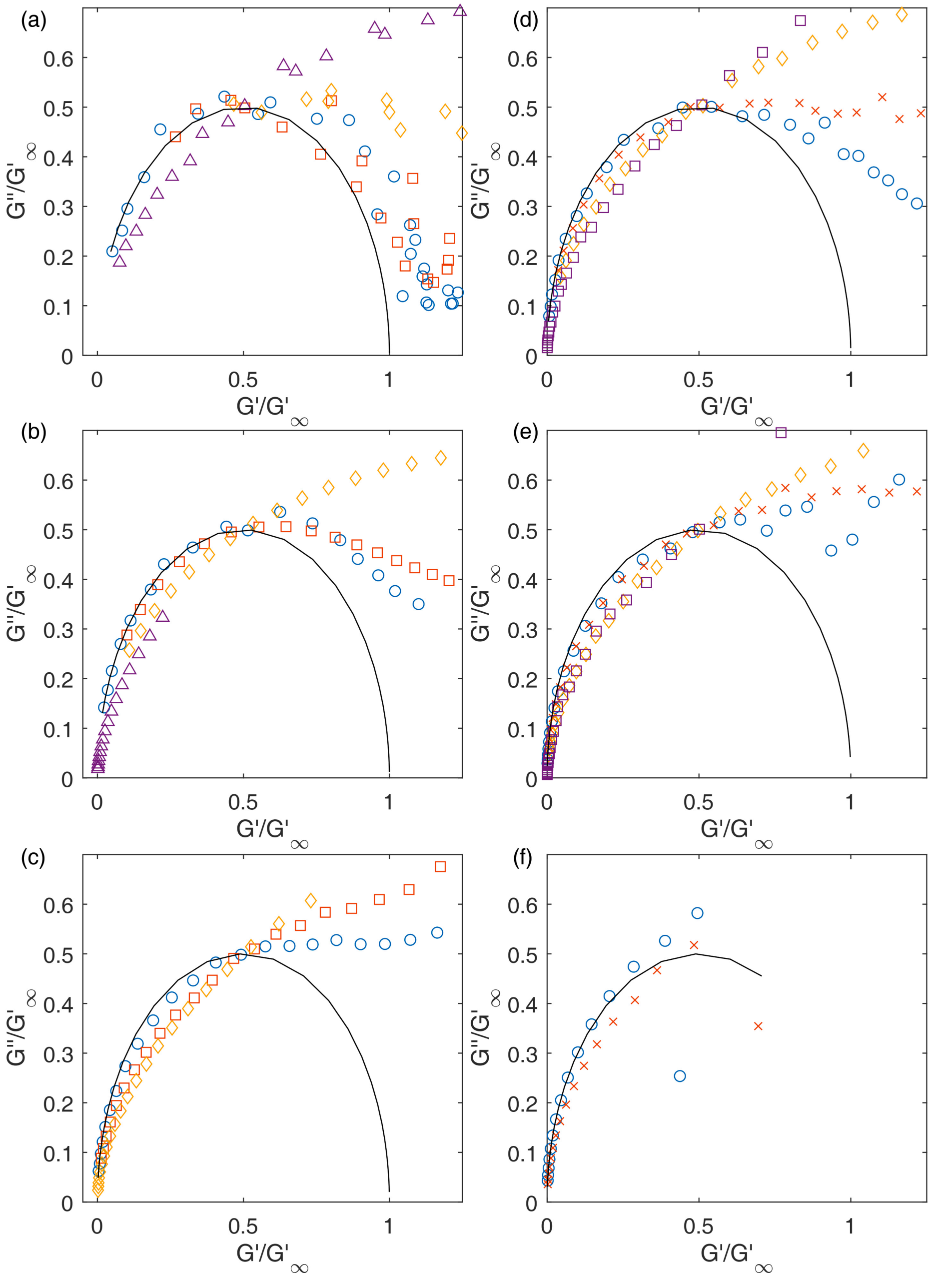

Figure S10 Cole-Cole plots for β-$C_{16}G_2$ solutions with 200 (a), 100 (b) and 50 mM (c) surfactant concentrations and for α- and β-$C_{16}G_2$ mixtures with 90 (d), 75 (e), and 50% (f) β-$C_{16}G_2$ ratios. The measurements were conducted at 60 (○), 50 (□), 40 (◊) and 30 °C (△).

Flow curves for mixtures of α- and β-$C_{16}G_2$ with different surfactant ratios are presented in Figure S11.

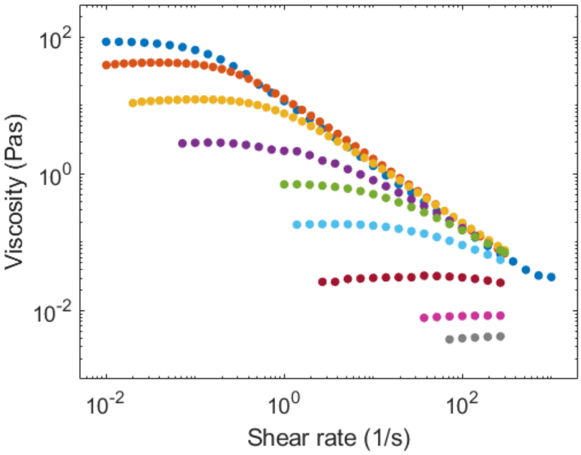

Figure S11 Viscosity of mixtures of α- and β-$C_{16}G_2$ at 100 mM. Ratio β-$C_{16}G_2$ from top to bottom (%): 100, 90, 75, 60, 50, 40, 25, 10, 0.

Results from DLS experiments for mixtures of α- and β-$C_{16}G_2$ with different surfactant ratios and temperatures are presented in Figure S12 and S13.

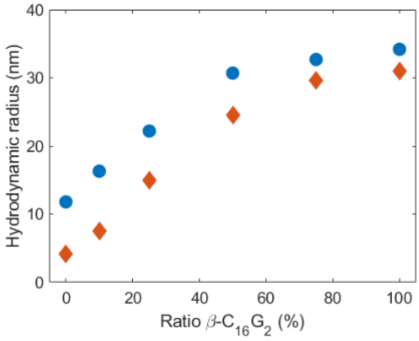

Figure S12 Hydrodynamic radius of micelles of 10 mM mixtures of α- and β-$C_{16}G_2$ at 50 °C (○) and 30 °C (◊).

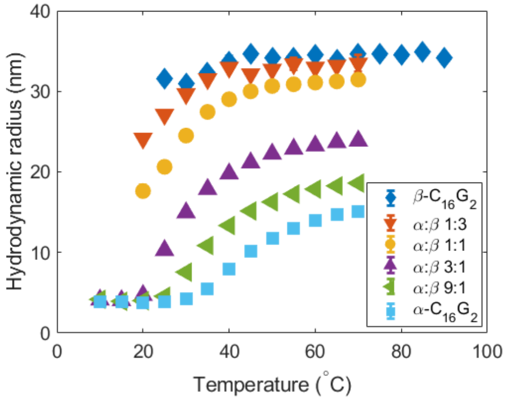

Figure S13 Hydrodynamic radius of α- and β-$C_{16}G_2$ micelles at 10 mM versus temperature.

Results from SANS experiments with mixtures of α- and β-$C_{16}G_2$ at 50 and 30 °C and 2 different contrasts with fits of a flexible cylinder model are presented in Figure S14. The parameters obtained from the model are presented in Table S2 for the protiated mixtures and in Table S3 for the mixtures with protiated α-$C_{16}G_2$ and tail deuterated β-$C_{16}G_2$.

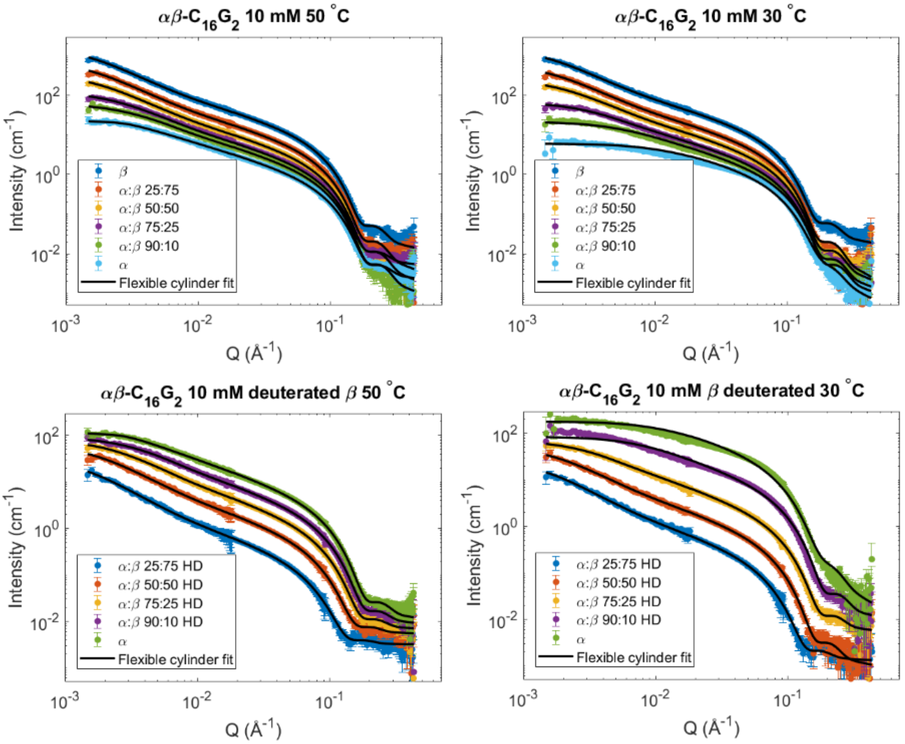

Figure S14 SANS data for mixtures of α- and β-$C_{16}G_2$ at 10 mM. The solid lines show the fit of a flexible cylinder model. Top left: protiated surfactants at 50 °C. Top right: protiated surfactants at 30 °C. Bottom left: protiated α-$C_{16}G_2$ mixed with tail deuterated β-$C_{16}G_2$ at 50 °C. Bottom right: protiated α-$C_{16}G_2$ mixed with tail deuterated β-$C_{16}G_2$ at 30 °C. The intensity of the data and fits have been offset for clarity.

Table S2. Parameters obtained from fitting a flexible cylinder model to the SANS data recorded for mixtures of α- and β-$C_{16}G_2$ with a total surfactant concentration of 10 mM. Radius (r), contour length (L) and persistence length (l_p).

	50 °C			30 °C		
Ratio / % β	r / Å	L / Å	l_p / Å	r / Å	L / Å	l_p / Å
0	20.4±0.2	1390±30	-	23.4±0.2	190±10	-
10	20.9±0.2	2150±60	285±9	20.6±0.2	880±20	370±15
25	21.2±0.2	3290±300	271±7	21.3±0.2	1950±40	380±15
50	21.7±0.1	6030±900*	275±5	22.1±0.2	4210±100*	310±20
75	22.2±0.2	7590±600*	281±5	22.8±0.2	6110±150*	300±40
100	22.7±0.2	8600±250	316±5	23.4±0.2	7040±200*	320±90

*The maximum dimension that could be probed with the experimental set up was ~4000 Å and greater values resulted from the mathematical model of the experimental data.

Table S3. Parameters obtained from fitting a flexible cylinder model to the SANS data recorded for protiated α-$C_{16}G_2$ mixed with tail deuterated β-$C_{16}G_2$ with a total surfactant concentration of 10 mM. Radius (r), contour length (L), persistence length (l_p) and scattering length density (SLD_{fit}).

	50 °C				30 °C			
Ratio / % β	r / Å	L / Å	l_p / Å	SLD_{fit} / 10^{-6} Å^{-2}	r / Å	L / Å	l_p / Å	SLD_{fit} / 10^{-6} Å^{-2}
10	21.0±0.2	1870±30	285±30	0.047±0.01	20.5±0.2	830±10	390±50	0.12±0.01
25	21.8±0.2	3140±80	288±15	0.91±0.01	21.8±0.2	1830±50	410±50	0.92±0.01
50	23.8±0.4	5540±300*	286±10	2.47±0.01	24.1±0.3	4610±300*	360±20	2.54±0.01
75	26.8±0.7	8340±900*	265±10	3.99±0.01	27.6±0.6	7410±600*	310±20	3.99±0.01

*The maximum dimension that could be probed with the experimental set up was ~4000 Å and greater values resulted from the mathematical model of the experimental data.

The distribution of surfactants in the micelles was calculated and presented in Figure S15.

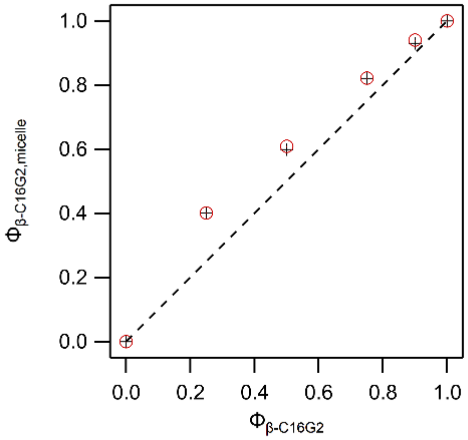

Figure S15. Distribution of surfactants in the micelles at 50 (○) and 30 °C (+) and different volume fractions of α- and β-$C_{16}G_2$ calculated from SANS.

SAXS results for mixtures of α- and β-$C_{16}G_2$ at 50 °C with fits of a core-shell cylinder model is presented in Figure S16 and the parameters obtained from the model is presented in Table S4.

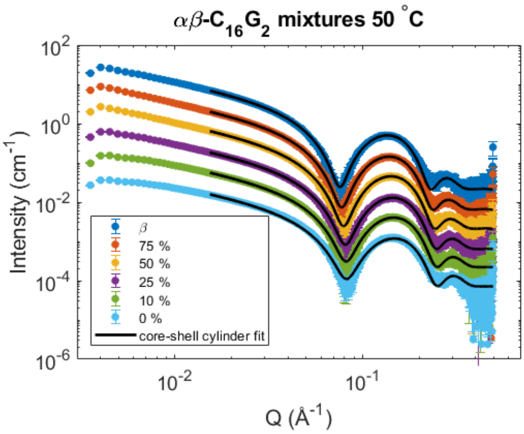

Figure S16 SAXS results for mixtures of α- and β-$C_{16}G_2$ at 10 mM and 50 °C fitted with a core-shell cylinder model. The intensity of the data and fits are offset for clarity.

Table S4. Micellar cross section dimensions obtained from core-shell cylinder model parameters used to fit the SAXS data of α- and β-$C_{16}G_2$ mixtures at 10mM and 50 °C. The length of the micelle was set to the one obtained from the flexible cylinder fit from the SANS data.

Ratio / % β	r_{core} / Å	shell thickness / Å
0	14.8	13.9
10	14.6	14.5
25	14.7	14.8
50	14.7	15.6
75	15.0	16.1
100	15.5	16.2

Reference

1. Midtgaard, S. R.; Darwish, T. A.; Pedersen, M. C.; Huda, P.; Larsen, A. H.; Jensen, G. V.; Kynde, S. A. R.; Skar-Gislinge, N.; Nielsen, A. J. Z.; Olesen, C.; Blaise, M.; Dorosz, J. J.; Thorsen, T. S.; Venskutonytė, R.; Krintel, C.; Møller, J. V.; Frielinghaus, H.; Gilbert, E. P.; Martel, A.; Kastrup, J. S.; Jensen, P. E.; Nissen, P.; Arleth, L., Invisible detergents for structure determination of membrane proteins by small-angle neutron scattering. *The FEBS Journal* **2018,** *285* (2), 357-371.

Paper III

Shear-induced nanostructural changes of worm-like micelles formed by sugar-based surfactants

J. Larsson, M. Wahlgren, L. Porcar, S. Ulvenlund, T. Nylander, A. Sanchez-Fernandez

Manuscript in preparation for submission

Shear-induced nanostructural changes of worm-like micelles formed by sugar-based surfactants

Johan Larsson,[a] Marie Wahlgren,[b,c] Lionel Porcar,[d] Stefan Ulvenlund,[b,c] Tommy Nylander,[a,e] Adrian Sanchez-Fernandez.[b]

[a]Physical Chemistry, Department Chemistry, Lund University, Box 124, 221 00 Lund, Sweden.
[b]Food Technology, Nutrition and Engineering, Lund University, Box 124, 221 00 Lund, Sweden.
[c]Enza Biotech AB, Scheelevägen 22, 22363 Lund, Sweden.
[d]Institut Laue-Langevin, DS / LSS, 71 avenue des Martyrs, 38000, Grenoble, France.
[e]NanoLund, Lund University, Lund, Sweden

The self-assembly of long tail sugar-based surfactants into worm-like micelles have recently been shown give rise to interesting rheological properties that can be tailored by means of subtle changes in molecular characteristics. In particular, the anomeric configuration in the surfactant headgroup was proved to control micelle structure, leading to profound changes in the nanostructure of the system and hence in macroscopic rheology. Here we explore the mechanistic origin of the flow properties of two anomers of hexadecylmaltoside (α- and β-$C_{16}G_2$) by directly connecting their different rheological behaviour to differences in micellar morphology by using rheo-small-angle neutron scattering. For this purpose, 1-3 plane SANS measurements, using a Couette cell geometry, probed the structural changes in the micellar phase under shear. The effect of surfactant anomeric configuration, surfactant concentration, temperature and mixing ratio of the two anomers were investigated. The segmental alignment of the micellar phase was studied under several flow conditions, showing that the shear-thinning behaviour relates to the re-arrangement of the worm-like micelles, whilst rod-like micelles are considerably less affected by the sample flow. The results are rationalised in terms of micelle alignment, as well as disruption of entanglement and branching, providing a detailed mechanism by which sugar-based surfactants control the rheology of the fluid.

Introduction

As society moves towards more environmentally friendly technologies, there is a need for sustainable surfactants that can give functional properties to consumer products (e.g. cosmetics and pharmaceutical formulations). Several of the relevant surfactants currently used in formulation technology are produced using chemicals derived from fossil raw materials (e.g. polysorbates). In addition, some ionic surfactants should be avoided in formulation technology as they can be harmful for the body (e.g. cause irritation in the skin or mucosa). Sugar-based surfactants, such as the maltoside surfactants used in this study, have low toxicity and can be produced using renewable materials.[1] The introduction of sugar-based surfactants are therefore part of the transition into more environmentally friendly products that is currently taking place. One key property that surfactants can give to consumer products is a specific rheological behaviour that can promote their colloidal stability and facilitate handling and administration, such as shear-thinning and viscoelastic properties. This is crucial for products such as shampoos, shower gels, cosmetic creams or pharmaceutical dispersions. Surfactants that form worm-like micelles (WLM) in solution confer these properties to the systems. WLM are semiflexible elongated self-assembled structures.[2] In solution, above the overlap concentration they entangle, resulting in intriguing and useful rheological behaviour.[3] At rest or low shear stress, WLM entanglement results in an increase in viscosity. With increasing shear stress the network collapses through different relaxation modes and the viscosity of the system gradually decreases.[2] Thus, WLM solutions behave as non-Newtonian shear-thinning fluids. The entanglements also gives WLM solutions viscoelastic properties, meaning that at short time scales it behaves as an elastic material and at long time scales it behaves as a viscous material.[4] Polymers in solution behave in a similar way but, unlike polymers WLM subunits (i.e. surfactant monomers) are not covalently bound. Thus, WLM are equilibrium structures, which continuously break and reform, giving rise to different relaxation modes (e.g. reptation and breakage).

Nevertheless, the systems are possible to describe with a single relaxation time (τ), which is obtained from the frequency at which the viscous and elastic moduli have identical values.[5]

As the change in the rheological behaviour from that of a dilute WLM dispersion is attributed to the formation of an entangled network, the shear thinning has been related to the disruption of such a network when stress is applied.[6] A common picture is to attribute the change in viscosity to the alignment of the WLM in the flow direction.[7-8] In addition, other relaxation modes can be observed in WLM systems under shear. Simulations have shown that micelle rupture increases with shear, resulting in a decrease of the mean micelle length, which becomes a contributing factor to the shear thinning behaviour.[9]

Since the flow properties are relevant for several of the applications of WLM (e.g. drag-reducing agents and rheology modifiers), it is important to have knowledge about the effect of flow on the WLM systems. Rheo-SANS is a technique which combines rheometry and small-angle neutron scattering (SANS) to study the structure of colloidal systems when subjected to shear.[10-11] With rheo-SANS, a sample can be examined in three different planes upon shearing (flow-vorticity (1-3), gradient-vorticity (2-3) and flow-gradient (1-2)) by varying the angle and position of the sample relative to the incident beam, yielding complementary information. These are schematically represented in Figure 1.[10] Measurements in the 1-3 plane provide information on the average structure across the gap of the Couette and can be used to detect inhomogeneities along the vertical vorticity direction. The 2-3 plane is investigated by having the beam tangential to the sheared sample. When studying the 1-2 plane the cell is rotated 90° to have to axis of rotation parallel to the beam.

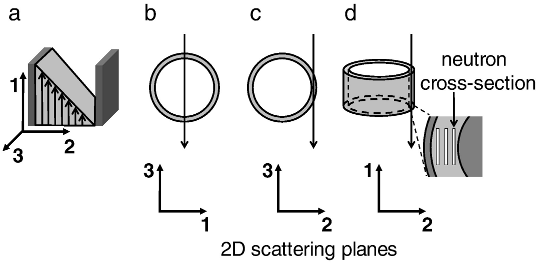

Figure 1. Accessible scattering planes using a Couette cell geometry. (a) Coordinate components of the flow: 1 – flow, 2 – gradient, and 3 – vorticity directions. Projections of the shear cell along the neutron beam direction (black arrow): (b) radial, (c) tangential, and (d) axial. Reproduced from Eberle and Porcar, *Curr. Opin. Colloid Interface Sci.* **2012,** 17 (1), 33-43; with permission from Elsevier.

Rheo-SANS has been used in several studies of WLM and been able to give a deeper understanding of the microscopic origin of their rheological behaviour. Measurements in the 1-3 plane were used to show that WLM align in the flow direction,[12] that the alignment increases with increasing shear rate and that there is an exponential dependence between the alignment and the viscosity.[13] Measurement along the 1-2 plane of a WLM system formed by a cationic/anionic surfactant mixture of 1.5 wt% CTAT and SDBS in D_2O showed that the alignment is increasing with decreasing distance to the moving cylinder wall and that the onset of the shear thinning regime coincide with the onset of alignment closest to the moving wall.[14] The scattering from the 1-2 plane also revealed that several WLM systems separate into two phases during shear, one isotropic low shear phase close to the static wall and one anisotropic high shear phase close to the moving cylinder, a phenomenon referred to as shear banding.[7, 15-16] There are also WLM systems where no shear banding arises and this was attributed to the formation of branched micelles.[17] Almost all surfactant systems investigated by rheo-SANS have been based on ionic surfactants, but there are a few studies of non-ionic surfactants showing alignment of elongated micelles.[18-19] As for the ionic systems, alignment of non-ionic elongated micelles was observed and this was shown to be connected to the rheology of the system. As such, $C_{16}E_6$, was shown to form relatively short rod-like micelles that aligned at very high shear rates[18]. On the contrary, a novel class of sugar-based surfactants with a polyethylene glycol linker forms WLM that showed an onset of alignment at much lower shear rates, *ca.* 10 s^{-1}.[19] With this background, we begin to grasp the mechanistic origin of the shear thinning behaviour of WLM systems. However, further investigations are required to elucidate the connection between the nanostructure of the micellar phase and the macroscopic response of the system under flow, especially those composed by non-ionic micelles.

The self-assembly and rheological behaviour of the two anomers of hexadecylmaltoside (α- and β-$C_{16}G_2$) have been previously investigated.[20-21] It was shown that these surfactants form elongated micelles in solution, which results in interesting rheological properties that can be modulated by blending the two anomers. It was also shown that the elongation can be controlled with variation of both concentration and temperature. This possibility to control the micelle morphology, from globular micelles to WLM, allows fine tuning the rheological properties of the system. In this work we use rheo-SANS to investigate the α- and β-$C_{16}G_2$ systems in order to determine the mechanistic origin of the shear thinning behaviour. Here, the effect of shear upon the nanostructure of the system is reported under different conditions (temperature, surfactant concentration, and mixing ratio) and connected to the rheological behaviour of the system.

Experimental

Materials

n-Hexadecyl-α-D-maltopyranoside (α-$C_{16}G_2$) was purchased from Ramidus AB and n-hexadecyl-β-D-maltopyranoside (β-$C_{16}G_2$) was purchased from Anatrace Inc. The purity of these surfactants is ≥97%, as confirmed by HPLC spectroscopy.[20] D_2O was purchased from Sigma Aldrich (99.9% atom-D). Surfactant solutions in D_2O were prepared under mild agitation at 40 °C.

Rheo-SANS

The scattering experiment was conducted on D22 at the Institute Laue-Langevin (Grenoble, France).[22] An Anton Paar MCR 501 rheometer with the SANS set up was used with a Couette geometry (cup diameter 30 mm; cylinder diameter 28 mm, path length 2 mm) as the sample stage.[23] The temperature in the instrument was set to either 30 or 50 ˚C for the experiments performed here. The neutron wavelength was 6 Å and three sample-to-detector distances were used (2.8, 5.6 and 17.6 m) which gives access to a sufficiently wide q-range of 0.002581 – 0.3564 $Å^{-1}$. The data was reduced using the standard protocols of the beamline, accounting for signal of the sample environment, detector efficiency and background noise using the GRASP software.[24]

Data analysis of isotropic and anisotropic scattering data was done in GRASP. Anisotropic scattering was analysed by averaging the scattered intensity from perpendicular angular sectors (vertical or horizontal) with a fixed angle of 18° (Figure 2). The intensity was also studied as a function of azimuthal angle (φ) in a narrow q-range $q^*=0.05 \pm 0.005$. The zero angle was set in the top section of the detector, as marked in Figure 1b, and increases clockwise around the detector. An alignment factor (A_f) was calculated from the angular intensity according to Equation 1.[14]

$$A_f(q^*) = \frac{\int_0^{2\pi} I(q^*,\varphi)\cos(2(\varphi-\varphi_0))d\varphi}{\int_0^{2\pi} I(q^*,\varphi)d\varphi} \qquad (1)$$

where φ_0 is the angle of maximum intensity, which was defined as the angle zero for the integration. The alignment factor is 0 for an isotropic sample and increases up to a maximum value of 1 with increasing nanoscale alignment.

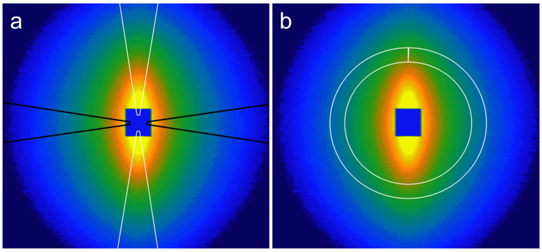

Figure 2. Analysis of anisotropic scattering. (a) vertical (white) and horizontal (black) sectors with an angle of 18° used for averaging anisotropic scattering. (b) section used for the study of intensity as a function of azimuthal angle.

Results and discussion

Previous rheological investigations of α- and β-$C_{16}G_2$ have shown that the rheological behaviour of the system varies with concentration, temperature, and α/β ratio.[20-21] The two anomers show remarkable differences as β-$C_{16}G_2$ solutions were highly viscous and non-Newtonian while α-$C_{16}G_2$ showed a low viscosity and a Newtonian behaviour. The distinct difference in behaviour between the two anomers was hypothesised to arise from the different micellar structure. However, the systems were only investigated in the dilute regime. It was also found that differences in viscosity induced by changes in temperature and composition were observed only at low shear rates. At high shear rates, the differences vanish, and all samples show the same viscosity. Changes in concentration, on the other hand, were found to impact the viscosity over the whole shear rate regime investigated (Figure 3a-c).

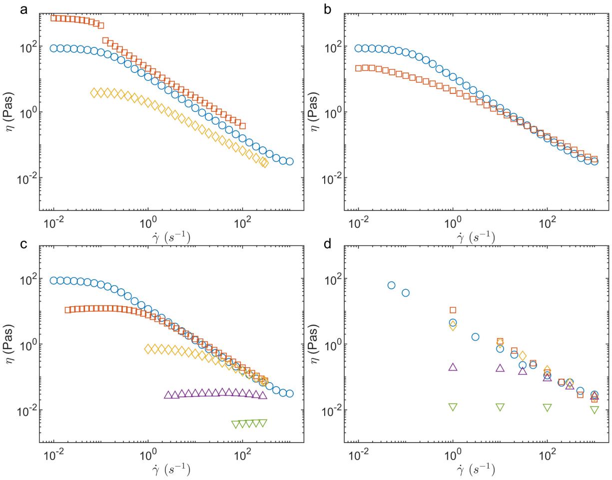

Figure 3. Viscosity versus shear rate for the $C_{16}G_2$ system at different conditions. (a) β-$C_{16}G_2$ at 50 °C at different concentrations in H_2O. 200 (□), 100 (○) and 50 mM (◊). (b) 100 mM β-$C_{16}G_2$ at 50 (○) and 30 °C (□). 100 mM mixtures of α- and β-$C_{16}G_2$ at 50 °C in H_2O (c) and D_2O (d). 100% β (○), 75% β (□), 50% β (◊), 25% β (△) and 0% β (▽). (d) Discrete values of the flow curve at which the rheo-SANS measurements were taken.

In order to reveal the mechanism behind the observed behaviour, rheo-SANS experiments were performed on the systems and the viscosity was measured simultaneously as the SANS data were collected. Initially, the viscosity values at different shears in the rheo-SANS setup were compared to the reported values (Figure 3a, b, c).[21] The flow curves obtained for 100 mM α- $C_{16}G_2$, β-$C_{16}G_2$, and mixtures of those in D_2O at 50 °C are presented in Figure 3d. As previously shown for these surfactants in H_2O,[21] the system evolves from a Newtonian behaviour at 100% α-$C_{16}G_2$ to a shear-thinning fluid at 100% β-$C_{16}G_2$. Some differences in the absolute values of viscosity can be found between the two configurations. This could be attributed to the influence of the isotopic effect from exchanging H_2O for D_2O, as it has been shown to slightly affect micelle structure and result in larger micelles in D_2O.[20, 25-26]

As previously observed in H_2O, the viscosity of all samples falls onto a common "master curve" at high shear rates (>100 s^{-1}),[21] and this behaviour is reproduced also in D_2O. One key difference is the measurement time. For the rheo-SANS measurements each point is measured for at least 15 minutes while for the rheology flow curves this was done for 15 seconds. Thus, the rheo-SANS measurements were particularly useful to reveal any time-dependant behaviour. For most of the samples studied no time dependence was observed except for 200 mM β-$C_{16}G_2$, which shows a thixotropic behaviour at the lower shear rates with a change in viscosity from 1088 to 505 Pas over 30 minutes at a shear rate of 0.05 s^{-1}. This change in the rheological behaviour is observed at the same region where a discontinuity in the flow curve occur (see Figure 3a) and thus likely has the same root cause.

In the rheo-SANS measurements, the main concentration investigated was 100 mM of surfactant (5.6 wt%). For 100% β-$C_{16}G_2$ the scattered neutrons go from an isotropic scattering pattern at low shear rates to a distinct anisotropic pattern at high shear rates, as seen in Figure 4. This is due to the alignment of the WLM in the flow direction, which has been previously observed for WLM subjected to shear.[11] In contrast, no anisotropic scattering is seen for 100 mM α-$C_{16}G_2$ up to shear rates of 1000 s^{-1} (Figure 5).

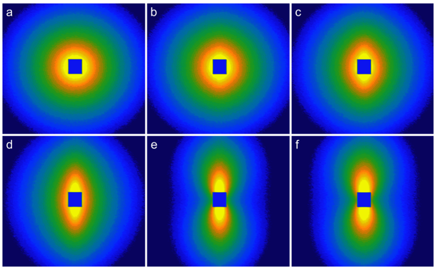

Figure 4. 2D detector images for the 5.6 m sample-to-detector configuration for 100 mM β-$C_{16}G_2$ at 50 °C at different shear rates: (a) 0, (b) 10, (c) 30, (d) 100, (e) 200 and (f) 1000 s^{-1}. High intensity is shown in yellow and low intensity in blue. The blue rectangle in the middle is the beam stop.

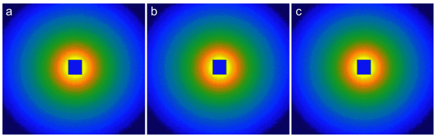

Figure 5. 2D detector image for the 5.6 m sample-to-detector configuration of different shear rates: (a) 0, (b) 100 and (c) 1000 s^{-1} for 100 mM α-$C_{16}G_2$ at 50 °C. High intensity is shown in yellow and low intensity in blue. The blue rectangle in the middle is the beam stop.

This difference between the two surfactants is likely to be directly related to the differences in micelle structure. The rotational diffusion decreases with increasing micelle length, resulting in alignment at lower shear rates for more elongated structures.[27] The results confirm that the micelles formed by β-$C_{16}G_2$ are more elongated than those of α-$C_{16}G_2$, as previously shown for the surfactant in the dilute regime. However, despite big differences in the scattering under flow, the static 1D averaged scattering is surprisingly similar for the two surfactants (Figure 6). We hypothesise that the morphology of the micelles does not undergo significant structural transitions from the dilute to the semi-dilute regime, as judged from the rheology data, and thus β-$C_{16}G_2$ still forms WLM and α-$C_{16}G_2$ shorter rod-like micelles.[21] Therefore, the similarity in the scattering curves is attributed to the influence of the structure factor. As the concentration of micelles increases, the contribution from intermicellar interactions becomes more apparent and incidentally results in scattering curves that look similar. This is also seen for the 100 and 200 mM β-$C_{16}G_2$ as showed in Figure S1.

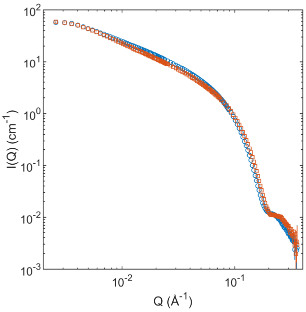

Figure 6. SANS data of 100 mM β-$C_{16}G_2$ (blue ○) and α-$C_{16}G_2$ (red □) at 50 °C under zero shear.

In Figure 7 the scattering in the vertical and horizontal sectors of the 2D data are displayed for 100 mM β-$C_{16}G_2$ at 50 °C under different shear rates. With increasing shear rate the anisotropy of the scattered intensity increases and the difference in intensity between the sectors increases, with the vertical sector showing the highest intensity. At 100 s^{-1} there is an upturn in the intensity in the vertical sector at lower q which is not seen for the horizontal sector. At 1000 s^{-1} this upturn is not as clear, but it is also visible for the horizontal sector. It is suspected that air bubbles are introduced in the sample at high shear rates and that this is the cause of the upturn. Another less likely option is that shear induced structures are formed. Such structures has been seen in other WLM systems, for example for hexadecyltrimethylammonium tosyalte.[28]

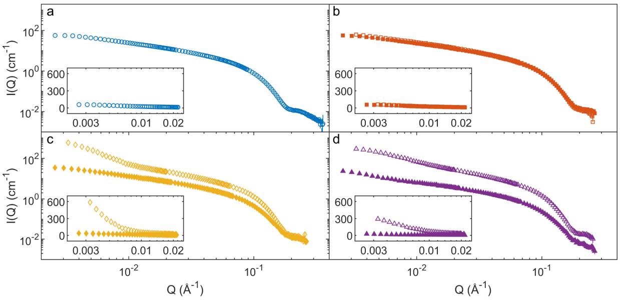

Figure 7. Average intensity from the vertical (unfilled) and horizontal (filled) sectors for 100 mM β-$C_{16}G_2$ at 50 °C. Results shown for shear rates of 0 (blue ○), 10 (red □), 100 (yellow ◊) and 1000 (purple △) s^{-1}.

The intensity as a function of azimuthal angle at q=0.05 ± 0.005 Å for 100 mM β-$C_{16}G_2$ and α-$C_{16}G_2$ at 50 °C and different shear rates is shown in Figure 8a and b. For β-$C_{16}G_2$ the intensity is independent of angle up to a shear rate of 1 s^{-1}. Above that shear rate, the intensity becomes anisotropic showing a maximum at 180° and minima at 90 and 270°. The intensity at the maximum (180°) and at the minima (90 and 270°) increases and decreases, respectively, up to a shear rate of 300 s^{-1}. Above 300 s^{-1}, this trend seems to reverse, as seen in Figure 8c where the difference in intensity at 180° and 90° for different shear rates compared to zero shear is presented. The scattered intensity seems to slightly decrease at the highest shear rates and the effect remains for the subsequent measurement. This drop in maximum intensity at high shear rates has been seen for another sugar-based surfactant system where it was explained as slip at the wall of the geometry.[19] For α-$C_{16}G_2$ the angle-variation in intensity at different shear rates becomes rather small, in stark contrast to the behaviour of β-$C_{16}G_2$ micelles. As the differences in the scattered intensity are so small (see Figure 8c), these could be attributed to subtle segmental alignment of the α-$C_{16}G_2$ short rods.

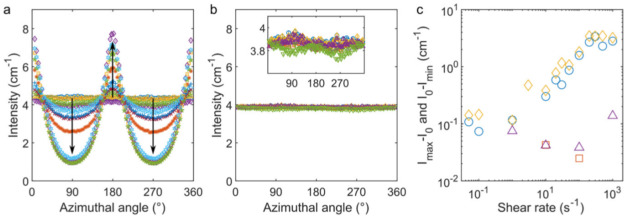

Figure 8. Intensity as a function of azimuthal angle for 100 mM β-$C_{16}G_2$ at 50 °C (a) and 100 mM α-$C_{16}G_2$ at 50 °C (b) for q=0.05 ± 0.005 Å and shear rates from 0 to 1000 s^{-1}. The evolution of the data upon increasing shear follows the direction marked with the black arrows. c) Difference in intensity for different shear rates and at no shear at 180° (β (○) and α (□)) and 90° (β (◊) and α (△)).

In order to relate the scattering anisotropy to changes in the micelle and network structure, the alignment factor (A_f) was calculated from the scattering data using Equation 1. This is presented for 100 mM mixtures of α- and β-$C_{16}G_2$ with different surfactant ratios in Figure 9a.

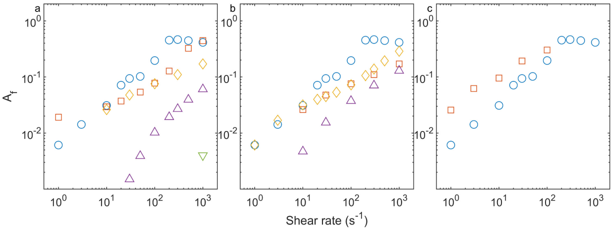

Figure 9. Alignment factor versus shear rate for the $C_{16}G_2$ system in D_2O at different conditions. (a) 100 mM mixtures of α- and β-$C_{16}G_2$ at 50 °C. 100% β (○), 75% β (□), 50% β (◊), 25% β (△) and 0% β (▽). (b) 100 mM 100% β-$C_{16}G_2$ at 50 (○) and 30 °C (□) and 50% β-$C_{16}G_2$ at 50 (◊) and 30 °C (△). (c) β-$C_{16}G_2$ at 50 °C at 200 (□) and 100 mM (○).

As foreseen for the change in 2D scattered intensity, the alignment of micelles occurs when shear is applied to the sample. For all samples containing β-$C_{16}G_2$, A_f increases with increasing shear rate, even at the lowest β-content (i.e. 25% β-$C_{16}G_2$), whilst 100% α-$C_{16}G_2$ only displays minor alignment. For the sample containing 100% β-$C_{16}G_2$, A_f plateaus at *ca.* 0.45 above 200 s^{-1}. This is probably the shear rate at which the micelles reaches equal alignment over the Couette gap, as this has previously been showed for 1.5 wt% mixtures of CTAT and SDBS in D_2O.[14] For the surfactant mixtures, A_f monotonically decreases with decreasing ratio of β-$C_{16}G_2$. The boundary case is obtained for 100 mM α-$C_{16}G_2$ (0% β-$C_{16}G_2$), for which no effective alignment is observed except for the highest measured shear rate, 1000 s^{-1}. This distinct behaviour is attributed to the significantly shorter micelles of α-$C_{16}G_2$ in comparison to the WLM formed by β-$C_{16}G_2$ based on the investigations of the dilute regime.[21] Mixtures of the two anomers form micelles with intermediate contour lengths to those of the pure anomers. These morphological differences are the cause to the distinct alignment in the mixed micelle systems under shear.

A_f is about the same for 50, 75 and 100% β-$C_{16}G_2$ in the surfactant anomer mixture at a shear rate of 10 s^{-1}. At higher shear rates, the alignment for 50 and 75% β-$C_{16}G_2$ is similar, while it is higher for 100% β-$C_{16}G_2$. However, the A_f-values for 25% β-$C_{16}G_2$ are lower than those for higher β-$C_{16}G_2$ ratios in the entire shear rate range.

Some differences between the changes in viscosity and alignment, i.e. A_f-values, with shear rate are observed (See Figure 3). Although high shears clearly induce micelle alignment, for 100 mM β-$C_{16}G_2$ shear thinning starts at shear rates of ca. 0.1 s^{-1} whilst A_f starts to increase around 1 s^{-1}. This could be related to a net alignment in the system on a larger length scale than is accessible in this experiment, while there is still isotropy on a segmental scale.[17]

For the systems showing the same viscosity values upon shear (100, 75 and 50% β-$C_{16}G_2$), the variations in A_f with shear rate show the same trend and a similar slope, but the absolute values are shifted. Considering the Maxwellian behaviour previously reported for these systems,[21] micelle breakage is the dominant relaxation mode for the micelles. As such, micelles with high β-$C_{16}G_2$ content align and break upon shear but they potentially do it in segments of different length, with longer segments at higher β-$C_{16}G_2$ ratios. As the rotational diffusion of longer segments is slower, the segmental alignment is more pronounced for those.

Changes in temperature are also shown to have an effect on micelle behaviour under shear. A_f is lower at 30 °C compared to 50 °C, see Figure 9b. This is again related to micelle morphology, as micelles were seen to increase in length from 30 °C to 50 °C in the dilute regime. Also, 100% β-$C_{16}G_2$ shows higher A_f–values than 50% β-$C_{16}G_2$ at each temperature, indicating similar relaxation mechanism but with different segmental lengths.

A comparison of the alignment of β-$C_{16}G_2$ at two different concentrations (100 and 200 mM) reveals that the onset of alignment starts at lower share rate for the higher concentration, as seen in Figure 9c. The shear rate dependence is similar for the two concentrations between 1 and 100 s^{-1}. The difference in the A_f–values can therefore be related to two factors that influence the rotational diffusion of the micelles: (1) typically the elongation of WLM increases with increasing concentration, and (2) the higher volume fraction of micelles causes more micelle entanglement. For the 200 mM samples, above 100 s^{-1} the anisotropy is lost, and the intensity is drastically decreased for the 200 mM sample (data not shown). This is believed to be caused by the high shear which cause highly turbulent flow for that sample. This effect introduces bubbles which decreased the effective scattering volume inside the Couette.

No evidence was found for shear banding, as has been shown for other WLM systems. Calabrese et. al. demonstrated how shear banding is displayed in the 2D detector images for the 1-3 scattering plane, with a combination of isotropic and anisotropic scattering,[14] which is not seen in this work. Another sign of the absence of shear banding for the systems investigated here is a continuous flow curve without hysteresis, as previously reported.[17] An exception to this is seen at the highest investigated concentration (200 mM). At this concentration a thixotropic behaviour was observed, which might indicate the onset of a shear banding behaviour. However, no direct evidence has been obtained with the characterisation performed here. It is suggested that the presence of branches, instead of entanglement points, in the micelles hinders shear banding.[17] As the structural characterisation was only performed in the dilute regime where no intermicellar interactions are present,[20] there is a possibility that the increased concentration induces micelle branching. The same report also states that branching lowers A_f due to the perpendicular direction of a branch point. This could explain that a higher A_f than 0.45 is not reached.

Conclusions

The self-assembly of hexadecylmaltoside has been shown to act as a rheological modifier, inducing shear-thinning behaviour with tailorable viscosity. Here, we have investigated the origin of this behaviour. Although, it was not possible to determine micelle morphology at high concentration, the variation in micelle alignment suggests that the morphological characterisation in the dilute regime still holds. Upon shear, the entangled network of WLM formed by β-$C_{16}G_2$ begins to align, whilst the shorter rod-like aggregates of α-$C_{16}G_2$ only show weak alignment at very high shear rates. This is connected to the rheology of each system, as the longer micelles result in non-Newtonian behaviour and the shorter aggregates do not modify the rheology of the system. Segmental alignment correlates with the reduction of viscosity in connection to micelle morphology in the surfactant mixtures. A decrease in alignment is observed for decreasing ratio of β-$C_{16}G_2$, which connects to the formation of shorter micelles as seen in the dilute regime.

Variations in concentration and temperature also showed an effect in the resulting rheology that is connected to the micelle structure. At the higher surfactant concentration, the alignment is more pronounced in comparison to the lower concentrated sample. This was attributed to two effects, the formation of longer micelles and a more entangled network at higher surfactant concentration. Temperature induces a similar variation in micelle alignment. Higher temperatures, which have been shown to result in longer micelles, experience earlier and more pronounce alignment upon shear.

Previous rheological characterisation of the system showed that micelle breakage was the dominant relaxation mode upon shear. Based on this rheo-SANS results, the observed alignment arises from the orientation of micelle segments in the direction of the flow. In addition, longer micelles might result in longer segments upon breakage. As longer segments align faster due to their slower rotational diffusion, more pronounced alignment is observed for the systems with neat or higher ratio of β-$C_{16}G_2$. As such, the mechanism of the rheological modification induced by the self-assembly of α- and β-$C_{16}G_2$ is shown to be connected to the nanoscale structure of the micelles. These results provide a detailed understanding on the function-structure relationship of the sugar-based self-assemblies, assisting the development of new technologies, such as response materials and drag-reducing agents, based on these sustainable surfactants.

References

1. von Rybinski, W.; Hill, K., Alkyl Polyglycosides—Properties and Applications of a new Class of Surfactants. *Angewandte Chemie International Edition* **1998**, *37* (10), 1328-1345.
2. Dreiss, C. A., Wormlike micelles: where do we stand? Recent developments, linear rheology and scattering techniques. *Soft Matter* **2007**, *3* (8), 956-970.
3. Ezrahi, S.; Tuval, E.; Aserin, A., Properties, main applications and perspectives of worm micelles. *Advances in Colloid and Interface Science* **2006**, *128-130*, 77-102.
4. Chu, Z.; Dreiss, C. A.; Feng, Y., Smart wormlike micelles. *Chemical Society Reviews* **2013**, *42* (17), 7174-7203.
5. Cates, M., Reptation of living polymers: dynamics of entangled polymers in the presence of reversible chain-scission reactions. *Macromolecules* **1987**, *20* (9), 2289-2296.
6. García, B. F.; Saraji, S., A new insight into the dependence of relaxation time on frequency in viscoelastic surfactant solutions: From experimental to modeling study. *Journal of Colloid and Interface Science* **2018**, *517*, 265-277.
7. Arenas-Gómez, B.; Garza, C.; Liu, Y.; Castillo, R., Alignment of worm-like micelles at intermediate and high shear rates. *Journal of Colloid and Interface Science* **2020**, *560*, 618-625.
8. Takeda, M.; Kusano, T.; Matsunaga, T.; Endo, H.; Shibayama, M.; Shikata, T., Rheo-SANS Studies on Shear-Thickening/Thinning in Aqueous Rodlike Micellar Solutions. *Langmuir* **2011**, *27* (5), 1731-1738.
9. López-Aguilar, J. E.; Webster, M. F.; Tamaddon-Jahromi, H. R.; Manero, O., A new constitutive model for worm-like micellar systems – Numerical simulation of confined contraction–expansion flows. *Journal of Non-Newtonian Fluid Mechanics* **2014**, *204*, 7-21.
10. Eberle, A. P. R.; Porcar, L., Flow-SANS and Rheo-SANS applied to soft matter. *Current Opinion in Colloid & Interface Science* **2012**, *17* (1), 33-43.
11. Calabrese, M. A.; Wagner, N. J., New Insights from Rheo-small-angle Neutron Scattering. In *Wormlike Micelles: Advances in Systems, Characterisation and Applications*, The Royal Society of Chemistry: 2017; pp 193-235.

12. Hayter, J. B.; Penfold, J., Use of viscous shear alignment to study anisotropic micellar structure by small-angle neutron scattering. *The Journal of Physical Chemistry* **1984,** *88* (20), 4589-4593.

13. Förster, S.; Konrad, M.; Lindner, P., Shear Thinning and Orientational Ordering of Wormlike Micelles. *Physical Review Letters* **2005,** *94* (1), 017803.

14. Calabrese, M. A.; Rogers, S. A.; Porcar, L.; Wagner, N. J., Understanding steady and dynamic shear banding in a model wormlike micellar solution. *Journal of Rheology* **2016,** *60* (5), 1001-1017.

15. Helgeson, M. E.; Vasquez, P. A.; Kaler, E. W.; Wagner, N. J., Rheology and spatially resolved structure of cetyltrimethylammonium bromide wormlike micelles through the shear banding transition. *Journal of Rheology* **2009,** *53* (3), 727-756.

16. Divoux, T.; Fardin, M. A.; Manneville, S.; Lerouge, S., Shear Banding of Complex Fluids. *Annual Review of Fluid Mechanics* **2016,** *48* (1), 81-103.

17. Liberatore, M. W.; Nettesheim, F.; Vasquez, P. A.; Helgeson, M. E.; Wagner, N. J.; Kaler, E. W.; Cook, L. P.; Porcar, L.; Hu, Y. T., Microstructure and shear rheology of entangled wormlike micelles in solution. *Journal of Rheology* **2009,** *53* (2), 441-458.

18. Cummins, P. G.; Staples, E.; Penfold, J.; Heenan, R. K., The geometry of micelles of the poly(oxyethylene) nonionic surfactants C16E6 and C16E8 in the presence of electrolyte. *Langmuir* **1989,** *5* (5), 1195-1199.

19. Moore, J. E.; McCoy, T. M.; de Campo, L.; Sokolova, A. V.; Garvey, C. J.; Pearson, G.; Wilkinson, B. L.; Tabor, R. F., Wormlike micelle formation of novel alkyl-tri(ethylene glycol)-glucoside carbohydrate surfactants: Structure–function relationships and rheology. *Journal of Colloid and Interface Science* **2018,** *529*, 464-475.

20. Larsson, J.; Sanchez-Fernandez, A.; Mahmoudi, N.; Barnsley, L. C.; Wahlgren, M.; Nylander, T.; Ulvenlund, S., Effect of the Anomeric Configuration on the Micellization of Hexadecylmaltoside Surfactants. *Langmuir* **2019,** *35* (43), 13904-13914.

21. Larsson, J.; Sanchez-Fernandez, A.; Leung, A. E.; Schweins, R.; Wu, B.; Nylander, T.; Ulvenlund, S.; Wahlgren, M., Molecular structure of maltoside surfactants controls micelle formation and rheological behavior. *Journal of Colloid and Interface Science* **2021,** *581*, 895-904.

22. ILL https://www.ill.eu/users/instruments/instruments-list/d22/description/instrument-layout (accessed 2020-12-07).

23. Anton Paar https://www.anton-paar.com/corp-en/products/details/rheooptics-rheo-sanssaxs-small-angle-neutron-or-x-ray-scattering/ (accessed 2020-12-07).

24. ILL https://www.ill.eu/users/support-labs-infrastructure/software-scientific-tools/grasp/ (accessed 2020-12-07).

25. Ericsson, C. A.; Söderman, O.; Garamus, V. M.; Bergström, M.; Ulvenlund, S., Effects of Temperature, Salt, and Deuterium Oxide on the Self-Aggregation of Alkylglycosides in Dilute Solution. 1. n-Nonyl-β-d-glucoside. *Langmuir* **2004,** *20* (4), 1401-1408.

26. Ericsson, C. A.; Söderman, O.; Garamus, V. M.; Bergström, M.; Ulvenlund, S., Effects of temperature, salt, and deuterium oxide on the self-aggregation of alkylglycosides in dilute solution. 2. n-Tetradecyl-beta-D-maltoside. *Langmuir: The ACS Journal Of Surfaces And Colloids* **2005,** *21* (4), 1507-1515.

27. Keep, G. T.; Pecora, R., Reevaluation of the dynamic model for rotational diffusion of thin, rigid rods in semidilute solution. *Macromolecules* **1985,** *18* (6), 1167-1173.

28. Berret, J.-F.; Gamez-Corrales, R.; Oberdisse, J.; Walker, L.; Lindner, P., Flow-structure relationship of shear-thickening surfactant solutions. *EPL (Europhysics Letters)* **1998,** *41* (6), 677.

Shear-induced nanostructural changes of worm-like micelles formed by sugar-based surfactants

Johan Larsson,[a] Marie Wahlgren,[b,c] Lionel Porcar,[d] Stefan Ulvenlund,[b,c] Tommy Nylander,[a,e] Adrian Sanchez-Fernandez.[b]

[a]Physical Chemistry, Department Chemistry, Lund University, Box 124, 221 00 Lund, Sweden.

[b]Food Technology, Nutrition and Engineering, Lund University, Box 124, 221 00 Lund, Sweden.

[c]Enza Biotech AB, Scheelevägen 22, 22363 Lund, Sweden.

[d]Institut Laue-Langevin, DS / LSS, 71 avenue des Martyrs, 38000, Grenoble, France.

[e]NanoLund, Lund University, Lund, Sweden

The static 1D averaged scattering for 100 and 200 mM β-$C_{16}G_2$ is showed in Figure S1. In the mid- and high-q range, the form factor looks similar and the intensity is higher for the 200 mM sample. At low q the scattered intensity is the same for the two concentrations. This is probably an effect of a higher contribution from the structure factor, as expected from a higher concentration.

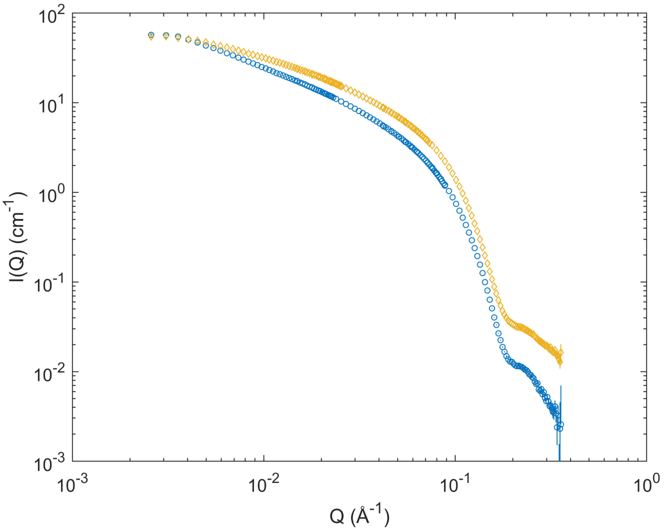

Figure S1. Static SANS of 100 (blue ○) and 200 mM (yellow ◊) β-$C_{16}G_2$ at 50 °C.

Paper IV

Tail unsaturation tailors the thermodynamics and rheology of a self-assembled sugar-based surfactant

J. Larsson, A. E. Leung, C. Lang, B. Wu, M. Wahlgren, T. Nylander, S. Ulvenlund, A. Sanchez-Fernandez

Journal of Colloid and Interface Science **2021**, 585, 178-183

Journal of Colloid and Interface Science 585 (2021) 178–183

Contents lists available at ScienceDirect

Journal of Colloid and Interface Science

journal homepage: www.elsevier.com/locate/jcis

Short Communication

Tail unsaturation tailors the thermodynamics and rheology of a self-assembled sugar-based surfactant

Johan Larsson [a], Anna E. Leung [b], Christian Lang [c], Baohu Wu [c], Marie Wahlgren [d], Tommy Nylander [a,e], Stefan Ulvenlund [d,f], Adrian Sanchez-Fernandez [d,*]

[a] Physical Chemistry, Department of Chemistry, Box 124, 221 00 Lund, Sweden
[b] European Spallation Source, Box 176, 221 00 Lund, Sweden
[c] Jülich Centre for Neutron Science (JCNS) at Heinz Maier-Leibnitz Zentrum (MLZ), Forschungszentrum Jülich GmbH, Lichtenbergstr. 1, 85748 Garching, Germany
[d] Food Technology, Engineering and Nutrition, Box 124, 221 00 Lund, Sweden
[e] NanoLund, Lund University, Box 124, 221 00 Lund, Sweden
[f] EnzaBiotech AB, Scheelevägen 22, 22363 Lund, Sweden

GRAPHICAL ABSTRACT

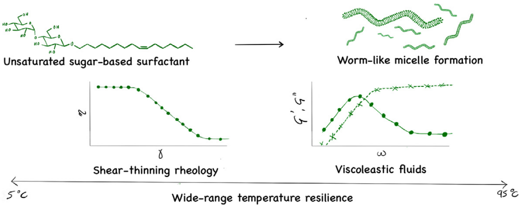

ARTICLE INFO

Article history:
Received 22 October 2020
Revised 16 November 2020
Accepted 17 November 2020
Available online 21 November 2020

Keywords:
Unsaturated surfactant
Sugar-based surfactant
Worm-like micelle
Viscoelastic fluid
Small-angle scattering

ABSTRACT

Hypothesis: The self-assembly of long-tail surfactants results in the formation of nanoscale structures, e.g. worm-like micelles, with the ability to modify the rheology of the system. However, micelle formation, and thus the alteration of the rheology, is subject to the high Krafft temperature of saturated long-tail surfactants. Hexadecylmaltosides are sustainable surfactants that, in solution, form tailorable viscoelastic fluids. The preparation of monounsaturated sugar-based surfactants is hypothesised to reduce the Krafft point compared to the saturated analogues, therefore increasing the temperature range where the surfactant remains in the micellar form.

Experiments: Here we report the synthesis and characterisation of a novel sugar-based surfactant with an unsaturated C16-tail, namely palmitoleyl-β-D-maltoside (β-$C_{16\text{-}1}G_2$). Differential scanning calorimetry was used to probe the temperature stability of the system. The rheology of β-$C_{16\text{-}1}G_2$ solutions was investigated by means of rotational and oscillatory rheology, and these results were connected to the mesoscopic structure of the system as shown by small-angle neutron and X-ray scattering, and dynamic light scattering.

Findings: The presence of a double bond on the alkyl chain moiety leads to a depression in the Krafft point, allowing the surfactant to form a thermodynamically stable micellar solution over a wide range

---

* Corresponding author.
E-mail address: adrian.sanchez-fernandez@food.lth.se (A. Sanchez-Fernandez).

https://doi.org/10.1016/j.jcis.2020.11.063

of temperatures, i.e. 5–95 °C. The surfactant self-assembles into worm-like micelles which, upon entanglement in the semi-dilute regime, result in the formation of a non-Newtonian, viscoelastic fluid. These observations have important implications in the development of new sustainable formulated products, enabling the preparation of surfactant phases with remarkable thermal resilience.

1. Introduction

The morphology of surfactant self-assemblies can be described in terms of the monomer packing, expressed as the so-called critical packing parameter, which in turn gives the preferred curvature of the surfactant at the interface with the solvent [1]. Apart from the common morphologies for the micelles (e.g. spherical, ellipsoidal, and cylindrical), surfactants can self-assemble into very long semiflexible aggregates, called worm-like micelles (WLM) [2]. The most studied group of WLM-forming surfactants are ionic surfactants in salt solutions, where the electrostatic repulsion between the headgroups of the surfactants is screened by the salt, decreasing the average micelle curvature [3,4]. High concentrations of surfactants in these solutions result in entangled networks of WLM. These systems show viscoelasticity, which is important for several applications, e.g. modification of the rheological properties of formulated products [5,6].

The surfactants prone to forming the most elongated micelles and, thus, the most viscous aqueous solutions are those with long alkyl chains (≥16). However, those surfactants also show the lowest solubility and the highest Krafft points, which limits their use in technological applications at room temperature [7]. Amphiphilic molecules with a double bond in the alkyl chain show higher solubility in water and lower Krafft points compared to the saturated analogues [8]. The inclusion of a chain unsaturation thus allows for the self-assembly of long-tail surfactants (e.g. up to 22 carbons) into micellar structures over a wider temperature range. Raghavan et al. reported the behaviour of monounsaturated C_{22} cationic surfactants with very low Krafft points (<0 °C) [9]. The change in the rheological behaviour, associated with the formation of entangled WLM, was induced by the addition of salts and the viscoelasticity was retained up to high temperatures (90 °C). The synthesis and self-assembly of unsaturated C_{18} betaines were studied by Kelleppan et al., showing that a monounsaturated tail leads to a reduction of the Krafft point from 50 °C for the saturated surfactant analogue to below 2.5 °C for the unsaturated surfactant [10]. This allowed the system to form WLM at room temperature and display non-Newtonian behaviour. Moore et al. have studied long-chain unsaturated surfactants with sugar units as the headgroup and a polyethylene glycol linker between the headgroup and tail [11,12]. The Krafft point was observed to be lower when the alkyl tail contained a double bond compared to a saturated chain. This allowed surfactants with up to C_{22} tails to remain soluble at room temperature and to form viscous WLM solutions.

Since society is striving towards using more environmentally friendly products, it is important to find surfactants that can be manufactured from renewable raw materials. Indeed, sugar-based surfactants can be produced by sustainable means and have rich self-assembly behaviour [13]. The self-assembly behaviour and rheological properties of hexadecylmaltosides in aqueous solutions have recently been shown to strongly depend on the anomeric configuration of the surfactant [14,15]. In particular, it was shown that the equatorial configuration of the headgroup (β) leads to the formation of WLM with remarkable viscoelastic properties [15]. However, these surfactants were found to have a Krafft point above room temperature, thus limiting their possible technological applicability. Here, for the first time, the synthesis and characterisation of an unsaturated-tail sugar-based surfactant, palmitoleyl-β-D-maltoside (β-$C_{16\text{-}1}G_2$), is presented. The characteristic transition temperatures, rheological behaviour and micelle structure for this surfactant in aqueous solution were studied and compared to the saturated analogue, hexadecyl-β-D-maltoside (β-$C_{16}G_2$).

2. Results and discussion

Fig. 1a shows the molecular structure of the synthesised surfactant palmitoleyl-β-D-maltoside. Details of the synthesis and NMR spectroscopic data are included in the ESI. The temperature at which an aqueous solution of 50 mM β-$C_{16\text{-}1}G_2$ dissolves was characterised using differential scanning calorimetry (DSC) and compared to the same concentration of the saturated analogue, β-$C_{16}G_2$. Fig. 1b presents the DSC thermogram of 50 mM β-$C_{16\text{-}1}G_2$ and 50 mM β-$C_{16}G_2$ between 5 and 95 °C.

The DSC results do not show any change in heat capacity, Cp, between 95 °C and 5 °C for 50 mM of the unsaturated β-$C_{16\text{-}1}G_2$, while a peak for the saturated β-$C_{16}G_2$ is observed around 27 °C. This peak is associated with the dissolution enthalpy of the saturated surfactant at this concentration. No peak was observed for β-$C_{16\text{-}1}G_2$, as this surfactant remains dissolved even after storing the surfactant solution at 4 °C for several weeks. This behaviour was visually confirmed for all the different β-$C_{16\text{-}1}G_2$ concentrations prepared during this study, i.e. from 1 mM to 100 mM. These results confirm that one of the key features of the tail unsaturation, i.e. the lowering of the Krafft point relative to the saturated analogue, applies to sugar-based surfactants in the same way as has

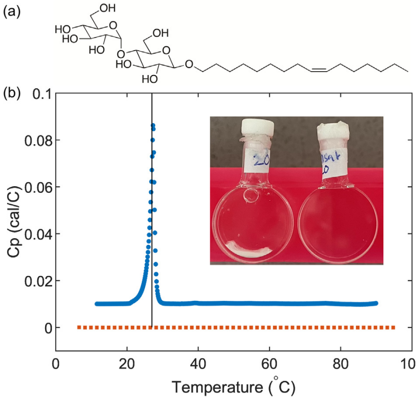

Fig. 1. (a) Molecular structure of β-$C_{16\text{-}1}G_2$ and (b) DSC thermogram of 50 mM β-$C_{16\text{-}1}G_2$ (■) and 50 mM β-$C_{16}G_2$ (●). The black vertical line marks the Krafft temperature of β-$C_{16}G_2$ at 27 °C. Inset: Photograph of aqueous solutions of 20 mM β-$C_{16}G_2$ (left) and 20 mM β-$C_{16\text{-}1}G_2$ (right) after 72 h stored at room temperature.

been previously reported for ionic [9], zwitterionic [10], and ethoxylated non-ionic surfactants [11].

One of the macroscopic fingerprints of WLM formation is the non-Newtonian character of the fluid. The behaviour of a 100 mM β-C$_{16\text{-}1}$G$_2$ solution at 25 °C was therefore probed using linear and oscillatory rheology. In addition, the tensile strength of a 100 mM β-C$_{16\text{-}1}$G$_2$ sample was characterised using tensile strength texture analysis at 25 °C and these results were compared with those from a 100 mM β-C$_{16}$G$_2$ sample. The results from the rheological and mechanical characterisation of the surfactant solutions are shown in Fig. 2.

The flow curve shows that the system is a viscous, non-Newtonian shear thinning liquid with a zero-shear viscosity of 150 Pas (Fig. 2a). At increasing shear, the micelles align in the direction of the flow, decreasing the number of entanglement points and thus also the viscosity. The reproducible jump in viscosity at shear rates of 0.2–0.3 s^{-1} indicates the presence of a yield point. We hypothesise that this change in the viscosity might indicate a regime with thixotropic behaviour, but further investigation is required to elucidate the origin of this. The oscillatory rheology results (Fig. 2b) display a viscoelastic behaviour, where the viscous modulus (G″) is dominant at low frequencies and the elastic modulus (G′) is dominant at high frequencies. The relaxation time (τ) can be calculated from the inverse of the angular frequency (ω) where G′ = G″ (i.e. 13.5 Pa), yielding τ = 5 s. The Maxwellian model (see ESI) fits relatively well to the data (Fig. 2c). This strongly indicates that the system can be described using a single relaxation time as the network relaxation is dominated by micelle breakage rather than reptation [16]. The small deviation of G′ at high frequencies reveals that the system is not perfectly Maxwellian. There is also a deviation from the model for G″ at high frequencies. This is a common deviation for WLM systems and is attributed to the presence of fast relaxation modes that are not accounted for in the Maxwell model (e.g. stretching and cross-sectional fluctuations) [17].

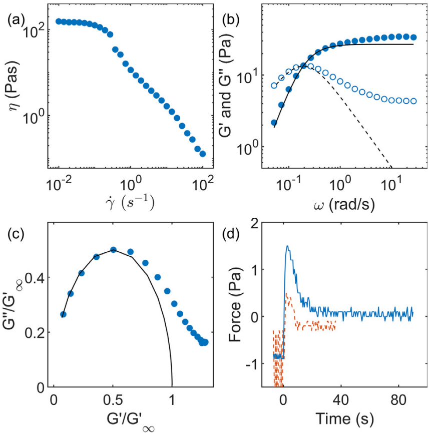

Fig. 2. Rheological and mechanical properties of an aqueous solution of 100 mM β-C$_{16\text{-}1}$G$_2$ at 25 °C. (a) Viscosity as a function of shear rate. (b) Oscillatory shear frequency sweep results and fits for a strain of 10%: Elastic modulus G′ (●), viscous modulus G″ (○). The solid and dashed lines are the Maxwell model fit of G′ and G″, respectively. (c) Normalized Cole-Cole plot with the black line showing the Maxwell fit. (d) Tensile strength texture analysis of 100 mM of the unsaturated β-C$_{16\text{-}1}$G$_2$ at 25 °C (blue solid line) and 100 mM of the saturated β-C$_{16}$G$_2$ at 50 °C (red dashed line).

The rheological properties of β-C$_{16\text{-}1}$G$_2$ resemble that of β-C$_{16}$G$_2$ in the sense that it is both shear-thinning and viscoelastic [15]. The zero-shear viscosity is slightly higher for β-C$_{16\text{-}1}$G$_2$ than for β-C$_{16}$G$_2$ (86 Pas), but upon shearing the viscosity becomes very similar for both surfactants. The yield point is also seen for both systems, but at higher concentrations for β-C$_{16}$G$_2$ (200 mM) [15]. Interestingly, the viscoelastic properties of β-C$_{16\text{-}1}$G$_2$ are better described with the Maxwell model than those of β-C$_{16}$G$_2$. This is most evident at high frequencies, where G″ displays a more distinct decrease and G′ is closer to reaching a plateau for β-C$_{16\text{-}1}$G$_2$ than β-C$_{16}$G$_2$ [15]. As the relaxation time of both systems is similar, the origin of this difference could be attributed to the micelle internal dynamics (e.g. β-C$_{16\text{-}1}$G$_2$ break faster than the β-C$_{16}$G$_2$) [18]. The rheological properties of five unsaturated non-ionic surfactants that form viscoelastic WLM solutions at room temperature were reported by Moore et al. [12]. Two of these, referred to as Glc-EO4-C22:1 and Gal-EO3-C18:1 in the original report, have a longer relaxation time (*ca.* 200 and 25 s respectively) than β-C$_{16\text{-}1}$G$_2$, even at lower concentrations (19.2 and 25.6 mM). An explanation for the remarkable rheological behaviour of these surfactants can be attributed to their long alkyl tail (C$_{22}$ and C$_{18}$), which promotes the formation of more elongated and entangled WLM than those reported here.

Despite the close similarities observed by the linear and oscillatory rheology measurements of the two systems compared here, an obvious difference in properties is that on visual inspection the unsaturated surfactant solutions appear to have a notably more "stringy" flow behavioud than the saturated counterpart. To quantify this difference, tensile strength texture analysis was employed. In this method, the force required to lift a probe from a sample solution is measured as a function of the distance travelled. The data reveal that a significantly larger force is required to lift the probe from the 100 mM β-C$_{16\text{-}1}$G$_2$ solution compared to the 100 mM β-C$_{16}$G$_2$ solution (Fig. 2d). Furthermore, the β-C$_{16\text{-}1}$G$_2$ solution sticks to the probe, resulting in the formation of a liquid column even when the probe is several centimetres above the surface of the solution, see Fig. S11. This behaviour is not seen for β-C$_{16}$G$_2$ where the contact between the sample and the probe is lost immediately when the probe is lifted above the surface of the solution. It is noteworthy that this stark difference in behaviour is not captured in the other rheological properties of the system and that it cannot be correlated to the current structural models of the micelles in the dilute regime. However, it may be hypothesised that the "slimy" and "stringy" character of the unsaturated surfactant solutions could be attributed to the formation of transient micellar structures induced by the extensional flow [19].

The non-Newtonian character of sugar-based surfactant solutions has been previously attributed to the formation and entanglement of WLM [15,20]. In order to probe the origin of the non-Newtonian behaviour for the unsaturated surfactant, the structure of β-C$_{16\text{-}1}$G$_2$ micelles was determined using small-angle neutron scattering (SANS), small-angle X-ray scattering (SAXS) and dynamic light scattering (DLS). SANS and SAXS data, together with the DLS results, are presented in Fig. 3.

At 10 mM surfactant concentration, the system is expected to be in the dilute regime, as previously reported for the saturated analogue [15]. Under these conditions, the structure of the micelles could be extracted with no need to account for intermicellar interactions. The results from the structural characterisation of the β-C$_{16\text{-}1}$G$_2$ micelles reveal the formation of WLM with an average contour length of 9200 ± 600 Å and a persistence length of the rigid domains of the micelle of 215 ± 5 Å. The size of the micelle cross-section was found to be 15.1 ± 0.2 Å for the radius of the hydrophobic core and 14.5 ± 0.3 Å for the thickness of the solvated headgroup layer. DLS results show that the micelle structure is

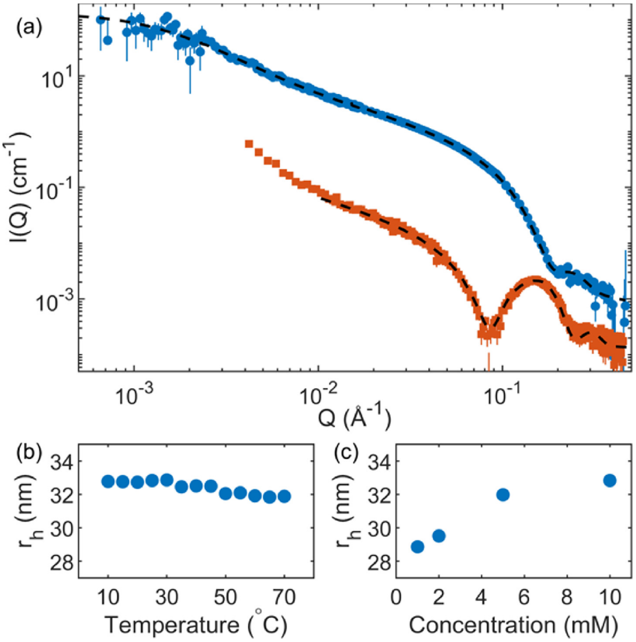

Fig. 3. (a) SAXS (■) and SANS (●) data and best fits of 10 mM β-$C_{16\text{-}1}G_2$ at 50 °C in H_2O and D_2O, respectively. The black dashed lines represent the fits using the core–shell ellipsoid to the SAXS data and flexible cylinder model to the SANS data. Hydrodynamic radius (r_h) for 10 mM β-$C_{16\text{-}1}G_2$ in H_2O (b) at different temperatures and (c) for different concentrations of β-$C_{16\text{-}1}G_2$ at 25 °C. Where not visible, error bars are within the marker size.

hardly affected by temperature changes (Fig. 3b), but there is a slight increase in micellar size with increasing concentration (Fig. 3c), potentially associated with a change in the contour length [14]. Furthermore, the headgroup solvation, i.e. the volume fraction of solvent in the headgroup region, was calculated from the fitted scattering length density of the headgroup region (X-ray SLD: $10.6 \pm 0.1 \times 10^{-6}$ Å^{-2}) and resulted in a value of 0.73 ± 0.03.

Interestingly, the contour length of the β-$C_{16\text{-}1}G_2$ micelles was found, within the experimental error, to be the same as that of the β-$C_{16}G_2$ micelles (8600 ± 200 Å). The micelle cross-section was found to be slightly smaller in the case of the unsaturated surfactant compared to that of the saturated analogue (15.5 ± 0.1 Å core radius and 16.2 ± 0.1 Å shell thickness) [15]. The differences in the cross-section are potentially attributed to changes in the conformational entropy of the tail domain (i.e. monomer packing) between the unsaturated and saturated surfactants, as observed for lipid bilayers [21]. These structural similarities are consistent with both surfactants having a similar rheological behaviour, such as the same relaxation time. The main structural difference is observed in the micelle flexibility, where the persistence length of the β-$C_{16\text{-}1}G_2$ micelles is significantly shorter than that of the β-$C_{16}G_2$ micelles (316 ± 10 Å) [15]. This difference may be attributed to the difference in the cross-sectional size of the micelles, where a thicker micelle requires more energy to bend and thus promotes a longer persistence length due to geometrical constraints [22].

3. Conclusions

The synthesis and behaviour of the first unsaturated sugar-based surfactant in aqueous solution are reported. The preparation of a maltoside surfactant with a C_{16} monounsaturated tail (9Z) prompted a significant reduction of the Krafft point compared to the saturated counterpart [14]. Unlike other non-ionic surfactant systems [23], the solutions of β-$C_{16\text{-}1}G_2$ are not affected by clouding at high temperatures. This allowed the palmitoleyl surfactant to remain soluble from just above 0 °C up to almost 100 °C. Solutions of this surfactant show a marked non-Newtonian character, as the micellar phase leads to the formation of a viscoelastic fluid of Maxwellian character. This behaviour mimics that of the saturated surfactant at similar concentrations, with the exception of the apparent stringiness quantified by the tensile strength texture analysis [15]. Structural analysis of the micelles using a combination of scattering techniques revealed the formation of worm-like micelles, which are present in a wide range of concentrations and temperatures. The dimensions of the palmitoleyl micelles were found to be similar to those of the saturated analogue [14,15]. However, the aggregates of the palmitoleyl surfactant are more flexible than those of the saturated surfactant, which could relate to the differences in the rheological behaviour.

The greatest advantage of the preparation of sugar-based surfactants with unsaturated long tails is that it facilitates the preparation of viscosity modifiers that remain soluble in a wide temperature range, i.e. from the freezing point to the boiling point of water. This work contributes to the elaboration of a library of amphiphiles with potential applications in a variety of technologies, e.g. formulation technology and stimuli-responsive materials, with the advantage of presenting relatively simple synthetic procedure and sustainable character [11,12]. Furthermore, these results expand the possibilities of developing sugar-based surfactants where the micro- and macroscopic behaviour of the system is finely tuned through changes in the molecular structure of the surfactant, e.g. changes in the anomeric configuration and degree of tail saturation, with minimal or no change in the chemical composition of the system [14,15,24,25].

4. Experimental section

Palmitoleyl-β-D-maltoside ((*Z*)-Hexadec-9-en-1-yl-β-D-maltoside, β-$C_{16\text{-}1}G_2$) was synthesized and characterised (^{1}H, ^{13}C NMR spectroscopy, and mass spectrometry) at the Deuteration and Macromolecular Crystallisation DEMAX platform (ESS, Sweden). β-$C_{16\text{-}1}G_2$ was synthesised according to literature procedures for the *n*-dodecyl analogue [26], via a Koenigs-Knorr glycosylation reaction between 2,3,6,2′,3′,4′,6′-hepta-O-acetyl-α-D-maltosyl bromide and palmitoleyl alcohol, followed by hydrolysis of the acetyl groups. Palmitoleyl alcohol was produced from palmitoleic acid, using the standard reducing reagent lithium aluminium hydride. *n*-Hexadecyl-β-D-maltoside (β-$C_{16}G_2$) was purchased from Anatrace Inc. Water of Milli-Q purity and D_2O (Sigma Aldrich, 99.9% D) were used in the experiments presented here.

DSC measurements were performed on a MicroCal VP-DSC instrument using a scan rate of 30 °C/h between 5 °C and 95 °C, and water as the reference. Linear and oscillatory rheology was performed on an Anton Paar MCR 301 at 25 °C using a cone-plate geometry with a cone diameter of 25 mm, a cone angle of 1° and a gap of 0.048 mm. The flow curves were recorded in a shear rate range between 0.01 and 100 s^{-1} with 7 measurements per decade. The linear viscoelastic region (LVER) was determined (see ESI), and subsequent experiments were conducted at a constant strain of 10% over the angular frequency range of 0.05–100 rad/s. Tensile strength texture analysis was conducted using a TA.XT2i instrument, Stable Micro Systems, with a hemispherical cylinder probe with a diameter of 6 mm. The applied force on the probe was 1 g and the trigger force was 1 g which submerged the probe in the sample. After 60 s the probe was lifted from the solution with a speed of 1 mm/s and the force required was recorded.

The hydrodynamic radius of the micelles (r_h) was determined using a Zetasizer Nano-ZS, Malvern Instruments Ltd. Measurements were performed at temperatures between 70 °C and 10 °C, with 5 °C steps. Samples were equilibrated for 5 min at each temperature and triplicates were measured for each data point. Correlation functions showed a single exponential decay and, thus, data were analysed using the cumulants method.

SAXS experiments were performed on a SAXSlab Ganesha pinhole instrument, JJ X-ray System Aps, equipped with a Xenocs X-ray microsource and a two-dimensional 300 k Pilatus detector, Dectris Ltd. Images were collected at two given sample-to-detector distances using a wavelength of $\lambda = 1.54$ Å. The configurations gave a combined momentum transfer (Q) range of 0.004–0.75 Å^{-1}. The azimuthally averaged intensities (I(Q)) were subtracted for the contribution of the solvent and sample stage and put to absolute scale by calibration against water.

SANS experiments were performed at the Heinz Maier-Leibnitz Zentrum, (MLZ) on the KWS-3 and KWS-2 instrument (Garching, Germany) [27,28]. On KWS-3 the wavelength of the neutrons was 12.8 Å, and two different sample-to-detector distances were used, 1.15 and 9.15 m. On KWS-2 three detector distances were used (2, 8 and 20 m) and the wavelength of the neutrons was 5 Å for 2 and 8 m and 10 Å for 20 m. The samples were loaded in quartz cuvettes with a 2-mm path length and measured at 50 °C. The raw data were reduced according to the protocol of each beamline and solvent contribution was subtracted to obtain the output files in (I(Q), in absolute intensity, vs. Q. Data from the two instruments were merged, yielding a combined Q range of 0.000183–0.0187 Å^{-1}.

Simultaneous analysis of the SAXS and SANS data was performed in SasView 4.2.2 by fitting to flexible cylinder and core–shell cylinder form factor models [29–31], conforming to the micellar shape, as previously reported for WLM of sugar-based surfactants [14].

For further details on the surfactant synthesis, experimental considerations and data analysis refer to the ESI.

CRediT authorship contribution statement

Johan Larsson: Methodology, Investigation, Formal analysis, Writing - original draft, Writing - review & editing, Visualization. **Anna E. Leung:** Investigation, Resources, Writing - review & editing. **Christian Lang:** Investigation, Resources, Writing - review & editing. **Baohu Wu:** Investigation, Resources. **Marie Wahlgren:** Methodology, Investigation, Writing - review & editing, Funding acquisition. **Tommy Nylander:** Investigation, Writing - review & editing, Funding acquisition. **Stefan Ulvenlund:** Investigation, Writing - review & editing, Funding acquisition. **Adrian Sanchez-Fernandez:** Conceptualization, Methodology, Investigation, Formal analysis, Writing - original draft, Writing - review & editing.

Declaration of Competing Interest

The authors declare that they have no known competing financial interests or personal relationships that could have appeared to influence the work reported in this paper.

Acknowledgements

The Authors would like to thank the Swedish Research Council Formas (Grant 2015-666) for funding J.L. The research was also performed with financial support from Vinnova - Swedish Governmental Agency for Innovation Systems within the NextBioForm Competence Centre. This project has received funding from the European Union's Horizon 2020 research and innovation programme under grant agreement No 731019 (EUSMI). This work is based upon experiments performed on the KWS-2 and KWS-3 instruments, operated by JCNS at the Heinz Maier-Leibnitz Zentrum (MLZ), Garching, Germany (Proposal No. 16341 and 15556). This work benefited from the use of the SasView application, originally developed under NSF award DMR-0520547. SasView contains code developed with funding from the European Union's Horizon 2020 research and innovation programme under the SINE2020 project, grant agreement No 654000.

Appendix A. Supplementary material

Supplementary data to this article can be found online at https://doi.org/10.1016/j.jcis.2020.11.063.

References

[1] J.N. Israelachvili, D.J. Mitchell, B.W. Ninham, Theory of self-assembly of hydrocarbon amphiphiles into micelles and bilayers, J. Chem. Soc., Faraday Trans. 2 (72) (1976) 1525.

[2] M.E. Cates, S.J. Candau, Statics and dynamics of worm-like surfactant micelles, J. Phys.: Condens. Matter 2 (33) (1990) 6869–6892.

[3] G. Porte, J. Appell, Y. Poggi, Experimental investigations on the flexibility of elongated cetylpyridinium bromide micelles, J. Phys. Chem. 84 (23) (1980) 3105–3110.

[4] L.J. Magid, Z. Li, P.D. Butler, Flexibility of elongated sodium dodecyl sulfate micelles in aqueous sodium chloride: a small-angle neutron scattering study, Langmuir 16 (26) (2000) 10028–10036.

[5] J. Yang, Viscoelastic wormlike micelles and their applications, Curr. Opin. Colloid Interface Sci. 7 (5) (2002) 276–281.

[6] Z. Chu, C.A. Dreiss, Y. Feng, Smart wormlike micelles, Chem. Soc. Rev. 42 (17) (2013) 7174–7203.

[7] C.A. Dreiss, Wormlike micelles: where do we stand? Recent developments, linear rheology and scattering techniques, Soft Matter 3 (8) (2007) 956–970.

[8] C. Tanford, The Hydrophobic Effect: Formation of Micelles and Biological Membranes, John Wiley & Sons Inc, New York, 1980.

[9] S.R. Raghavan, E.W. Kaler, Highly viscoelastic wormlike micellar solutions formed by cationic surfactants with long unsaturated tails, Langmuir 17 (2) (2001) 300–306.

[10] V.T. Kelleppan, J.E. Moore, T.M. McCoy, A.V. Sokolova, L.D. Campo, B.L. Wilkinson, R.F. Tabor, Self-assembly of long-chain betaine surfactants: effect of tailgroup structure on wormlike micelle formation, Langmuir 34 (3) (2018) 970–977.

[11] J.E. Moore, T.M. McCoy, L. de Campo, A.V. Sokolova, C.J. Garvey, G. Pearson, B.L. Wilkinson, R.F. Tabor, Wormlike micelle formation of novel alkyl-tri(ethylene glycol)-glucoside carbohydrate surfactants: structure–function relationships and rheology, J. Colloid Interface Sci. 529 (2018) 464–475.

[12] J.E. Moore, T.M. McCoy, A.V. Sokolova, L. de Campo, G.R. Pearson, B.L. Wilkinson, R.F. Tabor, Worm-like micelles and vesicles formed by alkyl-oligo (ethylene glycol)-glycoside carbohydrate surfactants: the effect of precisely tuned amphiphilicity on aggregate packing, J. Colloid Interface Sci. 547 (2019) 275–290.

[13] W. von Rybinski, K. Hill, Alkyl polyglycosides—properties and applications of a new class of surfactants, Angew. Chem. Int. Ed. 37 (10) (1998) 1328–1345.

[14] J. Larsson, A. Sanchez-Fernandez, N. Mahmoudi, L.C. Barnsley, M. Wahlgren, T. Nylander, S. Ulvenlund, Effect of the anomeric configuration on the micellization of hexadecylmaltoside surfactants, Langmuir 35 (43) (2019) 13904–13914.

[15] J. Larsson, A. Sanchez-Fernandez, A.E. Leung, R. Schweins, B. Wu, T. Nylander, S. Ulvenlund, M. Wahlgren, Molecular structure of maltoside surfactants controls micelle formation and rheological behavior, J. Colloid Interface Sci. 581 (2021) 895–904.

[16] M.E. Cates, Reptation of living polymers: dynamics of entangled polymers in the presence of reversible chain-scission reactions, Macromolecules 20 (9) (1987) 2289–2296.

[17] J.F. Berret, J. Appell, G. Porte, Linear rheology of entangled wormlike micelles, Langmuir 9 (11) (1993) 2851–2854.

[18] M.E. Cates, Dynamics of living polymers and flexible surfactant micelles : scaling laws for dilution, J. Phys. France 49 (9) (1988) 1593–1600.

[19] D. Sachsenheimer, C. Oelschlaeger, S. Müller, J. Küstner, S. Bindgen, N. Willenbacher, Elongational deformation of wormlike micellar solutions, J. Rheol. 58 (6) (2014) 2017–2042.

[20] B.F. García, S. Saraji, A new insight into the dependence of relaxation time on frequency in viscoelastic surfactant solutions: from experimental to modeling study, J. Colloid Interface Sci. 517 (2018) 265–277.

[21] M. Deleu, M. Paquot, T. Nylander, Effect of fengycin, a lipopeptide produced by bacillus subtilis, on model biomembranes, Biophys. J. 94 (7) (2008) 2667–2679.

[22] J. Appell, G. Porte, Y. Poggi, Quantitative estimate of the orientational persistence length of flexible elongated micelles of cetylpyridinium bromide, J. Colloid Interface Sci. 87 (2) (1982) 492–499.

[23] P.O. Cummins, J.B. Hayter, J. Penfold, E. Staples, A small-angle neutron scattering investigation of shear-aligned hexaethyleneglycolmonohexadecylether (C16E6) micelles as a function of temperature, Chem. Phys. Lett. 138 (5) (1987) 436–440.

[24] C.A. Ericsson, O. Söderman, S. Ulvenlund, Aggregate morphology and flow behaviour of micellar alkylglycoside solutions, Colloid. Polym. Sci. 283 (12) (2005) 1313–1320.

[25] F. Nilsson, O. Söderman, I. Johansson, Four different C8G1Alkylglucosides. anomeric effects and the influence of straight vs branched hydrocarbon chains, J. Colloid Interface Sci. 203 (1) (1998) 131–139.

[26] S.R. Midtgaard, T.A. Darwish, M.C. Pedersen, P. Huda, A.H. Larsen, G.V. Jensen, S.A.R. Kynde, N. Skar-Gislinge, A.J.Z. Nielsen, C. Olesen, M. Blaise, J.J. Dorosz, T. S. Thorsen, R. Venskutonytė, C. Krintel, J.V. Møller, H. Frielinghaus, E.P. Gilbert, A. Martel, J.S. Kastrup, P.E. Jensen, P. Nissen, L. Arleth, Invisible detergents for structure determination of membrane proteins by small-angle neutron scattering, The FEBS J. 285 (2) (2018) 357–371.

[27] V. Pipich, Z. Fu, KWS-3: Very small angle scattering diffractometer with focusing mirror, J. Large-scale Res. Facilities JLSRF 1 (2015) 31.

[28] A. Radulescu, N.K. Székely, M.-S. Appavou, KWS-2: Small angle scattering diffractometer, J. Large-scale Res. Facilities JLSRF 1 (2015).

[29] J.S. Pedersen, Analysis of small-angle scattering data from colloids and polymer solutions: modeling and least-squares fitting, Adv. Colloid Interface Sci. 70 (1997) 171–210.

[30] J.S. Pedersen, P. Schurtenberger, Scattering functions of semiflexible polymers with and without excluded volume effects, Macromolecules 29 (23) (1996) 7602–7612.

[31] M.C. Doucet, Jae Hie, Alina, Gervaise, Bakker, Jurrian, Bouwman, Wim, Butler, Paul, Campbell, Kieran, Gonzales, Miguel, Heenan, Richard, Jackson, Andrew, Juhas, Pavol, King, Stephen, Kienzle, Paul, Krzywon, Jeff, Markvardsen, Anders, Nielsen, Torben, O'Driscoll, Lewis, Potrzebowski, Wojciech, Ferraz Leal, Ricardo, Richter, Tobias, Rozycko, Piotr, Snow, Tim, Washington, Adam, SasView version 4.2.2, 2019. https://doi.org/10.5281/zenodo.2652478.

Supplementary material for

Tail unsaturation tailors the thermodynamics and rheology of a self-assembled sugar-based surfactant

Johan Larsson,[a] Anna E. Leung,[b] Christian Lang,[c] Baohu Wu,[c] Marie Wahlgren,[d] Tommy Nylander,[a,e] Stefan Ulvenlund,[d,f] Adrian Sanchez-Fernandez.[d]*

[a]Physical Chemistry, Department of Chemistry, Box 124, 221 00 Lund, Sweden
[b]European Spallation Source, Box 176, 221 00 Lund, Sweden
[c]Jülich Centre for Neutron Science (JCNS) at Heinz Maier-Leibnitz Zentrum (MLZ), Forschungszentrum Jülich GmbH, Lichtenbergstr. 1, 85748 Garching, Germany
[d]Food Technology, Engineering and Nutrition, Box 124, 221 00 Lund, Sweden
[e]NanoLund, Lund University, Box 124, 221 00 Lund, Sweden
[f]EnzaBiotech AB, Scheelevägen 22, 22363 Lund, Sweden
Corresponding author: adrian.sanchez-fernandez@food.lth.se

Synthesis

General experimental

Palmitoleic acid ((*Z*)-hexadec-9-en-1-oic acid) was from Larodan AB, Sweden. 2,3,6,2',3',4',6'-Hepta-O-acetyl-α-D-maltosyl bromide was from Carbosynth Ltd, United Kingdom. All other chemical compounds were purchased from Sigma-Aldrich. NMR spectra were recorded on a Varian Unity INOVA 400 MHz spectrometer with a 5 mm ^{1}H/^{13}C auto-switchable gradient-probe, operating at 400 and 100 MHz respectively for proton (^{1}H) and carbon (^{13}C) nuclei. ^{13}C NMR spectra were ^{1}H-decoupled. Spectra were recorded at 298 K. The residual signal of the solvent was used to reference the chemical shifts of the sample, expressed in parts per million (ppm).

Palmitoleyl alcohol ((*Z*)-hexadec-9-en-1-ol)

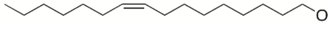

To a stirred suspension of $LiAlH_4$ (151 mg, 3.98 mmol) in dry THF (4 mL) was added a solution of palmitoleic acid (1.00 g, 3.93 mmoL) in dry THF (4 mL). The mixture was stirred at room temperature until complete consumption of the starting material was observed by TLC (70:30:1 hexane:diethyl ether:acetic acid; bromocresol green to visualise). Aqueous NH_4Cl (1 M, 4 mL) and water (1 mL) were added and the mixture was extracted into diethyl ether (3 x 15 mL). The combined organic extracts were washed with brine (50 mL), dried ($MgSO_4$) filtered and concentrated under reduced pressure to provide the title compound as a clear oil which required no further purification (924 mg, 98%). ^{1}H NMR (400 MHz, $CDCl_3$) δ 0.88 (m, 3 H), 1.27-1.43 (complex, 19 H), 1.56 (quint., *J* = 6.9 Hz, 2 H), 2.01 (apparent q, *J* = 6.3 Hz, 4 H), 3.64 (t, *J* = 6.6 Hz, 2 H), 5.35 (m, 2 H) (Figure 1). ^{13}C NMR (100 MHz, $CDCl_3$) δ 14.2, 22.8, 25.9, 27.3, 27.4, 29.1, 29.4, 29.5, 29.6, 29.9, 31.9, 32.9, 63.2, 129.95, 130.09 (Figure 2).

2,3,6,2',3',4',6'-Hepta-O-acetyl-palmitoleyl-β-D-maltoside

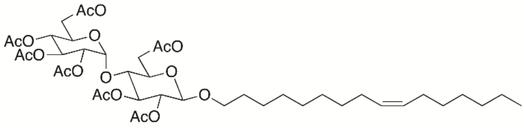

2,3,6,2',3',4',6'-Hepta-O-acetyl-α-D-maltosyl bromide (1.70 g, 2.44 mmol) and 4 Å molecular sieves (1.85 g) were added to anhydrous DCM (40 mL). A solution of palmitoleyl alcohol (1.75 g, 7.28 mmol) in anhydrous DCM (40 mL) was added and the mixture stirred for 30 minutes at room temperature. Silver carbonate (815 mg, 2.96 mmol) and silver perchlorate (802 mg, 3.87 mmol) were added and the flask was covered with foil and stirred vigorously for one hour under argon, then filtered through a celite plug, which was washed with DCM (40 mL). The solvent was removed from the filtrate under reduced pressure to provide a sticky yellow gum. Purification via flash column chromatography (gradient elution: 30-40% EtOAc in hexane; visualised with Hanessian's stain) provided the pure title compound as a white solid (526 mg, 25%). ^{1}H NMR (400 MHz, $CDCl_3$) δ 0.88 (t, *J* = 6.5 Hz, 3 H), 1.27 (s, 18 H), 1.53 (s, 4 H), 2.00-2.04 (complex, 19 H), 2.10 (s, 3 H), 2.14 (s, 3 H), 3.47 (m, 1 H), 3.67 (m, 1 H), 3.84 (dt, *J* = 9.6, 6.3 Hz, 1 H), 3.95-4.05 (complex, 3 H), 4.24 (m, 2 H), 4.47 (dd, *J* = 12.0, 2.3 Hz, 1 H), 4.51 (d, *J* = 8.0 Hz, 1 H), 4.81 (dd, *J* = 9.4, 8.1 Hz, 1 H), 4.86 (dd, *J* = 10.5, 4.0 Hz, 1 H), 5.05 (apparent t, *J* = 9.8 Hz, 1 H), 5.25 (apparent t, *J* = 9.2 Hz, 1 H), 5.36 (m, 1 H), 5.41 (d, *J* = 4.0 Hz, 1 H) (Figure 3). ^{13}C NMR (100 MHz, $CDCl_3$) δ 14.2, 20.717, 20.721, 20.75, 20.77, 20.83, 21.0, 21.1, 22.8, 26.0, 27.33, 27.36, 29.1, 29.39, 29.44, 29.5, 29.6, 29.87, 29.90, 31.9, 61.7, 63.1, 68.2, 68.6, 69.5, 70.1, 70.4, 72.2, 72.4, 72.9, 75.6, 95.7, 100.5, 129.9, 130.1, 169.6, 169.7, 170.1, 170.4, 170.6, 170.7 (Figure 4).

Palmitoleyl-β-D-maltoside

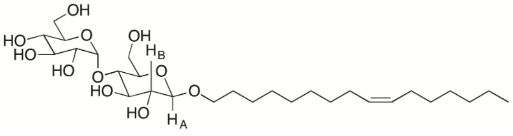

2,3,6,2',3',4',6'-Hepta-O-acetyl-palmitoleyl-β-D-maltoside (643 mg, 792 μmol) was dissolved in anhydrous methanol (25 mL). A solution of sodium methoxide in methanol (0.5 M, 1.84 mL, 0.92 mmol) was added and the mixture was stirred at room temperature under a nitrogen atmosphere for 24 hours. Amberlite® IR-120 H (hydrogen form), pre-rinsed with methanol, was added and the mixture stirred until the pH reached 5 (starting pH = 8). The resin was removed via filtration and the filtrate was concentrated under reduced pressure to afford a cream-coloured solid. Flash column chromatography (gradient elution: 10-15% methanol in dichloromethane; Hanessian's stain to visualise) provided the title compound as a white solid (395 mg, 93%). The anomeric configuration of the β-maltoside was assigned by the magnitude of the $J_{A,B}$ coupling constant in the ^{1}H NMR spectrum (7.8 Hz, indicative of axial-axial and not axial-equatorial coupling). ^{1}H NMR (400 MHz, CD_3OD) δ 0.90 (m, 3 H), 1.32 (s, 18 H), 1.62 (apparent quint., J = 7.0 Hz, 2H), 2.01-2.04 (complex, 4 H), 3.20-3.29 (complex, 2 H), 3.36 (m, 1 H), 3.44 (dd, J = 9.7, 3.7 Hz, 1 H), 3.51-3.56 (complex, 2 H), 3.59-3.71 (complex, 4 H), 3.79-3.92 (complex, 4 H), 4.26 (d, J = 7.8 Hz, 1 H), 5.16 (d, J = 3.7 Hz, 1 H), 5.35 (m, 2 H) (Figure 5 and 6). ^{13}C NMR (100 MHz, CD_3OD) δ 14.4, 23.7, 27.1, 28.1, 30.0, 30.3, 30.61, 30.62, 30.80, 30.83, 30.87, 32.9, 62.2., 62.8, 71.0, 71.5, 74.2, 74.7, 74.8, 75.1, 76.6, 77.9, 81.4, 102.9, 104.3, 130.8 (Figure 7, 8 and 9).

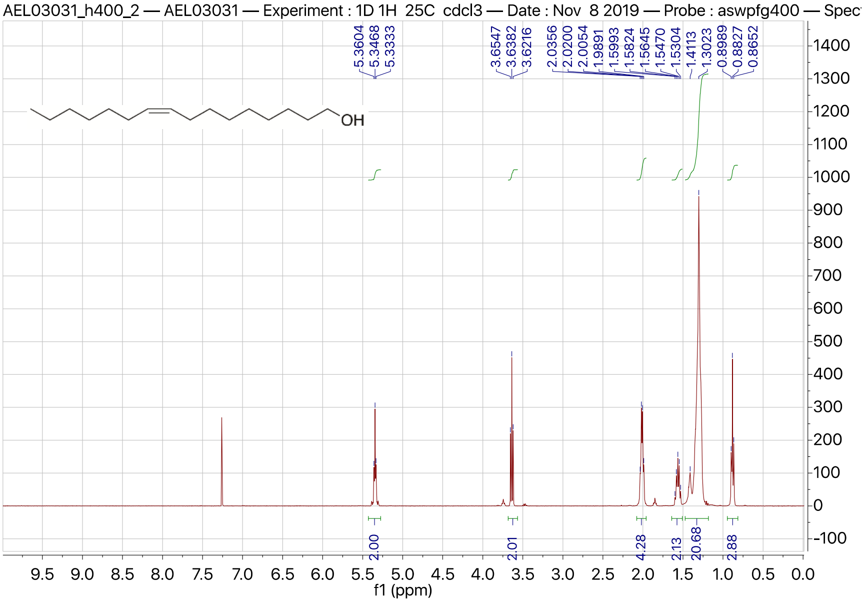

Figure 1. ^{1}H NMR spectrum of palmitoleyl alcohol (400 MHz, $CDCl_3$).

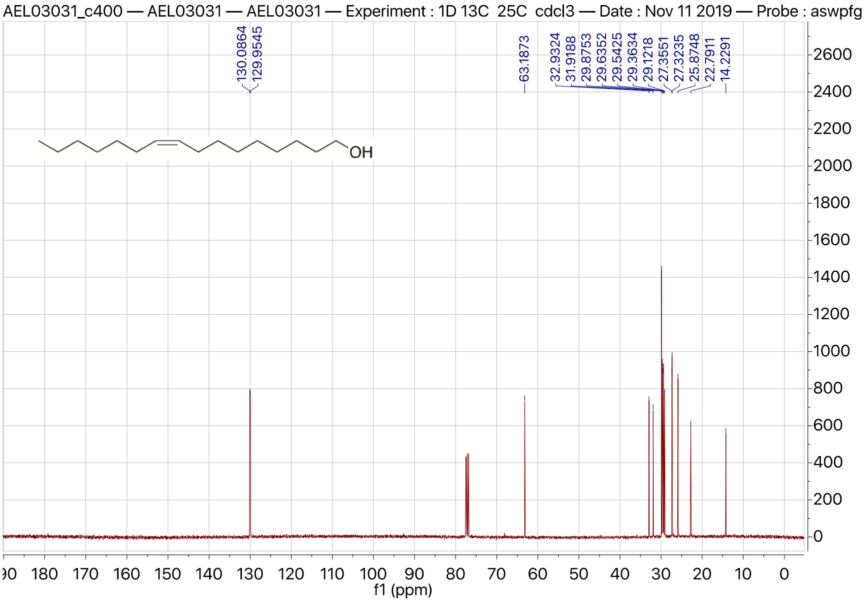

Figure 2. ^{13}C NMR spectrum of palmitoleyl alcohol (100 MHz, $CDCl_3$).

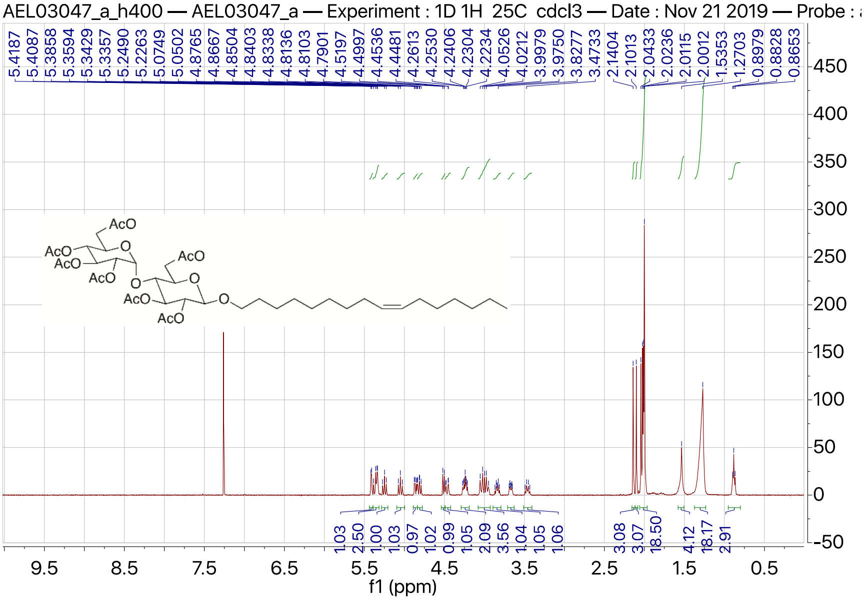

Figure 3. ^{1}H NMR spectrum of 2,3,6,2’,3’,4’,6’-hepta-O-acetyl-palmitoleyl-β-D-maltoside (400 MHz, CDCl$_3$).

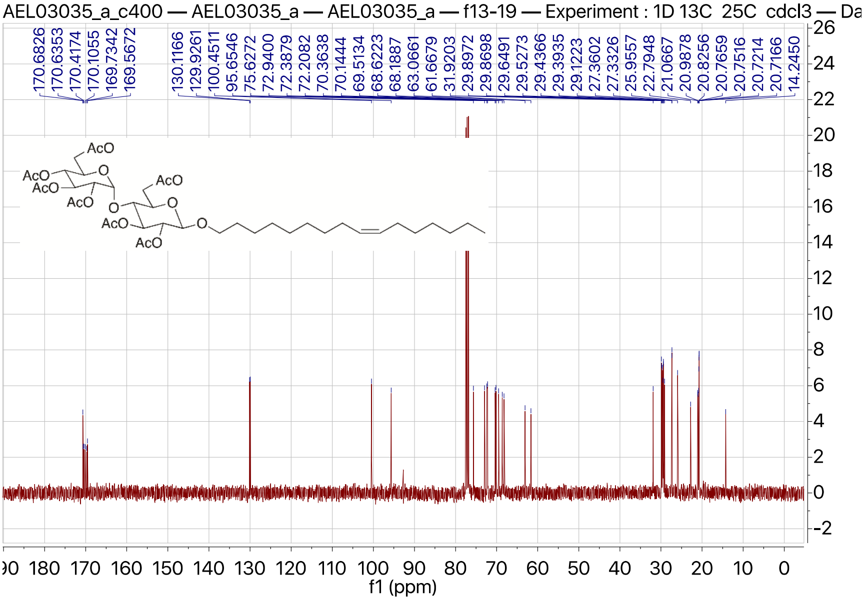

Figure 4. ^{13}C NMR spectrum of 2,3,6,2’,3’,4’,6’-hepta-O-acetyl-palmitoleyl-β-D-maltoside (100 MHz, CDCl$_3$).

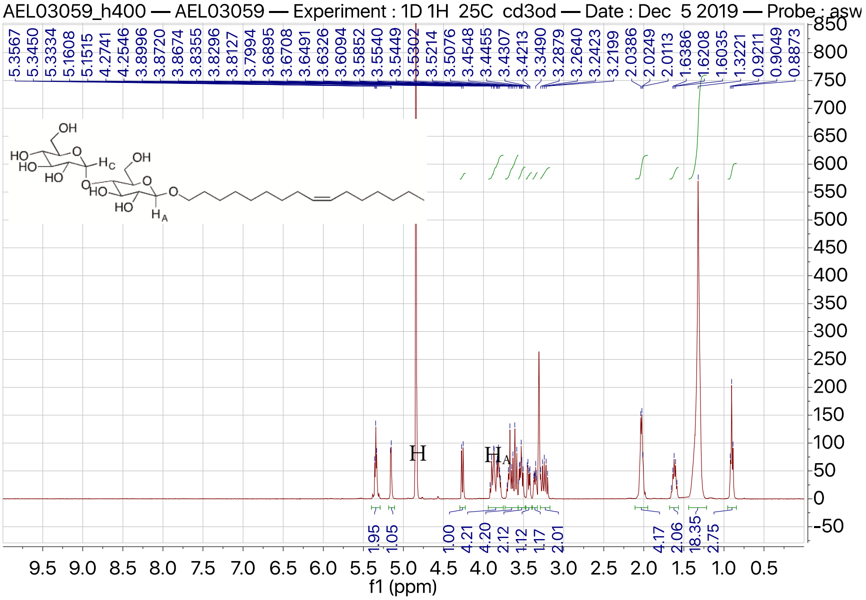

Figure 5. ^{1}H NMR spectrum of palmitoleyl-β-D-maltoside (400 MHz, CD_3OD).

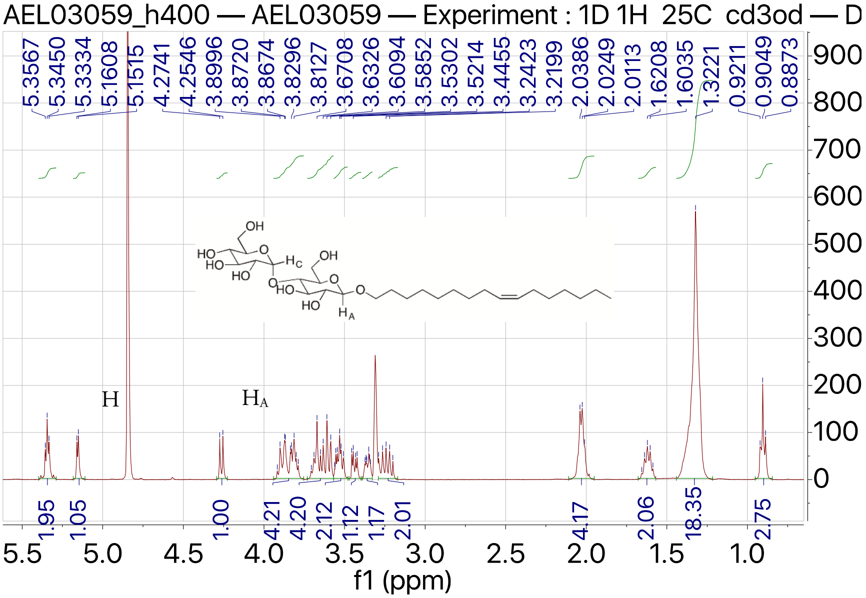

Figure 6. ^{1}H NMR spectrum of palmitoleyl-β-D-maltoside (400 MHz, CD_3OD) (expansion).

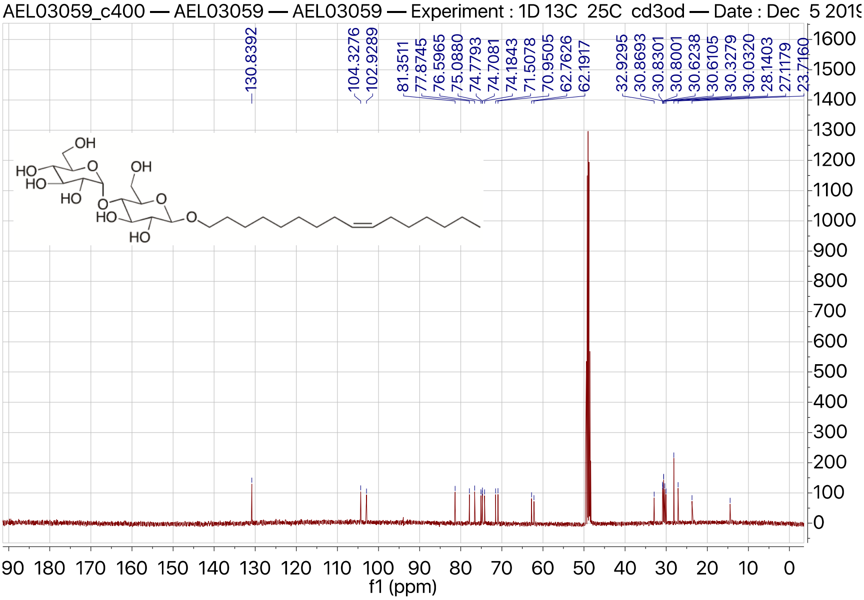

Figure 7. ^{13}C NMR spectrum of palmitoleyl-β-D-maltoside (100 MHz, CD_3OD).

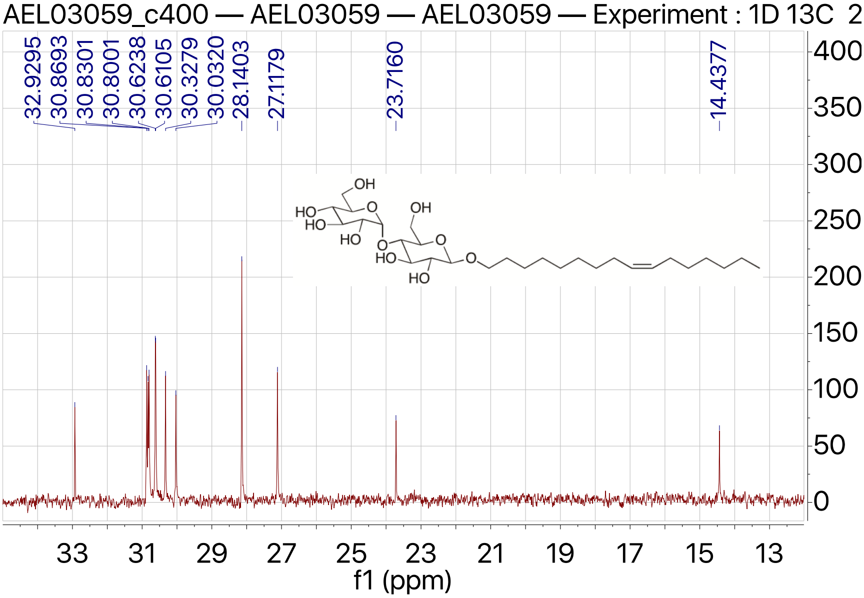

Figure 8. ^{13}C NMR spectrum of palmitoleyl-β-D-maltoside (100 MHz, CD_3OD) (12-35 ppm).

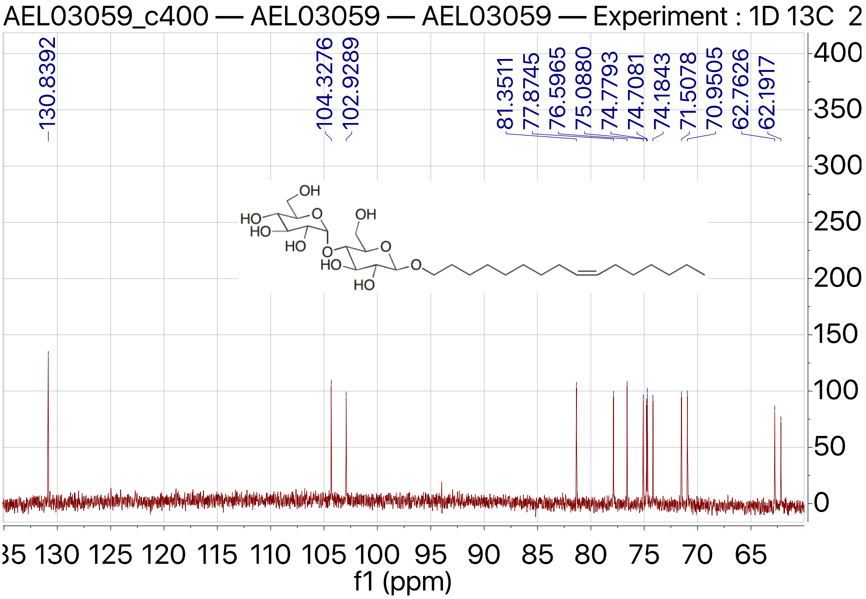

Figure 9. ^{13}C NMR spectrum of palmitoleyl-β-D-maltoside (100 MHz, CD_3OD) (60-135 ppm).

Methods

Differential Scanning Calorimetry (DSC). The solvation temperature of the surfactants was studied in a VP-DSC instrument manufactured by MicroCal. Samples with 50 mM surfactant concentrations were prepared and stored at 5 °C to equilibrate overnight. The measuring cell was filled with surfactant sample and the reference cell was filled with water. The volume of both cells was 0.5219 ml. The samples were scanned from 5 to 95 °C at a rate of 30 °C/h.

Rheology. The rheology measurements were performed by using an Anton Paar MCR 301 rheometer and the data were analysed in the software RheoPlus. A cone-plate geometry with a cone diameter of 25 mm, a cone angle of 1˚ and a gap of 0.048 mm was used for the experiment. The flow curves were recorded at a shear rate range of 0.01–100 s^{-1} with 7 measurements per decade. The linear viscoelastic region (LVER) was determined, and oscillatory rheology experiments were performed at a constant strain of 10 % over the angular frequency range 0.05-100 rad/s at a constant temperature of 25 ˚C.

Considering the Maxwellian behaviour displayed by the samples, the oscillatory rheology data were fitted using the following equations:

$$G' = G'_{\infty}\frac{(\omega\tau)^2}{1+(\omega\tau)^2} \tag{1}$$

$$G'' = G'_{\infty}\frac{\omega\tau}{1+(\omega\tau)^2} \tag{2}$$

where G' and G'' is the elastic and viscous modulus respectively, G'_∞ is the plateau value of G' at high frequencies, ω is the angular frequency and τ is the relaxation time.

Tensile strength texture analysis was conducted using a TA.XT2i instrument, Stable Micro Systems, with a hemispherical cylinder probe with a diameter of 6 mm. The applied force on the probe was 1 g and the trigger force was 1 g which submerged the probe in the sample. After 60 s the probe was lifted from the solution with a speed of 1 mm/s and the force required was recorded.

Dynamic Light Scattering (DLS). The hydrodynamic radius (r_H) of the micelles was determined through measurements of the apparent diffusion coefficient of those using DLS. The Zetasizer Nano-ZS (Malvern Instruments Ltd., Worshestershire, UK) with a 4 mW He-Ne laser was used with a wavelength configuration of 632.8 nm in back-scattering mode (2θ=173°, where 2θ is the scattering angle). Samples were loaded into PMMA semi-micro disposable cuvettes (BRAND GmbH) and measured in 5 °C steps upon equilibration from 70°C to 10 °C. Triplicates were measured for every data point. As the correlation functions showed a single exponential decay, data were analysed using the cumulants method implement in the Malvern Zetasizer software.

Small angle x-ray and neutron scattering. Small angle x-ray scattering (SAXS) experiments were performed on a SAXSlab Ganesha pinhole instrument, JJ X-ray System Aps, equipped with an X-ray microsource (Xenocs) and a two-dimensional 300k Pilatus detector (Dectris Ltd., Switzerland). The X-ray wavelength was λ = 1.54 Å. Images were collected at three given sample-to-detector distances, and the azimuthally averaged intensities as a function of the scattering vector $q = (4\pi/\lambda) \sin(\theta)$, were subtracted for the contribution of the capillaries filled with solvent and put to absolute scale by calibration against water.

Small angle neutron scattering (SANS) experiments were performed on the KWS-3 and KWS-2 instruments at the Heinz Maier-Leibnitz Zentrum (MLZ, Garching, Germany). On KWS-3 two different sample-to-detector distances were measured (1.15 and 9.15 m) and the wavelength of the neutrons was 12.8 Å. These configurations provided a combined Q range of 0.000183–0.0187 $Å^{-1}$. On KWS-2 three detector distances were used (2, 8 and 20 m) and the wavelength of the neutrons were 5 Å for 2 and 8 m, and 10 Å for 20 m. The combined Q-range from this experiment was 0.0024-0.46 $Å^{-1}$. The samples were injected in 2-mm path length quartz cuvettes and loaded in a temperature-controlled sample changer at 50 °C. The output data for these experiments were formatted as I(Q), in absolute intensity, vs. Q.

Scattering data analysis was performed using SasView 4.2.2. Two different form factors were used to describe the different structural features of the micelles. A core-shell cylinder model was used to determine the dimensions of the micelle cross-section using the high-Q expansion of the SAXS data (>0.01 $Å^{-1}$). SANS data were fitted using a flexible cylinder model that describes the contour length and persistence length of the micelles. Both models were sequentially refined using the optimised results from previous fits. A detailed description of the analysis of the SAXS and SANS data is included in our previous work.[1]

Results

Rheology

The linear viscoelastic regime for 100 mM β-palmitoleoylmaltoside (β-$C_{16\text{-}1}G_2$) in H_2O at 25 °C was determined by performing an amplitude sweep at three different shear rates. The results are presented in Figure 10.

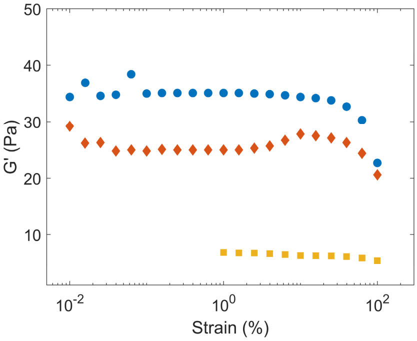

Figure 10. Amplitude sweep for 100 mM β-$C_{16\text{-}1}G_2$ in H_2O at 25 °C at an angular frequency of 10 (blue circle), 1 (red diamond) and 0.1 (yellow square) rad/s.

Texture

The texture analysis of 100 mM β-$C_{16\text{-}1}G_2$ resulted in the formation of a long, thin filament which was not seen for hexadecylmaltoside (β-$C_{16}G_2$), see Figure 11. The results from tensile strength texture analysis are included and discussed in the main text (Figure 2d).

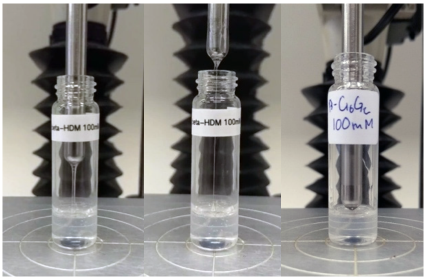

Figure 11. Images from tensile strength texture analysis of 100 mM β-$C_{16\text{-}1}G_2$ (left and middle) and β-$C_{16}G_2$ (right).

Reference

1. Larsson, J.; Sanchez-Fernandez, A.; Mahmoudi, N.; Barnsley, L. C.; Wahlgren, M.; Nylander, T.; Ulvenlund, S., Effect of the Anomeric Configuration on the Micellization of Hexadecylmaltoside Surfactants. *Langmuir* **2019,** *35* (43), 13904-13914.

Paper v

Interfacial behaviour and structure of sugar-based surfactants at the solid-liquid interface

J. Larsson, M. Wahlgren, A. E. Leung, A. Sanchez-Fernandez, J. Cooper, N-J. Steinke, S. Ulvenlund, T. Nylander

Manuscript in preparation for submission

Interfacial behaviour and structure of sugar-based surfactants at the solid-liquid interface

Johan Larsson,[a] Marie Wahlgren[b], Adrian Sanchez-Fernandez,[b] Anna Leung,[c] Jos Cooper,[d] Nina-Juliane Steinke,[d] Stefan Ulvenlund,[b,e] Tommy Nylander[a,f,g]
[a]Physical Chemistry, Department of Chemistry, Lund University, Box 124, 221 00 Lund, Sweden.
[b]Food Technology, Nutrition, and Engineering, Lund University, Box 124, 221 00 Lund, Sweden.
[c]European Spallation Source, Box 176, 221 00 Lund, Sweden.
[d]ISIS Spallation Source, STFC, Rutherford Appleton Laboratory, Didcot, UK.
[e]Enza Biotech AB, Scheelevägen 22, 22363 Lund, Sweden.
[f]NanoLund, Lund University, Lund, Sweden.
[g]LINXS - Lund Institute of Advanced Neutron and X-ray Science, IDEON Building: Delta 5, Scheelevägen 19, 22370 LUND, Sweden

Abstract

The interfacial behaviour of surfactants is crucial for their function in many applications. In the present work, adsorption of the α- and β-anomer of hexadecylmaltoside (α-$C_{16}G_2$ and β-$C_{16}G_2$) at a hydrophobic solid-liquid interface was investigated by means of ellipsometry and neutron reflectometry, with a particular focus on the effects of the headgroup configuration on the formed layer structure. A significant difference between the two anomers was observed, where the adsorbed amount was higher for the β-anomer. This was attributed to conformational differences of the two headgroups that allows for the β-anomer to be packed more efficiently. The adsorbed film was found to not conform to models of a surfactant monolayer, but instead, a more intriguing structure is suggested in which a thin layer of surfactants is adsorbed to the interface onto which a layer of micelles is adsorbed. This structure is likely to originate from the potential attractive intermolecular interactions that also control the bulk solution behaviour, namely hydrophobic interactions, and supported by the formation of hydrogen bonds between the sugar headgroups. Adsorption from a 50:50 mixture of the two enantiomers showed a 40:60 ratio of α-$C_{16}G_2$:β-$C_{16}G_2$ at the surface. Showing a preferential adsorption of the surfactant that gives the smaller headgroup area.

Introduction

Surfactant behaviour at interfaces is critical for numerous applications such as stabilisation of dispersions and foams, detergency, and technical application like oil recovery and corrosion inhibition[1]. Thus, surfactant adsorption has been extensively studied with a plethora of techniques[2-3] including quartz microbalance,[4] atomic force microscopy,[3] null-ellipsometry,[5] and neutron reflectometry (NR).[6] While null-ellipsometry primarily provides information about the thickness and refractive index of the film, or in fact in many cases just the adsorbed amount, neutron reflectometry has the potential to provide a more detailed understanding of the structure of the surfactant layer. Surfactant layer structures at the liquid-air and solid-liquid interfaces have been extensively studied using NR, starting with the pioneering work of Thomas et al more than 30 years ago.[7-9] NR has since then emerged as a key technique to reveal the surfactant layer structure, also on hydrophobized silicon surfaces and surfaces with polymer layers.[10-12] One particular strength of NR is that utilisation of contrast isotope variation provides an opportunity to elucidate structure and composition for adsorption from mixed surfactant systems, where the R. K. Thomas group in Oxford also was pioneers.[6]

The adsorption of a surfactant to a given interface is dependent both on the characteristics of the interface (hydrophobicity, charge, roughness, and heterogeneity), and the properties of the surfactant (e.g. charge and hydrophobicity) as well as the solution conditions. In general, surfactants are considered to form six possible structures at the solid-liquid interface (Figure 1).[13] All these structures entail bilayers or monolayers of the surfactant and this is what is normally observed at solid interfaces. In contrast to this, at the air-water interface, NR has shown that deviation from the expected monolayer does occur showing one or two additional bilayers up to several multilayers, as described in detail by Thomas and Penfold.[14] This can be related to changes in solution conditions, like the addition of multivalent counter ions, that promote the surfactant intermolecular attractive interactions.

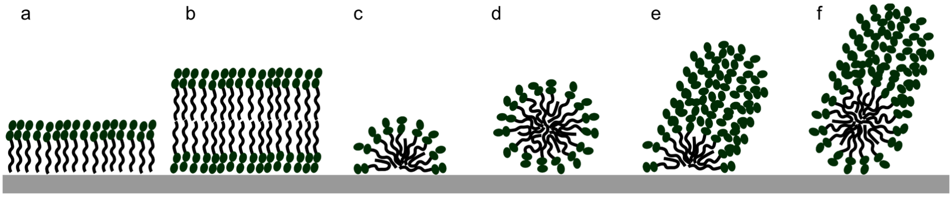

Figure 1. Schematic illustration of possible film structures of adsorbed surfactants at interfaces. (a) monolayer, (b) bilayer, (c) hemimicelle, d) micelle, (e) cylindrical hemimicelle, and (f) cylindrical micelle.

The adsorption of nonionic surfactants at an amorphous hydrophobic surface has almost exclusively been described as a monolayer with a thickness roughly corresponding to the length of an extended surfactant molecule.[15-17] However, several other types of structures have been observed. For example, hemispherical cylinders have been observed for PEG-surfactants[18] and sugar surfactants[19] at crystalline graphite. There are also studies that report the formation of hemimicelles of the adsorbed surfactants on an amorphous hydrophobic surface.[20] This was shown for both ionic and nonionic surfactants with the common feature that they form spherical micelles in solution.

The driving force for adsorption to hydrophilic surfaces are often weaker than for hydrophobic ones, especially for nonionic surfactants. Thus, several sugar-based surfactants have been observed not to adsorb to hydrophilic silica, which is in contrast to polysorbate and other PEG-based surfactants that are known to adsorb as bilayers to these types of surfaces.[21] Interestingly enough, Matsson et al. observed that alkylglycosides do adsorb on a titania interface.[5] They found that the adsorbed amount was about what would be expected for a double layer for all surfactants, independent of both the headgroup and the tail group size. Except for $C_{10}G_1$ where they saw larger variations in adsorbed amount and in some cases at temperatures where the surfactant crystalises in water adsorption in excess of what is expected for bilayer. It has also been reported that n-dodecyl-β-D-maltoside adsorbs to aluminium.[22] Mixtures of surfactants represent yet another degree of complexity and for example mixtures of n-dodecyl-β-D-maltoside and ethoxylated phenol decyl ether has been shown to both adsorb in a synergetic way on silica (leading to a higher amount adsorbed than for the individual surfactants) and in an antagonistic way on aluminium (leading to lower amounts adsorbed from the mixture compared to the surfactant that has the highest amount adsorbed).[23]

Recently, we have studied the self-aggregation of n-hexadecyl-α-D-maltopyranoside (α-$C_{16}G_2$) and n-hexadecyl-β-D-maltopyranoside (β-$C_{16}G_2$) in solution.[24-25] The maltoside family of surfactants is of great interest as they can be produced using fossil-free technology and are biodegradable, making them attractive and sustainable alternatives to many existing traditionally produced surfactants. In terms of self-aggregation, large differences were observed between the two surfactants, originating from effects of the headgroup configuration. In the dilute regime, β-$C_{16}G_2$ forms worm-like micelles that at more concentrated solutions give rise to high viscosity and viscoelastic behaviour. In stark contrast, α-$C_{16}G_2$ forms shorter micelles and gives a much lower viscosity. Interestingly enough, the two surfactants form mixed micelles where the ratio between the two anomers controls the rheological properties, making it possible to tune these. In the present work, we will investigate to what extent headgroup conformation affects the adsorption to solid surfaces in the same way as it does the self-aggregation in bulk.

Experimental

n-Hexadecyl-α-D-maltopyranoside (α-$C_{16}G_2$) and n-hexadecyl-β-D-maltopyranoside (β-$C_{16}G_2$) were purchased from Ramidus AB and Anatrace Inc. respectively. The purity of both surfactants was stated to be ≥97% by the suppliers, which was verified by HPLC spectroscopy in previous work.[24] The tail-deuterated versions of the surfactants (d_{31}-α-$C_{16}G_2$ and d_{31}-β-$C_{16}G_2$, 98.5 ± 2.0%D) were synthesized at the Deuteration and Macromolecular Crystallisation DEMAX platform (ESS, Sweden) according to the previously reported procedure.[25] The purity and deuteration of the material were controlled by ^{1}H and ^{13}C NMR spectroscopy and mass spectrometry. D_2O (99.9 atom%D) was obtained from ISIS spallation source and the water used in this work was of Milli-Q purity.

The substrate surfaces used for the investigation of surfactant adsorption at the solid-liquid interface were polished silicon blocks (Siltronix, Archamps-France) with the dimensions 8x5x1.5 cm for reflectometry and silicon wafers for ellipsometry obtained from SWI (Semiconductor Wafer, Inc., Taiwan), both with a silicon oxide layer at the surface. The spontaneously formed silicon oxide layer on the silicon blocks was about 10 Å, while the oxide layer was thermally grown to about 300 Å in thickness on the silicon wafers for ellipsometry. This increased the sensitivity of the ellipsometry measurements. The silicon substrates were cleaned, first in an alkaline mixture of 25% NH_4OH, 30% H_2O_2, and water (1/1/5 by volume), then in an acidic mixture of 32% HCl, 30% H_2O_2, and water (1/1/5 by volume), in both cases at 80 °C for 5 min. They were then rinsed with water and ethanol and plasma cleaned at low pressure. The surfaces were hydrophobized through silanization with 1 ml dimethyloctylchlorosilane in a desiccator which was evacuated with a vacuum pump for 20 min, closed, and stored overnight. To remove excess silane the substrates were sonicated for 20 min in THF and ethanol after which they were stored under ethanol until use.

In situ null ellipsometry experiments were performed on a Rudolph Research ellipsometer type 43603-200E with a xenon arc lamp as a light source filtered to a wavelength of 4015 Å. The substrate surfaces were attached in a trapezoid cuvette with a volume of 5 ml for which the temperature was controlled with a water bath at 25 °C. Before each adsorption measurement, the optical properties of the bare substrates were characterized in both air and water according to the procedure described by Tiberg and Landgren.[26] To correct for potential optical imperfections these were averaged from four different zones. In the experiments, the ellipsometric angles Ψ and Δ were determined, where Ψ is the amplitude and Δ is the phase shift of the reflected polarized light. From these, the thickness and refractive index of the adsorbed surfactant layer could be obtained, and these were used to calculate the adsorbed amount (Γ) with de Feijter's equation, see Equation 1.[27]

$$\Gamma = \frac{(n_f - n_0)d_f}{d_n/d_c} \tag{1}$$

where n_f is the refractive index of the adsorbed film, n_0 is the refractive index of the medium, d_f is the thickness of the film, and d_n/d_c is the refractive index increment. When the substrate was fully characterized, aliquots of surfactant stock-solution were added to the cuvette with water to the desired concentration and the adsorption was followed until the adsorbed amount reached steady state.

Specular neutron reflectometry experiments were performed on the Offspec reflectometer at the ISIS spallation source (Didcot, UK).[28] Two different angles of incidence (θ) were used, 0.5 and 2°, for every sample, and the neutron wavelength (λ) was 1 to 14 Å. The reflectivity (R) was measured as a function of the momentum transfer Q, where $Q = 4\pi\sin(\theta)/\lambda$.). The bare surfaces were characterized to determine the structure of the silicon oxide for one block and the silane layer was characterized for all blocks. Prior to the experiments, the blocks were first flushed with the pure solvent used in the experiment, and then with the surfactant solution. The adsorbed surfactant film was examined at 30 °C for 5 contrasts, namely protiated surfactant in D_2O (Contrast 1) and contrast matched silicon (CMSi, SLD = 2.07 10^{-6} Å^{-2}) (Contrast 2) and deuterated surfactant in D_2O (Contrast 3), CMSi (Contrast 4) and H_2O (Contrast 5). To ensure that the adsorption of surfactants did not affect the underlaying surface, one experiment where the surfactant was rinsed from the system was conducted. As reported in Figure S1 in the ESI the surface was found to be clean, since after rinsing with solvent the adsorbed layer desorbed and the bare hydrophobized surface was recovered

The data were analysed using the refnx software,[29] where slab layer models with different scattering length densities, SLD, and thickness were simultaneously fitted to experimental data recorded for the corresponding system with different isotope contrasts. The parameters that were expected to be the same for the different contrasts were linked. SLD for the different layers was set based on the SLDs for the surfactant or for some layers the maltoside headgroup, see Table 1. The parameters that were fitted was the layer thicknesses and the amount of solvent in each layer.

Table 1. SLD and roughness used for the model fitted to the NR results.

			SLD (10^{-6} Å^{-2})	Roughness (Å)
SiO_x			3.47	3
Silane			-0.4	3
Maltoside headgroup		D_2O	3.75	3
		CMSi	2.62	
		H_2O	1.77	
Surfactant (both tail and headgroup)	protiated	D_2O	1.51	3
		CMSi	0.99	
	deuterated	D_2O	5.55	
		CMSi	5.03	
		H_2O	4.64	

Results and discussion

The adsorption at the solid-liquid interface was first studied using ellipsometry. The adsorption isotherms for α- and β-$C_{16}G_2$ and β-$C_{12}G_2$ at hydrophobized silica are presented in Figure 2. For the $C_{16}G_2$ surfactants, the adsorption started at 0.1 μM for both anomers and the maximum adsorption was reached at 3 μM. The maximum adsorbed amount was 3.4 and 3.9 μmol/m^2 for α- and β-$C_{16}G_2$ respectively. This corresponds to an area per molecule of 50 and 43 Å^2 for α- and β-$C_{16}G_2$ respectively, assuming a monolayer. For most surfactants, the adsorption levels off when the concentration reaches the cmc. This seems to be the case also for $C_{16}G_2$, since the maximum adsorbed amount is reached at a concentration close to the cmc obtained from tensiometry experiments reported previously (about 2 μM).[24] The obtained values for the area per molecule are in agreement with values previously reported for similar surfactants.[30-31] For β-$C_{12}G_2$ fewer data points were collected at the low concentrations, but the adsorption appears to start at the same concentration as for $C_{16}G_2$. Since the cmc is about 100 times higher for β-$C_{12}G_2$ (200 μM), the isotherm is not as steep and the maximum adsorbed amount (3.5 μmol/m^2, 47 Å^2 per molecule) is reached above this concentration. The head group area calculated here is very similar to the one for adsorption at titania oxide found by Matsson *et al.*[5] It is still larger than what could be expected for a close-packed layer of maltoside surfactants, as a comparison the molecular area of n-tetradecyl-β-D-maltoside at the air-water interface calculated from tensiometry is 35 Å^2.[32] However, it is smaller than what is seen as the head group area for the micelles which was 60.1 and 53.8 Å^2, for α- and β-$C_{12}G_2$, respectively.

The kinetics of adsorption for α- and β-$C_{16}G_2$ is presented in Figure 2b where the adsorbed amount after 4 consecutive additions of surfactant is displayed. At the two lower concentrations adsorption is sluggish and equilibrium is reached after more than 1 h. At 2 and 3 μM it is much faster, and equilibrium is reached already after ca 500 s for both surfactants. At 1 mM the equilibrium was reached in ca. 1 min, see Fig S2 in ESI. As can be seen the adsorbed amount of α- $C_{16}G_2$ and β-$C_{12}G_2$ are quite similar but lower than for β-$C_{16}G_2$. It is interesting to note that β-$C_{16}G_2$ forms worm-like micelles in solution while both α-$C_{16}G_2$ and β-$C_{12}G_2$ forms spherical to ellipsoidal micelles.[24, 33] It is thus likely that the difference seen in the bulk is also reflected in the adsorption behaviour of these surfactants. This suggests that the structure at the interface could resemble the one in the bulk.

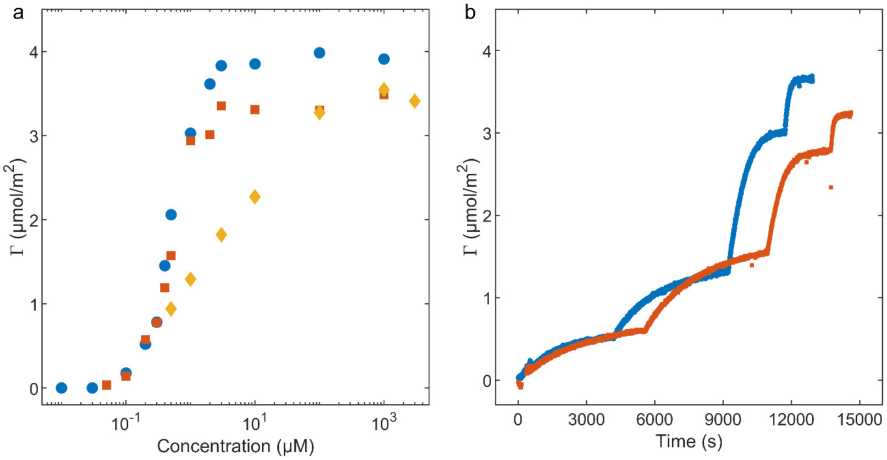

Figure 2. Ellipsometry results for the adsorption on hydrophobized silica for β-$C_{16}G_2$ (blue ○), α-$C_{16}G_2$ (red □), and β-$C_{12}G_2$ (yellow ◊) at 25 °C. (a) Adsorption isotherm. (b) Adsorption kinetics where the concentration is increased in 4 steps, representing 0.2, 0.4, 1, and 2 μM for β-$C_{16}G_2$ and 0.2, 0.4, 1, and 3 μM for α-$C_{16}G_2$. The additions were made after 83, 4214, 9218, and 11700 seconds for β-$C_{16}G_2$ and after 94, 5571, 10924, and 13710 s for α-$C_{16}G_2$.

The slow kinetic seen at the low concentrations are indicative of a diffusion-limited process that reflects the low monomer concentration of surfactants with a long alkyl chain. This, in turn, highlights the necessity to consider depletion effects in studies of such systems, as we have previously pointed out in relation to cmc determination by tensiometry.[24]

The adsorption on the hydrophilic surface of bare silica was also studied. In line with what has been seen for other sugar-based surfactants, there was no measurable adsorption of the surfactants to this surface.[5, 30, 34] The difference in adsorption of PEG-based surfactants and sugar surfactants on bare silica could originate from the possibility of sugar surfactants to act as both hydrogen bond donors and acceptors which could mean that the interactions with the water molecules are stronger than with the surface.

The structure of the adsorbed surfactant layers of $C_{16}G_2$ and $C_{12}G_2$ on hydrophobized silica was further studied with NR. The bare silica and hydrophobized surface were characterized and was found to have an 11.1 Å thick oxide layer and 3.4 Å thick silane layer. The adsorption of four surfactant systems, namely β-$C_{16}G_2$, α-$C_{16}G_2$, β-$C_{12}G_2$, as well as 1:1 mixture of α- and β-$C_{16}G_2$, has been studied here and the NR results in Contrast 1 (D_2O) are presented in Figure 3. There is a clear difference in the features of the reflectivity curves of the systems, which makes it evident that the structure of the adsorbed layer is different between the cases. The first eye-catching difference is the presence of a marked fringe for α- and β-$C_{16}G_2$ around Q=0.05, which is not present for either the mixtures of these two surfactants or for β-$C_{12}G_2$. This fringe appears at a slightly lower Q for β-$C_{16}G_2$, indicating a thicker structure. The location of this fringe is at Q-

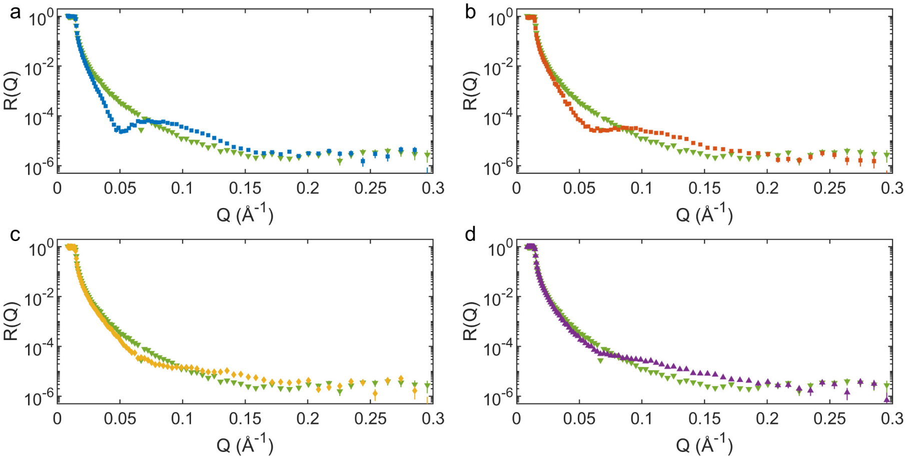

Figure 3. NR results for adsorption of protiated surfactant in D_2O at the hydrophobized silica interface. (a) 20 µM β-$C_{16}G_2$, (b) 20 µM α-$C_{16}G_2$, (c) 1 mM β-$C_{12}G_2$, and (d) 20 µM 1:1 mixture of α- and β-$C_{16}G_2$ compared to the bare silanized surface (green ▽).

values that are substantially lower than what would be expected for a monolayer. This indicates that the film could be either a multilayer or a monolayer with a concentrated micelle layer on top. Another thing that sticks out is that the mixture of α- and β-$C_{16}G_2$ does not fall between the curves of the pure anomers, and that the adsorption of the mixture rather seems to be antagonistic and less than either of the two. One should be aware that the Krafft point of the $C_{16}G_2$ is around 27 °C (and hence close to the 30°C used in the experiments),[35] and that this may affect the results. However, we did not observe any precipitation/clouding under the experimental conditions used.

Most studies of surfactant adsorption on hydrophobic surfaces or at the liquid/air interface have reported the formation of surfactant monolayer structure. Consequently, this structure was the starting point for the fitting procedure. However, this structure did not provide a satisfactory model, as can be seen in Figure 4.

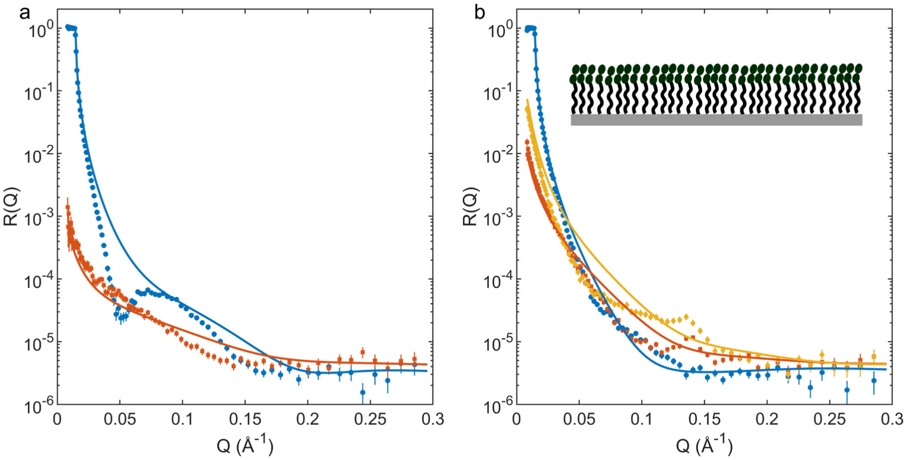

Figure 4. Neutron reflectivity results for adsorption of 20 µM of (a) protiated and (b) tail deuterated β-$C_{16}G_2$ in D_2O (blue ○), CMSi (red □), and H_2O (yellow ◊) on hydrophobized silica. The solid lines are fits with the expected parameters of a monolayer. Inset: Schematic structure of a monolayer.

Here, the reflectivity of an adsorbed layer of 20 µM β-$C_{16}G_2$ is shown for five contrasts with a fit of a model with the expected parameters for a monolayer for this surfactant (20 Å hydrophobic tail region and 10 Å headgroup region).

When fitting the data to different models it became apparent that in order to get a good fit, the model had to include several layers of surfactants. Initially, a model with only the lipid tails close to the surface and then layers of maltoside headgroups alternating with a surfactant layer was tested. However, this did not fit the data for all contrast. Instead, a model using one adsorbed layer of surfactants followed by alternating SLDs for maltoside headgroups and surfactant was used to fit the model to the experimental data. The model that best fits the NR-data for β-$C_{16}G_2$ is presented in Figure 5 and the fitting parameters in Table 2. We here want to stress that these results are from a simultaneous fit of data from 5 different isotopic contrasts, assuming that out of total 7 OH groups in the maltoside headgroup, 3 of the hydrogens are exchanged CMSi and 7 in D2O.

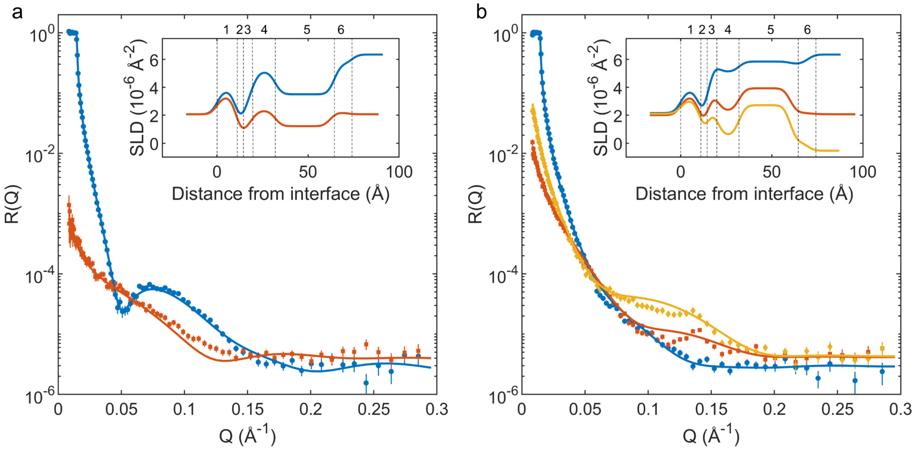

Figure 5. Neutron reflectivity results for adsorption of 20 µM (a) protiated and (b) tail deuterated β-$C_{16}G_2$ in D_2O (blue ○), CMSi (red □), and H_2O (yellow ◊) on hydrophobized silica. The solid lines represent the theoretical fit. The insets display the SLD profile as a function of distance from the Si interface based on the fitted model and the dashed lines and numbers show the different layers in the model.

Table 2. Thickness and solvent content in the layers of the model that best fits the experimental NR data for β-$C_{16}G_2$ and α-$C_{16}G_2$.

		β-$C_{16}G_2$		α-$C_{16}G_2$	
		Layer thickness (Å)	Solvent (v/v,%)	Layer thickness (Å)	Solvent (v/v,%)
1	SiO_x	11.1±0.4	10±2	11.1±0.4	10±2
2	Silane	3.4±0.9	10±3	3.4±0.9	10±3
3	Surfactant monomers	5.3±0.5	36±4	4.9±0.2	44±1
4	Maltoside headgroup	12.2±0.5	53±3	10.6±0.2	58±2
5	Surfactants in micelle	32.5±0.8	41±1	19.1±0.2	31±1
6	Maltoside headgroup	9.65±3	74±8	9.7±0.5	40±3

A structure that is in line with the fitted thicknesses and solvent content of the layers is depicted in Figure 6. It consists of an adsorbed thin layer of surfactants lying down on the surface, on top of which most likely cylindrical micelles are adsorbed. The size of the combined layers indicates that the micelles are slightly compacted compared to the SANS and SAXS data for the worm-like micelles in solution. The radius for the micelles was estimated to be 31 Å while for the adsorbed micelles they would be around 27 Å. Still, the difference is small, and the NR layers could be slightly diffuse.

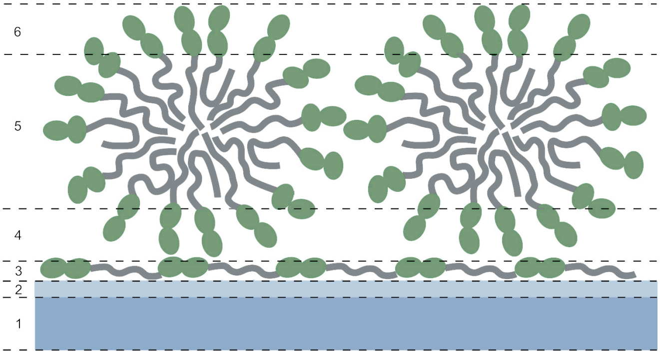

Figure 6. Schematic illustration of the modelled structure from NR. The layers in the model are displayed with the dashed lines and the numbers.

A similar model describes the adsorption of α-C$_{16}$G$_2$, but with a thinner layer, as shown in Table 2 and Figure 7. It is interesting to note a few things about the differences between the two systems. Firstly, the size of the inner layer is quite similar and only slightly lower than what would be expected for a surfactant laying flat (parallel) on the surface. The second layer is in size with but again slightly smaller than the headgroup region of the micelles (14.4 and 15.1 for α and β respectively).[24] The largest difference between α and β is observed for the core of the surfactant micelle layer (layer 5 in Figure 6), where the α layer is considerably smaller than the corresponding β layer that, as stated above, is close to what could be expected from the micelle. The α-C$_{16}$G$_2$ micelle in solution is a sphere or short rod with a headgroup area of 60 Å^2, while β-C$_{16}$G$_2$ forms wormlike micelles with a headgroup area of 54 Å^2. The larger headgroup size of α-C$_{16}$G$_2$ could allow for the formation of oblate surface micelles. This explains the lower adsorbed amount observed by ellipsometry at the same time as it is consistent with a better packing of the structures at the surface indicated by the lower solvent content compared to the outer maltoside layer.

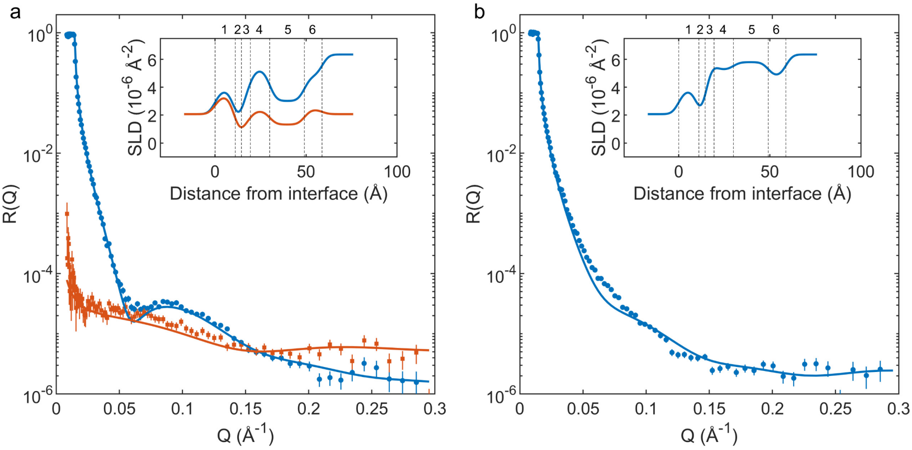

Figure 7. Neutron reflectivity results for adsorption of 20 µM (a) protiated and (b) tail deuterated α-C$_{16}$G$_2$ in D$_2$O (blue ○) and CMSi (red □) on hydrophobized silica. The solid lines represent the theoretical fits. The insets display the SLD profile as a function of distance from the Si interface based on the fitted model and the dashed lines and numbers show the different layers in the model.

The thickness of the inner headgroup layer (4) appears to be thicker than the outer layer (6), indicating that the headgroups of the surfactants laying on the surface (layer 3) stick out of the surface, adding to the thickness of layer 4.

In order to compare the $C_{16}G_2$ systems with a surfactant that has been more thoroughly investigated we also studied the adsorption of β-$C_{12}G_2$ (Figure S3 and Table S1 in ESI). One additional advantage of this surfactant is that it does not have a Krafft temperature close to the one studied in these experiments. β-$C_{12}G_2$ was also initially fitted to a one-layer model and as for the $C_{16}G_2$ surfactants, such a model could not explain the NR data. A few other models were tested but finally, we settled for fitting the data to the same model as for the $C_{16}G_2$ surfactants. The results show a reasonable agreement with the data. The main difference seen is that all the layers of β-$C_{12}G_2$ contain more water than the layers for β-$C_{16}G_2$ indicating less efficient packing of this surfactant. There is also a difference between the size of the lipid layer of the adsorbed micelle and as should be this layer is thinner for β-$C_{12}G_2$ than for β-$C_{16}G_2$, which has a longer acyl-chain. However, as for β-$C_{16}G_2$, the layer thickness is closer to what would be expected for a micelle rather than for a layer with interpenetrating chains. The results from the comparison of the three surfactants indicate that the configuration of the headgroup plays a considerable role for the structure obtained at the surface.

The NR results for the α- and β-$C_{16}G_2$ mixtures were not possible to fit to the same model as for the anomerically pure systems. Instead, a one-layer surfactant model gave the best fit to the data with a thickness similar to that of the α-$C_{16}G_2$ film (Figure S4 and Table S1 in ESI). This indicates a different structure for the surfactant mixtures, instead of the more anticipated intermediate structure that was found in the case of the mixed micelles. As we used a mixture of deuterated α-$C_{16}G_2$ and hydrogenated β-$C_{16}G_2$, we could calculate the ratio of surfactants in the adsorbed film, based on the fitted SLD. This gave a volume ratio of ca. 40:60 of α:β and thus offset from the bulk concentration with 10%. This is the opposite compared to that found for the mixed micelles where the content of α was slightly higher than β, then attributed to the more hydrophobic character of this anomer. The conditions at the surface are different than in the bulk and the finite available area could favour the β-anomer, since it appears that this can be packed in a more efficient way.[24]

The structures found to best rationalize the NR data are hence not in line with the structures commonly reported for these types of adsorbed surfactants. For hydrophobic surfaces, the majority of previous studies describe the adsorption as monolayers. Interestingly, Dang *et al* has seen that $C_{12}G_2$ adsorb to a hydrophobic poly(methyl methacrylate) surface in an orientation that is quite similar to what we depict in our model with the maltoside headgroups standing perpendicular to the surface and a layer thickness of the adsorbed layer as measured with AFM of 13.8 Å.[36] This lends support to the idea that a very thin layer of surfactants can be formed at hydrophobic surfaces. The formation of a secondary layer on top of the first thin layer is even more uncommon for solid surfaces but has for instance been seen for the air-water interface.[14] For carbohydrate-based surfactants it is known that hydrogen interaction plays a key role also for adsorption at hydrophobic surfaces and thus the combination of a thin layer of adsorbed maltoside surfactants on a hydrophobic surface could function as an anchor for the micelles.

Conclusion

In this work, we have shown that the headgroup conformation of n-hexadecyl-D-maltopyranoside does affect the adsorbed amount on solid hydrophobic surfaces and that the β-anomer of hexadecylmaltoside adsorb in a denser layer than the α-anomer. Both anomers adsorb with more than one layer at the surface and the model that gives the best fit for the neutron reflectometry data is one where there is a dense layer of surfactants at the surface with an adsorbed layer of micelles on top of this layer. For mixtures of these surfactants, the surface behaviour seems to change, and it appears that the structure of the adsorbed film is different from the pure anomers.

Acknowledgement

The authors are thankful to Swedish Research Council Formas (Grant 2015-666) for the funding for J.L. The research in this study was also performed with financial support from Vinnova - Swedish Governmental Agency for Innovation Systems within the NextBioForm Competence Centre.

References

1. Schramm, L. L.; Stasiuk, E. N.; Marangoni, D. G., 2 Surfactants and their applications. *Annu. Rep. Prog. Chem., Sect. C: Phys. Chem.* **2003,** *99*, 3-48.
2. Tiberg, F.; Brinck, J.; Grant, L., Adsorption and surface-induced self-assembly of surfactants at the solid–aqueous interface. *Current Opinion in Colloid & Interface Science* **1999,** *4* (6), 411-419.
3. Paria, S.; Khilar, K. C., A review on experimental studies of surfactant adsorption at the hydrophilic solid-water interface. *Adv Colloid Interface Sci* **2004,** *110* (3), 75-95.
4. Kwek, J. W.; Kim, S., Characterization of Adsorption Behavior of Sucrose Monolaurate on Gold Substrate Using the Quartz Crystal Microbalance (QCM). *Journal of Surfactants and Detergents* **2016,** *19* (4), 775-783.
5. Matsson, M. K.; Kronberg, B.; Claesson, P. M., Adsorption of Alkyl Polyglucosides on the Solid/Water Interface: Equilibrium Effects of Alkyl Chain Length and Head Group Polymerization. *Langmuir* **2004,** *20* (10), 4051-4058.
6. Penfold, J.; Thomas, R. K., Probing Surfactant Adsorption at the Solid–Solution Interface by Neutron Reflectometry. In *Interface Science and Technology*, Imae, T., Ed. Elsevier: 2007; Vol. 14, pp 87-115.
7. Hayter, J. B.; Highfield, R. R.; Pullman, B. J.; Thomas, R. K.; McMullen, A. I.; Penfold, J., Critical reflection of neutrons. A new technique for investigating interfacial phenomena. *Journal of the Chemical Society, Faraday Transactions 1: Physical Chemistry in Condensed Phases* **1981,** *77* (6), 1437-1448.
8. Lee, E. M.; Thomas, R. K.; Penfold, J.; Ward, R. C., Structure of aqueous decyltrimethylammonium bromide solutions at the air water interface studied by the specular reflection of neutrons. *The Journal of Physical Chemistry* **1989,** *93* (1), 381-388.
9. Bayerl, T. M.; Thomas, R. K.; Penfold, J.; Rennie, A.; Sackmann, E., Specular reflection of neutrons at phospholipid monolayers. Changes of monolayer structure and headgroup hydration at the transition from the expanded to the condensed phase state. *Biophysical Journal* **1990,** *57* (5), 1095-1098.
10. Zhang, Z.; Orski, S.; Woys, A. M.; Yuan, G.; Zarraga, I. E.; Wagner, N. J.; Liu, Y., Adsorption of polysorbate 20 and proteins on hydrophobic polystyrene surfaces studied by neutron reflectometry. *Colloids Surf B Biointerfaces* **2018,** *168*, 94-102.
11. Li, P. X.; Dong, C. C.; Thomas, R. K.; Wang, Y. L., Adsorption of gemini surfactants with partially fluorinated chains at three different surfaces: neutron reflectometry results. *Langmuir* **2011,** *27* (2), 656-64.
12. Howse, J. R.; Steitz, R.; Pannek, M.; Simon, P.; Schubert, D. W.; Findenegg, G. H., Adsorbed surfactant layers at polymer/liquid interfaces. A neutron reflectivity study. *Physical Chemistry Chemical Physics* **2001,** *3* (18), 4044-4051.
13. Zhang, R.; Somasundaran, P., Advances in adsorption of surfactants and their mixtures at solid/solution interfaces. *Adv Colloid Interface Sci* **2006,** *123-126*, 213-29.
14. Thomas, R. K.; Penfold, J., Multilayering of Surfactant Systems at the Air–Dilute Aqueous Solution Interface. *Langmuir* **2015,** *31* (27), 7440-7456.
15. Grant, L. M.; Ederth, T.; Tiberg, F., Influence of Surface Hydrophobicity on the Layer Properties of Adsorbed Nonionic Surfactants. *Langmuir* **2000,** *16* (5), 2285-2291.
16. Tiberg, F., Physical characterization of non-ionic surfactant layers adsorbed at hydrophilic and hydrophobic solid surfaces by time-resolved ellipsometry. *Journal of the Chemical Society, Faraday Transactions* **1996,** *92* (4), 531-538.

17. Thirtle, P. N.; Li, Z. X.; Thomas, R. K.; Rennie, A. R.; Satija, S. K.; Sung, L. P., Structure of Nonionic Surfactant Layers Adsorbed at the Solid/Liquid Interface on Self-Assembled Monolayers with Different Surface Functionality: A Neutron Reflection Study. *Langmuir* **1997,** *13* (20), 5451-5458.

18. Patrick, H. N.; Warr, G. G.; Manne, S.; Aksay, I. A., Self-Assembly Structures of Nonionic Surfactants at Graphite/Solution Interfaces. *Langmuir* **1997,** *13* (16), 4349-4356.

19. Holland, N. B.; Ruegsegger, M.; Marchant, R. E., Alkyl Group Dependence of the Surface-Induced Assembly of Nonionic Disaccharide Surfactants. *Langmuir* **1998,** *14* (10), 2790-2795.

20. Wolgemuth, J. L.; Workman, R. K.; Manne, S., Surfactant Aggregates at a Flat, Isotropic Hydrophobic Surface. *Langmuir* **2000,** *16* (7), 3077-3081.

21. Stubenrauch, C., Sugar surfactants — aggregation, interfacial, and adsorption phenomena. *Current Opinion in Colloid & Interface Science* **2001,** *6* (2), 160-170.

22. Zhang, L.; Somasundaran, P.; Mielczarski, J.; Mielczarski, E., Adsorption Mechanism of n-dodecyl-β-D-maltoside on Alumina. *Journal of Colloid and Interface Science* **2002,** *256* (1), 16-22.

23. Zhang, R.; Somasundaran, P., Aggregate Formation of Binary Nonionic Surfactant Mixtures on Hydrophilic Surfaces. *Langmuir* **2005,** *21* (11), 4868-4873.

24. Larsson, J.; Sanchez-Fernandez, A.; Mahmoudi, N.; Barnsley, L. C.; Wahlgren, M.; Nylander, T.; Ulvenlund, S., Effect of the Anomeric Configuration on the Micellization of Hexadecylmaltoside Surfactants. *Langmuir* **2019,** *35* (43), 13904-13914.

25. Larsson, J.; Sanchez-Fernandez, A.; Leung, A. E.; Schweins, R.; Wu, B.; Nylander, T.; Ulvenlund, S.; Wahlgren, M., Molecular structure of maltoside surfactants controls micelle formation and rheological behavior. *Journal of Colloid and Interface Science* **2021,** *581*, 895-904.

26. Tiberg, F.; Landgren, M., Characterization of thin nonionic surfactant films at the silica/water interface by means of ellipsometry. *Langmuir* **1993,** *9* (4), 927-932.

27. De Feijter, J. A.; Benjamins, J.; Veer, F. A., Ellipsometry as a tool to study the adsorption behavior of synthetic and biopolymers at the air–water interface. *Biopolymers* **1978,** *17* (7), 1759-1772.

28. Dalgliesh, R. M.; Langridge, S.; Plomp, J.; de Haan, V. O.; van Well, A. A., Offspec, the ISIS spin-echo reflectometer. *Physica B: Condensed Matter* **2011,** *406* (12), 2346-2349.

29. Nelson, A. R. J.; Prescott, S. W., refnx: neutron and X-ray reflectometry analysis in Python. *Journal of applied crystallography* **2019,** *52* (Pt 1), 193-200.

30. Zhang, L.; Somasundaran, P.; Maltesh, C., Adsorption of n-Dodecyl-β-d-maltoside on Solids. *Journal of Colloid and Interface Science* **1997,** *191* (1), 202-208.

31. Ericsson, C. A.; Söderman, O.; Garamus, V. M.; Bergström, M.; Ulvenlund, S., Effects of temperature, salt, and deuterium oxide on the self-aggregation of alkylglycosides in dilute solution. 2. n-Tetradecyl-beta-D-maltoside. *Langmuir: The ACS Journal Of Surfaces And Colloids* **2005,** *21* (4), 1507-1515.

32. Ericsson, C. A.; Söderman, O.; Garamus, V. M.; Bergström, M.; Ulvenlund, S., Effects of Temperature, Salt, and Deuterium Oxide on the Self-Aggregation of Alkylglycosides in Dilute Solution. 2. n-Tetradecyl-β-d-maltoside. *Langmuir* **2005,** *21* (4), 1507-1515.

33. Dupuy, C.; Auvray, X.; Petipas, C.; Rico-Lattes, I.; Lattes, A., Anomeric Effects on the Structure of Micelles of Alkyl Maltosides in Water. *Langmuir* **1997,** *13* (15), 3965-3967.

34. Stubenrauch, C.; Claesson, P. M.; Rutland, M.; Manev, E.; Johansson, I.; Pedersen, J. S.; Langevin, D.; Blunk, D.; Bain, C. D., Mixtures of n-dodecyl-β-d-maltoside and hexaoxyethylene dodecyl ether — Surface properties, bulk properties, foam films, and foams. *Advances in Colloid and Interface Science* **2010,** *155* (1-2), 5-18.

35. Larsson, J.; Leung, A. E.; Lang, C.; Wu, B.; Wahlgren, M.; Nylander, T.; Ulvenlund, S.; Sanchez-Fernandez, A., Tail unsaturation tailors the thermodynamics and rheology of a self-assembled sugar-based surfactant. *Journal of Colloid and Interface Science* **2020.**

36. Dang, F.; Hasegawa, T.; Biju, V.; Ishikawa, M.; Kaji, N.; Yasui, T.; Baba, Y., Spontaneous Adsorption on a Hydrophobic Surface Governed by Hydrogen Bonding. *Langmuir* **2009**, *25* (16), 9296-9301.

Electronic supporting information for

Interfacial behaviour and structure of sugar-based surfactants at the solid-liquid interface

Johan Larsson,[a] Marie Wahlgren[b], Adrian Sanchez-Fernandez,[b] Anna Leung,[c] Jos Cooper,[d] Nina-Juliane Steinke,[d] Stefan Ulvenlund,[b,e] Tommy Nylander[a,f,g]
[a]Physical Chemistry, Department of Chemistry, Lund University, Box 124, 221 00 Lund, Sweden.
[b]Food Technology, Nutrition, and Engineering, Lund University, Box 124, 221 00 Lund, Sweden.
[c]European Spallation Source, Box 176, 221 00 Lund, Sweden.
[d]ISIS Spallation Source, STFC, Rutherford Appleton Laboratory, Didcot, UK.
[e]Enza Biotech AB, Scheelevägen 22, 22363 Lund, Sweden.
[f]NanoLund, Lund University, Lund, Sweden.
[g]LINXS - Lund Institute of Advanced Neutron and X-ray Science, IDEON Building: Delta 5, Scheelevägen 19, 22370 LUND, Sweden

Results

After surfactant adsorption on hydrophobized silica the surface was rinsed to monitor the desorption of 20 µM β-$C_{16}G_2$ at 30 °C in D_2O with NR (Figure S1). After several hours of rinsing the clean silanized surface was recovered.

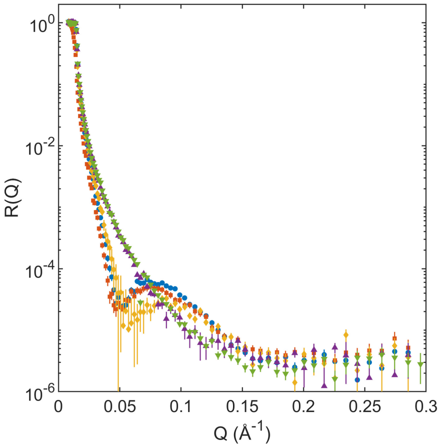

Figure S1. NR for 20 µM β-$C_{16}G_2$ at 30 °C in D_2O at different stages during rinsing. Before rinse (blue ○), first (red □), second (yellow ◊) and third (purple △) measurement after start of rinse. Bare surface before adsorption is included for reference (green ▽).

The kinetics of the adsorption of β-$C_{12}G_2$ at the hydrophobized silica interface at 25 °C is presented in Figure S2.

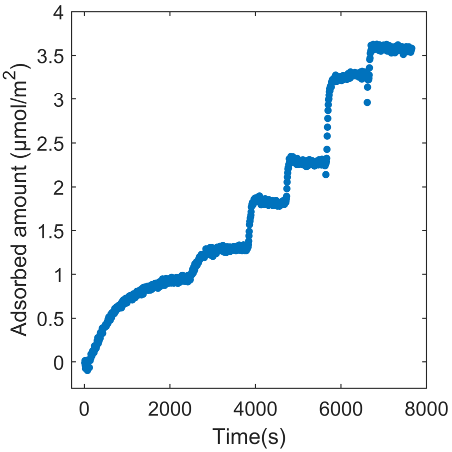

Figure S2. Adsorption kinetics for β-$C_{12}G_2$ at 25 °C on the hydrophobized silica surface determined by ellipsometry. The sample concentration was step-wise increased (0.5, 1, 3, 10, 100 and 1000 µM) with consecutive additions at the following times 84, 2455, 3792, 4688, 5627, 6616, 7891, 8727, 10097 s.

The structure of the adsorbed film of mixtures of α- and β-$C_{16}G_2$ at 20 µM and 30 °C was investigated with NR, see Figure S3 and Table S1. It was fitted with a one-layer surfactant model.

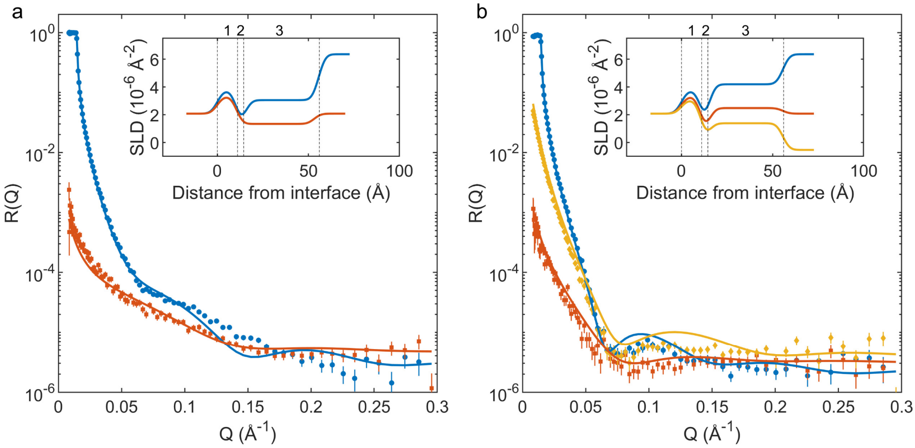

Figure S3. Neutron reflectivity results for adsorption of mixtures of α- and β-$C_{16}G_2$ at 20 µM and 30 °C, (a) protiated surfactants and (b) protiated β-$C_{16}G_2$ and tail deuterated α-$C_{16}G_2$ in D_2O (blue ○), CMSI (red □), and H_2O (yellow ◊) on hydrophobized silica. The solid lines represent the theoretical fit. The insets display the SLD profile as a function of distance from the Si interface based on the fitted model and the dashed lines and numbers show the different layers in the model.

The structure of the adsorbed film tail deuterated β-$C_{12}G_2$ at 20 µM and 30 °C was investigated with NR, see FigureS4 and TableS1.

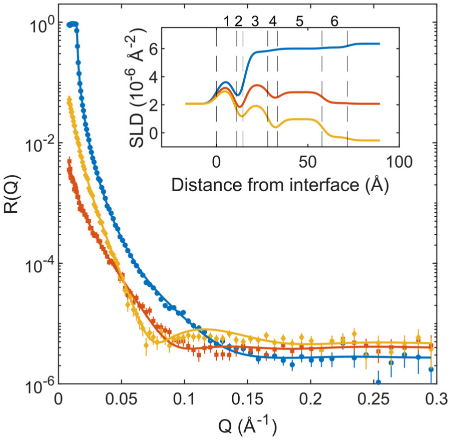

Figure S4. Neutron reflectivity results for adsorption of tail deuterated β-$C_{12}G_2$ at 20 µM and 30 °C in D_2O (blue ○), CMSI (red □), and H_2O (yellow ◊) on hydrophobized silica. The solid lines represent the theoretical fit. The insets display the SLD profile as a function of distance from the Si interface based on the fitted model and the dashed lines and numbers show the different layers in the model.

Table S1. Thickness and solvent content in the layers of the model that best fits the experimental NR data for β-$C_{16}G_2$ and α-$C_{16}G_2$.

		α- and β-$C_{16}G_2$ mixture		β-$C_{12}G_2$	
		Layer thickness (Å)	Solvent (v/v,%)	Layer thickness (Å)	Solvent (v/v,%)
1	SiO_x	11.1±0.4	10±2	11.1±0.4	10±2
2	Silane	3.4±0.9	10±3	3.4±0.9	10±3
3	Surfactant	41.1±0.2	32±3	13.5±0.3	46.3±0.8
4	Inner maltoside			5.4±0.3	83±3
5	Surfactant in micelle			24.3±0.7	67.7±0.7
6	Outer maltoside			14.0±3.0	90±2

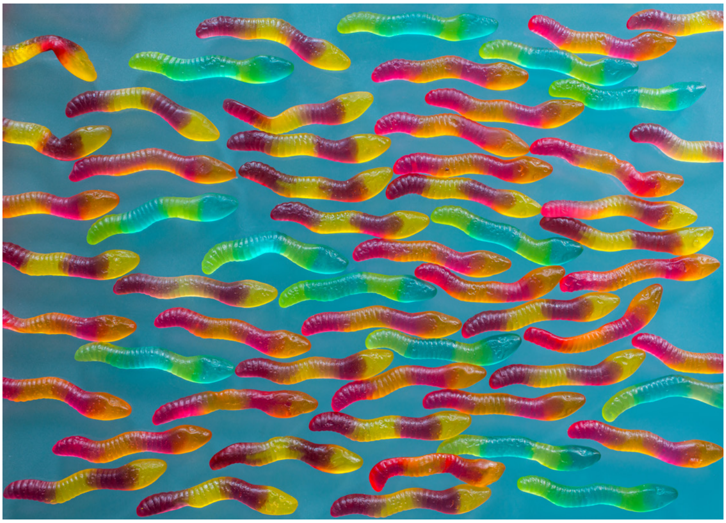

Sugar-based surfactants, or alkylglycosides, is a sustainable class of surfactants that is a promising candidate to replace the fossil-based surfactants that are mostly used today. To utilize them to their full potential more knowledge is required about their performance. In this thesis the behaviour of the alkylglycoside $C_{16}G_2$, and how its behaviour is affected by small changes in its molecular structure, has been studied. The anomeric configuration was found to have a large impact as β-$C_{16}G_2$ was found to have higher adsorption at surfaces and form more elongated cylindrical micelles than α-$C_{16}G_2$. The worm-like micelles of β-$C_{16}G_2$ gave highly viscous, shear thinning and viscoelastic solutions, in difference to α-$C_{16}G_2$ that had much lower viscosity. The effect of introducing a double bond in the tailgroup of β-$C_{16}G_2$ was also investigated, where a significant decrease in the Krafft point was seen, while the formation of elongated micelles and viscous solutions was still evident.

Printed by Media-Tryck, Lund 2021
NORDIC SWAN ECOLABEL 3041 0903

LUND
UNIVERSITY

ISBN: 978-91-7422-776-5

Physical Chemistry
Faculty of Science
Lund University